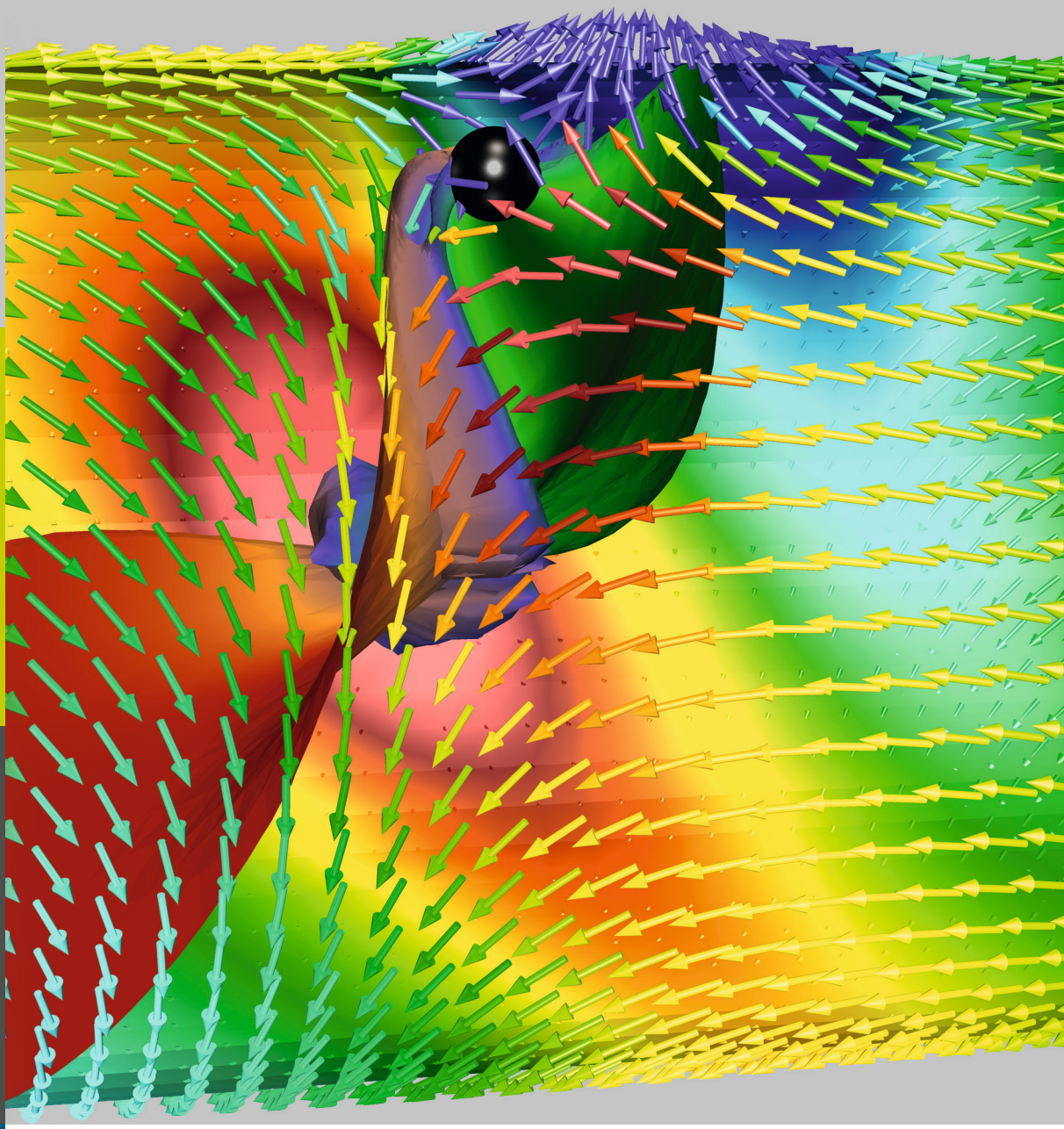

# Multiscale Multimodel Simulation of Micromagnetic Singularities

Christian Andreas

Member of the Helmholtz Association

JÜLICH
FORSCHUNGSZENTRUM

Schriften des Forschungszentrums Jülich
Reihe Schlüsseltechnologien / Key Technologies Band / Volume 88

Forschungszentrum Jülich GmbH
Peter Grünberg Institute (PGI)
Electronic Properties (PGI-6)

# Multiscale Multimodel Simulation of Micromagnetic Singularities

Christian Andreas

Schriften des Forschungszentrums Jülich
Reihe Schlüsseltechnologien / Key Technologies Band / Volume 88

ISSN 1866-1807 ISBN 978-3-89336-983-6

Bibliographic information published by the Deutsche Nationalbibliothek.
The Deutsche Nationalbibliothek lists this publication in the Deutsche Nationalbibliografie; detailed bibliographic data are available in the Internet at http://dnb.d-nb.de.

| | |
|---|---|
| Publisher and Distributor: | Forschungszentrum Jülich GmbH<br>Zentralbibliothek<br>52425 Jülich<br>Tel: +49 2461 61-5368<br>Fax: +49 2461 61-6103<br>Email: zb-publikation@fz-juelich.de<br>www.fz-juelich.de/zb |
| Cover Design: | Grafische Medien, Forschungszentrum Jülich GmbH |
| Printer: | Grafische Medien, Forschungszentrum Jülich GmbH |
| Copyright: | Forschungszentrum Jülich 2014 |

Schriften des Forschungszentrums Jülich
Reihe Schlüsseltechnologien / Key Technologies, Band / Volume 88

D 464 (Dissertation, Universität Duisburg-Essen/Université de Strasbourg, 2014)

ISSN 1866-1807
ISBN 978-3-89336-983-6

The complete volume is freely available on the Internet on the Jülicher Open Access Server (JUWEL) at www.fz-juelich.de/zb/juwel

# Abstract

During the last decades, the research on fundamental magnetic structures, like domain walls, spinwaves and vortices, resulted in a detailed understanding of the magnetization dynamics in ferromagnetic materials, without which the development of modern storage devices would not have been possible. On the pathway to this level of understanding micromagnetic simulations played an important role due to their ability to reproduce experimental results in great detail and, especially, to predict magnetic patterns and their dynamic properties. An example of the predictive power is the research field of vortex dynamics. Another fundamental magnetic structure is the Bloch point, which is particularly complex since the description of the processes and energy terms responsible for its formation lie within the scope of the continuum theory of micromagnetism, but the study of its detailed properties requires a different framework. In terms of topology and concerning the exchange energy density, the Bloch point displays a point singularity in the theory of micromagnetism.

Bloch points are not a marginal phenomenon; they play, *e.g.*, an important role as transient structures during the switching of vortex cores and reside inside of the archetypal example of vortex domain walls in solid cylindrical nanowires. In the 1960s, E. Feldtkeller and W. Döring described and characterized Bloch points with the then available methods, yet their dynamics eluded a detailed description, since on one hand a large volume is necessary to stabilize a Bloch point structure and on the other hand an atomistic description of its center is required. To solve this problem we developed a multiscale multimodel simulation framework in the context of this thesis, which is able to detect automatically Bloch points as well as other micromagnetically critical structures. In that simulation kit we apply a classical Heisenberg model to the critical regions, while using the framework of micromagnetism for the remaining sample, which is discretized with finite elements. The program allows not only for a static examination of Bloch points residing in a localized Heisenberg approximated region, but also for dynamic simulations due to its ability to detect regions of interest automatically as well as to track them with the multimodel region.

The simulations within this thesis focus on ferromagnetic cylindrical nanowires with vortex domain walls. The simulations describe the depinning field necessary to trigger a propagation of the domain wall with the Bloch point in its center and the impact of the relative orientation of the lattice to the Bloch point propagation direction. In addition, we could identify different propagation patterns of the structure consisting of domain wall and Bloch point. In addition to regimes with a continuous domain wall movement, this thesis highlights and discusses several complex modes of domain wall/Bloch point propagation. In particular, we find a propagation regime in which the Bloch point and domain wall propagate with constant velocity above the minimum spin wave phase velocity. This velocity remains constant within a broad interval of external field strength. Using analytic calculations we could ascribe this maximum velocity, which is a feature of potential interest from a technological perspective, to an intrinsic property of the Bloch point.

In a second part of the study, we show with our simulations that the Bloch point structure has preferential positions within the atomic lattice, and that it has a strong

tendency to remain on the facets of the Wigner-Seitz cell of the atomic lattice. This is not only true for its equilibrium configuration but also during its propagation. Hence, the degree of freedom of the Bloch point is reduced to a two-dimensional surface. By means of high resolution simulations in space and time we identify the possible pathways along which a Bloch point can propagate inside the lattice. By this, for the first time, a detailed description of the Bloch point propagation directions becomes possible.

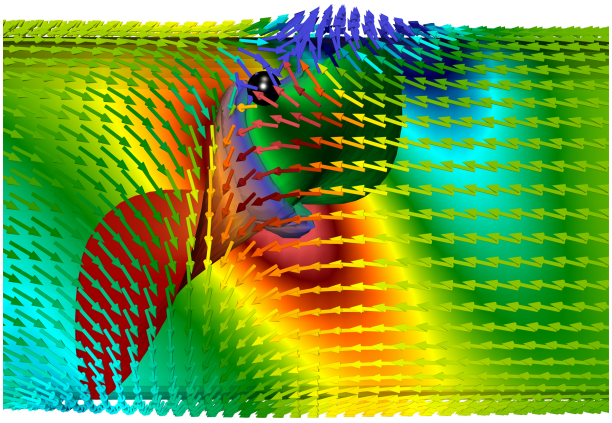

A Bloch point (black sphere) propagating in a vortex domain wall with bad chirality can leave the sample, which results in a structural change of the domain wall. The rainbow color scale represents the Skyrmion number density on the surface of the sample at the moment of the Bloch point expulsion.

# Zusammenfassung

Die Erforschung der fundamentalen magnetischen Strukturen, angefangen von Domänen über Spinwellen bis hin zu Wirbeln, hat in den vergangenen Jahrzehnten zu einem detaillierten Verständnis der Magnetisierungsdynamik in ferromagnetischen Materialien geführt, ohne das moderne Speichermedien nicht denkbar wären. Um zu diesem Verständnis zu gelangen, spielten mikromagnetische Simulationen eine große Rolle, welche nicht nur in der Lage waren, experimentelle Resultate mit großer Genauigkeit zu reproduzieren, sondern auch Vorhersagen über neue Strukturen und deren Dynamik zu treffen. Ein Beispiel dieser Vorhersagekraft ist die Wirbeldynamik. Eine weitere fundamentale Struktur neben den oben genannten ist der Blochpunkt, dessen Existenz zwar vom Mikromagnetismus erfasst wird, aber nicht vollständig beschrieben werden kann, da Blochpunkte eine Singularität in dieser Theorie darstellen.

Blochpunkte treten zum einen beim Schalten von Wirbelkernen als temporäre Struktur und zum anderen als Kern der Wirbeldomänenwand in zylindrischen Drähten auf. Im Rahmen der damals bestehenden Möglichkeiten wurden sie bereits in den 60er Jahren theoretisch von E. Feldtkeller und W. Döring beschrieben, jedoch entzog sich ihre Dynamik einer detaillierten Betrachtung, da einerseits ein großes Volumen zur Stabilisierung und andererseits eine atomistische Beschreibung des Kerns notwendig ist. Aus diesem Grund wurde im Rahmen der vorliegenden Arbeit ein Multiskalen- Multimodellsimulationsprogramm entwickelt, das automatisch sowohl Blochpunkte als auch andere mikromagnetisch kritische Strukturen detektiert und diese im Rahmen eines klassischen Heisenbergmodells simuliert, während die restliche Probe mikromagnetisch mit der Methode der finiten Elemente untersucht wird. Dieses Programm ermöglicht nicht nur eine statische Untersuchung von Blochpunkten mit einer lokalisierten heisenbergmodellierten Region, sondern auch und insbesondere dynamische Untersuchungen der Blochpunktdynamik, da es eine automatische Verfolgung derselben implementiert.

Die Simulationen beziehen sich auf ferromagnetische zylindrische Drähte, in denen sich Wirbeldomänenwände ausbilden. Die durchgeführten Simulationen beschreiben quantitativ das notwendige magnetische Ablösungsfeld, um eine Bewegung des Blochpunkts und der umgebenden Wand hervorzurufen, und identifizieren verschiedene Propagationsmoden des Systems aus Blochpunkt und Domänenwand. Neben solchen Moden, in denen eine kontinuierliche Bewegung beobachtet werden kann, ergeben sich aus den Simulationen mehrere spezielle Bewegungsmuster, die in der vorliegenden Arbeit detailliert diskutiert werden. Besonders herauszuheben ist der technologisch wahrscheinlich interessanteste Bereich, in dem die Einheit aus Blochpunkt und Domänenwand über ein breites Intervall externer Feldstärken und Drahtdurchmesser eine konstante und hohe Geschwindigkeit oberhalb der minimalen Spinwellenphasengeschwindigkeit annimmt. Eine solche konstante Geschwindigkeit wird im Rahmen dieser Arbeit durch analytische Rechnungen auf eine intrinsische Eigenschaft des Blochpunkts zurückgeführt.

Ferner zeigen die Simulationen, dass das Zentrum eines Blochpunkts sowohl in Ruhe als auch während einer Propagation auf der Oberfläche der Wigner-Seitzzelle des atomaren Gitters liegt, wodurch seine Bewegungsfreiheit auf eine Oberfläche ein-

geschränkt ist. Aus zeitlich und räumlich hoch aufgelösten Rechnungen ergeben sich die möglichen Pfade, entlang derer ein Blochpunkt propagieren kann, wodurch eine vertiefte Beschreibung seines Verhaltens in den verschiedenen Propagationsrichtungen möglich wird.

# Résumé Français

La compréhension des structures magnétiques à l'échelle micro- et nanoscopique a fait des progrès fulgurants dans le dernier siècle. Les techniques pour améliorer les connaissances scientifiques ainsi que la motivation pour ce domaine de recherche n'ont cessé d'augmenter. Tandis qu'au début du XX$^{\text{ème}}$ siècle la recherche sur les structures magnétiques était essentiellement d'intérêt fondamental, elle est devenue plus orientée vers les applications technologiques dans les dernières décades. Avec l'établissement de la théorie du micromagnétisme dans les années 60 [1–5] un cadre mathématique est devenu disponible pour l'étude théorétique des structures magnétiques. Les résultats obtenus avec cette théorie du continu sont en accord parfait avec les structures en domaines observées expérimentalement dans les matériaux ferromagnétiques, comme des parois en domaines [6–8], des vortex [9, 10], ou des ondes de spin. Normalement, la structure atomique peut être négligée car les échelles de longueur (largeur d'une paroi, taille d'un vortex etc.) de ces configurations magnétiques sont entre 10 et 100 nm, bien au-delà de la taille de la maille atomique. La seule exception en ce qui concerne la fiabilité des simulations effectuées dans le cadre du micromagnétisme sont les singularités micromagnétiques appelées points de Bloch [11, 12] où l'aimantation change sa direction de 180° dans une constante de réseau au centre de la structure. Si le calcul était fait dans le cadre du micromagnétisme, la densité d'énergie d'échange montrerait une singularité car cette théorie ne considère pas la structure atomique de la matière. Par conséquent, les points des Bloch représentent des défauts topologiques qui ne peuvent pas être étudiés correctement dans le seul cadre de la théorie du micromagnétisme. Les points de Bloch se forment, par exemple, comme des structures temporaires pendent le renversement de l'aimantation dans les cœurs de vortex [9], quand des domaines du type « bubble » sont nucléés [13], ou dans le cas archétype du renversement de l'aimantation dans des cylindres formés de matériaux magnétiques doux [14].

Même si les équations fondamentales du micromagnétisme sont bien connues, il est très compliqué de les utiliser pour obtenir des solutions pour la structure de l'aimantation, au moins analytiquement. Déjà le calcul de la dynamique de l'aimantation dans le cas d'une seule paroi magnétique dans un nano-ruban ferromagnétique mince ne peut être traitée analytiquement qu'en utilisant des fortes simplifications et approximations et, donc, nécessite des approches numériques pour des prédictions plus fiables. Les méthodes numériques les plus diffusées se distinguent par leurs méthodes de discrétisation, connues sous le nom de *différences finies* et *éléments finis*.

L'approche des différences finies se base typiquement sur un réseau régulier des cellules de discrétisation équidistantes de forme cubique ou de parallélépipède. Avec cette approche, il est relativement simple d'approximer des opérations de différentiations spatiales ainsi que des intégrations en utilisant des quotients de différences. On rencontre des difficultés au périmètre des échantillons si leur géométrie contient des surfaces qui ne suivent pas exactement les bords des cellules de discrétisation. Dans ces cas-là, on utilise typiquement une approximation dite « escalier » qui peut induire des effets numériques faux plus au moins prononcés. Contrairement à la méthode des différences finies, le système de discrétisation de la méthode des éléments finis (FEM

– Finite Element Method) utilise des points de discrétisation qui peuvent être placés dans des positions ajustables. Ceci permet d'approximer la forme d'un échantillon de façon bien plus précise, en plaçant une partie des nœuds, c'est-à-dire les points de discrétisation, exactement sur les bords de l'échantillon. Les nœuds sont typiquement connectés par des lignes ou par des éléments de bord. Les logiciels de simulation micromagnétiques, basés soit sur les différences finies [15] ou sur les éléments finis [16] développés dans les dernières décennies ont démontrés clairement leur précision et leur capacité avérée de fournir des prédictions fiables pour plusieurs structures magnétiques.

Dans la première moitié du XX$^{\text{ème}}$ siècle, les structures magnétiques à l'échelle micro- et nanométrique n'étaient que d'intérêt fondamental ; mais les requêtes liées au progrès de la technologie du stockage de l'information ont joué un rôle moteur dans la recherche durant les dernières dizaines d'années. En plus de cet intérêt lié au stockage de données dans des couches minces magnétiques, comme par exemple sur des disques ou des bandes magnétiques, une approche précoce visait l'utilisation de structures magnétiques plus complexes, où des structures magnétiques en forme de bulles « bubbles » (couches magnétiques avec anisotropie perpendiculaire qui permettent le renversement local de l'aimantation dans des régions circulaires) [13] étaient considérées comme unités d'information. Cependant, les obstacles technologiques des dispositifs à base de structures bubble étaient plus hauts que ceux que l'on devait surmonter pour obtenir la haute densité de stockage de données qui est aujourd'hui utilisé de façon commode dans la technologie des disques durs. Si la demande pour une augmentation de densité de stockage de données continue d'augmenter, une transition pourrait devenir nécessaire qui amènerait à un nouveau concept de stockage qui serait différent de la solution de stockage à deux dimensions sur des disques rotatifs. L'extraction et l'écriture de grandes quantités de données nécessitent aussi des niveaux de vitesse d'opération élevées des dispositifs. Ceci représente un sujet passionnant pour la recherche fondamentale aussi bien que pour la recherche industrielle.

Un candidat pour l'avenir des dispositifs de stockage est la mémoire du type « racetrack » proposé par S. Parkin en 2008 [17]. Dans ce système, une chaîne de parois en domaines dans un nano-ruban magnétique, qui servent comme unités d'information, est déplacée par un courant électrique polarisé en spin. Grâce au couple du transfert de spin, les domaines et les parois peuvent être déplacées vers les dispositifs de lecture et d'écriture sans aucun mouvement mécanique. Cette méthode aurait le potentiel de remplacer les disques magnétiques rotatifs qui sont actuellement utilisés dans les dispositifs de disques durs modernes. Un « racetrack » bidimensionnel peut être représenté par un registre de décalage constitué, par exemple, d'un réseau de rubans ferromagnétiques minces déposés sur un substrat, typiquement préparé avec des méthodes de lithographie électronique. D'autre part, des nanofils cylindriques pourraient être très prometteurs pour une version tridimensionnelle d'une mémoire de type racetrack, où les propriétés particulières des parois de vortex pourraient être exploitées. Un arrangement perpendiculaire des nanofils pourrait augmenter la densité de stockage de manière significative. Dans le cas de nanotubes magnétiques des études récents [18, 19] conduites avec des simulations numériques basées sur la théorie du micromagnétisme ont démontré que ce type de parois est extrêmement stable et

qu'il peut atteindre des vitesses au-delà de 1000 m/s sans subir des instabilités structurelles ou des turbulences. Dans une expérience de pensée, la réduction du diamètre interne d'un nanotube comprenant une paroi du type vortex mènerait à une transition géométrique vers un nanofil solide. Ceci aurait pour conséquence la formation d'un point dans le centre de la paroi qui ne représente pas seulement le centre de la paroi frontale, avec deux directions axiales opposées (head-to-head ou tail-to-tail), mais aussi le centre de la structure en vortex autour de ce point. Toutes les directions possibles peuvent être trouvées dans la proximité de ce point, ce qui correspond exactement à la définition d'un point de Bloch selon A. Hubert [20] et est en même temps l'exemple archétypique discuté ci-dessus d'un point de Bloch dans un nanocylindre ferromagnétique [21, 22].

La description des structures magnétiques fortement inhomogènes, comme les points de Bloch, dépasse les limites de validité de la théorie du continu. Ces structures doivent être étudiées avec des modèles atomistiques, surtout si les inhomogénéités magnétiques ont lieu à des échelles de longueurs similaires à la constante du réseau atomique [23]. Dans le cadre de cette thèse, nous avons fait un premier pas vers la formulation analytique nécessaire à l'établissement d'un lien entre les propriétés micromagnétiques, définies par l'aimantation de saturation et la constante d'échange, et un modèle de Heisenberg, décrit par un ensemble de paramètres d'échange, de la structure atomique, de la constant du réseau et du nombre de magnetons de Bohr par site atomique. Pour obtenir un critère avec lequel on peut identifier ces structures fortement inhomogènes, nous avons d'abord étudié le cas d'une spirale régulière et homogène, ce qui permette un traitement analytique. Pur l'étude de cette spirale de spin, nous avons considéré le Permalloy, un matériau avec des propriétés bien connues (aimantation de saturation de 1,0 T et constante d'échange de $1{,}3 \cdot 10^{-11}$ J/m) et une structure cristalline cubique à corps centré (bcc) correspondante à celle de la phase $\alpha$ du fer. Avec ce système nous avons analysé les erreurs systématiques induites par le micromagnétisme par rapport au modèle classique de Heisenberg. Ces résultats nous ont conduits à la conclusion que les erreurs systématiques diminuent rapidement avec la longueur d'onde de la spirale, notamment à 1 % pour une longueur de 9, et à 0,1 % pour une longueur de 29 constantes de réseau. Des erreurs de cet ordre de grandeur sont tolérables et nous utilisons ce critère pour estimer la taille de la région qui doit être simulée avec un modèle de Heisenberg dans le cas d'une forte inhomogénéité dans la structure magnétique. L'une des études multi-échelle les plus pertinentes a été rapportée par Jourdan et al. [24, 25]. Dans cette étude, les auteurs ont combiné un modèle de Heisenberg à un modèle micromagnétique. Ils ont utilisé une méthode de différences finies comme maille de base avec un raffinement du maillage jusqu'à la taille d'une constante de maille atomique dans la proximité des « zones d'intérêt », c'est-à-dire un point de Bloch, pour étudier la configuration d'équilibre du point de Bloch. Au début de cette thèse, aucune méthode numérique multi-échelles capable d'étudier la dynamique des points de Bloch se propageant dans un échantillon n'avait encore été rapportée.

Nous avons donc développé un pack de simulations multi-échelles et multi-modèles qui opèrent entièrement sur des cartes graphiques, en utilisant le cadre CUDA. Dans ce pack de simulations, l'interaction d'échange est traitée avec un modèle atomistique

de Heisenberg dans la proximité du point de Bloch, alors que la structure magnétique dans le reste de l'échantillon est calculée en utilisant le logiciel micromagnétique TetraMag [26] préalablement développé dans notre équipe et également optimisé pour l'utilisation de CUDA. Le fait que les points de Bloch et ainsi que d'autres structures fortement inhomogènes se forment et se propagent dynamiquement nous a conduit à encapsuler les régions qui sont calculées avec le modèle de Heisenberg dans une région de transition sphérique bien définie dans laquelle les modèles atomistiques et du continu sont utilisés. Cette transition sert à connecter la région de Heisenberg avec la structure micromagnétique avoisinante. Ces sphères de multi-modèles peuvent être ajoutés, enlevées, ou déplacées au fur et à mesure dans l'échantillon micromagnétique. Les processus d'insertion, déplacement ou suppression sont effectués automatiquement par le logiciel. Ceci permet de suivre exactement la position d'un point de Bloch pendant la propagation. Dans un processus de synchronisation, la maille d'éléments finis imprime l'orientation de l'aimantation sur le bord de la sphère multi-modèle. Simultanément, la région atomique dans la sphère multi-modèle passe l'information sur l'orientation de l'aimantation vers les nœuds dans le volume de la sphère. Cette synchronisation bidirectionnelle est décrite en détail dans la section 6.4.

La structure de la sphère multi-modèle consiste en trois entités :

1. Un noyau avec un rayon d'environ 30 mailles atomiques où l'orientation des moments magnétiques est calculée en utilisant un modèle de Heisenberg.

2. Une région de transition ayant la forme d'une coquille sphérique avec une épaisseur de quelque dizaine de mailles atomiques. Dans cette coquille, les deux modèles sont appliqués pour le calcul de l'interaction d'échange. Grâce à une interpolation soigneusement calibrée et à une procédure de pondération qui considère la position, nous obtenons une transition entre les deux modèles sans heurts.

3. Une coquille externe sphérique d'environ 10 nm d'épaisseur où seulement le modèle micromagnétique est appliquée. Dans cette région une variation graduelle et très prononcée de la taille des éléments finis est effectuée ; Celle-ci évolue d'une taille correspondant à la maille atomique jusqu'à la taille de base du maillage de l'échantillon (typiquement plusieurs nanomètres).

Cette structure assure en premier lieu que les calculs dans un volume de taille suffisante soient effectués en utilisant le model précis de Heisenberg et, deuxièmement, elle garantit la compatibilité des deux modèles, ce qui exclue la possibilité d'erreurs numériques importantes. Troisièmement, cette approche permet que les nœuds d'un maillage A ne reçoivent des informations sur l'orientation de l'aimantation ou des moments magnétiques d'un maillage B que si la taille de la maille B est au moins aussi petite que les cellules de Voronoi entourant le nœud. Ce dernier point est assuré seulement pendant que la sphère multi-modèle se trouve entièrement à l'intérieur de l'échantillon, mais au moment où le point de Bloch approche la surface de l'échantillon, on peut rencontrer une situation où une partie de la sphère sort du volume de l'échantillon. Dans cette situation la partie de la sphère multi-modèle qui se trouve à l'extérieur est désactivée pour préserver la forme de l'échantillon. La surface de la

sphère multi-modèle est formée par des nœuds avec des cellules de Voronoi qui sont bien plus petites que les cellules de base qui fournissent l'information sur la direction de l'aimantation [27]. Pour traiter cette situation, nous avons développé des zones de raffinement de maillage prédéfinies que nous appelons « calottes ». Ces structures agissent comme une couche de maillage supplémentaire appliquée au bord de l'échantillon et capable de combler efficacement l'écart de taille entre les cellules du maillage de base et le maillage partiel de la sphère multi-modèle qui reste à l'intérieur. Dans le cas de fils cylindriques, une seule forme de calottes est suffisante, grâce à la symétrie. La discrétisation des zones de calotte est effectuée avec des maillages différents ayant des distributions de nœuds adaptés à une certaine distance entre la sphère multi-modèle et la surface. Nous préparons plusieurs calottes ; Chacune correspond à un intervalle de distance de la sphère et le choix de la carotte se fait de façon interchangeable en fonction de la distance entre le centre de la sphère et la surface. Or, ces zones peuvent faire le pont entre les tailles très différentes des mailles qui se produisent à la surface dès qu'une sphère multi-modèle sort partiellement du volume de l'échantillon.

L'équation de Landau-Lifshitz-Gilbert [28–30] définie l'évolution temporelle de l'orientation magnétique locale, c'est-à-dire, de la direction de l'aimantation dans les régions traitées dans la théorie du continu. Il suffit d'ajouter des changements mineurs pour appliquer l'équation afin de calculer l'orientation des moments magnétiques dans le modèle de Heisenberg. Nous utilisons le solveur d'équations CVODE de la bibliothèque numérique SUNDIALS [31] pour l'intégration numérique de l'équation de Landau-Lifshitz-Gilbert dans les deux modèles.

Le kit de simulations multi-modèles a été testé soigneusement pour plusieurs cas. Le premier test adresse la possibilité d'artéfacts induits par la présence de la sphère multi-modèle avec ses multiples étapes d'interpolation par rapport à un cas traité sans la sphère multi-modèle, en utilisant des simulations micomagnétiques usuelles. Pour cela, le cas de la giration d'un vortex dans un disque ferromagnétique est traité. Ce système est bien compris et largement documenté dans le cadre du micomagnétisme classique [32–34]. Avec ce test nous démontrons que les différences entre les résultats obtenus avec les deux logiciels, le calcul purement micromagnétique d'un côté et celui de multi-modèle, est négligeable. Un second test est utilisé pour examiner des changements d'énergie liés à la génération, la suppression et le déplacement de plusieurs sphères multi-modèles. Pour ce test nous avons utilisé un cylindre court, avec un seul domaine d'aimantation homogène. Ce test montre que les erreurs numériques introduites par la méthode correspondent à l'effet d'un champ avec des fluctuations aléatoires inférieures à 0,1 mT. Ces fluctuations sont tolérables puisque les champs externes typiquement appliqués dans cette thèse sont entre 1 mT et 100 mT.

Pour étudier la dynamique des points de Bloch, nous avons choisi deux systèmes contenant des parois du type vortex dans des nanofils cylindriques de Permalloy de 4 µm de longueur, ayant des diamètres de 60 nm et 80 nm. Cette différence de diamètre nous permet de nous assurer que les effets observés ne sont pas restreints à un ensemble spécifique de paramètres. La géométrie cylindrique nous permet d'examiner la structure magnétique d'équilibre statique d'une paroi avec un vortex contenant un point de Bloch au centre ainsi que les propriétés dynamiques de ce système. Pour cela,

nous avons simulé la dynamique qui se développe sous l'effet d'un champ magnétique appliqué dans la direction axiale.

En premier lieu, nos études étaient focalisées sur la structure du point de Bloch à l'équilibre statique, c'est-à-dire, sans champ magnétique externe. À cet effet nous avons analysé la structure de la paroi en domaine en fonction de la distance au point de Bloch. Dans ce cas, deux variables sont particulièrement intéressantes : l'angle du flux magnétique (in-flow angle) $\gamma$ et la largeur de la paroi. La valeur absolue de $\gamma$ correspond à la composante radiale de l'aimantation sur l'iso-surface $m_z = 0$ de la paroi, où l'axe z correspond à l'axe du cylindre. Le signe de $\gamma$ représente une mesure de l'hélicité du point de Bloch. Dans la plupart des études sur la structure des points de Bloch rapportées dans la littérature [11, 12, 35, 36] l'angle $\gamma$ est le seule paramètre libre avec lequel la structure du point de Bloch est modélisée, et on suppose généralement que la valeur de $\gamma$ est isotrope.

Nos résultats montrent que la valeur d'équilibre calculée en utilisant le cadre multi-modèle dépend effectivement de la distance au point de Bloch. En outre, nos résultats prouvent que ce n'est que dans la proximité immédiate du point de Bloch (dans l'ordre de quelques nanomètres) que la valeur de $\gamma$ peut être considérée comme étant isotrope et donc comparable à des estimations précédentes, où la structure avait été calculée en utilisant un modèle du continu. Pour des cylindres avec un petit diamètre l'angle du flux $\gamma$ ne change que de quelque dégrée, mais la variation spatiale augmente fortement dans des cylindres de plus grand diamètre. La seconde variable importante est la largeur locale de la paroi, qui est proportionnelle à la dérivée $\mathrm{d}m_z/\,\mathrm{d}z$ sur l'iso-surface $m_z = 0$. Dû au changement de l'orientation magnétique de 180° dans une seule maille atomique au centre du point de Bloch, la largeur de la paroi possède intrinsèquement une forte dépendance radiale. Selon des modèles analytiques qui supposent une valeur isotrope de $\gamma$ la largeur de la paroi, par conséquence, augmente de façon linéaire avec la distance $r$. Avec l'approche multi-modèle, nous avons pu montrer que la largeur de la paroi augmente de façon fortement non-linéaire et bien plus rapidement que ne l'avait prédit les modèles analytiques précédents (voir aussi chapitre 9).

Du point de vue atomistique, une topographie d'énergie d'échange peut être définie à l'intérieur d'une cellule atomique. Un tel profil spatial de l'énergie mène à des positions interatomiques préférentielles et défavorables pour le point de Bloch [37]. Il est donc simple de prédire que pour le déplacement d'un point de Bloch selon l'axe du nanocylindre ferromagnétique, son axe facile, un champ minimal d'une valeur non-nulle soit nécessaire pour initialiser la propagation du point de Bloch. En exécutant des simulations où le champ externe est supposé augmenter lentement et de façon continue avec le temps, nous avons calculé le champ de depiégeage pour des orientations différentes de la maille atomique par rapport à l'axe du cylindre et pour des interactions différentes des moments magnétiques avoisinants. Si l'on ne considère qu'une interaction entre plus proches voisins, nous avons identifié un champ de depiégeage relativement haut, de l'ordre de 1,8 mT lorsque l'axe du cylindre est dans la direction (100) du réseau atomique. Par contre, des champs considérablement inférieurs, d'environ 0,4 mT, sont obtenus dans le cas d'une orientation de l'axe du cylindre selon (110) et (111). En utilisant des modèles plus complexes, ou pas seulement les plus proches

voisins sont considérées mais une totalité de dix coquilles atomiques correspondant à 144 voisins dans le cas d'un réseau bcc, nous avons trouvé une réduction importante du champ de depiégeage dans la direction (100), mais pas de changements notables du champ de depiégeage dans la direction (110) et (111). Ces résultats permettent de conclure que la structure atomique joue un rôle important, particulièrement dans le cas où les champs externes sont faibles.

Ayant l'information sur le champ de depiégeage, nous avons analysé la dynamique du point de Bloch sous l'influence de champs plus élevés qui entament une propagation de l'ensemble de la paroi et le point de Bloch. Dans le cas de nanocylindres, pour des raisons de symétrie (voir aussi chapitre 11), il existe deux chemins distincts pour la dynamique de parois du type vortex pouvant être distingués selon leur bonne ou mauvaise chiralités, par analogie avec des études précédentes sur la dynamique de parois en vortex dans des nanotubes [18, 19]. Les parois de bonne chiralité sont plus stables que celles avec une mauvaise chiralité, d'où le nom donné à ce cas.

La dynamique des parois de mauvaise chiralité est qualitativement similaire pour les nanofils de différents diamètres. Nous nous limitons donc à l'analyse des nanofils de 60 nm de diamètre. Dans ce cas-là, la dynamique se divise en trois parties : premièrement, un régime stable à bas champs; deuxièmement, un régime instable caractérisé par la décomposition de la structure de la paroi qui change de géométrie; et finalement, un régime où la chiralité se renverse. Le régime à champs faibles est stable jusqu'à des valeurs du champ externe de 4 mT. La vitesse de la paroi augmente avec la valeur du champ appliqué. Elle est d'environ 380 m/s pour un champ de 2 mT et va jusqu'à 500 m/s pour un champ de 4 mT. Nos simulations montrent que l'angle de flux $\gamma$ ainsi que l'angle $\zeta$ qui représente l'analogue de l'angle $\gamma$, mais localisé sur la surface du nanofil, augmentent avec le champ externe. Au-dessus de 4 mT, l'angle $\zeta$ atteint une valeur critique de 45°. Ceci mène à une déstabilisation de la paroi. Cet angle critique a été identifié pour le fil de 60 nm et pour le fil de 80 nm de diamètre et correspond parfaitement à l'angle critique dans le modèle de Walker [38], au-dessus duquel un changement du mode de propagation de la paroi a été prévu : le collapse de Walker (en anglais : *Walker breakdown*).

Nos simulations montrent que des champs externes capables de tourner l'aimantation sur la surface du nanofil par un angle au-dessus de $\zeta > 45°$ conduisent la paroi vers le deuxième régime. Dès que l'angle critique de $\zeta$ est atteint, une paire de vortex et anti-vortex est créé sur la surface du nanofil. Le vortex et l'anti-vortex se propagent en direction opposée l'un de l'autre sur le périmètre du fil. À partir du moment où le vortex et l'anti-vortex sont dans des positions diamétralement opposées sur la surface du fil, le point de Bloch est expulsé à proximité de l'anti-vortex. Ce processus entraîne l'inversion de l'index de skyrmion de l'anti-vortex en changeant sa polarité. Le résultat est un changement de l'index global de skyrmion vers zéro. Localement, deux régions avec une densité positive d'index de skyrmion restent autour du vortex et de l'anti-vortex. Celles-ci sont accompagnées par deux régions avec une valeur négative de densité de skyrmions. Ces deux paires de régions de charges topologiques opposées se compensent parfaitement dans leur contribution à l'index de skyrmion total. La paroi obtenue après cette conversion ressemble à l'état « C », une configuration bien connue dans des disques magnétiques doux. La paroi de type C se propage avec une

vitesse très faible, de l'ordre de quelque mètre par second, ce qui est de deux ordres de grandeur plus lent que la vitesse de propagation originale.

Dans le troisième mode de mauvaise chiralité, le champ externe déclenche une inversion de l'angle $\zeta$ avant que le vortex puisse être éjecté. Ainsi, la chiralité change de mauvaise en bonne, et après cela la paroi se propage comme dans le cas de bonne chiralité.

Les parois de bonne chiralité sont beaucoup plus stables et suppriment efficacement le « breakdown » de Walker ou l'inversion de chiralité. Elles ont des modes de propagation différents. Le premier est le régime *infra-magnonique*, dans lequel la paroi et le point de Bloch atteignent des vitesses inférieures à la vitesse de phase minimale des ondes de spin dans le nanofil. D'un autre côté, des parois et des points de Bloch qui se propagent avec une vitesse *ultra-magnonique* peuvent montrer des modes de propagation laminaires, oscillatoires, ou turbulents. Le régime infra-magnonique se produit dans le cas où les champs sont suffisamment forts pour dépasser la barrière de piégeage des points de Bloch, mais assez faibles pour que l'unité de point de Bloch et paroi ne dépasse pas la vitesse minimale de phase des ondes de spin, une valeur qui correspond à $v_{\mathrm{min}}^{\mathrm{ph}} = 1150\,\mathrm{m/s}$ pour le cylindre de 60 nm et $v_{\mathrm{min}}^{\mathrm{ph}} = 980\,\mathrm{m/s}$ pour le cylindre de 80 nm de diamètre. Ces valeurs ont été dérivées numériquement avec les relations de dispersion obtenues avec les simulations. Dans ce régime infra-magnonique nous trouvons que la mobilité du point de Bloch ou de la paroi dépend de l'orientation de l'axe du cylindre par rapport au réseau atomique. A l'équilibre, la paroi et le point de Bloch montrent une symétrie cylindrique, qui reflète la symétrie de l'échantillon. Si l'on applique un champ faible, avec une valeur juste au-dessus du champ de depiégeage, le point de Bloch et la paroi commencent à se propager le long de l'axe du cylindre en préservant la symétrie cylindrique. Une augmentation du champ externe aboutit à une vitesse supérieure de la paroi, par analogie au cas bien connu de la propagation de parois dans des nano-rubans planaires [39] ou dans des nanotubes [18]. Un peu comme les observations que nous avons faites concernant le cas du champ de depiégeage, des orientations différentes de l'axe du cylindre par rapport au réseau atomique mènent à des vitesses maximales différentes pour la même valeur du champ appliqué. Pour ces parois qui se propagent avec des vitesses infra-magnoniques nous observons un deuxième mode de propagation, au moins dans le cas du fil plus fin de 60 nm. Après une certaine période, qui devient plus longe si le champ est augmenté, le centre de la paroi présente une inclinaison qui enchaine la perte de la symétrie cylindrique. Ceci est accompagné par un changement de vitesse, un ralentissement jusqu'à environ 300 m/s, une valeur qui (dans le régime discuté ici) ne dépend ni de la valeur du champ appliqué, ni de l'orientation relative entre le champ et le réseau atomique. Ce résultat nous mène à la conclusion que deux régimes infra-magnoniques sont possibles ; chacun d'eux permet une propagation stationnaire.

Au moment où le champ externe est assez fort pour déplacer la paroi et le point du Bloch avec une vitesse ultra-magnonique, le régime de 300 m/s discuté ci-dessus devient instable et est remplacé par un nouveau mode de propagation, qui est aussi indépendant de l'orientation du réseau atomique. Dans un premier intervalle de valeurs de champ externe, le point de Bloch se propage doucement et sans oscillations. En plus, il n'est pas décalé par rapport au centre de la paroi vortex. Notre groupe a

récemment démontré [40] qu'une propagation ultra-magnonique entraine une excitation forte et spontanée de queues d'ondes de spin au-devant et à l'arrière de la paroi. Nous observons le même phénomène aussi pour les parois du type vortex avec un point de Bloch, où la vitesse de phase des queues d'ondes de spin formées spontanément est équivalente à la vitesse de propagation de la paroi et du point de Bloch. Lorsque la paroi et le point de Bloch atteignent une vitesse critique d'environ 1300 m/s, une augmentation ultérieure du champ n'entraîne plus une accélération de la paroi. Autrement dit, ceci correspond à une réduction de la mobilité de la paroi jusqu'à 0 m/sT. Nous obtenons ce résultat pour les deux diamètres considérés.

Nous déterminons un modèle simplifié unidimensionnel dans le cadre du micromagnétisme pur, où nous permettons une variation homogène de l'ange du flux $\gamma$. En accord avec nos simulations, le modèle reproduit une vitesse maximale du point de Bloch, et aussi la possibilité d'un canal supplémentaire qui permet un couplage du point de Bloch avec les ondes de spin générées spontanément. Un tel couplage a été observé dans nos simulations pour les deux diamètres de fils considérés. Ce couplage de la propagation du point de Bloch avec les ondes de spin qui sont excités grâce à l'effet Cherenkov de spin [40] est caractéristique pour le second mode de propagation dans le régime ultra-magnonique. Dans ce régime, le point de Bloch se propage dans un mouvement formant une spirale autour de l'axe central du cylindre avec la fréquence des queues d'ondes de spin attachées à la paroi. Dans ce mouvement, le point de Bloch reste décalé par rapport au centre de la paroi, et nous trouvons que la distance entre le point de Bloch et la paroi augmente avec la valeur du champ appliqué. Malgré ce couplage non-linéaire, les simulations montrent que le mouvement en forme de spirale stabilise effectivement la propagation de la paroi et la vitesse du point de Bloch. Le résultat est que la vitesse est saturé dans une large gamme de champs externes ; autrement dit la vitesse de la paroi reste constante même si le champ externe augmente. Ce phénomène est observé dans les simulations dans un intervalle entre 25 mT et 70 mT dans le cas du fil de 60 nm et entre 10 mT et 17 mT pour le fil avec 80 nm de diamètre.

Naturellement, ce n'est pas possible d'amortir la vitesse du point de Bloch décalé par rapport à la paroi pour des champs très forts. Dans le dernier régime de propagation, la distance entre le point de Bloch et la paroi atteint plusieurs centaines de nanomètres, ce qui a pour conséquence une forte accumulation d'énergie d'échange. Cette accumulation d'énergie d'échange continue jusqu'au point où une valeur critique est obtenue. Celle-ci est suffisante pour la nucléation d'une paire de points de Bloch de polarité opposée. Dès qu'une de ces paires de points de Bloch est nucléée dans le fil, on trouve temporairement trois points de Bloch dans le système. Un phénomène similaire avait été prédit sur la base de simulations purement micromagnétiques [41] et cela a maintenant pu être confirmé par notre approche multi-échelles / multi-modèles. Après la nucléation d'une paire, un des nouveaux points de Bloch reste connecté à la paroi sur l'iso-surface $m_z = 0$. Cependant, le point de Bloch initial forme avec le deuxième point de Bloch une « goutte » : une région localisée et isolée dont l'aimantation est opposée au champ magnétique et à l'aimantation environnante. Après quelques picosecondes, les deux points de Bloch de la « goutte » se rapprochent et finalement s'annihilent. Grâce à leurs configurations de polarités opposées, leur pro-

cessus d'annihilation n'a aucune influence sur l'index de skyrmion totale du système. La séquence de nucléation et annihilation de paires de points de Bloch permet une augmentation de la vitesse de propagation de la paroi, vu que maintenant la vitesse de la paroi n'est plus limitée par la vitesse maximale du point de Bloch, grâce à ce nouveau canal qui ressemble à des sauts de points de Bloch.

Le champ de depiégeage et le régime de propagation infra-magnonique dans la bonne chiralité indiquent que la propagation d'un point de Bloch peut être fortement influencée par les détails du réseau atomique sous-jacent. Vu que le logiciel nous permet d'identifier exactement la position d'un point de Bloch pendant son mouvement, et vu que cela peut être fait avec une résolution spatiale de quelques pico-mètres, nous avons analysé la position du point de Bloch et sa position dans une cellule élémentaire du réseau et dans une cellule unitaire cubique de structure bcc. En projetant la position du point de Bloch dans des pas de temps différents dans la première cellule primitive du réseau, nous avons obtenu une cartographie de la distribution de probabilité du point de Bloch pendant sa propagation. Cette distribution de probabilité est presque parfaitement localisée sur certaines surfaces de la cellule de Wigner-Seitz. Dans le cas de propagation à vitesses infra-magnoniques, nous avons trouvé que le point de Bloch préfère se propager sur les surfaces quadratiques et essaie plutôt d'éviter les surfaces hexagonales. Dans le cas de propagation ultra-magnonique, la distribution de densité change légèrement. Cependant, la quantité d'énergie plus élevée introduite dans le système avec le champ externe permette au point de Bloch d'accéder occasionnellement aussi aux surfaces hexagonales, en plus des surfaces quadratiques. Toutefois, la densité de probabilité d'un point de Bloch sur une surface hexagonale reste fortement réduite de plusieurs ordres de grandeur par rapport aux surfaces quadratiques.

Afin d'analyser la dynamique de propagation de façon plus détaillée, nous avons répété les simulations de la propagation du point de Bloch induite par un champ externe de 4 mT et pour un champ de 30 mT, mais cette fois-ci nous avons calculé la position du point de Bloch chaque 3 fs. Cette haute résolution temporelle nous donne accès à entre 20 et 100 points de données pour la position du point de Bloch dans chaque cellule cubique traversée pendant la propagation. Elle permet donc de déterminer avec haute résolution spatiale et temporelle la vitesse du point de Bloch. Ces études montrent qu'un point de Bloch qui entre sur une surface hexagonale accélère jusqu'à 5000 m/s, tandis que la vitesse moyenne est bien inférieure, de l'ordre de 1300 m/s. Ce comportement fournit une indication pour une forte force répulsive qui restreint la position du point de Bloch sur les surfaces quadratiques de la cellule de Wigner-Seitz dans le cas d'un réseau bcc.

En conclusion, nous avons réalisé dans cette thèse la première étude dynamique multi-modèle de la structure micromagnétique fondamentale d'un point de Bloch. Après avoir soigneusement détaillé les algorithmes qui ont été développés et utilisées, nous avons fourni une description des propriétés du point de Bloch en étudiant un nanocylindre magnétiquement doux. Pour des parois du type vortex, nous avons dérivé le champ de depiégeage pour des diamètres différents du nanocylindre et nous avons démontré que celui-ci dépend de l'orientation du réseau atomique. Nous avons analysé les formes et les différents régimes de propagation du point de Bloch et des parois qui

se développent dans les deux chiralités. En fonction de la force du champ appliqué, nous avons trouvé trois modes de propagation caractéristiques pour le cas de mauvaise chiralité : un mouvement lent et laminaire, un régime de déstabilisation (*breakdown regime*), et un régime où la chiralité est invertie. Nous avons par ailleurs démontré une grande différence entre la propagation infra- et ultra-magnonique, particulièrement en ce qui concerne l'influence de l'orientation du réseau atomique par rapport à la direction de propagation. Pour les points de Bloch et les parois se propageant avec vitesse ultra-magnonique, nous avons identifié trois modes typiques de propagation : un mode laminaire, un mode oscillatoire et un mode turbulent. Au moyen de calculs analytiques, nous avons conclu que la vitesse maximale trouvée dans les premiers deux modes ultra-magnoniques peut être attribuée à une propriété intrinsèque de la structure du point de Bloch. En outre, nous avons analysé la propagation du point de Bloch en nous focalisant sur la densité de probabilité de sa position à l'intérieur de la cellule unitaire du réseau atomique. Nous avons montré que les points de Bloch se trouvent presque exclusivement sur certaines surfaces et sur les bords de la cellule de Wigner-Seitz.

Même si certains résultats sont probablement au-delà de la résolution actuellement disponible dans des expériences, plusieurs effets, comme la dépendance qualitative des vitesses de propagation dans les divers régimes pourraient être expérimentalement accessibles. Le régime de propagation très stable à vitesse ultra-magnonique dans le cas de bonne chiralité pourrait être particulièrement intéressant aussi bien du point de vue fondamental que dans une perspective d'applications. La propagation de parois avec une vitesse constante et indépendante de la valeur précise du champ appliqué pourrait être une caractéristique très favorable pour des dispositifs de stockage d'avenir qui utilisent les parois magnétiques comme unité d'information dans un registre de décalage. La méthode multi-modèle développée dans le cadre de cette thèse devrait aussi être applicable dans d'autres domaines de simulations, comme par exemple dans le développement de simulateurs des structures en domaines pour des matériaux multiferroïques, où l'interaction des structures en domaines et des parois avec le réseau atomique devrait être généralement plus importante que dans le cas des matériaux ferromagnétiques classiques.

# Contents

# Part II. Numerics



# Part III. Numerical results

# Appendix

# 1
# Motivation

The understanding of micro- and nanoscopic magnetic structures developed during the last century, when techniques to gather knowledge as well as the motivation for research improved with enormous speed. While research on magnetic patterns was mainly of fundamental scientific interest in the beginning of the 20th century, it became more technology-oriented during the last decades. With the establishment of the micromagnetic theory in the 1960s [1–5] a mathematical frame became available to study magnetic structures theoretically and to describe complex magnetic patterns, like cross-tie domain walls [6], or the dynamics of domain walls [7, 8] and vortices [9, 10] in general.

In the first half of the last century nano- to micrometer dimensioned magnetic patterns were of fundamental research interest only, yet the demands for a better understanding of magnetic properties and magnetization processes connected with the advancing storage technology became a driving force of research during the last two decades. Despite important progress made in the technology of data storage in magnetic films, *e.g.*, magnetic tapes or discs, an early approach to use complex magnetic structures for storage devices tried to exploit magnetic domain walls in bubble materials [13] as units of information. Nevertheless, the technological obstacles of bubble material devices were higher than those that had to be overcome to achieve the nowadays used convenient hard drive technology.

The milestone discovery of the giant magneto resistance (GMR) effect, for which P. Grünberg [42, 43] and A. Fert [44] have been rewarded with the Nobel Prize in Physics, and its enhancement by the tunnel magneto resistance (TMR) effect [45] allowed for an enormous reduction of price and area per bit in the magnetic hard drive technology. In both effects, the electric resistance of a sandwich structure consisting of at least two ferromagnetic layers separated by a non-magnetic layer depends strongly on the relative magnetic orientation between both magnetic layers. The practical difference between the two effects lies in the non-magnetic material, which is metallic in the case of the GMR and insulating in the case of the TMR effect. In devices

exploiting the TMR or the GMR effect one uses the exchange bias effect to pin one "fixed" layer to an underlying antiferromagnetic thin film, whereas the other layer is free to change its orientation. Thus, already a small external magnetic field results in a strong change of electrical resistance, with a high signal-to-noise ratio in the range of several hundred percent. With those highly sensitive sensors, the area per bit in a hard drive disk becomes the limiting factor. Eventually, a transition from a two-dimensional magnetic storage solution on rotating discs to a novel type of storage systems might be necessary, if the demand for higher data storage densities increases further. Retrieving and storing large amounts of data also requires high operating speeds of the devices. This represents an exciting topic for both, fundamental and industrial research.

As mentioned before, even though domain patterns on thin ferromagnetic films are important from a technological perspective, fundamental research has studied a broad variety of different magnetic structures. Most of those systems have in common that their static and dynamic properties are either strongly surface dependent or essentially two-dimensional. A broad arsenal of different experimental methods has been developed in the last decades to study such structures. Scanning techniques allow for a detailed study of static magnetic configurations. An example of this family of methods is the magnetic force microscopy (MFM) [46, 47] making use of the force acting between a magnetized tip as a result of the magnetic stray field gradient originating from the magnetic structure of the sample. A second example is the spin-polarized scanning tunneling microscopy (SP-STM) [48], for which the spin-polarization of the tunneling electrons is analyzed by a magnetic tip. Hence, this technique is sensitive to the spin-resolved density of states in the vicinity of the surface. Another powerful technique for the detailed study of the magnetic structure at the surface of a sample is scanning electron microscopy with polarization analysis (SEMPA) [49, 50], where an unpolarized electron beam is used to emit spin-polarized electrons from the ferromagnet. An important feature of SEMPA is the possibility to analyze simultaneously three orthogonal components of the local magnetization, thereby allowing for an unambiguous image of the magnetic structure. A drawback of this method is its relatively low data acquisition rate, which results from a low signal-to-noise ratio.

Time resolved measurements are necessary to understand the complex dynamic processes in ferromagnetic samples. Such measurements are often based on the illumination of a large part of a sample with X-rays, electromagnetic waves, or electrons. Examples thereof include the magneto-optical Kerr effect, discovered by J. Kerr in 1877 [5, 51], which relies on the change in the polarization angle of light after reflection from the ferromagnetic surface. This rotation results from the interaction of the photons with the magnetized surface during the reflection process. This technique has been used, *e.g.*, to image the dynamics of vortex gyration [34]. It is also applicable for the in-lab detection of domain wall propagation along elongated structures like thin strips or, an aspect that is more important for this thesis, for cylindrical nanowires. Higher resolution imaging can be achieved using X-rays due to the shorter wavelength. X-ray magnetic circular dichroism (XMCD) techniques [52, 53] use the different absorption cross-sections of left and right handed polarized X-ray beams of

a ferromagnet with a magnetization along the propagation axis of the X-rays. Taking the difference between the spectra obtained from the two opposite circular polarization directions can significantly enhance the signal obtained for the magnetization component along the direction of the X-rays. If applied at an absorption edge of the material, images with high lateral resolution in the range of some nanometers can be obtained with a single pulse of radiation [53–55].

A combination of experimental techniques and simulations allows one to attack the above mentioned technological challenges, *e.g.*, the increase of storage density following in a self-fulfilling prophecy manner an exponential function analogous to Moore's law. Obviously, a doubling of storage density in two-dimensional structures every two to three years would result eventually in a density higher than one bit per atom, which might display an upper limit for storage density. Another limit is already encountered by nowadays hard drives. Small ferromagnetic particles tend to lose their ferromagnetic order and orientation already at temperatures below the Curie temperature, which is the superparamagnetic limit [56, 57], limiting the minimum area per bit of a ferromagnetic storage device. In materials with high anisotropy the superparamagnetic limit becomes important at smaller sizes, which allows one to use smaller areas per bit. The drawback of these materials is that it is more difficult to switch a bit, which results in the technological dilemma to demand at the same time a high thermal stability, a high memory density and a possibility for a switching of bits. In addition, the rotation of traditional hard drive discs requires a very stable environment. These systems suffer of an elevated risk of a mechanical failure. The racetrack memory proposed by S. Parkin [17], in which a chain of several magnetic domain walls is driven by an external current along an elongated ferromagnetic structure, could resolve these problems. It uses the spin transfer torque effect [58] to displace domains and domain walls, acting as units of information in a shift register — without any mechanically moving part. A prototype of a two dimensional racetrack memory chip was presented by IBM in November of 2011. Its two dimensional version might provide an alternative to flash memory used in solid state drives, but will face eventually a lower limit of area per bit The transition from two dimensional to three dimensional tracks could be considered as a major milestone. A possible approach to achieve that might be the replacement of the flat ferromagnetic strips grown on a substrate by cylindrical nanowires inside of a template.

A common technique to fabricate arrays of nanowires utilizes electrodeposition in porous alumina templates [59, 60]. This could provide an intrinsic three dimensional structure for this kind of memory building blocks. Magnetic nanocylinders are an archetypal example of analytic micromagnetism, for which textbooks derive three modes of magnetic reversal, namely curling, buckling and a uniform reversal [1–3]. However, the model of infinite extension along the axis on which these reversal modes are based is an idealization that is not suitable for real nanowires. Finite-size effects can play an important role in switching processes. In fact, these finite-size effects lead to a different type of reversal mode, namely the nucleation and propagation of domain walls. The ends of the nanocylinder act as nucleation sites and the type of domain wall depends on its radius and material: transverse domain walls nucleate in nanowires of small diameter[61], whereas in nanowires with a sufficiently large

diameter vortex domain walls [14, 21, 22, 62, 63] are the energetically favored structure, which propagates along the cylinder axis during the reversal of magnetization. The former benefits from the absence of a Döring mass [64] preventing a structural instability [61], yet it suffers from a low propagation velocity.

Vortex domain walls in cylindrical nanowires might be a promising candidate for future technological devices. For the case of nanotubes it has recently been shown [18, 19] that this type of domain wall is extremely stable and can reach velocities beyond 1000 m/s without experiencing structural instabilities or turbulences. We will show in this thesis that a similar behavior also applies to such domain walls in solid nanocylinders. Prior to this thesis vortex domain walls in solid nanocylinders were studied in the framework of micromagnetism, which is problematic due to the presence of a Bloch point singularity in its center, which represents a topological defect in the vector field of magnetization. Bloch points are regions of maximal inhomogeneity of the magnetic structure, and they typically carry a magnetostatic monopole charge in addition to a topological charge. These structures are well known in the theory of micromagnetism [11–13] since they often play a decisive role in micromagnetic switching processes [14]. However, they cannot be simulated reliably with usual micromagnetic codes for various reasons: Bloch points can lead to large discretization errors with a low convergence rate, artificial numerical pinning effects and, most of all, because the micromagnetic form of the exchange term is no longer valid in these situations of strong inhomogeneities [23]. To reliably study the dynamics of Bloch points it is necessary to treat them within an atomistic model, which is a challenging task since a comparatively large magnetic volume is required to stabilize these structures of high energy density, which develop owing to the cumulative effect of the long-range dipolar interaction.

This thesis is dedicated to solve the problem of the micromagnetic structure around Bloch points and their magnetic-field driven dynamics. The Bloch point and its surrounding is studied numerically on the basis of a multimodel simulation. This is achieved by treating the vicinity of the Bloch point by means of a Heisenberg model and the surrounding sample in the framework of the continuum theory of micromagnetism. With such a simulation framework, which locates and traces Bloch points automatically and tracks their position within a region simulated using a three-dimensional classical Heisenberg model, we are able to reveal the dynamics of Bloch points propagating inside the atomic crystal lattice of a ferromagnetic cylindrical nanowire. Even though no experimental data has been reported so far on the Bloch point dynamics, we are confident that our theoretical and numerical studies provide reliable predictions of the magnetization dynamics on these structures.

Three parts represent the main pillars of this thesis. The first one is based on purely analytic theory, the second one is dedicated to the numerical implementation of the multimodel simulation kit and the last one describes the numerically obtained results of Bloch point statics and dynamics.

The first part starts with an introduction to the **fundamentals of micromagnetism and the Heisenberg model**. There, we introduce the energy contributions of the system described in the two models with a particular focus on the exchange and the demagnetizing energy. In addition, we explain in the first chapter the transition

from energy contributions to the concept of an external field necessary for dynamic simulations applying the Landau-Lifshitz-Gilbert equation [28–30].

In the third chapter we introduce the **basic micromagnetic structures** on the foundation of micromagnetism. Thereby, we discuss different domain wall types and fundamental aspects of magnetic vortices. At the end of this chapter, we provide a short overview of the Bloch point and compare it to the other micromagnetic structures.

Chapter 4 focuses on an **analytic treatment of Bloch points** in the framework of micromagnetism, with which we derive the energy contributions that play an important role for the analysis of Bloch points. After a discussion of the systematic difficulties of the exchange energy calculation of Bloch points, we determine its analytic continuum model properties, such as, *e.g.*, the dependence of the demagnetizing energy on the inflow-angle. By applying the aforementioned results we develop a simple analytic model from which a maximum steady-state Bloch point propagation velocity is derived.

The numerical part of this thesis is summarized starting from chapter 5, which includes a mathematical introduction to the **finite element method**. After discussing some fundamental aspects we introduce the method that we have developed for the mapping between different finite element meshes. There, we focus on the mathematical and numerical considerations and discuss pitfalls that can occur when treating two overlapping finite element meshes.

Chapter 6 describes the key elements that have been developed for the **implementation** of the multimodel simulation. Those key elements consist of the treatment of the sample in the framework of micromagnetism and the algorithms taking care of the multimodel implementation itself.

The implementation chapter is followed by a description of **numerical stability tests**. Those tests focus on the effects of abrupt mesh transitions and show that the boxing of one finite element mesh into another does not result in strong numerical artifacts in our implementation if the discretization is chosen sufficiently small. Furthermore, we discuss in that chapter the negligible value of energetic artifacts due to insertion, propagation and removal of our multimodel environment.

The last part of this thesis is dedicated to the numerically obtained results using the multimodel implementation explained in the preceding part. This part provides an introduction to **Bloch points in nanowires**. In addition, we derive in chapter 8 the spin wave dispersion relation and discuss its importance for the succeeding chapters.

Without an external magnetic field the magnetic configuration of the sample relaxes and the **equilibrium Bloch point configuration** results, which is the subject of chapter 9. In that chapter we deduce the influence of material parameters and nanowire diameter on the inflow angle, which is a characteristic parameter to describe the Bloch point configuration.

Chapter 10 addresses the question of the **depinning of Bloch points** under the influence of an external field. There, we calculate the field that is necessary to initiate the propagation of a Bloch point, together with the domain wall surrounding it in the case of a single-crystal cylindrical nanowire. It is further shown that the value of the

depinning field depends on the orientation of the crystal lattice with respect to the driving field.

The domain wall dynamics in cylindrical structures is strongly chirality dependent [19], *i.e.*, it depends on the sense of rotation of the vortex and the field direction. In chapter 11 we define and discuss the different **chiralities of vortex domain walls** that can develop in cylindrical nanocylinders and discuss their properties under the influence of an axial external magnetic field. Two Bloch point configurations can develop in this system, which are labeled as **bad chirality Bloch points** and **good chirality Bloch points**, whose differences are discussed in chapter 12 and chapter 13, respectively. For both configurations we describe the modes of propagation. Especially for the good chirality Bloch points we determine the effect of different lattice orientations inside of the cylindrical nanowire and show that this orientation plays an important role only in the case of submagnonic Bloch point propagation in good chirality. The term *submagnonic* is used here to denote velocities below the minimum phase velocities of spin waves in the material. The faster, supermagnonic Bloch point propagation, is investigated in section 13.2 to section 13.4. There we show that, as predicted in the first part of this thesis, a maximum Bloch point propagation velocity exists, which is constant over a broad interval of external field values. Such a constant velocity in the range of 1000 m/s, would represent an important feature that could be exploited in three dimensional racetracks.

The last chapter of this thesis summarizes our results on the **Bloch point positions inside of the lattice**, obtained with a picometer and femtosecond resolution. There, we reveal that the path of a moving Bloch point is to a large extent constrained to the surface of the Wigner-Seitz cell, and that certain facets are favored during the propagation.

# Part I.
# Theory

# 2

# Fundamentals of micromagnetism and the Heisenberg model

In order to describe magnetism several theories have been developed to account for different length scales, ranging from the (sub-)atomic to the cosmic one. In this thesis we focus on structures of sizes up to several micrometers, which narrows the number of applicable theories significantly. On an atomic length scale, ab-initio calculations serve well to derive fundamental material properties and parameters [3]. In most cases numerical simulations performed on powerful computer clusters or supercomputers are necessary to obtain realistic results. The high computational demand restricts the size of treatable sample size and often makes it necessary to assume certain approximations, such as periodic boundary conditions.

On a somehow larger length scale, if the primary interest is not the electronic structure but rather the arrangement of magnetic moments, the classical Heisenberg model [65] is a good approximation. It is characterized by interacting magnetic moments located at atomic lattice positions. The model incorporates intrinsically the atomic structure of matter and describes the exchange interaction by means of coupling constants. Ab-initio calculations can provide the values of these coupling constants as well as the number of Bohr magnetons per lattice side.

Most of the typical micromagnetic structures, such as domain walls or vortices, in ferromagnetic materials develop on length scales much larger than the atomic lattice constant. This renders an atomistic treatment unnecessary and allows for a further transition from discrete atomic moments to a continuum description. This continuum theory aims at describing the structure and the dynamics of the magnetization as a continuous, directional vector field, and it is known as the theory of micromagnetism

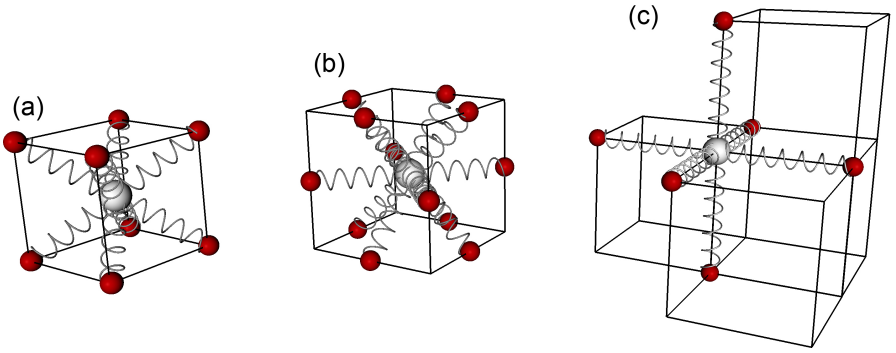


**Figure 2.1** – Sketches of nearest-neighbor interactions in a) body-centered cubic lattices, b) face-centered cubic lattices and c) simple cubic lattices.

[1, 2]. In homogeneous ferromagnetic materials there are only few situations in which magnetic configurations are encountered, whose characteristic length scales are comparable to the atomic one and which therefore demand an atomic treatment. The most prominent example is the Bloch point [12, 66], which is the central topic of this thesis.

In order to lay out the theoretical basis, we begin this chapter with a reminder of the Heisenberg model and formulate the exchange and magnetostatic interaction as well as the influence of an external magnetic field. Afterwards we continue with a similar outline of micromagnetism with a particular focus on the connection between both models.

## 2.1 Classical Heisenberg model

Heisenberg models [65] deal with individual spins or magnetic moments at discrete positions. They are often discussed as a link between ab-initio theory approaches and mesoscopic theories. They are a subject of numerous comprehensive textbooks on the quantum theory of magnetism [67, 68] and their approximations. Within this work we will restrict our analysis to the classical Heisenberg model, in which we assume that magnetic moments $\boldsymbol{\mu}_i$ are located at lattice sites $i$ of the underlying material and that these magnetic moments are free to rotate continuously. This enables us to take into account the atomic and lattice structure of matter intrinsically, while neglecting quantum effects. Figure 2.1 sketches the nearest-neighbor Heisenberg exchange interactions inside of the three most common cubic Bravais lattices: body-centered cubic (bcc), face-centered cubic (fcc) and simple cubic (sc).

### 2.1.1 Exchange interaction

In general, the exchange interaction is a pure quantum mechanical effect originating in the exclusion principle of fermions, which needs to be treated in a lower scale theory. In the Heisenberg model, however, the exchange integrals, which occur in ab-initio calculations as a quantum mechanical effect, can be approximated by exchange constants $J_{ij}$ which quantify the exchange interaction between magnetic moments at lattice positions $i$ and $j$. The most common formulation [3] describe the exchange energy in a system of magnetic moments $\boldsymbol{\mu}_i = \mu_i \cdot \mathbf{m}_i$ by

$$E_{\mathrm{xc}} = -\sum_{i,j} J_{ij}\ \mathbf{m}_i \cdot \mathbf{m}_j \quad , \tag{2.1}$$

where the indices run over all magnetic moments in the system, and $\mathbf{m}_i$ and $\mathbf{m}_j$ denote the normalized orientation of the magnetic moments at lattice sites $i$ and $j$, respectively. The absolute value of the interacting magnetic moments ($\mu_i$) are encapsulated in the exchange constants $J_{ij}$.

The nomenclature in the literature is not entirely consistent. In addition to some occasionally different prefactors or different summation patterns, such as a tridiagonalization of the $J_{ij}$ matrix, Eq. 2.1 can be formulated also in a form in which the scalar product refers to the vectors of the magnetic moments $\boldsymbol{\mu}_i$ and $\boldsymbol{\mu}_j$. In the following we will use Eq. 2.1, in which the exchange matrix elements represent energies.

The knowledge of the lattice structure and lattice constant allows for the calculation of the volume $V_i$ corresponding to each lattice site $i$, which in the case of Bravais lattices is rather easy to calculate [69] and helps defining the exchange energy density at each atomic position $i$:

$$e_{\mathrm{xc}}^{(i)} = -\sum_{j} \frac{J_{ij}}{V_i}\ \mathbf{m}_i \cdot \mathbf{m}_j \tag{2.2}$$

This form of the exchange energy density will be important in Sec. 2.3 to formulate the evolution of the magnetic moment orientation.

### 2.1.2 Zeeman energy

An external field $\mathbf{H}_{\mathrm{ext}}$ acting on an ensemble of magnetic moments gives rise to a potential energy of

$$E_{Zee} = -\mu_0\ \sum_i \boldsymbol{\mu}_i \cdot \mathbf{H}_{\mathrm{ext}} \quad . \tag{2.3}$$

In the volume associated with the magnetic moment $i$ the Zeeman energy density

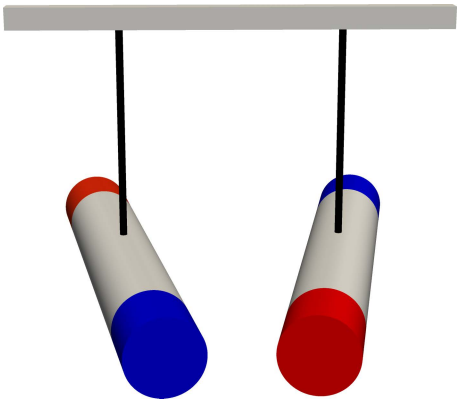

(a) Coulomb's experiment with two bar magnets

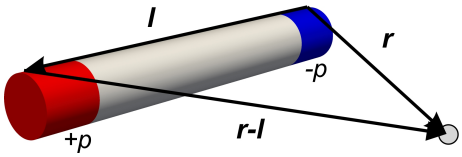


(b) On the definition of a magnetic dipole moment (see text).

**Figure 2.2** – Sketches of a) Coulomb's torsion balance experiment with two bar magnets and (b) the positive and negative pole ($+p$ and $-p$) separated by the vector $\mathbf{l}$ of a dipole moment.

is

$$e_{\text{zee}}{}^{(i)} = -\frac{\mu_i}{V_i}\,\mathbf{m}\cdot\mathbf{H}_{\text{ext}} \quad . \tag{2.4}$$

### 2.1.3 Magnetostatic energy

The equations describing the magnetostatic energy and the corresponding stray field can be derived following different lines of argumentation. For example, several books about magnetism and electrodynamics [70, 71] formulate the magnetic $\mathbf{B}$ field as the curl of a vector potential $\mathbf{A}^{(\mathbf{B})}$:

$$\mathbf{B} = \boldsymbol{\nabla}\times\mathbf{A}^{(\mathbf{B})} \tag{2.5}$$

In a second approach, which is particularly suited for magnetostatic fields of ferromagnets, the magnetic $\mathbf{H}$ field, is expressed as a gradient field of a scalar potential $U$, in analogy to the electric $\mathbf{E}$ field:

$$\mathbf{H} = -\boldsymbol{\nabla}U \tag{2.6}$$

As this formulation corresponds to the line of argumentation also used in the micromagnetic description in Sec. 2.2.3, we briefly discuss it by following the lecture notes of H. Kronmüller [72]. As it is deduced from Coulomb's experiment, sketched in Fig. 2.2(a), the force that two poles $p_1$ and $p_2$ exert on each other is

$$\mathbf{F} = k\,\frac{p_1\,p_2}{r^2}\,\frac{\mathbf{r}}{r} \quad , \tag{2.7}$$

where for magnetic poles the proportionality constant yields $k = 1/4\pi\mu_0$ in the SI system and where $r$ denotes the distance between the poles $p_1$ and $p_2$. By splitting Eq. 2.7 into a product

$$\mathbf{F} = p_1 \cdot \mathbf{H} \tag{2.8}$$

one obtains the magnetic field originating from pole $p_2$ at the location of $p_1$

$$\mathbf{H} = k \, \frac{p_2}{r^2} \, \frac{\mathbf{r}}{r} \tag{2.9}$$

and the scalar potential of one (hypothetical) isolated pole $p$ at position $r = 0$ reads

$$U = k \, \frac{p}{r} \quad . \tag{2.10}$$

Isolated magnetic monopoles are forbidden by Maxwell's equation, but Eq. 2.10 can be used in terms of the dipole concept. Two monopoles with pole strength $(+p, -p)$ separated by the distance $\mathbf{l}$ have the dipole moment (sketched in Fig. 2.2(b))

$$\mu_0 \, \boldsymbol{\mu} = p \, \mathbf{l} \tag{2.11}$$

inducing the potential

$$U_{\mathrm{dip}} = U^+ + U^- = k \, p \, \left( \frac{1}{|\mathbf{r} - \mathbf{l}|} - \frac{1}{|\mathbf{r}|} \right) \quad . \tag{2.12}$$

Since the distance between the two poles in a magnetic dipole is infinitesimally small, a Taylor expansion can be truncated after the first term resulting in

$$U_{\mathrm{dip}} = -k \, p \, \mathbf{l} \cdot \boldsymbol{\nabla} \left( \frac{1}{r} \right) = -k \, p \, \mathbf{l} \cdot \frac{\mathbf{r}}{r^3} \quad , \tag{2.13}$$

where $r$ now denotes the distance from the dipole. Equation 2.13 in conjunction with Eq. 2.11 can be rewritten to

$$U_{\mathrm{dip}} = -\frac{1}{4\pi} \, \boldsymbol{\mu} \cdot \frac{\mathbf{r}}{r^3} \tag{2.14}$$

resulting in the field

$$\mathbf{H}_{\mathrm{dip}} = \frac{1}{4\pi} \left( \frac{-\boldsymbol{\mu}}{r^3} + 3 \frac{\boldsymbol{\mu} \cdot \mathbf{r}}{r^5} \cdot \mathbf{r} \right) \quad . \tag{2.15}$$

Then the B-field resulting from an ensemble of magnetic moments $\boldsymbol{\mu}_i$ reads

$$\mathbf{B}(\mathbf{r}) = \frac{\mu_0}{4\pi} \sum_i \left( \frac{3\left[(\mathbf{r}-\mathbf{r}_i)\cdot\boldsymbol{\mu}_i\right]\cdot(\mathbf{r}-\mathbf{r}_i)}{(\mathbf{r}-\mathbf{r}_i)^5} - \frac{\boldsymbol{\mu}_i}{(\mathbf{r}-\mathbf{r}_i)^3} \right) \quad , \tag{2.16}$$

which corresponds to a total energy of

$$E_{\mathrm{Dip}} = -\frac{\mu_0}{4\pi} \sum_i \boldsymbol{\mu}_i \sum_{j\neq i} \left( \frac{3\left[(\mathbf{r}_i-\mathbf{r}_j)\cdot\boldsymbol{\mu}_j\right]\cdot(\mathbf{r}_i-\mathbf{r}_j)}{(\mathbf{r}_i-\mathbf{r}_j)^5} - \frac{\boldsymbol{\mu}_j}{(\mathbf{r}_i-\mathbf{r}_j)^3} \right) \quad . \tag{2.17}$$

## 2.2 Micromagnetic energy contributions

The theory of micromagnetism accounts for ferromagnetic mesoscopic particles and aims at the description and prediction of the static and dynamic properties of fundamental magnetic structures including domain walls [7, 28], vortices [5] or spin waves occurring in such particles. A singular structure, called Bloch point or Feldtkeller singularity [11, 12], represents in many ways an exception because it is predicted, but not accurately described, by micromagnetic theory.

One might start a historic overview of micromagnetism in 1932, when F. Bloch derived the ground state of a Bloch domain wall — nowadays named after him — by means of energy minimization using analytic expressions for exchange and anisotropy energy [7]. In section 3.1.1 we will follow his calculations to derive a formulation of the exchange length — a characteristic length scale of micromagnetism.

In 1935 Landau and Lifshitz laid out the fundamentals of domain theory, and many aspects of what is now part of micromagnetic theory [28]. The paper by Landau and Lifshitz included a dynamic equation which has later been reformulated in a slightly different but mathematically equivalent fashion by T.L. Gilbert [29, 30]. The Landau-Lifshitz or the Landau-Lifshitz Gilbert equation describe the motion of the vector field of the magnetization. Both use a phenomenological damping constant to account for dissipative processes. In 1963 W.F. Brown published *Micromagnetics* [1] in which he assembled the full theory of micromagnetism.

Micromagnetism is a continuum theory and it therefore neglects atomic effects in the description of the statics and dynamics of the magnetization, which is defined as the density of magnetic moments. One of the fundamental assumptions of micromagnetic theory is that the magnetization of a homogeneous ferromagnet can be represented as a directional field with a modulus that is constant in space and time: the saturation magnetization $M_s$, a material parameter. Static structures are obtained either by energy minimization methods or, which is equivalent, by seeking solutions where the torque exerted by the local effective field on the local magnetization is zero throughout the sample [1]. The result of dynamic calculations depends only on the initial magnetic conditions, since the mathematical problem can be considered as an initial value-problem, at least in discretized numerical methods [73]. The dependence on the initial value, *i.e.*, on the history of the sample, also reflects in hysteretic effects; a fundamental property in ferromagnetism.

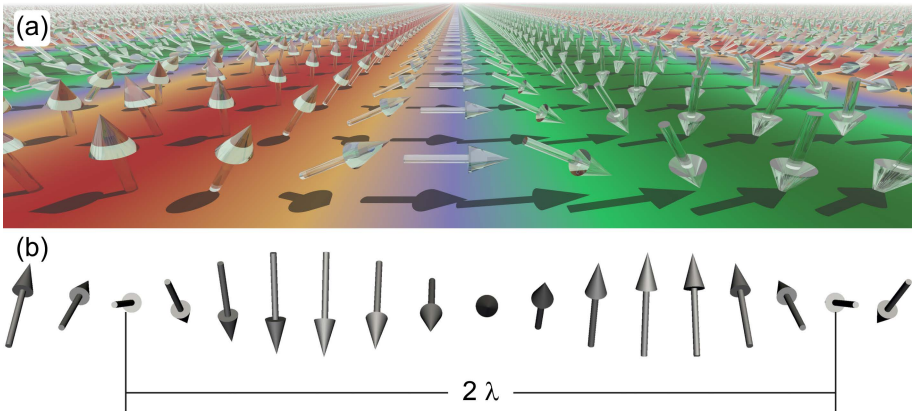


**Figure 2.3** – Sketch of a spin spirals of Bloch (a) and Neél type (b). We denote the half cycle wave length wit $\lambda$. The exchange energy density of both types is according to Eq. 2.18 is $e_{\mathrm{xc}}^{\mathrm{MM}} = A\pi^2/\lambda^2$.

Often dynamic micromagnetic simulations can be performed safely also if temperature effects are omitted. The tacit assumption is that the system's temperature is well below the Curie temperature. It is thereby assured that the saturation magnetization remains constant. In an attempt to model ultrafast, laser-induced magnetization processes recent approaches allowing for the possibility of a time and space dependent value of $M_s$, by using the Landau-Lifshitz-Bloch equation (LLB) [74, 75].

In the following sections we describe the fundamental energy terms of micromagnetism with particular emphasis on exchange and stray field energy, which are the minimum ingredients to describe a ferromagnetic domain pattern or domain wall structure. With the intention to motivate a multi-model implementation of the Heisenberg model into the theory of micromagnetism, we outline the limits of validity of micromagnetic theory, which can be defined as those situations in which the underlying equations of micromagnetism and the Heisenberg model cease to be equal.

### 2.2.1 Exchange energy

In his review of 1949, C. Kittel [76] derived a formulation of micromagnetic exchange energy density from the Heisenberg model formulation by assuming small angular changes of the magnetic moments between two neighboring lattice sites. The commonly used formulation of exchange energy density in micromagnetism is

$$e_{\mathrm{xc}} = A \sum_{\alpha}^{x,y,z} \frac{\partial \mathbf{m}}{\partial x_\alpha} \cdot \frac{\partial \mathbf{m}}{\partial x_\alpha} \tag{2.18}$$

with the exchange stiffness $A$ and the normalized orientation of magnetization $\mathbf{m}$. As pointed out by A. Aharoni in 1979 [77] the underlying assumption of small derivatives

$\frac{\partial \mathbf{m}}{\partial x_\alpha}$ needs to be taken seriously. For that reason we compare Eq. 2.18 with Eq. 2.2. Equation 2.2 can be reformulated using the angle $\vartheta_{ij}$ between magnetic moments $i$ and $j$:

$$\begin{aligned} e_{\mathrm{xc}}^{(i)} &= -\sum_j \frac{J_{ij}}{V_i} \mathbf{m}_i \cdot \mathbf{m}_j \\ &= -\sum_j \frac{J_{ij}}{V_i} \cos\vartheta_{ij} \quad . \end{aligned} \tag{2.19}$$

Then Eq. 2.19 can be expanded into a Taylor series

$$e_{\mathrm{xc}}^{(i)} = -e_0^{(i)} + \sum_j J_{ij}/V_i \left( \frac{\vartheta_{ij}^2}{2} - O(\vartheta_{ij}^4) \right) \tag{2.20}$$

with offset energy density $e_0^{(i)} = \sum_j J_{ij}/V_i$. As we report in Ref. [23, 78] the exchange stiffness $A_i$ can be derived for a given set of exchange constants $J_{ij}$ in the vicinity of a lattice site $i$ by using a spin spiral with arbitrary, but long half cycle wave length $\lambda$, which is sketched in Fig. 2.3.

In a ferromagnetic crystalline sample, Eq. 2.18 and 2.19 are magnetically isotropic, so that one can choose the direction of the spin spiral in $x$ direction without loss of generality

$$\mathbf{m}(x) = \begin{pmatrix} \sin(\pi\ x/\lambda) \\ \cos(\pi\ x/\lambda) \\ 0. \end{pmatrix} \quad , \tag{2.21}$$

for which the Heisenberg and micromagnetic exchange formulations should be identical. Note that $e_0$ needs to be set to zero in order to equate the energy levels of the two models.

Combining Eq. 2.20 and Eq. 2.21 for the spin spiral yields

$$\sum_j J_{ij}/V_i \left[ \left( \pi \frac{\Delta x_{ij}}{\lambda} \right)^2 /2 + O(\Delta x_{ij}^4) \right] = A_i\ \frac{\pi^2}{\lambda^2} + O(1/\lambda^4) \quad , \tag{2.22}$$

where $\Delta x_{ij}$ is the difference of the $x$-coordinates of lattice sites $i$ and $j$. By comparing coefficients it follows that terms of higher order than $1/\lambda^2$ are neglected in the micromagnetic formulation.

Equation 2.22 can be used to calibrate the exchange stiffness near the lattice site $i$. As in micromagnetism the exchange stiffness $A$ is assumed to be a position-independent material parameter. Therefore, the average of $A_i$ with respect to the

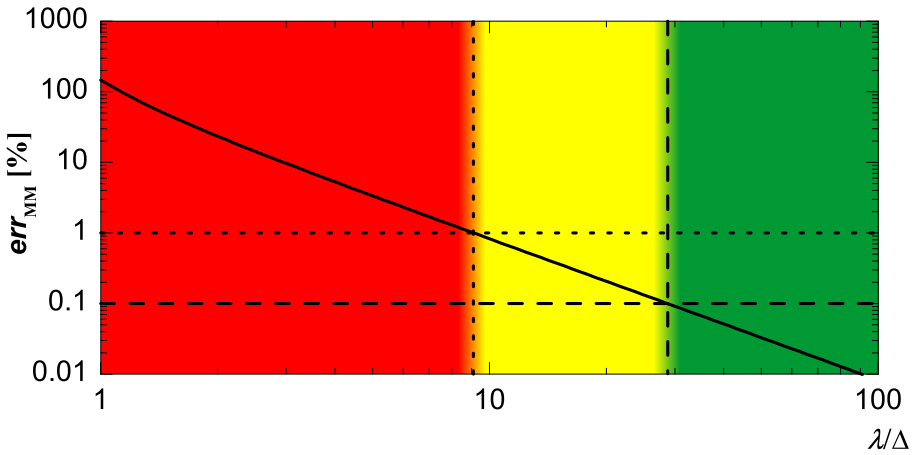


**Figure 2.4** – Error estimate of the intrinsic micromagnetic exchange energy. The graph displays the deviation of the continuum expression from the value resulting from the Heisenberg model. The abscissa denotes the spin spiral half-wave length in units of $\Delta$, where $\Delta$ is the distance between neighboring lattice sites in the direction of the spin spiral. The dashed and the dotted lines indicate the spin spiral wave length for which an intrinsic micromagnetic error of $1\,\%$ and $0.1\,\%$, respectively, can be expected.

volume share of species $i$ leads to the micromagnetic exchange constant $A$:

$$A = \frac{1}{\sum\limits_i V_i} \sum_i V_i \left( \sum_j \frac{J_{ij} \Delta x_{ij}^2}{2V_i} \right) \quad . \tag{2.23}$$

This formulation includes the special case of nearest-neighbors interaction as previously mentioned by C. Kittel [76], but extends it to an arbitrary number of interacting neighbors that can be taken into account in Heisenberg model calculations.

### Accuracy of the micromagnetic description on atomic length scales

Equation 2.23 was derived under the assumption of a long spin spiral wave length $\lambda$. But for spirals with a short wave length the first order Taylor approximation is insufficient and leads to systematic errors. This becomes particularly important in regions of highly inhomogeneous magnetic structures, such as Bloch points.

After subtracting the offset energy contribution $e_0^{(i)}$ from Eq. 2.19 we can compare the result to the combination of Eq. 2.18 and Eq. 2.23, which is the micromagnetic expression for the exchange energy density of the spin spiral for a given set of Heisenberg exchange constants. By doing so, one obtains an estimate of the deviation of the micromagnetic from the Heisenberg model for short wave lengths $\lambda$ in monoatomic lattices. In order to keep the equation as accessible as possible, we only retain the most dominant interaction partner. Then the systematic error of micromagnetism in

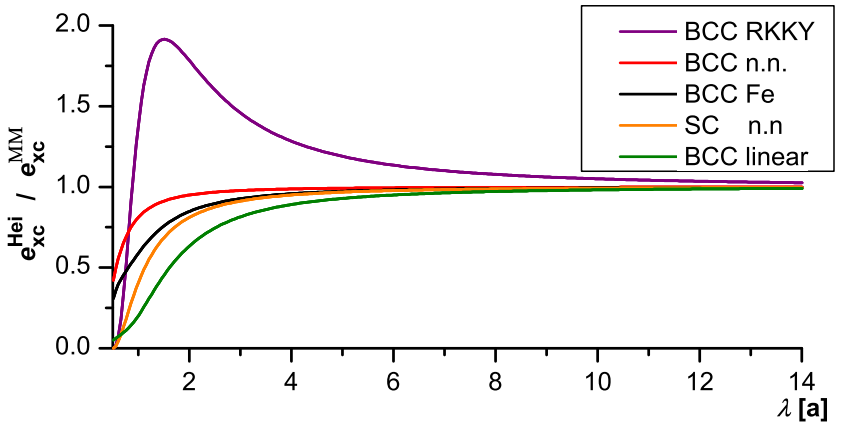


**Figure 2.5** – Comparison of the exchange energy density of a spin spiral with wave length $\lambda$ and lattice constant $a$ calculated with a Heisenberg model and with analytic micromagnetism for different material configurations (Footnote 1 on page 19). With decreasing wave length the micromagnetic calculation imposes a singular behavior resulting in a strongly incorrect estimate of the exchange energy.

that material reads

$$\mathrm{err}_{MM} = \frac{\pi^2 \Delta^2}{2\lambda^2} \Big/ \left(1 - \cos\left(\pi \, \frac{\Delta}{\lambda}\right)\right) - 1 \tag{2.24}$$

with $\Delta$ the distance between magnetic moment $i$ and $j$ along the direction of the spin spiral.

The plot of Eq. 2.24 in Fig. 2.4 shows that for a short wave length $\lambda$ the intrinsic micromagnetic error increases exponentially, while for $\lambda > 9\Delta$ it drops below 1 % (dashed line) and below 0.1 % for $\lambda > 29\Delta$ (dotted line), respectively. In modern micromagnetic codes local numerical errors are usually deep in the sub-percent regime. In view of this high accuracy, these intrinsic model errors of several percent cannot be tolerated and using a Heisenberg model becomes decisive in these situations. Intrinsic micromagnetic errors below 0.1 % in the green region of Fig. 2.4 can be considered as negligible. In these cases, using an atomistic Heisenberg model would be a waste of computational resources. These considerations lead to the conclusion that between $9\Delta$ and $29\Delta$ a transition from one model to the other should be implemented in order to obtain a balanced trade-off between avoidance of systematic errors and numerical costs.

An analysis as shown in Fig. 2.4 can be performed to study the systematic errors of different materials as a function of the half-wave length $\lambda$. Figure 2.5 displays the ratio of the Heisenberg exchange energy density and analytic micromagnetic exchange energy density denoted by $e_{\mathrm{xc}}^{\mathrm{Hei}}$ and $e_{\mathrm{xc}}^{\mathrm{MM}}$, respectively, for different material parame-

ters [1] and lattice types. From Fig. 2.5 it can be deduced that for most ferromagnetic material parameters micromagnetic theory overestimates the exchange energy density for short wavelength $\lambda$ imposing a singular behavior in the vicinity of $\lambda \approx 0$. A special case is the example of the material labeled as bcc RKKY. It shows an underestimation of exchange energy density by micromagnetic calculations for $\lambda > 1.5a$, which is equivalent to the twofold distance between nearest neighbors. Owing to the alternating Heisenberg exchange constants with increasing distance the resulting micromagnetic exchange stiffness is positive, yet the antiferromagntic contributions in the Heisenberg model weaken the ferromagnetic order significantly. For $\lambda < a$ the exchange interaction is governed by nearest neighbors, yielding the same overestimation by the micromagnetic approximation as observed for the other material configurations.

### 2.2.2 Zeeman energy

The contribution of an external field $\mathbf{H}_{\text{zee}}$ to the total energy can be derived in a straightforward way from the Heisenberg formulation presented in Sec. 2.1.2.

By replacing the individual magnetic moments $\boldsymbol{\mu}_i$ with the magnetization $\mathbf{M}(\mathbf{r})$ the sum in Eq. 2.3 converts into an integral, from which the Zeeman energy density is obtained:

$$e_{\text{zee}} = -\mu_0 \ (\mathbf{H}_{\text{zee}} \cdot \mathbf{M}) \tag{2.25}$$

The value of the Zeeman energy density is minimal if the external field and magnetization are oriented parallel to each other.

### 2.2.3 Demagnetizing energy

The demagnetizing energy originates from the magnetostatic field induced by the magnetic configuration and is described by Maxwell's equation [70]. In non-magnetic materials and in vacuum, the magnetic induction $\mathbf{B}$ and the magnetic field $\mathbf{H}$ are connected linearly by the vacuum permeability $\mu_0$ outside of a magnetic material, while inside of a ferromagnetic material it reads

$$\mathbf{B} = \mu_0 \ (\mathbf{H} + \mathbf{M}) \quad . \tag{2.26}$$

[1] The labels bcc and sc refer to the used Bravais lattice type. Materials with *n.n.* include the 8 nearest neighbors in case of bcc and the 6 nearest neighbors in case of sc, while the *bcc RKKY*, *bcc Fe* and *bcc linear* material include the 144 nearest neighbors located on 10 sphere shells $s$ each having a different Heisenberg exchange constant $J_S$:

- bcc RKKY: $\{J_s\} = \{1, -0.9, 0.8, -0.7, .., -0.1\}$ mRy
- bcc linear: $\{J_s\} = \{1, 0.9, 0.8, .., 0.1\}$ mRy
- bcc Fe: $\{J_s\} = \{1.432, 0.815, -0.016, -0.126, -0.146, -0.062, 0.001, 0.015, -0.032, 0.187\}$ mRy according to the exchange constants of iron published by Pajda et al. [79].

According to Helmholtz's theorem every vector field can be decomposed into a divergence-free (df) and an irrotational (irr) part, with which one can write

$$\mathbf{B} = \mu_0 \ (\mathbf{H}_{\mathrm{df}} + \mathbf{H}_{\mathrm{irr}} + \mathbf{M}) \quad . \tag{2.27}$$

To determine the physical origin of the two quantities $\mathbf{H}_{\mathrm{df}}$ and $\mathbf{H}_{\mathrm{irr}}$ the curl of Eq. 2.27 is taken, resulting in

$$\boldsymbol{\nabla} \times \mathbf{B} = \mu_0 \ \boldsymbol{\nabla} \times (\mathbf{H}_{\mathrm{df}} + \mathbf{M}) \quad . \tag{2.28}$$

According to Ampère's Law the left hand side decomposes into

$$\boldsymbol{\nabla} \times \mathbf{B} = \mu_0 \ \left( \mathbf{j} + \epsilon_0 \frac{\partial \mathbf{E}}{\partial t} \right) \tag{2.29}$$

with $\mathbf{j}$ the total current, $\epsilon_0$ the vacuum permeability and $\mathbf{E}$ the electric field. $\mathbf{j}$ includes three types of currents [71]: those associated with $\boldsymbol{\nabla} \cdot \mathbf{M} = \mathbf{j}_{\mathrm{mag}}$, free currents $\mathbf{j}_{\mathrm{free}}$, and those due to electric polarization $\mathbf{j}_{\mathrm{pol}}$. Hence, $\mathbf{H}_{df}$ has to be associated with:

$$\boldsymbol{\nabla} \times \mathbf{H}_{\mathrm{df}} = \epsilon_0 \ \frac{\partial \mathbf{E}}{\partial t} + \mathbf{j}_{\mathrm{free}} + \mathbf{j}_{\mathrm{pol}} \quad . \tag{2.30}$$

None of those contributions stem from the magnetization and one can thus conclude that the demagnetizing field has to be represented by $\mathbf{H}_{\mathrm{irr}}$. For that reason we change the index irr to dem. An irrotational field $\mathbf{H}_{\mathrm{dem}}$ can be represented as the gradient of a scalar potential $U$:

$$\mathbf{H}_{\mathrm{dem}} = -\boldsymbol{\nabla} U_{\mathrm{dem}} \tag{2.31}$$

Gauss's law for magnetism reads

$$0 = \boldsymbol{\nabla} \cdot \mathbf{B} = \mu_0 \ (-\boldsymbol{\nabla} \cdot (\boldsymbol{\nabla} U_{\mathrm{dem}}) + \boldsymbol{\nabla} \cdot \mathbf{M}) \quad , \tag{2.32}$$

which results in Poisson's equation

$$\Delta U_{\mathrm{dem}} = \boldsymbol{\nabla} \cdot \mathbf{M} \quad . \tag{2.33}$$

The general solution of Eq. 2.33 is given by

$$U_{\mathrm{dem}}(\mathbf{r}) = \frac{1}{4\pi} \left[ -\int\limits_{\Omega'} \frac{\boldsymbol{\nabla} \cdot \mathbf{M}(\mathbf{r}')}{|\mathbf{r} - \mathbf{r}'|} \, \mathrm{d}^3 r' + \int\limits_{\partial\Omega'} \frac{\mathbf{M}(\mathbf{r}') \cdot \mathbf{n}}{|\mathbf{r} - \mathbf{r}'|} \, \mathrm{d}^2 r' \right] \quad . \tag{2.34}$$

It consist of a volume integral over the ferromagnetic volume $\Omega'$ and a surface integral over the surface of $\Omega'$ where the vector $\mathbf{n}$ is the outwards oriented surface normal.

Due to their analogy to electric charges in electrostatics and their role as sources of the magnetostatic scalar potential the terms in the two integrands of Eq. 2.34 can be identified in the following way:

$$\rho = \quad -\mu_0 \ (\boldsymbol{\nabla} \cdot \mathbf{M}) \quad \text{volume charge density} \tag{2.35}$$

$$\sigma = \quad \mu 0 \ (\mathbf{M} \cdot \mathbf{n}) \quad \text{surface charge density} \tag{2.36}$$

With the knowledge of $\mathbf{H}_{\mathrm{dem}}$ the demagnetizing energy density is calculated analogous to the Zeeman energy density

$$e_{\mathrm{dem}} = -\mu_0/2 \ \mathbf{H}_{\mathrm{dem}} \cdot \mathbf{M} \quad . \tag{2.37}$$

The demagnetizing energy density is positive definite [2, 4, 80, 81], hence volume charges and surface charges cannot compensate each other. This leads to Brown's pole avoidance principle [4], which states that a magnetic structure tends to avoid magnetic charges. The tendency of the system to avoid surface charges often results in an alignment of magnetization with the surface. This effect is often referred to as *shape anisotropy*, even though it is a pure magnetostatic effect, which is not related to crystalline anisotropy (Sec. 2.2.4).

### Comparison with the Heisenberg model

Recalling Eq. 2.16

$$\mathbf{B}(\mathbf{r}) = \frac{\mu_0}{4\pi} \sum_i \frac{3\left[(\mathbf{r}-\mathbf{r}_i)\cdot\boldsymbol{\mu}_i\right]\cdot(\mathbf{r}-\mathbf{r}_i)}{(\mathbf{r}-\mathbf{r}_i)^5} - \frac{\boldsymbol{\mu}_i}{(\mathbf{r}-\mathbf{r}_i)^3} \quad , \tag{2.38}$$

one can associate the volume $V_i$ to each magnetic moment $\boldsymbol{\mu}_i$. Note that Eq. 2.38 is only valid for $\mathbf{r} \notin \{\mathbf{r}_i\}$. A transition from a summation to an integration transforms the expressions $\boldsymbol{\mu}_i/V_i$ into the magnetization and $\mathbf{B}(\mathbf{r}) \to \mu_0 \mathbf{H}_{\mathrm{dem}}$ so that Eq. 2.38 changes to

$$\mathbf{H}_{\mathrm{dem}}(\mathbf{r}) = \frac{M_s}{4\pi} \int_\Omega \left( \frac{3\left[(\mathbf{r}-\mathbf{r}')\cdot\mathbf{m}(\mathbf{r}')\right]\cdot(\mathbf{r}-\mathbf{r}')}{(\mathbf{r}-\mathbf{r}')^5} - \frac{\mathbf{m}(\mathbf{r}')}{(\mathbf{r}-\mathbf{r}')^3} \right) \mathrm{d}^3 r' \quad , \tag{2.39}$$

which yields the same result as the application of Eq. 2.34 on Eq. 2.31.

Unlike the exchange interaction, the demagnetizing field of a highly inhomogeneous structure does not show a strongly diverging behavior. As an example, the Barber pole-like spin spiral structure

$$\mathbf{m} = \begin{pmatrix} 0 \\ \cos \pi \ x/\lambda \\ \sin \pi \ x/\lambda \end{pmatrix} \tag{2.40}$$

is free of volume charges since $\nabla \mathbf{m} = 0$ is valid everywhere. The only contribution to the demagnetizing energy is due to surface charges. The opposite example is the spin spiral of type

$$\mathbf{m} = \begin{pmatrix} \cos \pi x/\lambda \\ \sin \pi x/\lambda \\ 0 \end{pmatrix} \quad , \tag{2.41}$$

which has volume charges proportional to $\pi/\lambda$. Those would diverge for short wavelengths $\lambda$ as well as the resulting field $\mathbf{H}_{\mathrm{dem}}$ and the demagnetizing energy density.

In general, this behavior can be problematic and needs careful analysis which can be achieved by a close analytic examination of the structure of interest. The contribution of the demagnetizing energy to the total energy for the strongly inhomogeneous structure of a Bloch point will be discussed in chapter 4, in which we show that the demagnetizing energy density of a Bloch point does not diverge.

### 2.2.4 Anisotropies

The crystalline structure of a material breaks the isotropy of the system, which results in preferred orientations of magnetization, the easy axes. A dominant effect inducing magnetocrystalline anisotropy is the quenching of the orbital magnetic moments originating from the competition between spin-orbit coupling and the electrostatic potential of the lattice [5]. In case of the elementary ferromagnetic materials, *i.e.*, iron, cobalt and nickel those are the 3d orbitals.

Although anisotropy is negligible in the studied systems, we briefly discuss, for completeness, the cases of the uniaxial, cubic, and surface anisotropy. Those basic anisotropy terms consider only local effects and can be included equivalently in the Heisenberg formulation.

**The uniaxial anisotropy** depends on the angle between the magnetization direction $\mathbf{m}$ and the easy axis $\mathbf{k}_{\mathrm{U}}$. Considering the first two significant orders it reads [5]

$$e_{\mathrm{K_u}} = -K_u^{(1)} \left(\mathbf{m} \cdot \mathbf{k}_{\mathrm{U}}\right)^2 + K_u^{(2)} \left(\mathbf{m} \cdot \mathbf{k}_{\mathrm{U}}\right)^4 \quad . \tag{2.42}$$

with material parameters $K_u^{(1)}$ and $K_u^{(2)}$. Because of time inversion symmetry [80] only even powers of the scalar product are considered. Note that odd powers of the scalar product would result in an easy direction — not in an easy axis. In case of $K_u^{(2)} = 0$ uniaxial anisotropy has an easy axis for $K_u^{(1)} > 0$ along $\mathbf{k}_{\mathrm{U}}$ and in case of $K_u^{(1)} < 0$ an easy plane perpendicular to $\mathbf{k}_{\mathrm{U}}$.

If $K_u^{(2)} \neq 0$ the situation becomes somewhat more complex, including the configuration of an easy cone as a possible solution [82]. Figure 2.6 shows the opening angle $\vartheta$ between $\mathbf{k}_{\mathrm{U}}$ and $\mathbf{m}$ yielding a minimum uniaxial anisotropy energy of the easy cone for different values of $K_u^{(1)}$ and $K_u^{(2)}$ with the easy-axis and easy-plane as limiting configurations.

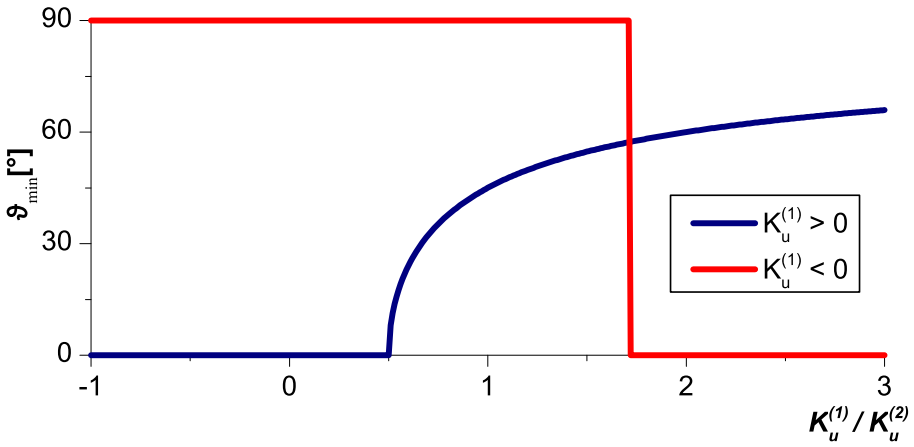


**Figure 2.6** – Angle $\vartheta = \arccos(\mathbf{m} \cdot \mathbf{k}_\mathrm{U})$ yielding a minimum of the uniaxial anisotropy energy for different values of $K_u^{(1)}$ and $K_u^{(2)}$.

**Cubic anisotropy** can be found in materials with cubic crystal lattices. If the cubic axes are aligned with the $x$,$y$, and $z$ direction, the energy density reads

$$e_{\mathrm{K_c}} = K_c^{(1)} \left(m_x^2\, m_y^2 + m_y^2\, m_z^2 + m_x^2\, m_z^2\right) + K_c^{(2)}\, m_x^2\, m_y^2\, m_z^2 \tag{2.43}$$

with material constants $K_c^{(1)}$ and $K_c^{(2)}$. Contrary to the uniaxial anisotropy, where the term with $K_u^{(2)}$ represents a higher-order correction, the two energy density terms of the cubic anisotropy are, generally speaking, of equal importance.

**Surface anisotropy** plays an important role in nanostructures with low volume to surface ratio, *e.g.* magnetic films, and was introduced by L. Néel [83]. Its first order energy density can be written as

$$e_{\mathrm{K_s}} = K_s \left[1 - (\mathbf{m} \cdot \mathbf{n})^2\right] \tag{2.44}$$

with $K_s$ the surface anisotropy material constant, and $\mathbf{n}$ the surface normal.

## 2.3 Dynamics of magnetization and magnetic moments

### 2.3.1 Effective field

So far we have discussed the individual energy contributions to the total energy. A stable magnetization distribution corresponds to a local minimum of the total

energy, which is mathematically represented by the variational problem $\delta e_{\mathrm{tot}} = 0$. The prerequisite of micromagnetism to preserve the absolute value of the magnetization in space and time adds the constraint $|M_s \mathbf{m}| = \mathrm{const}$.

In a non-equilibrium configuration the magnetization undergoes a precessional motion around an effective magnetic field and eventually relaxes in the direction of this field, resulting in a stable magnetic configuration. While the external and demagnetizing energy is derived from magnetic fields governed by Maxwell's equations, the effective field contributions of exchange and anisotropy energy need to be constructed from thermodynamic principles. W. F. Brown introduced the effective field [1] as a result of the variation of energy density with respect to the magnetization:

$$\mathbf{H}_{\mathrm{eff}} = -\frac{1}{\mu_0 \, M_s} \frac{\delta e}{\delta \mathbf{m}} \tag{2.45}$$

Applying Eq. 2.45 to the micromagnetic exchange energy density (Eq. 2.18) results in

$$\mathbf{H}_{\mathrm{xc}} = \frac{2A}{\mu_0 \, M_s} \, \Delta \mathbf{m} \quad , \tag{2.46}$$

where $\Delta = \boldsymbol{\nabla} \cdot \boldsymbol{\nabla}$ denotes the Laplace operator acting on the individual magnetization components.

In order to derive a corresponding effective field for the Heisenberg model, we consider the Heisenberg exchange energy formulation of Eq. 2.2. To apply the concept of Eq. 2.45 on Eq. 2.2, we have to take the following aspects into account:

1. Eq. 2.20 has a non-zero negative value for the saturated state, namely ${e_{\mathrm{xc}}}^{(i)} = -\sum_j J_{ij}/V_i$ in contrast to the micromagnetic exchange energy density.
2. The resulting Heisenberg exchange field should be zero for a saturated, *i.e.*, homogeneous magnetization as in the case of the micromagnetic formulation of the exchange field for the same reason as for the first point.

In general, a variation $\delta e / \delta \mathbf{m}$ eliminates constant energy offsets. For that reason we can gauge the Heisenberg exchange energy density so that it is zero in the ground state by modifying Eq. 2.2 to

$$e_i = \sum_j \frac{J_{ij}}{V_i} \, \mathbf{m}_i \cdot (\mathbf{m}_i - \mathbf{m}_j) \quad . \tag{2.47}$$

The fraction $1/\mu_0 M_s$ of Eq. 2.45 is then replaced by $V_i/\mu_0 \mu_i$ inside the volume $V_i$. This provides all the necessary components to define the Heisenberg exchange field and one obtains

$$\mathbf{H}_{\mathrm{xc(i)}}^{(\mathrm{Hei})} = \frac{V_i}{\mu_0 \, \mu_i} \sum_j \frac{J_{ij}}{V_i} \, (\mathbf{m}_j - \mathbf{m}_i) \quad . \tag{2.48}$$

The additional term $-\mathbf{m}_i$ ensures the validity of point 2 and shifts the energy by a physically irrelevant offset. It does not change the dynamics since the Landau-Lifshitz-Gilbert equation depends only on the cross-product of exchange field and magnetic orientation, as will be discussed in the next section.

### 2.3.2 Landau-Lifshitz-Gilbert equation

A homogeneous magnetic field $\mathbf{H}_{\text{eff}}$ acting on a magnetic moment $\boldsymbol{\mu}$ exerts a torque $\boldsymbol{\tau}$ on the magnetic moment. The torque $\boldsymbol{\tau}$ is, by definition, the time derivative of the angular momentum $\mathbf{L}$:

$$\boldsymbol{\tau} = \boldsymbol{\mu} \times \mathbf{H}_{\text{eff}} = \frac{\mathrm{d}\mathbf{L}}{\mathrm{d}t} \tag{2.49}$$

The angular momentum $\mathbf{L}$ is proportional to the magnetic moment

$$\mathbf{L} = -\frac{\boldsymbol{\mu}}{\gamma_0} \tag{2.50}$$

with the gyromagnetic ratio $\gamma_0 = g|e|\mu_0/2m_e$ as proportionality constant, where $|e|$ is the electron charge, and $m_e$ the electron mass. The Landé factor [84, 85] [2] $g \approx 2$ indicates that the magnetic moment originates purely from the electron spin. For real materials $g$ differs from 2 due to spin-orbit coupling. For example, Fe has a gyromagnetic ration of $g \approx 2.1$ in the absence of an external field [87].

The time derivative of the magnetic orientation can be expressed by

$$\frac{\partial \mathbf{m}}{\partial t} = -\gamma_0 \ [\mathbf{m} \times \mathbf{H}_{\text{eff}}] \quad . \tag{2.51}$$

This equation is valid for the Heisenberg model as well as for micromagnetic theory.

In a real material dissipative processes result in a damping of the precession and the magnetization tends to align to the effective field with time. To account for damping Eq. 2.51 needs to be extended. The most important extensions in this sense are due to L.D. Landau and M.L. Lifshitz [28] and to T.L. Gilbert [29, 30].

Landau and Lifshitz included damping into Eq. 2.51 by an additional torque term perpendicular to both, the magnetic orientation and the precessional term:

$$\frac{\partial \mathbf{m}}{\partial t} = -\gamma_0 \ [\mathbf{m} \times \mathbf{H}_{\text{eff}}] - \alpha \ [\mathbf{m} \times (\mathbf{m} \times \mathbf{H}_{\text{eff}})] \tag{2.52}$$

In this formulation the dissipative processes have no influence on the precessional frequency. Gilbert provided an alternative with an implicit damping term that acts

[2] $g$ can be calculated by quantum electrodynamics or measured experimentally. The value provided by NIST is $g = 2.00231930436153(53)$ [86]

perpendicular to the magnetic orientation and its time derivative

$$\frac{\partial \mathbf{m}}{\partial t} = -\gamma_0 \ [\mathbf{m} \times \mathbf{H}_{\text{eff}}] + \alpha \ \left[\mathbf{m} \times \left(\frac{\partial \mathbf{m}}{\partial t}\right)\right] \quad . \tag{2.53}$$

As long as $|\mathbf{m}| = \text{const}$ is valid, Eq. 2.53 can be transformed into the explicit form of Eq. 2.52, which is more suitable for numeric analyses:

$$\frac{\partial \mathbf{m}}{\partial t} = -\frac{\gamma_0}{1+\alpha^2} [\mathbf{m} \times \mathbf{H}_{\text{eff}}] - \frac{\alpha\gamma_0}{1+\alpha^2} [\mathbf{m} \times (\mathbf{m} \times \mathbf{H}_{\text{eff}})] \quad , \tag{2.54}$$

which is the Landau-Lifshitz-Gilbert (LLG) equation as it is implemented in the codes used for this thesis.

# 3
# Basic micromagnetic structures

Magnetization configurations in ferromagnetic samples can feature highly complex patterns, which are too complicated to be solved analytically. Many characteristic properties can be analyzed in terms of a small number of fundamental micromagnetic structures, such as domains, spin waves, domain walls, (anti-)vortices and Bloch points. To a certain extent these fundamental structures can be analyzed analytically [6, 7, 83, 88], but in order to obtain realistic results on the micromagnetic properties of a specific sample it is usually necessary to employ numerical methods.

Flux closed domain patterns in soft magnetic thin film elements, which are generated by the minimization of the magnetostatic energy, can also be constructed geometrically using the van den Berg scheme [89–91] consisting of two steps: first, a set of circles is drawn inside of the sample, each having at least two boundaries of the sample as tangents. In a second step the domains are constructed by connecting the central points of the circles. As an example, Fig. 3.1 shows the construction of the Landau and the diamond state in a rectangular sample using the van den Berg scheme.

## 3.1 Domain walls

In the framework of domain theory, a ferromagnetic sample is subdivided into differently oriented and homogeneously magnetized regions, where domain walls are considered as line defects displaying an abrupt transition between the domains. The early description by Weiss of the domain theory [92] has later been extended by micromagnetic theory, according to which domain walls possess an internal structure and a finite extension resulting from the interplay of different energy contributions.

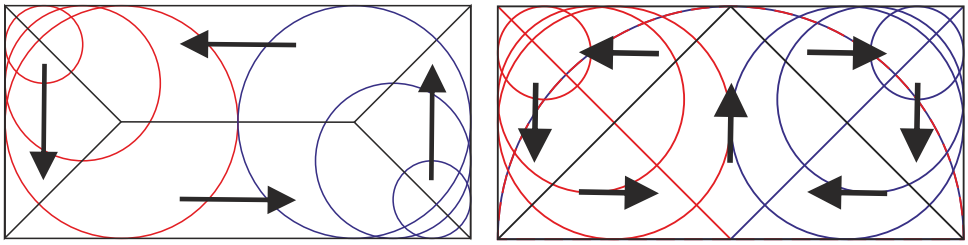

(a) Landau state (b) Diamond state

**Figure 3.1** – Sketches of the Landau and the diamond state, which are typical domain patterns in thin film elements, constructed using the van den Berg scheme.

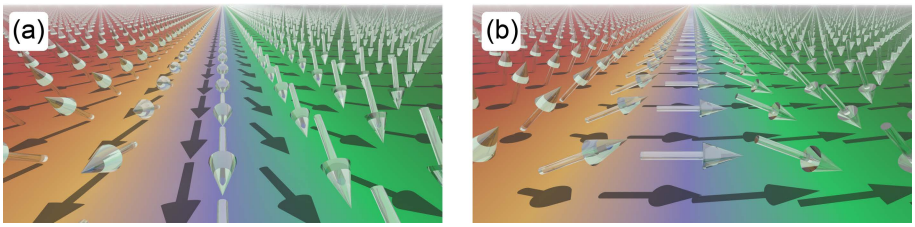


**Figure 3.2** – Sketches of a Bloch (a) and a Neél wall (b) extended in a plane.

In one dimensional analytic models two main types of domain walls can be distinguished: the Bloch [7] and the Néel wall [83]. In numerous experimental and numerical studies of the past years on long and thin soft-magnetic strips, a new type of domain wall has been studied: head-to-head or tail-to-tail domain walls in elongated samples [39] have attracted much interest. This type of domain wall is fundamentally different from both, a Bloch wall and a Néel wall.

### 3.1.1 Bloch wall

In a bulk ferromagnetic sample with uniaxial anisotropy the typical domain walls are Bloch walls [4, 5, 7] which are characterized by a rotation of the magnetization parallel to the domain wall plane, whereas the magnetization orientation inside of the domains are parallel to the domain wall plane. The 180° Bloch wall, like the Néél wall, separates domains with opposite magnetization direction. The magnetization in the domains is parallel to the domain wall plane. This type of rotation is divergence-free, hence no volume charges are generated. In the limit of an infinitely extended crystal surface charges are negligible, too. Therefore, only the interplay between exchange interaction and magnetocrystalline anisotropy defines the domain wall shape. In case of first order uniaxial anisotropy with positive anisotropy constant the angle $\vartheta$ between

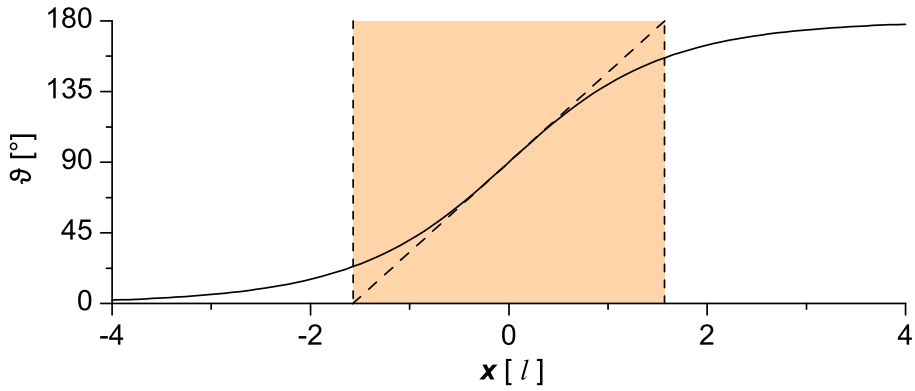


**Figure 3.3** – Slope of Bloch and Neél type domain walls in units of their characteristic length according to Eq. 3.3 and Eq. 3.5, respectively. The dashed lines indicate the domain wall width according to Lilley's definition [93].

the magnetization orientation and the easy-axis ($x$-axis) can be derived to [7]

$$\tan\vartheta = \exp\left(\frac{x}{\sqrt{A/K_{\mathrm{U}}^{(1)}}}\right) \quad . \tag{3.1}$$

A schematic representation of a Bloch wall is shown in Fig. 3.2 (a).

According to Lilley's definition [93], the Bloch domain wall width is

$$\Delta_{DW} = \pi\sqrt{A/K_{\mathrm{U}}^{(1)}} \quad , \tag{3.2}$$

from which an exchange length can be derived

$$l_{\mathrm{K}} = \sqrt{A/K_{\mathrm{U}}^{(1)}} \quad . \tag{3.3}$$

This exchange length serves as a characteristic length scale, describing the typical extension of magnetic structures in the material dominated by the interplay between anisotropy and exchange interaction.

### 3.1.2 Néel wall

In the case discussed above the magnetostatic interaction was neglected and only the uniaxial anisotropy and exchange interaction played a role in the calculation. However, in realistic samples — especially in those relevant for nanotechnology — magnetic charges play a significant role. In a one dimensional approximation, where the direction of the magnetization only depends on the distance from the domain wall center, L. Néel has derived in 1953 a domain wall transition in thin films [83], where

magnetostatic interactions are decisive. In the Néel wall, the magnetic structure is determined by the competing interactions of the exchange and of magnetostatics. Néel demonstrated [83] that in thin films, a domain wall type with an inplane rotation of the magnetization has a lower energy than the Bloch wall. This domain wall type, which is now named after Néel, has a magnetization profile that can be derived analytically to

$$\cos\vartheta = \tanh\left(\frac{x}{\sqrt{2A/\left(\mu_0\ M_s^2\right)}}\right) \quad , \tag{3.4}$$

where $\vartheta$ is the angle enclosed with the domain wall plane ($y$-axis) and the rotation occurs in the $xy$-plane. The profile is shown in Fig. 3.2 (b).

Like in the case of a Bloch wall, an exchange length can be defined

$$l_\mathrm{s} = \sqrt{2A/\left(\mu_0 M_s^2\right)} \quad . \tag{3.5}$$

For materials with low or nearly vanishing magnetocrystalline anisotropy, $l_\mathrm{s}$ defines the characteristic length scale of magnetic inhomogeneities. For Permalloy ($Ni_{80}Fe_{20}$) it yields

$$l_\mathrm{s} \approx 5.7\,\mathrm{nm} \ll l_\mathrm{K} \approx 294\,\mathrm{nm} \quad , \tag{3.6}$$

while for pure iron both exchange lengths have a value of approximately 2.1 nm. The smallest of these two exchange lengths $l_\mathrm{K}$ and $l_\mathrm{s}$ provides a useful estimate of the typical size of magnetic structures in these materials. This information can help to find a suitable discretization size in numerical simulations. However, the value of the exchange length does not rule out the possibility of structures changing on significantly shorter length scales, like, *e.g.*, the structure of a Bloch point.

### 3.1.3 Head-to-head domain wall

In the description of Bloch and Néel walls one assumes infinitely extended structures. In the case of the Bloch wall this allows one to neglect the surface integral contribution in the scalar potential of the demagnetizing field (Eq. 2.34). But in elongated structures, such as flat or cylindrical nanowires, such approximations are not adequate and the shape anisotropy contributes decisively to the total energy. It determines the magnetization direction in the domains along the wire [39]. The resulting domain wall configurations are either of head-to-head or tail-to-tail type.

In contrast to the assumptions made concerning the boundary conditions for Bloch and Néel walls, the magnetization in domain walls separated by head-to-head or tail-to-tail walls is perpendicular to the domain wall plane. It is therefore inappropriate to label those domain walls Bloch or Néel type domain walls. Since these domain walls are very important for modern research in nanopatterned magnetic materials, it is necessary to obtain a description for these walls, too. This is usually performed with numerical studies and, to a lesser extent, analytically [94].

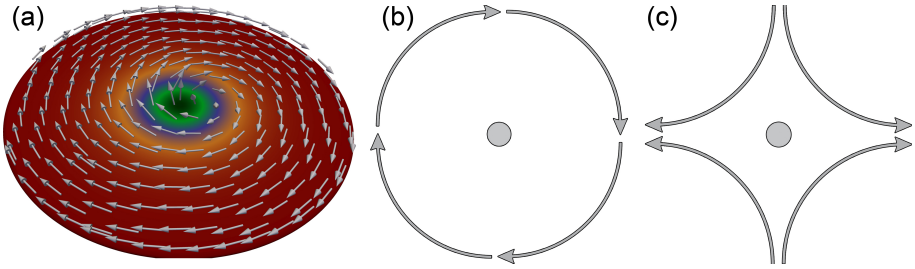


**Figure 3.4** – a) Example of a vortex structure in a ferromagnetic disc. The magnetization rotates in a concentric way around the vortex core, inside of which the magnetization points perpendicular to the vortex plane. The schematics on the right show how the structure of a vortex (b) compares to that of an antivortex (c).

## 3.2 Vortices

Magnetic vortices are regions in which the magnetization circulates in a plane around a central point, the vortex core. They usually develop in extended thin films or in sufficiently large thin-film elements. The structure closes the magnetic flux and is divergence-free, which makes it a particularly favorable arrangement to minimize the magnetostatic energy. In the center of the vortex, *i.e.*, in the core region, the magnetization turns out of the plane. This allows for a smooth change of the magnetization and prevents a singularity of the micromagnetic exchange energy in the center. Fulfilling the pole avoidance principle [4], the nanometer sized core is source of only a low amount of surface charges.

In a definition analogous to the domain wall width [93] the radius of a vortex core can be defined as

$$r_{\mathrm{core}} = \left( \frac{\mathrm{d}\sin(\phi)}{\mathrm{d}r} \right)^{-1} \quad , \tag{3.7}$$

where $\phi$ is the polar angle of the in-plane magnetization at $r = 0$.

In their variational approach for a film of thickness $h$, Usov and Peschany derived [88] as vortex core radius

$$r_{\mathrm{core}} = 0.68 l_{\mathrm{exc}} \left( \frac{h}{l_{\mathrm{exc}}} \right)^{1/3} \quad . \tag{3.8}$$

In addition to the polarization $p = \pm 1$ a vortex is characterized by its winding number, which can be defined by the contour integral

$$n = 1/2\ \pi \oint \frac{\mathrm{d}\phi}{\mathrm{d}S}\,\mathrm{d}S \tag{3.9}$$

around the perimeter $S$ of the vortex. The winding number is a topological invariant.

It can also be used to characterize the anti-vortex, a structure that is mathematically similar to a vortex since the magnetization rotates by $2\pi$ on a loop around the center, but with a very different magnetic structure that leads to a high density of magnetic volume charges, cf. Fig 3.4 c). In the case of an (anti-)vortex the polarization can be combined with the winding number, leading to the Skyrmion number or Pontryagin index [95]

$$Q = 1/2\ n\ p \quad , \tag{3.10}$$

which is a topological invariant, too. In its general form, the Pontryagin index is defined in a somewhat more complex form which is not relevant for this study. One topologically admissible possibility of changing the Skyrmion number consists in the nucleation of either a vortex or an anti-vortex at a lateral boundary. Another way of changing the Skyrmion number is a Bloch point entering on one surface, propagating through the sample and leaving it again on the opposite site; a process which results in the switching of the polarity of the vortex [10, 96].

## 3.3 Bloch points

The Bloch point (or Feldtkeller singularity) [11, 12] represents a further fundamental micromagnetic structure in addition to spin waves, domain walls and vortices. It is a micromagnetic point singularity, around which every magnetic orientation is found at least once on any arbitrary closed shell containing the Bloch point, as formulated by A. Hubert [20]. As a consequence, the magnetic orientation near the core of a Bloch point experiences an abrupt change by 180°. The magnetization near the core is thus maximally inhomogeneous. The change by 180° on the length scale of the atomic lattice constant violates the basic assumption of micromagnetism according to which angular changes of the magnetization are small on an atomic length scale. Even though their quantitative analysis is problematic due to the overestimation of the exchange energy density in the close vicinity of the singularity (as discussed in Sec. 2.2.1) the properties of this topological defect have been discussed by various authors in the framework of micromagnetism [11, 12, 20, 35, 36, 63, 97] . The work of J. Reinhardt [37] can be considered as an exception, since there the exchange energy of a static Bloch point in cubic Bravais lattices has been calculated in terms of a Heisenberg model. D. Reinhardt estimated that the size of the region around the Bloch point that cannot be treated safely with micromagnetic theory lies in the range of some lattice constants. The result fits well with our estimates in Sec. 2.2.1, where we derived a critical range of nine lattice constants for a bcc lattice with Permalloy-like material parameters. In the following we restrict the discussion on some examples of important Bloch point structures and postpone the detailed analytic discussion of Bloch points in the micromagnetic framework to chapter 4 and the multimodel discussion to the third part of this thesis.

In the 1970s, magnetic bubbles [13, 98] became a focus of research with promising properties for magnetic storage devices. As described by Malozemoff and Slonczewski

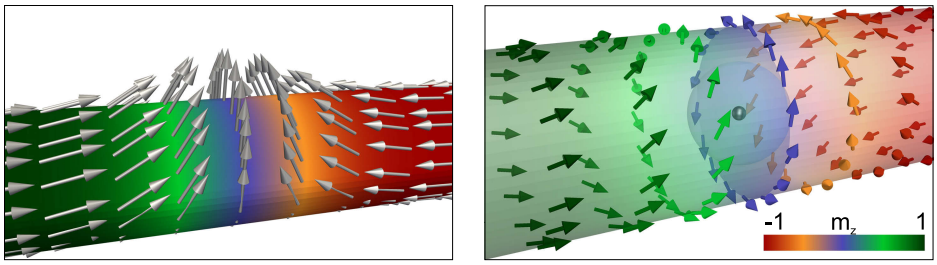


(a) Transverse wall (b) Vortex wall

**Figure 3.5** – Visualization of the two basic equilibrium domain wall types found in ferromagnetic nanocylinders with head-to-head or tail-to-tail domain walls, where the $z$ axis corresponds to the cylinder axis. Transverse walls (a) develop only in thin nanowires, whereas vortex domain walls with a Bloch point in their center (b) nucleate above a material dependent critical diameter, approximately 40 nm in the case of Permalloy (Py).

[13] different magnetic configurations are possible for bubbles. In the family of hard bubbles a Bloch point can significantly alter the bubble properties such as, *e.g.*, the mobility — the rate by which the velocity increases with an external magnetic field — is lower in the presence of a Bloch point. For a better understanding of the structure A. Hubert performed a thorough continuum analysis of those bubbles containing Bloch points [20] in the framework of micromagnetism, which represents a noticeable approximation, given the absence of an atomistic treatment of the Bloch point core.

Another example where Bloch points play an important role is the switching of vortex cores in ferromagnetic discs. The vortex core reversal has attracted much attention in the past decade [9, 10, 96, 99, 100]. There, a Bloch point is nucleated at one surface, propagates through the sample and leaves it again on the opposite side. The Bloch point nucleation is part of another process during the vortex core reversal, the annihilation of a vortex anti-vortex, which eventually results in a final magnetic state with a vortex structure that has a switched polarity in comparison to the original state.

Another example of Bloch points, which is the most important one for this thesis, is the vortex domain wall in solid cylindrical nanowires, which contains a Bloch point in its center. In general, cylindrical nanowires have often been discussed as examples to derive fundamental conclusions from analytic micromagnetic theory, since their axial symmetry allows for significant simplifications. For example, in the end of the 1950s W.F. Brown, E.H. Frei, S. Shtrikman, D.Treves and A. Aharoni discussed the reversal modes in an infinitely long (soft-)magnetic cylinder. For a general case, W.F. Brown [101] derived and analyzed a set of differential equations, whose eigenfunctions characterize a stable magnetization configuration. Almost at the same time, Frei et al. [102] applied such a variation technique in order to analyze the reversal modes in infinitely long cylinders, spheres and prolate ellipsoids. By “a bit of guesswork” and “symmetry considerations” [102] they identified three fundamental reversal modes, which for a long time have been considered the only possible ways by which magnetic

structures could switch: rotation in unison, curling, and buckling. Nevertheless, the "bit of guesswork" had two drawbacks. The buckling regime described in the early works was not an eigenstate of the cylinder system, an issue that has later been corrected owing to calculations by Brown, Aharoni and Shtrikman [103]. These authors also pointed out that, although the rotation in unison represents a possible reversal path, the corresponding coercive field is higher than that for the other two pathways. In both works [102, 103] the authors determined that for cylinder radii smaller than a critical value the buckling-type reversal mode has a lower coercive field, while for larger cylinder radii magnetic curling would be expected.

In spite of these important advances, there was still an important approximation or assumption which made a decisive difference: the hypothetical infinite cylinder neglects the property of cylinder caps. The importance of those cylinder ends was investigated by A. Arrott and coworkers [21, 22]. They predicted that as domain walls and Bloch points can nucleate at those caps, they play a significant role for the magnetic switching in general. In 2002 R. Hertel [104] and H. Forster et al. [105] studied domain walls in finite cylinders on the basis of micromagnetic simulations and described that the type of reversal mode depends on the diameter of the nanowire and that the domain walls propagate through the cylinder along the axial direction in order to reverse the magnetic orientation. Those resulting two domain wall types, namely the transverse and the vortex domain wall type are sketched in Fig. 3.5(a) and 3.5(b), respectively. While the former nucleates in cylinders of low diameter, the latter can be found in thicker wires.

# 4

# Analytic treatment of Bloch points

The analytic treatment of Bloch points in the framework of micromagnetism splits up into approaches maintaining the assumption of constant saturation magnetization, *e.g.*, those by Feldtkeller [11], Döring, Hubert [20] or A. Aharoni [77], and others introducing an additional term, *e.g.*, a Landau-type term, allowing for a local change of the saturation magnetization. Such an approach was taken in the pioneering work of Bloch point propagation by Galkina et al. [106]. Another important example is the work by Elías and Verga, who considered a radial dependence of the saturation magnetization to solve the problem of diverging exchange energy density in the close vicinity of the Bloch point core [35]. Using the same degree of freedom, namely the possibility of a reduction of the saturation magnetization, Lebecki et al. [97] used the Landau-Lifshitz-Bloch equation to model Bloch point dynamics. The approach solves the topologically critical character of a point defect in the vector field, but it does not remove the problem of abrupt changes in magnetic orientation. However, since the micromagnetic exchange field (see Sec. 2.2.1) scales with $1/M_s$, a singular behavior around the Bloch point can be avoided. Such an approximation is presumably sufficient to compensate for the intrinsic overestimation of exchange fields in micromagnetism in the vicinity of strongly inhomogeneous structures (s. Sec. 2.2.1). But as demonstrated by J. Reinhardt [37] and confirmed in chapter 14, in an atomic model the Bloch point resides between lattice sites, which makes a local reduction of magnetic moments unnecessary. In our approach we therefore remain within the classical micromagnetic approach, without varying the saturation magnetization.

Assuming a constant saturation magnetization in its vicinity, Döring and Feldtkeller [11, 12] proposed an analytic expression for the magnetic orientation of a Bloch point in the framework of micromagnetism that can be written in a generalized form

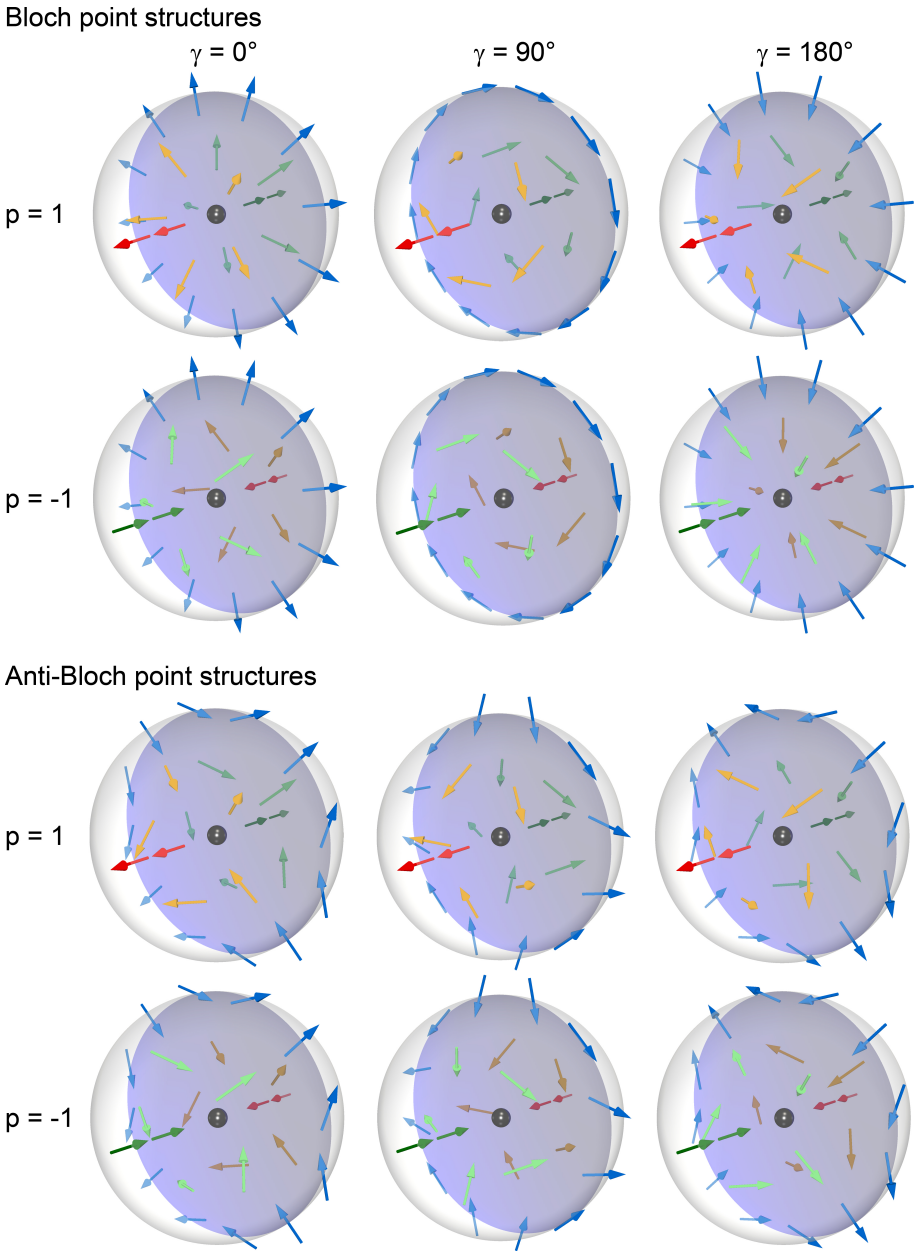


**Figure 4.1** – Visualization of various possible magnetic orientations around a Bloch point center for different inflow-angles $\gamma$, vorticities $n = \pm 1$ and outwards pointing magnetization at the poles $p = \pm 1$.

as

$$\begin{aligned} m_x &= \cos(\Phi)\sin(\Theta) \\ m_y &= \sin(\Phi)\sin(\Theta) \\ m_z &= \cos(\Theta) \\ \Theta &= p\ \vartheta + \pi\ (1-p)/2 \\ \Phi &= n\ \phi + \gamma \end{aligned} \tag{4.1}$$

with azimuthal angle $\vartheta$ and polar angle $\phi$. The parameter $p = \pm 1$ indicates an outwards pointing magnetization at the poles for $p = 1$ and an inwards pointing one for $p = -1$. The angle $\gamma$ describes the inflow of magnetization resulting, *e.g.*, in vortex-like or hedgehog states, as sketched in Fig. 4.1. The parameter $n = 1$ describes a Bloch point with vortex like structure in the $m_z = 0$ plane, while $n = -1$ generates an anti-vortex structure. In analogy to anti-vortices we label Bloch points with vorticity $n = -1$ as anti-Bloch point.

In the continuum theory the position of a Bloch point can be defined as the point where $m_\alpha = 0$ isosurfaces of the magnetization components belonging to three linear independent directions $\alpha$ cross in one point. Note that, since the definition of a Bloch point and its center origins from a continuum theory, this definition is strictly speaking not sufficient in a discrete model. In an atomistic model, the position of a Bloch point can be determined in an analogous way by means of a volume interpolation of the magnetic moments on the lattice sites around the Bloch point.

## 4.1 Pontryagin index

One of the defining properties of a Bloch point is a Pontryagin index of $Q = \pm 1$, which is always fulfilled in the case of Eq. 4.1 as long as $\gamma$ is independent of $\vartheta$ and $\phi$.

$$Q = \frac{1}{4\pi} \int \sin\Theta \, \mathrm{d}\Theta \, \mathrm{d}\Phi = p\ n = \pm 1 \quad . \tag{4.2}$$

Mathematically, magnetic configurations with $\gamma = \gamma(\vartheta, \phi)$ are possible, but this would introduce additional inhomogeneity to the system, resulting in increased exchange energy. Therefore, we retain the assumption of spatially constant $\gamma$ and postpone a more general discussion to the third part of this thesis, where the structure around a Bloch point is analyzed in terms of a numerical approach.

## 4.2 Micromagnetic Bloch point exchange energy density

The micromagnetic exchange energy density of a Bloch point as described in Eq. 4.1 can be calculated as follows: The spatial derivatives of $\mathbf{m}$ are given by

$$\frac{\partial m_x}{\partial x_\alpha} = -\frac{\partial \phi}{\partial x_\alpha}\sin(\Phi)\sin(\Theta) + p\,\frac{\partial \vartheta}{\partial x_\alpha}\cos(\Phi)\cos(\Theta) \tag{4.3}$$

$$\frac{\partial m_y}{\partial x_\alpha} = \frac{\partial \phi}{\partial x_\alpha}\cos(\Phi)\sin(\Theta) + p\,\frac{\partial \vartheta}{\partial x_\alpha}\sin(\Phi)\cos(\Theta) \tag{4.4}$$

$$\frac{\partial m_z}{\partial x_\alpha} = -p\frac{\partial \vartheta}{\partial x_\alpha}\sin(\Theta) \quad , \tag{4.5}$$

which can be used in conjunction with Eq. 2.18 to obtain

$$e_{\mathrm{xc}} = A\sum_{\alpha=x,y,z}\left(\frac{\partial \vartheta}{\partial x_\alpha}\right)^2 + \left(\frac{\partial \phi}{\partial x_\alpha}\right)^2 \sin^2\Theta \tag{4.6}$$

$$= A\left[(\nabla\vartheta)^2 + (\nabla\phi)^2\sin^2\Theta\right] \tag{4.7}$$

$$= A\left[\frac{1}{r^2} + \frac{1}{r^2}\frac{\sin^2\Theta}{\sin^2\vartheta}\right] \quad . \tag{4.8}$$

Due to $\sin\Theta = \sin\vartheta$ one obtains eventually

$$e_{\mathrm{xc}} = \frac{2A}{r^2} \quad . \tag{4.9}$$

The resulting exchange energy density depends only on the distance $r$ to the Bloch point center and is independent of $\gamma$. It features a singularity around $r = 0$, but nevertheless the total exchange energy inside of a sphere with radius $R$ is finite [12]:

$$E_{\mathrm{xc}} = 8\pi AR \tag{4.10}$$

In order to use the Gilbert-equation (Eq. 2.53) the exchange field needs to be known, which is given in spherical coordinates for $n = 1$ by

$$\begin{aligned}\mathbf{H}_{\mathrm{xc}} &= \frac{2\,A}{\mu_0\,M_s}\,\Delta\,\mathbf{m} \\ &= \frac{2\,A}{\mu_0\,M_s}\left[-\frac{\mathbf{m}}{r^2} + \frac{1}{r^2}\begin{pmatrix} \frac{\cos^2\vartheta}{\sin\vartheta}\,\cos(\phi+\gamma) \\ \frac{\cos^2\vartheta}{\sin\vartheta}\,\sin(\phi+\gamma) \\ -p\,\cos\vartheta \end{pmatrix} - \frac{1}{r^2}\begin{pmatrix} \cos(\phi+\gamma) \\ \sin(\phi+\gamma) \\ 0 \end{pmatrix}\right]\end{aligned} \tag{4.11}$$

The cross product $\mathbf{m}\times\mathbf{H}_{\mathrm{xc}}$ yields exactly zero, which means that the exchange interaction does not influence the dynamics of the Bloch points represented by Eq. 4.1.

## 4.3 Demagnetizing energy

For the case of $n = 1$ in Eq. 4.1 Gauss's theorem can be used to transform Eq. 2.34

$$\begin{aligned} U_{\mathrm{dem}} =& \frac{1}{4\pi\mu_0}\left[-\int\limits_{\Omega'}\frac{\boldsymbol{\nabla}\cdot\mathbf{M}(\mathbf{r}')}{|\mathbf{r}-\mathbf{r}'|}\,\mathrm{d}^3r' + \int\limits_{\partial\Omega'}\frac{\mathbf{M}(\mathbf{r}')\cdot\mathbf{n}}{|\mathbf{r}-\mathbf{r}'|}\,\mathrm{d}^2r'\right] \\ =& -\frac{M_s}{4\pi\mu_0}\int\limits_{\Omega'}(\mathbf{m}(\mathbf{r}')\cdot\boldsymbol{\nabla}_{\mathbf{r}'})\frac{1}{|\mathbf{r}-\mathbf{r}'|}\,\mathrm{d}^3\mathbf{r}' \quad , \end{aligned} \tag{4.12}$$

where $\boldsymbol{\nabla}_{\mathbf{r}'}$ acts only on $\mathbf{r}'$ and

$$\frac{1}{\mathbf{r}-\mathbf{r}'} = \sum_{l=0}^{\infty}\sum_{m=-l}^{l}\frac{4\pi}{2l+1}\frac{r_<^l}{r_>^{l+1}}Y_{l,m}(\vartheta,\phi)Y_{l,-m}(\vartheta',\phi') \quad . \tag{4.13}$$

The above equation displays the decomposition into spherical harmonics $Y_{lm}(\vartheta,\phi)$ with $r_< = \min(r,r')$ and $r_> = \max(r,r')$. The components of $\mathbf{m}(\mathbf{r}')$ in spherical coordinates are

$$m_{r'} = \cos(\gamma)\ \sin^2(\vartheta') + p\ \cos^2(\vartheta') \tag{4.14}$$

$$m_{\vartheta'} = \sin(\vartheta')\ \cos(\vartheta')(\cos(\gamma) - p) \tag{4.15}$$

$$m_{\phi'} = \sin(\gamma)\ \sin(\vartheta) \tag{4.16}$$

and the $\boldsymbol{\nabla}$ operator in spherical coordinates is defined by

$$\boldsymbol{\nabla}_{\mathbf{r}'} = \mathbf{e}_{\mathbf{r}'}\ \frac{\partial}{\partial r'} + \mathbf{e}_{\vartheta'}\ \frac{1}{r'}\frac{\partial}{\partial\vartheta'} + \mathbf{e}_{\phi'}\ \frac{1}{r'\sin(\vartheta')}\frac{\partial}{\partial\phi'} \quad . \tag{4.17}$$

Therefore Eq. 4.12 can be rewritten as

$$\begin{aligned}\frac{4\pi}{M_s}\,U_{\mathrm{dem}} = -\sum_{l=0}^{\infty}\sum_{m=-l}^{l}\frac{4\pi}{2l+1}\\ \int_{\Omega'}\Bigg(\left(\cos(\gamma)\ \sin^2(\vartheta')+p\ \cos^2(\vartheta')\right)\frac{\partial}{\partial r'}\\ +\frac{\sin(\vartheta')\ \cos(\vartheta')\ (\cos(\gamma)-p)}{r'}\frac{\partial}{\partial\vartheta'}\\ +\frac{\sin(\gamma)}{r'}\frac{\partial}{\partial\phi'}\Bigg)\\ \frac{r_<^l}{r_>^{l+1}}\ Y_{l,m}(\vartheta,\phi)\ Y_{l,-m}(\vartheta',\phi')\,\mathrm{d}\cos\vartheta'\,\mathrm{d}\phi'\,\mathrm{d}r' \quad .\end{aligned} \tag{4.18}$$

The spherical harmonics $Y_{l,-m}(\vartheta',\phi')$ depend on $\phi'$ by $e^{im\phi'}$. Due to the $\phi'$-integration from $-\pi$ to $\pi$ in spherical coordinates, all terms with $m \neq 0$ vanish as well as the terms containing derivatives with respect to $\phi'$. As a consequence, the $\phi'$ integration is trivial and results in a factor of $2\pi$.

After integration by parts, the term belonging to the derivative of $Y_{l,-m}(\vartheta',\phi')$ with respect to $\vartheta'$ transforms into an expression proportional to $Y_{l,-m}(\vartheta',\phi')$. Subsequently, all remaining terms of the integrand are proportional to $Y_{l,0}(\vartheta') = P_l(\cos\vartheta')$ or $\cos^2\vartheta' P_l(\cos\vartheta')$, where $P_l(\cos\vartheta')$ is the $l^{\mathrm{th}}$ Legendre's polynomial. Due to the orthogonality of the Legendre's polynomials only the terms with $l = 0$ and $l = 2$ are non-zero and contribute to the magnetostatic potential, which can then be derived exactly. For a spherical sample with radius $R$ this results in

$$U_{\mathrm{dem}} = -\frac{M_s}{24}\left(3r\ \cos(2\vartheta)\ (p-\cos(\gamma))+9p\ r-8p\ R+15r\ \cos(\gamma)-16R\ \cos(\gamma)\right) \quad , \tag{4.19}$$

which differs from the result by Pylypovskyi [36] by the physically unimportant offset summand $M_sR/3$. The demagnetizing energy can be calculated from the obtained stray field in two different ways. First, by considering

$$E_{\mathrm{dem}} = \frac{\mu_0}{2}\int_V \mathbf{H}_{\mathrm{dem}}\cdot\mathbf{H}_{\mathrm{dem}}\,\mathrm{d}V \quad , \tag{4.20}$$

which is effectively the approach Döring followed in Ref. [12], and second

$$E_{\mathrm{dem}} = -\frac{\mu_0\ M_s}{2}\int_V \mathbf{m}\cdot\mathbf{H}_{\mathrm{dem}}\,\mathrm{d}V \quad , \tag{4.21}$$

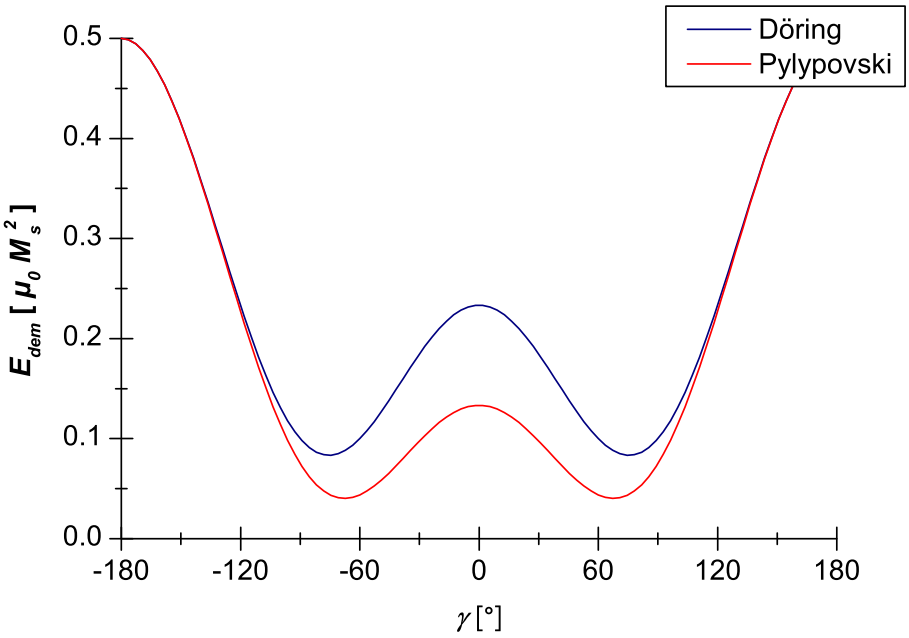


**Figure 4.2** – Magnetostatic energy density of a Bloch point inside a sphere as calculated by Pylypovskyi et al. [36] and by Döring [12] as a function of the inflow-angle $\gamma$.

which accounts also for the stray field energy outside of the sample and was used by Pylypovskyi et al. [36].

The difference between the two energy calculation methods arises from the contribution of the stray field energy outside of the sample that is considered properly in Eq. 4.21. Note that, in general, in Eq. 4.20 an integration of $\mathbf{H}_{\text{dem}} \cdot \mathbf{H}_{\text{dem}}$ over the full $\mathfrak{R}^3$ would be necessary instead of the integration over the spherical volume to calculate correctly the magnetostatic energy. Figure 4.2 compares the angular dependence of the total demagnetizing energy density for a sphere with $p = -1$ and $n = 1$. The plot indicates the existence of an equilibrium angle $\gamma$, which will be discussed in the forthcoming section.

## 4.4 Equilibrium Bloch point angle $\gamma$

In an exchange dominated system the magnetic configuration according to Eq. 4.1 is stable, as indicated by the vanishing torque exerted by the exchange field on the magnetization. The exchange energy of a Bloch point described by Eq. 4.1 is independent of $\gamma$. Hence, only the external and the demagnetizing field are responsible for lifting this degeneracy of Eq. 4.1 in $\gamma$.

The first calculations on the equilibrium angle $\gamma$ in the case of zero external field are due to Feldtkeller and Döring in the 1960s for an infinite ferromagnetic structure,

thereby neglecting the vanishing surface integral in Eq. 2.34. The structure of the magnetization was assumed to be according to Eq. 4.1. In his approach, Feldtkeller applied the pole-avoidance principle [11] of Eq. 2.34

$$\int_0^{\pi}\int_{-\pi}^{\pi} \boldsymbol{\nabla}\cdot\mathbf{M}\,\mathrm{d}\cos\vartheta\,\mathrm{d}\phi = 0 \tag{4.22}$$

and obtained for the case $n = 1$ an equilibrium angle

$$\cos(\gamma) = -\frac{p}{2} \quad . \tag{4.23}$$

The pole avoidance ansatz provides a mathematically easy pathway for the calculation of $\gamma$, but it neglects the influence of the Green's function in Eq. 2.34. To account for this term, Döring used the exact solution of Eq. 2.34 given by Eq. 4.19 in Ref. [12]. The same approach was used in recent studies by Pylypovskyi et al. [36] and Elías and Verga [35].

Döring estimated $\gamma$ by applying Eq. 4.20 and obtained

$$\cos(\gamma) = -p\,\frac{11}{29} \quad , \tag{4.24}$$

whereas Pylypovskyi et al., as well as Elías and Verga, used Eq. 4.21 resulting in

$$\cos(\gamma) = -\frac{p}{4} \quad . \tag{4.25}$$

## 4.5 Bloch point propagation — a simple model

So far we considered only the static magnetization configuration of a spherical sample, for which the demagnetizing potential can be calculated analytically. Because the value of the equilibrium angle $\gamma$ in Eq. 4.25 is close to the result by Lebecki et al. [97] as well as our simulation results discussed in chapter 8, we use the magnetostatic potential of Eq. 4.19 as first approximation of the potential in the vicinity of a Bloch point in a vortex domain wall in a cylindrical ferromagnetic wire. Even though this approach appears to be a coarse approximation of the reality, it provides a plausible explanation for effects of Bloch point dynamics described within this thesis, which were obtained from simulation studies.

We consider a Bloch point centered at $(x_c, y_c, z_c)$ in a round wire with the cylinder axis oriented along the $z$-direction. With

$$\begin{array}{rcl} r & = & \sqrt{(x-x_c)^2+(y-y_c)^2+(z-z_c)^2} \\ \cos\vartheta & = & \frac{z-z_c}{r} \\ \tan\phi & = & \frac{x-x_c}{y-y_c} \end{array} \tag{4.26}$$

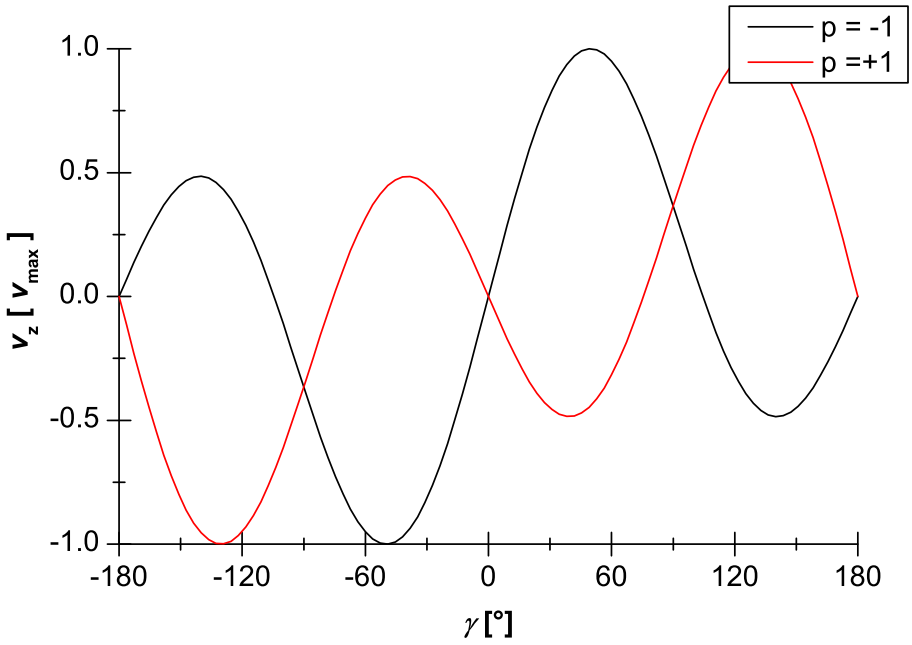


**Figure 4.3** – Visualization of the analytic Bloch point velocity in $z$-direction under the assumption of constant inflow angle $\gamma$ as a function of $\gamma$.

we can write the left-hand side of the Gilbert equation for the case of stationary Bloch point motion assuming a spatially and temporally constant value of $\gamma$

$$\frac{\mathrm{d}\mathbf{m}}{\mathrm{d}t} = \frac{\partial \mathbf{m}}{\partial \vartheta}\frac{\mathrm{d}\vartheta}{\mathrm{d}t} + \frac{\partial \mathbf{m}}{\partial \phi}\frac{\mathrm{d}\phi}{\mathrm{d}t} \quad . \tag{4.27}$$

The only time-dependent variables are, by definition, $x_c, y_c, z_c$. This leads to

$$\begin{aligned}\frac{\mathrm{d}\mathbf{m}}{\mathrm{d}t} = &\begin{pmatrix} \cos(\vartheta)\ \cos(\gamma + n\ \phi) \\ \cos(\vartheta)\ \sin(\gamma + n\ \phi) \\ -p\ \sin(\vartheta) \end{pmatrix} \cdot \\ &\frac{\sin(\vartheta)\,(\cos(\vartheta)\ \cos(\phi)v_x + \cos(\vartheta)\ \sin(\phi)v_y - \sin(\vartheta)\ v_z)}{r} + \\ &\begin{pmatrix} -n\ \sin(\vartheta)\ \sin(\gamma + n\ \phi) \\ n\ \cos(\gamma + n\ \phi)\sin(\vartheta) \\ 0 \end{pmatrix} \frac{\csc(\vartheta)\ (\sin(\phi)\ v_x - \cos(\phi)\ v_y)}{r} \quad ,\end{aligned} \tag{4.28}$$

where $v_x, v_y, v_z$ are the velocities in $x$, $y$, and $z$ direction, respectively. In the limit of $x_c \to 0$ and $y_c \to 0$ the azimuthal angle $\phi$ in the moving spherical coordinate system of the Bloch point is identical with the azimuthal angle $\Phi$ in the laboratory frame of

cylindrical coordinates. Therefore, we can identify

$$-v_\Phi = \sin(\phi)\ v_x - \cos(\phi)\ v_y \tag{4.29}$$
$$v_\rho = \cos(\phi)\ v_x - \sin(\phi)\ v_y \quad , \tag{4.30}$$

where $v_\Phi$ is the azimuth (spiraling) velocity of the Bloch point structure inside of the cylinder and $v_\rho$ is the radial velocity in cylindrical coordinates. Due to the assumption $x_c \to 0$ and $y_c \to 0$, a quasi-static solution of Eq. 4.28 with constant and non-zero $v_\rho$ is impossible in a cylindrical sample. Such a constant non-zero radial velocity would result in an expulsion of the Bloch point from the sample, which contradicts the assumption of quasi-static motion. Therefore, the left hand side of the Gilbert equation results in

$$\frac{\mathrm{d}\mathbf{m}}{\mathrm{d}t} = \begin{pmatrix} -\sin(\vartheta)\ \cos(\vartheta)\ \cos(\gamma+n\phi) \\ -\sin(\vartheta)\ \cos(\vartheta)\ \sin(\gamma+n\phi) \\ p\ \sin^2(\vartheta) \end{pmatrix} \frac{v_z}{r} + \begin{pmatrix} n\ \sin(\gamma+n\ \phi) \\ -n\ \cos(\gamma+n\ \phi) \\ 0 \end{pmatrix} \frac{v_\Phi}{r} \quad . \tag{4.31}$$

As mentioned on page 38 the torque exerted on the magnetization by the exchange field is zero, and an external magnetic field in $z$-direction exerts torques in $x$ and $y$ direction only. Thus, the $z$-component of the Gilbert equation provides the expression for $n = 1$ that needs to be averaged over the spherical region with radius $R$

$$\frac{-4\pi}{3}\ p\ R^2\ v_z = -\frac{8\pi}{45}\ M_s\ R^3\ \mu_0\ \gamma_0 (p\ \sin(\gamma) + 4\ \sin(\gamma)\ \cos(\gamma)) - \alpha\ \frac{1}{2}\ R^2\ \pi^2\ v_\phi \quad . \tag{4.32}$$

Hence, $v_z$ can be expressed as a function of $\gamma$:

$$v_z = \frac{2}{15}\ M_s\ R\ \mu_0\ \gamma_0\ (\sin(\gamma) + 4\ p \sin(\gamma)\ \cos(\gamma)) + \frac{9}{24}\ \alpha\ \pi\ v_\phi \quad , \tag{4.33}$$

which, after some rearrangement, reads

$$\begin{aligned} v_z &= v_{\max}\ \frac{\sin(\gamma) + 4p\ \sin(\gamma)\ \cos(\gamma)}{\Gamma} + \frac{9}{24}\ \alpha\ \pi\ v_\phi \\ v_{\max} &= \frac{2}{15}\ \Gamma\ M_s\ R\ \mu_0\ \gamma_0 \\ \Gamma &= \max\left(\sin(\gamma) + 4p\ \sin(\gamma)\ \cos(\gamma)\right) \approx 2.736 \quad . \end{aligned} \tag{4.34}$$

Here $R$ should be regarded as an effective radius. Note that according to Eq. 4.34 $v_z$ can increase by performing a spiraling rotation of the Bloch point around the axis of the cylinder in the limit of very small radii. This oscillation provides a channel for the Bloch point to couple to spin waves. Figure 4.3 visualizes the results according to Eq. 4.34 for the two Bloch point polarities $p = \pm 1$.

## 4.6 Summary

In this chapter an analytic view on the structure, the energy, and the dynamics of Bloch points has been presented within the micromagnetic framework. These results can provide a qualitative guideline for the discussions, the interpretation and the analysis of the properties of Bloch point structures obtained from multimodel simulations that will be discussed in the third part of this thesis. Assuming a spatially independent value of the inflow angle $\gamma$, we derived in Eq. 4.10 the micromagnetic exchange energy of a Bloch point in a spherical volume. We calculated for such a spherical sample the demagnetization energy for Bloch points with positive vorticity $n$ depending on the inflow-angle $\gamma$. From the application of different approximations we expect the equilibrium value of $\gamma$ for $p = 1$ between $60°$ and $75.5°$. In the last section of this chapter we pointed out that in the approximation of spatially constant $\gamma$ the axial velocity of a spherical region with the Bloch point in its center propagating in an extended sample should depend on the trigonometric functions of $\gamma$. The velocity is therefore bounded, and the equations provide a limit for the maximum velocity with which a Bloch point can propagate. An increase of its velocity appears to be only possible if the Bloch point undergoes a spiraling propagation around the polar axis of the spherical region. As we will demonstrate in the third part of this thesis Bloch points in a magnetic domain wall can indeed develop spontaneously such a spiraling propagation after reaching the limit of linear motion.

# Part II.
# Numerics

# 5
# Finite element method

Continuum theories are powerful tools to formulate physical models. But the underlying equations are usually too complex to be solved analytically, with only few exceptions which are limited to basic geometries and often rely on further simplifying assumptions. For example, in micromagnetism already the magnetization dynamics involving a single domain wall in a thin ferromagnetic strip is analytic treatable only with strong approximations and, therefore, requires numerical approaches for reliable predictions. While the analytical theory treats the spatial development in the form of a continuum, numerical representations of a given model usually rely on a discretization of the domain in which the problem is defined. The most widespread discretization methods are known as *finite differences* and *finite elements* [107]. The finite difference approach typically assumes equidistant cells, which makes it rather easy to approximate spatial differentiation and integration by means of difference quotients. Difficulties arise at the boundaries of samples if the sample boundaries do not follow exactly the edges of the discretization cells. This results in an inaccurate modeling of the sample shape as sketched in Fig. 5.1. Although the errors connected with the geometric approximation of curved or inclined facets can be reduced by choosing smaller discretization cells, a few fundamental problems remain which do not disappear in the limit of zero cell size. Firstly, the mesh introduces a numerical fourfold anisotropy due to the "staircase" approximation, which can lead to results that depend on the choice of the orientation of the grid [108], and secondly, the surface is often not properly scaled. In the example displayed in Fig. 5.1, for a disk of radius $R$, the circumference yields in finite differences $U = 8R$ instead of the real value of $U = 2\pi R$, irrespective of the size of the discretization cell.

In spite of these limitations, textbooks often refer to numerical concepts in the finite difference framework due to the easiness of the underlying mathematics and programming. Unlike the finite-difference method, the discretization scheme of the finite element method (FEM) uses discretization points at freely adjustable positions, which allows for a far more accurate approximation of the sample shape by plac-

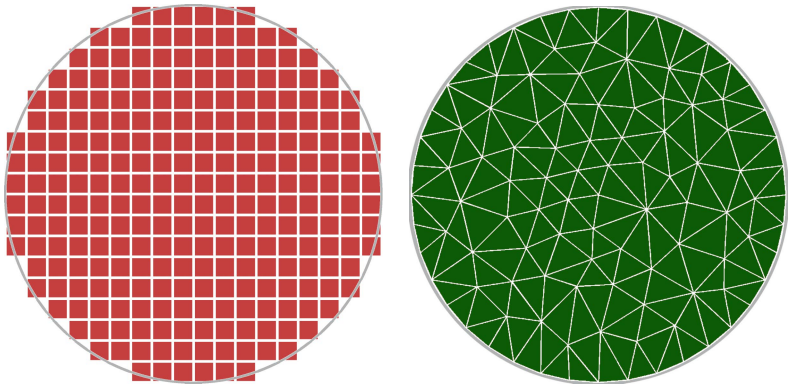

(a) Finite difference method (b) Finite element method

**Figure 5.1** – Numeric approximation of a circle with (a) finite differences and (b) finite elements.

ing a subset of nodes exactly on the boundary of the sample which are then usually connected by lines or flat surface elements. The volume is then filled with a problem-specific distribution of nodes, *i.e.*, the discretization points of the simplex elements (Sec. 5.1.1). The entity consisting of nodes and simplex elements is the finite-element mesh used for the problem. The price that has to be paid for this geometrical flexibility and freedom in placing the discretization points is that the filling of the volume with nodes as well as the handling of differentiation and integration are non-trivial mathematical tasks. For the mesh generation powerful programs and libraries like GMSH [109] are freely available. We have used GMSH to create most of the FEM meshes used for the numerical studies in this thesis. In this chapter we briefly introduce some fundamental concepts of finite element calculations and highlight the challenges that had to be solved to implement our multiscale - multimodel simulation software package. Further details of the finite element method can be found in the literature, *e.g.*, in Ref. [107].

## 5.1 Mathematical overview of FEM

### 5.1.1 Simplex elements

For finite element method calculations the volume of a given sample is completely and consistently subdivided into non-overlapping basic elements. Inside each element, a set of functions is defined that is used to interpolate between the values at the discretization points (nodes). For example, in a one-dimensional sample a simplex element can be a line segment, for which two points serve as nodes between which the discretized values are interpolated linearly. Higher-order interpolations are possible [107] by using additional nodes (discretization points), which in the case of a piecewise quadratic approximation are located at the midpoint of the edges of the simplex

element. In two dimensions the simplex element for linear interpolation is the triangle in which the nodes for interpolations are its corner vertices. In three dimensions the tetrahedron is the simplex element, again, with the corner vertices as nodes for the interpolation. By definition, a simplex element has d+1 vertices if d is the spatial dimension.

A remark on nomenclature: The nodes of the mesh can be indexed in two different ways. Either by using a combination of the simplex element index $n$ and a local node index $i$, *e.g.*, $f_i^{(n)}$ or by means of a global node index, *e.g.*, $f_{\mathfrak{a}}$.

### 5.1.2 Shape functions

In FEM a discretized approximation of a given function $f(\mathbf{r})$ is defined at the discretization points and interpolated piecewise inside of each simplex element. For each simplex element $n$ with $D$ nodes a unique set of $D$ interpolation functions $\{\eta_i^{(n)}\}$ is defined. These functions, which are named shape functions, depend only on the shape of the element. One of their fundamental properties is that they are only non-zero inside of their corresponding simplex element. Hence, a function $f(\mathbf{r})$ decomposed into $N$ simplex elements can be written as

$$f(\mathbf{r}) \approx \widetilde{f}(\mathbf{r}) = \sum_{n=1}^{N} \sum_{i=1}^{D} \eta_i^{(n)}(\mathbf{r})\ f_i^{(n)} \quad , \tag{5.1}$$

where $f_i^{(n)}$ are the discretized values of $f(\mathbf{r})$ at node $i$ of the simplex element $n$. Like any other weighting function, the set of shape functions has to be normalized everywhere inside of the simplex element. In the following we will focus on tetrahedral simplex elements with linear shape functions. In that case the vertices of the tetrahedra serve as nodes and the shape functions read

$$\eta_i^{(n)}(\mathbf{r}) = a_i^{(n)} + \sum_{\alpha=\{x,y,z\}} b_{i,\alpha}^{(n)}\ x_\alpha \quad , \tag{5.2}$$

where $a_i^{(n)}$,$b_{i,\alpha}^{(n)}$ are results of the set of linear equations

$$\eta_i^{(n)}(\mathbf{r}_j) = \delta_{ij} \tag{5.3}$$

using the Kronecker delta $\delta_{ij}$. It is noteworthy that the isosurfaces of shape function $\eta_i^{(n)}(\mathbf{r})$ are parallel to that face of the simplex element which does not contain the vertex $i$.

### 5.1.3 Spatial differentiation

By applying the approximation of Eq. 5.1 the spatial information on the function $f$ is effectively transferred to the spatial dependence of the shape functions. Therefore, a

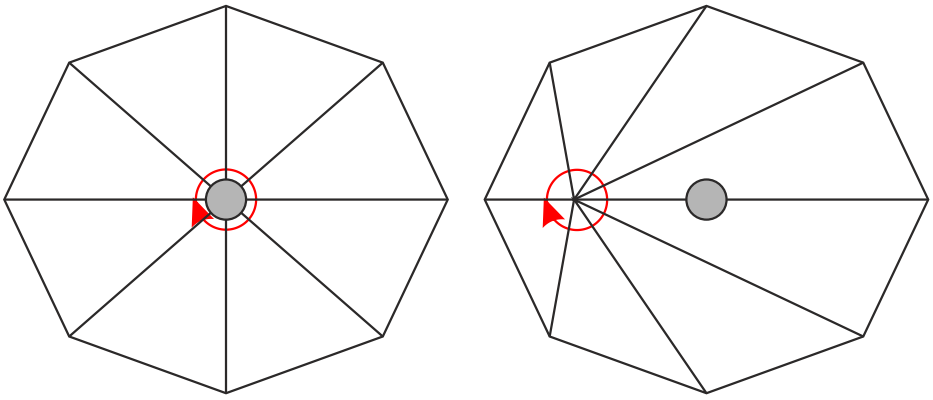

(a) Voronoi cell with isotropic tetrahedra (b) Voronoi cell with elongated tetrahedra

**Figure 5.2** – Sketches of Voronoi cells in two dimensions visualize the difference between the volume averaging by Eq. 5.6 and the solid angle averaging by Eq. 5.7. In case of the volume averaging the spatial differentiation is derived at the center of mass of the Voronoi cell — indicated by a grey dot — resulting in a numerical error if the element is elongated.

numerical approximation of the spatial derivative of $f$ along $\mathbf{k}$ can be written as,

$$\frac{\partial f(\mathbf{r})}{\partial \mathbf{k}} \approx \sum_{i=1}^{d} f_i^{(n)} \frac{\partial \eta_i^{(n)}(\mathbf{r})}{\partial \mathbf{k}} \qquad \text{for } \mathbf{r} \in \Omega_n \quad , \tag{5.4}$$

where $\Omega_n$ is the region of the simplex element $n$ formed by $d$ nodes.

The spatial derivatives inside of the simplex elements are well defined by the shape functions, whereas on the facets of the simplex element the derivatives can be discontinuous. In simplex elements the nodes are located on the corners of the element. Hence, in order to calculate the derivative at a node $\mathfrak{a}$ all simplex elements $n$ need to be involved, which contain node $\mathfrak{a}$ as a discretization point. The set of those simplex elements is the Voronoi cell [110] of node $\mathfrak{a}$, which we denote by $\mathfrak{V}_\mathfrak{a}$. Technically the derivative in direction $\mathbf{k}$ can be expressed by

$$\left.\frac{\partial f(\mathbf{r})}{\partial \mathbf{k}}\right|_{\mathbf{r}=\mathbf{r}_\mathfrak{a}} \approx \sum_{\mathfrak{b} \in \mathfrak{V}_\mathfrak{a}} \underline{\underline{\mathbf{D}}}_{\mathfrak{a},\mathfrak{b}}^{(\mathbf{k})} f_\mathfrak{b} \quad , \tag{5.5}$$

where the global index $\mathfrak{b}$ runs over all the nodes forming the Voronoi cell $\mathfrak{V}_\mathfrak{a}$.

In the case of tetrahedral elements at least two useful formulations of the tensor $\underline{\underline{\mathbf{D}}}_{\mathfrak{a},\mathfrak{b}}^{(\mathbf{k})}$ are possible. The choice depends on the further usage of the derived quantity. An average based on the volume contributions of the elements to the Voronoi cell is advantageous if the derivative is used as a part of a global quantity, such as an integration over the sample volume. But if an accurate estimate of the local quantity

is required, which depends only on the surrounding of node $\mathfrak{a}$, a weighting by the solid angle shares of the Voronoi cell of $\mathfrak{a}$ is generally the better choice to compensate the influence of elongated tetrahedra, which can have large volumes but only small solid angles as sketched in Fig. 5.2.

In the case of tetrahedral elements (Eq. 5.2), the matrix $\underline{\underline{\mathbf{D}}}_{\mathfrak{a},\mathfrak{b}}^{(\mathbf{x}_\alpha)}$ for the direction $\mathbf{x}_\alpha$ reads in the two described cases:

$$\underline{\underline{\mathbf{D}}}_{\mathfrak{a},\mathfrak{b}}^{(\mathbf{x}_\alpha)} = \frac{1}{\sum\limits_{n\in\mathfrak{V}_\mathfrak{a}} V^{(n)}} \sum_{n\in(\mathfrak{V}_\mathfrak{a}\cap\mathfrak{V}_\mathfrak{b})} V^{(n)}\, b_{j,\alpha}^{(n)} \quad \text{with } \mathfrak{b} \mathrel{\hat{=}} \{(n), j\} \tag{5.6}$$

$$\underline{\underline{\mathbf{D}}}_{\mathfrak{a},\mathfrak{b}}^{(\mathbf{x}_\alpha)} = \frac{1}{\sum\limits_{n\in\mathfrak{V}_\mathfrak{a}} S_i^{(n)}} \sum_{n\in(\mathfrak{V}_\mathfrak{a}\cap\mathfrak{V}_\mathfrak{b})} S_i^{(n)} b_{j,\alpha}^{(n)} \quad \text{with } \mathfrak{a} \mathrel{\hat{=}} \{(n), i\}, \mathfrak{b} \mathrel{\hat{=}} \{(n), j\} \tag{5.7}$$

where $\mathfrak{V}_\mathfrak{a}\cap\mathfrak{V}_\mathfrak{b}$ denotes the volume of those tetrahedra which contain both, node $\mathfrak{a}$ and node $\mathfrak{b}$ as discretization points, $V^{(n)}$ is the volume of tetrahedron $n$, and $S_i^{(n)}$ is the solid angle at the vertex $i$ of tetrahedron $n$. Both formulations have in common that the matrices can be calculated in a preprocessing step and stored as sparse matrices (s. Sec. 5.1.7).

### 5.1.4 Spatial integration

The integration of a function over the volume of the finite elements can be expressed as a matrix vector multiplication, similar to the case of spatial differentiation. Starting from Eq. 5.1 the volume integral of $f(\mathbf{r})$ over the volume of the sample is represented by

$$\int_V f(\mathbf{r})\,\mathrm{d}V \approx \sum_{n=1}^{N}\sum_{i=1}^{D} f_i^{(n)} \int_V \eta_i^{(n)}(\mathbf{r})\,\mathrm{d}V \quad . \tag{5.8}$$

In case of tetrahedral elements the integral $\int_V \eta_i^{(n)}(\mathbf{r})\,\mathrm{d}V$ yields $\frac{1}{4}V^{(n)}$, meaning that each of the four vertices of the tetrahedron corresponds to a volume of 1/4 of the tetrahedral volume and that each node of the mesh has an associated volume of 1/4 of the Voronoi cell volume. One can therefore write

$$\int_V f(\mathbf{r})\,\mathrm{d}V \approx \sum_{\mathfrak{a}} f_\mathfrak{a}\,\frac{V_\mathfrak{a}}{4} \quad , \tag{5.9}$$

where $\mathfrak{a}$ runs over all nodes of the mesh.

### 5.1.5 Laplace operator

The linear approximation of a function $f(\mathbf{r})$ inside of finite element cells, as used within this thesis, allows only for the definition of first order spatial derivatives. Due

to the piecewise linear representation, the function is not differentiable at the edges and facets shared by more than one element. The first order differentiation can be carried out by an appropriate averaging process, thereby ignoring the cell boundaries owing to the vanishing contribution of boundaries in Lebesgue-integrals. Second order derivatives, as they occur, *e.g.*, in the Laplace operator, are more complicated to handle.

We will discuss two approaches using the finite element method to handle equations of the form

$$h(\mathbf{r}) = a\ \Delta f(\mathbf{r}) \quad , \tag{5.10}$$

where $a$ is an arbitrary non-zero and real-valued constant.

The first method is mathematically simple, but numerically expensive. The derivative matrices from Eq. 5.6 or Eq. 5.7 can be applied twofold: first, the application of Eq. 5.6 or of Eq. 5.7 on the function $f(\mathbf{r})$ for all directions $x_\alpha$ results in the gradient of $f(\mathbf{r})$. The calculation of this gradient for a vertex $\mathfrak{a}$ involves all vertices of the Voronoi cell $\mathfrak{V}_\mathfrak{a}$. By using Eq. 5.6 or Eq. 5.7 again, but now applied to the discretized values of the derivative of $f(\mathbf{r})$ assigned to each node, one can calculate the divergence of the gradient of $f(\mathbf{r})$, which is the Laplace operator, by definition. This formulation of the Laplace operator can then be expressed by a single matrix

$$\underline{\underline{\mathbf{\Delta}}} = \sum_\alpha \underline{\underline{\mathbf{D}}}^{(x_\alpha)} \cdot \underline{\underline{\mathbf{D}}}^{(x_\alpha)} \quad . \tag{5.11}$$

The matrix $\underline{\underline{\mathbf{\Delta}}}$ has an untypical structure compared to the usual forms used in finite element calculations. While $\underline{\underline{\mathbf{D}}}^{(x_\alpha)}$, as most matrices occurring in finite element calculations, has non-zero components only for vertices which belong to the Voronoi cell of vertex $\mathfrak{a}$, the matrix $\underline{\underline{\mathbf{\Delta}}}$ has non-zero components for a much larger number of vertices. In general, the component $\underline{\underline{\mathbf{\Delta}}}_{\mathfrak{a},\mathfrak{b}}$ is non-zero if the vertex $\mathfrak{b}$ is part of the Voronoi cell of a vertex $\mathfrak{c}$ which is part of the Voronoi cell of vertex $\mathfrak{a}$. Therefore, the number of matrix elements of $\underline{\underline{\mathbf{\Delta}}}$ scales in first order approximation proportional to $m^2$, where $m$ is the average number of vertices per Voronoi cell. Note that in typical finite element matrices the number of non-zero components scales linearly with $m$. Although this method is generally very accurate in numerical terms, it is less rigorous in its mathematical formulation, since it starts from a discretized form of the first derivative to deduce an approximation for the second derivative.

The code therefore employs a different form, which is described in the following. The second approach transforms Eq. 5.10 to its equivalent weak form. To obtain the weak form the equation is scalar multiplied with an arbitrary test function $\phi(\mathbf{r})$ and integrated over the domain $\Omega$. In result the equality of both sides generally depends on the chosen test function. By requesting that the equality must hold for *any* test function $\phi(r)$ the equivalence with the original equation is restored, even though from a mathematical perspective the weak form is not identical since its solution has lower requirements concerning, *e.g.*, the differentiability than the strong, original form. The

weak formulation of Eq. 5.10 can be expressed by [107]

$$\int_{\Omega} h(\mathbf{r})\phi(\mathbf{r})\,\mathrm{d}\Omega = a \int_{\Omega} \phi(\mathbf{r})\ \Delta f(\mathbf{r})\,\mathrm{d}\Omega \tag{5.12}$$

defined within the region $\Omega$ with the surface $\partial\Omega$. Integration by parts of the right hand side of Eq. 5.12 results in

$$\int_{\Omega} h(\mathbf{r})\phi(\mathbf{r})\,\mathrm{d}\Omega = -a \int_{\Omega} [\boldsymbol{\nabla}\phi(\mathbf{r})]\cdot[\boldsymbol{\nabla} f(\mathbf{r})]\,\mathrm{d}\Omega + a \oint_{\partial\Omega} \phi(\mathbf{r})\ \boldsymbol{\nabla} f(\mathbf{r})\cdot\mathbf{n}\,\mathrm{d}\partial\Omega \quad , \tag{5.13}$$

where $\mathbf{n}$ is the surface normal. In micromagnetism the calculation of the exchange field is the most prominent example for which the Laplace operator is applied to the vector field of the magnetization. For the calculation of the exchange field at the boundary W.F. Brown and A. Aharoni [1, 4] suggested to use Rado-Wertmann boundary conditions, which in their simplest form are sometimes also called Brown boundary conditions. In the absence of surface anisotropy, those boundary conditions require that the derivative of the magnetization normal to the surface of a ferromagnetic sample is exactly zero:

$$\left.\frac{\partial \mathbf{m}}{\partial \mathbf{n}}\right|_{\partial\Omega} = \mathbf{0} \tag{5.14}$$

Effectively, this condition removes the surface integral from Eq. 5.13. Those boundary conditions can be justified for equilibrium configurations and provide also the necessary boundary conditions for finite difference micromagnetic codes, but mathematically they are not required in finite element calculations [73]. We implement Brown's boundary conditions and drop the surface integral. If particular boundary conditions should make it necessary to include the surface integral into the calculation, steps analogous to those for the volume integration need to be followed, to which we will come back at the end of this section.

The computational region $\Omega$ can be subdivided into the volumes of the finite elements $\Omega^{(n)}$ with

$$\begin{aligned} \Omega &= \bigcup \left\{\Omega^{(n)}\right\} \\ \Omega^{(i)} \bigcap \Omega^{(j)} &= 0 \quad \forall i \neq j \quad . \end{aligned} \tag{5.15}$$

Approximating $f(\mathbf{r})$, $h(\mathbf{r})$ and the test function $\phi(\mathbf{r})$ with the set of shape functions

$\left\{\eta_i^{(n)}\right\}$ we can write for $\mathbf{r} \in \Omega^{(n)}$:

$$\begin{aligned} f(\mathbf{r}) \approx \widetilde{f}(\mathbf{r}) &= \sum_{i=1}^{D} \eta_i^{(n)}(\mathbf{r})\ f_i^{(n)} \\ h(\mathbf{r}) \approx \widetilde{h}(\mathbf{r}) &= \sum_{i=1}^{D} \eta_i^{(n)}(\mathbf{r})\ h_i^{(n)} \\ \phi(\mathbf{r}) \approx \widetilde{u}(\mathbf{r}) &= \sum_{i=1}^{D} \eta_i^{(n)}(\mathbf{r})\ \phi_i^{(n)} \quad , \end{aligned} \tag{5.16}$$

where $D$ is the number of shape functions of the finite element $n$, which is $D = 4$ in our case of tetrahedra with linear shape functions.

Equation 5.13 in conjunction with Eq. 5.16 can be rewritten as:

$$\begin{aligned} \sum_{n=1}^{N}\sum_{i=1}^{D}\sum_{j=1}^{D} \phi_i^{(n)} h_j^{(n)} \int\limits_{\Omega^{(n)}} \eta_i^{(n)} \eta_j^{(n)}\, \mathrm{d}\Omega = \\ - a \sum_{n=1}^{N}\sum_{i=1}^{D}\sum_{j=1}^{D} \phi_i^{(n)} f_j^{(n)} \int\limits_{\Omega^{(n)}} \left(\boldsymbol{\nabla}\eta_i^{(n)}\right) \cdot \left(\boldsymbol{\nabla}\eta_j^{(n)}\right) \mathrm{d}\Omega \end{aligned} \tag{5.17}$$

The two volume integrations in Eq. 5.17 can be solved analytically. Due to the linearity of the shape functions we find

$$\int\limits_{\Omega^{(n)}} \left(\boldsymbol{\nabla}\eta_i^{(n)}\right) \cdot \left(\boldsymbol{\nabla}\eta_j^{(n)}\right) \mathrm{d}\Omega = \sum_{\alpha} b_{i,\alpha}^{(n)} b_{j,\alpha}^{(n)} V^{(n)} = g_{i,j}^{(n)} \tag{5.18}$$

with $V^{(n)}$ the volume of finite element $n$, and $\alpha$ the Cartesian coordinate directions in $d$ dimensions. The matrix $\underline{\underline{\mathbf{G}}} = \{g_{i,j}^{(n)}\}$ is the so called Galerkin matrix, which is an often appearing quantity in finite element simulations. The here shown Galerkin matrix uses local indexing, yet a transformation to global indices $(\mathfrak{a}, \mathfrak{b})$ is usually possible, too. The second integral in Eq. 5.17 is shape independent and reads [111]

$$\int\limits_{\Omega^{(n)}} \eta_i^{(n)} \eta_j^{(n)}\, \mathrm{d}\Omega = (1 + \delta_{i,j}) \frac{(d-1)!}{(d+1)!} V^{(n)} \quad . \tag{5.19}$$

If we focus now on the three dimensional case using tetrahedral simplex elements with linear shape functions, we can transform Eq. 5.17 in conjunction with Eq. 5.18

and Eq. 5.19 to

$$\sum_{n=1}^{N}\sum_{i=1}^{4}\phi_i^{(n)}\sum_{j=1}^{4}h_j^{(n)}\frac{1}{20}\left(1+\delta_{i,j}\right)V^{(n)} = -a\sum_{n=1}^{N}\sum_{i=1}^{4}\phi_i^{(n)}\sum_{j=1}^{4}f_j^{(n)}\sum_{\alpha}b_{i,\alpha}^{(n)}b_{j_\alpha}^{(n)}V^{(n)} \quad . \tag{5.20}$$

Since the test functions $\phi(\mathbf{r})$ are arbitrary, a comparison of coefficients can be used to define a set of linear equations in the form

$$\underline{\underline{\mathbf{A}}}\{h_{\mathfrak{a}}\} = \underline{\underline{\mathbf{B}}}\{f_{\mathfrak{a}}\} \quad . \tag{5.21}$$

The matrices are sparsely occupied $N \times N$ matrices where $N$ is the number of nodes in the mesh, in which only those components $\mathfrak{b}$ in a row $\mathfrak{a}$ are non-zero, whose corresponding vertices in the mesh belong to the Voronoi cell $\mathfrak{V}_{\mathfrak{a}}$.

The matrix equation can be solved numerically with one matrix vector multiplication to derive the right hand side of Eq. 5.21 in a first step, and in a second step by using a linear equation solver to find the solution of the remaining set of linear equations. Even though efficient algorithms exist to solve sets of linear equations, the numerical costs would be higher than in the approach represented by Eq. 5.11. Finite element approximations can only be considered as accurate, if the represented functions change little within one cell. On the basis of this argument and *a posteriori* verification the approximation of mass lumping can be justified, by which it is assumed that the resulting function $h(\mathbf{r})$ does not change within the cell:

$$\sum_{i}^{4}V^{(n)}\frac{1}{20}\left(1+\delta_{i,j}\right)\ h_i^{(n)} \approx \sum_{i}^{4}V^{(n)}\ \frac{1}{20}\left(1+\delta_{i,j}\right)\ h_j^{(n)} = \frac{1}{4}h_j^{(n)}\ V^{(n)} \tag{5.22}$$

The mass-lumping method simplifies Eq. 5.21 significantly so that only one matrix vector multiplication is necessary to derive a solution $\{h_{\mathfrak{a}}\}$:

$$h_{\mathfrak{a}} = -\frac{a}{\sum\limits_{n\in\mathfrak{V}_{\mathfrak{a}}}V^{(n)}}\sum_{n\in\mathfrak{V}_{\mathfrak{a}}}V^{(n)}\sum_{i=1}^{4}f_i^{(n)}\ g_{i,j}^{(n)} \tag{5.23}$$

with $j$ representing the local index inside of cell $n$ corresponding to the global index $\mathfrak{a}$.

The mathematical structure of Eq. 5.23 corresponds to a weighted summation of $f_i^{(n)}g_{i,j}^{(n)}$ with the cell volumes as weights which represents the center of mass of the Voronoi cell of node $\mathfrak{a}$. In homogeneous meshes, where differences in cell sizes correspond only to minor statistical fluctuations, this representation of the Laplace operator results in small and randomly distributed numerical errors, which can be neglected for high quality meshes. This is different in mesh coarsening situations, where the cell size changes strongly in one direction. In these cases this averaging

process can give rise to systematic errors in one direction, since the position of a vertex does not correspond to the center of mass of its Voronoi cell resulting in the same problem as discussed for the first order derivatives in section 5.1.3. Therefore, mesh size variations should be avoided or reduced to a minimum if they are inevitable.

If we assume for a moment that the Laplace operator can be applied everywhere so that we drop Brown's boundary conditions, the contribution of the surface integral in Eq. 5.13 need to be taken into account. Using again the finite element representation of $\phi(\mathbf{r})$ and $f(\mathbf{r})$ Eq. 5.13 can be rewritten as

$$\oint_{\partial\Omega} a\ \phi(\mathbf{r})\ \boldsymbol{\nabla} f(\mathbf{r})\,\mathrm{d}\partial\boldsymbol{\Omega} \approx a \sum_{n=1}^{N}\sum_{i=1}^{4}\sum_{j=1}^{4} B(n,i,j)\ \phi_i^{(n)}\ f_j^{(n)} \int \eta_i^{(n)} \left(\boldsymbol{\nabla}\eta_j^{(n)} \cdot \mathbf{n}\right) \mathrm{d}S \tag{5.24}$$

with $B(n,i,j) = 1$ for vertices $i$ and $j$ of cell $n$ being a boundary node of the mesh and zero otherwise, $\mathbf{n}$ the surface normal of those facets of tetrahedron $n$ representing a boundary of the mesh, for which the nodes $i$ and $j$ are two of the three corners of the triangle with surface element $\mathrm{d}S$. The integral can be solved analytically, so that eventually an additional matrix can be formulated to take into account the surface integral. Since all nodes involved in Eq. 5.24 are also considered in Eq. 5.23, it would not increase the numerical costs for solving Eq. 5.10 to include the surface integral represented by Eq. 5.24.

### 5.1.6 Demagnetization potential

Some effects in micromagnetism prohibit a treatment by simple matrix vector multiplications. The most prominent example is the calculation of the demagnetizing field according to Eq. 2.31. Instead of performing a twofold volume integral to calculate the field resulting from the magnetostatic long-range interaction, it is numerically more convenient to solve a partial differential equation and calculate the magnetostatic scalar potential. For simplicity we will drop the index "dem" in the following discussion. As introduced in Sec. 2.2.3, $U$ is the solution of the Poisson equation (Eq. 2.33 on page 20):

$$\Delta U = -\boldsymbol{\nabla} \cdot \mathbf{M} \quad , \tag{5.25}$$

which simplifies outside of the ferromagnetic material, due to the absence of a magnetization, to Laplace's equation.

For reasons of numerical convenience it is usually preferable to exclude points in space located outside of the region of interest, *i.e.*, the ferromagnetic sample. Hence, a direct treatment of the open boundary problem as described by Eq. 5.25 should generally be avoided. Fredkin and Koehler [112, 113] applied an elegant method to micromagnetic problems in order to consider this. Following the method described earlier, *e.g.*, by Salon and D'Angelo [114],they separated the problem into two parts,

one referring to the volume and another to the boundary. In this hybrid finite element / boundary element formulation, the potential $U$ is split into $U_1$ and $U_2$ with $U = U_1 + U_2$, where $U_1$ represents a solution of Poisson's equation inside of the sample $\Omega$ and $U_2$ the solution of Laplace's equation in the full $\mathfrak{R}^3$. This approach of a hybrid finite element/boundary element method shall be outlined in the following:

As the potential $U$ is a continuous function in the entire $\mathfrak{R}^3$, it yields on the boundary $\partial\Omega$ of the sample region $\Omega$

$$U^{(\mathrm{in})}\Big|_{\partial\Omega} = U^{(\mathrm{out})}\Big|_{\partial\Omega} \quad , \tag{5.26}$$

where the indices *in* and *out* denote an asymptotic approach to the boundary from the inside and from the outside, respectively.

Owing to Maxwell's equation $\boldsymbol{\nabla} \cdot \mathbf{B} = 0$, the component of $\mathbf{B}$ normal to the surface is continuous, as well:

$$\mathbf{B}^{(\mathrm{in})} \cdot \mathbf{n}\Big|_{\partial\Omega} = \mathbf{B}^{(\mathrm{out})} \cdot \mathbf{n}\Big|_{\partial\Omega} \tag{5.27}$$

which results in the jump condition

$$\left(\boldsymbol{\nabla} U^{(\mathrm{in})} - \boldsymbol{\nabla} U^{(\mathrm{out})}\right) \cdot \mathbf{n}\Big|_{\partial\Omega} = \mathbf{M} \cdot \mathbf{n}|_{\partial\Omega} \quad . \tag{5.28}$$

The separation of $U$ into two parts allows for (and requires) additional assumptions about the structure of $U_1$ and $U_2$ without loss of generality [16]. The volume charges should be accounted for by $U_1$ which represents the part of the solution that refers only to the volume, whereas $U_2$ shall depend on the value of $U_1$ at the boundary, thereby including the source term containing the surface charges, and on the geometry of the sample. Equation 5.25 can accordingly be transformed into the two parts

$$\Delta U_1 = \boldsymbol{\nabla} \cdot \mathbf{M} \tag{5.29}$$

$$\Delta U_2 = 0 \quad . \tag{5.30}$$

$U_1$ shall vanish outside of $\Omega$, which results also in $\boldsymbol{\nabla} U_1 = 0$ outside of $\Omega$. This consideration transforms the continuity condition of Eq. 5.26 to

$$\left(U_2^{(\mathrm{out})} - U_2^{(\mathrm{in})}\right)\Big|_{\partial\Omega} = U_1^{(\mathrm{in})}\Big|_{\partial\Omega} \quad . \tag{5.31}$$

Owing to the demand that only $U_1$ shall solve the inhomogeneous equation, thereby including the structure of $\mathbf{M}$ the jump condition represented by Eq. 5.28 transforms to

$$\boldsymbol{\nabla} U_1^{(\mathrm{in})} \cdot \mathbf{n}\Big|_{\partial\Omega} = \mathbf{M} \cdot \mathbf{n}|_{\partial\Omega} \quad . \tag{5.32}$$

Therefore, the gradient of $U_2$ in direction of the surface normal has to be continuous:

$$\nabla U_2^{(\mathrm{in})} \cdot \mathbf{n}\Big|_{\partial\Omega} = \nabla U_2^{(\mathrm{out})} \cdot \mathbf{n}\Big|_{\partial\Omega} \tag{5.33}$$

The open boundary problem described by Eq. 5.25 needs one additional boundary condition to be uniquely solvable. The natural choice is the demand of a vanishing of $U$ in infinite distance from $\Omega$:

$$\lim_{\mathbf{r}\to\infty} U(\mathbf{r}) = 0 \tag{5.34}$$

Similar to the Laplace operator (Sec. 5.1.5), the weak formulation of Eq. 5.29 for the calculation in the framework of finite elements results in a system of linear equations

$$\underline{\underline{D_{U1}}} \left\{ U_1^{(\mathfrak{a})} \right\} = \underline{\underline{\mathbf{D_m}}} \left\{ \mathbf{m}^{(\mathfrak{a})} \right\}, \tag{5.35}$$

where the Neumann boundary conditions can be incorporated into the tensor $\underline{\underline{\mathbf{D_m}}}$.

In contrast to the calculation of the exchange field, Eq. 5.35 eludes a solution by a single sparse-matrix vector multiplication. The system of linear equations needs to be solved numerically, for which standard methods exists [115]. To this point, the algorithm is a typical finite element problem. In the second part of the calculation $U_2$ needs to be calculated, which needs to respect the Neumann boundary conditions representing the continuity condition described by Eq. 5.33 as well as the Dirichlet boundary conditions in infinite distance from $\Omega$. This can be formulated as boundary element method problem.

By construction, $U_2$ depends only on the shape of $\Omega$ and the function $U_1$. Ref. [16, 113] describes that by application of potential theory $U_2$ can be calculated using the already known values of $U_1$ according to

$$U_2(\mathbf{r}) = \frac{1}{4\pi} \int\limits_{\partial\Omega} U_1(\mathbf{r}') \frac{\partial}{\partial \mathbf{n}(\mathbf{r}')} \frac{1}{|\mathbf{r}-\mathbf{r}'|} \,\mathrm{d}\mathbf{S}' + \left( \frac{\omega(\mathbf{r})}{4\pi} - 1 \right) U_1(\mathbf{r}) \quad , \tag{5.36}$$

where $\mathrm{d}\mathbf{S}'$ denotes the oriented surface element of $\Omega$ at position $\mathbf{r}'$, and where $\omega(\mathbf{r})$ is the solid angle subtended at the point $\mathbf{r}$ by the surface of the ferromagnetic region $\Omega$. Equation 5.36 can be formulated as a matrix-vector product

$$\left\{ U_2^{(\mathfrak{a})} \right\} = \underline{\underline{D_{U2}}}_{\mathfrak{a},\mathfrak{b}} \left\{ U_1^{(\mathfrak{b})} \right\} \quad . \tag{5.37}$$

The numerical problem of the matrix $\underline{\underline{D_{U2}}}$ stems from its density. In contradiction to all other matrices involved in our simulations $\underline{\underline{D_{U2}}}$ is densely populated, which results in a quadratic growth of the storage demand with the number of boundary elements. The quadratic growth would limit the number of boundary elements to

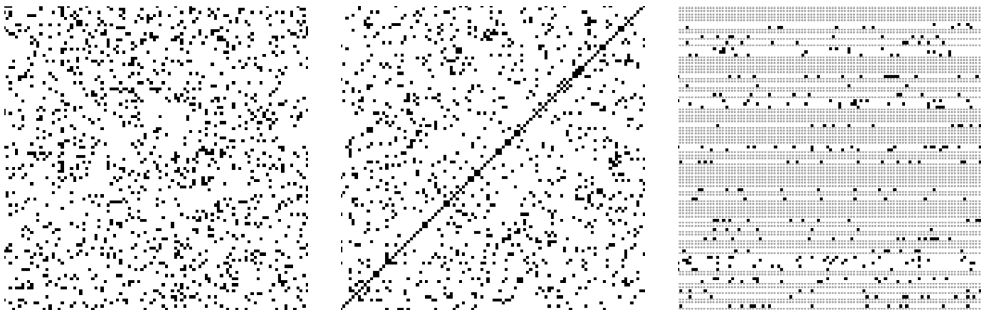

(a) Random population (b) Typical FEM population (c) Mapping population

**Figure 5.3** – Sketches of sparsely populated matrices with populated elements in black, unpopulated elements in white and non-considered rows in gray.

some ten thousands, *e.g.*, 100.000 boundary nodes would result in a memory demand of approximately 74 GB.

The usage of the hierarchical matrix method storage scheme using the HLIB [116, 117] library solves this issue in TetraMag, since the hierarchical matrix method represents an elaborated compression method for problems shaped like the Green's function present in Eq. 5.36. Figuratively, the influence of a surface node $\mathfrak{b}$ on a node $\mathfrak{a}$ needs to be calculated with high precision if they are close to each other, whereas for large distances the influence of a group of nodes $\{\mathfrak{b}\}$ can be approximated. The mathematical method of HLIB is to cluster vertices and to approximate the corresponding part of the matrix $\underline{\underline{D_{U2}}}$ by matrix-matrix multiplications of two rectangular matrices:

$$\underline{\underline{D_{m,n}}} = \underline{\underline{F_{m,k}}} \cdot \underline{\underline{G_{k,n}}} \tag{5.38}$$

The storage demand for the interaction matrices reduces from the order $m \cdot n$ to $k \cdot (m + n)$, which is significant, if $k$ is much smaller than $m$ and $n$. This is the case for all situations relevant in this thesis, which results in a typical reduction of storage demands by 95 %.

### 5.1.7 Sparse matrices

Matrices representing short range interactions, *e.g.*, the spatial derivative matrix, have in common that most of the matrix elements are exactly zero, because vertices are only influenced by those vertices inside their Voronoi cell. The family of such matrices is named *sparse matrices*, which can be stored in very memory efficient ways; considering a mesh with 100.000 vertices and a typical Voronoi cell size of 20 vertices, the potential memory saving by omitting vertices outside of the Voronoi cell is in the range of 99.98% in comparison to the full $N \times N$ matrix with $10^{10}$ elements. The necessary overhead for an efficient matrix storage is approximately as big as the

amount of memory to store the data itself, which cuts the memory saving to some 99.96% in our example. A further advantage of sparse data matrix storage [115] is that a large amount of unnecessary multiplications by zero is avoided, thereby increasing the calculation speed of a matrix-vector multiplication.

The typical sparse matrix storage schemes [115] have in common that they store the non-zero matrix elements and use additional arrays to address the value of a matrix element in the matrix. Depending on the matrix structure and usage, different sparse matrix schemes are favorable, which we will outline in the following.

The preferred storage scheme of a sparse matrix depends strongly on its purpose; a fast random-access format, *e.g.*, has different preconditions than one specialized for linear algebra operations, like the one used in this work.

Sparse matrix storage schemes for linear algebra, either follow the *Compressed Sparse Row* (CSR) or the *Compressed Sparse Column* (CSC) approach. In a sparse row(column) storage scheme the matrix elements belonging to a single row(column) are stored serially. That way, a single row can be addressed easily in CSR schemes to perform parallelized matrix vector multiplications. On the other hand a matrix-matrix multiplication is best parallelizable if the left matrix is stored in a CSR and the right one in a CSC scheme. Since all multiplications within this thesis can be expressed as matrix vector multiplications, only CSR schemes are implemented in our algorithms.

A common and flexible format for matrix storage is the Yale format [115]. For a $N$x$N$ matrix with $M$ non zero values it requires in a CSR scheme

1. One real value array $sa$ of length $M$ storing the matrix element values
2. One integer array $ia$ of length $M$ that saves the column indices of each matrix element
3. One integer array $ja$ of length $N+1$, in which $ja[j]$ provides the array index of the first non-zero matrix element of row $j+1$ in array $ia$ and $sa$. The last index is numerically necessary to define the total length of the array

The scheme has a high degree of flexibility and can be used for all randomly populated sparse matrices as sketched in Fig. 5.3(a). Sparse matrices involved in finite element operations have usually non-zero diagonal elements as sketched in Fig. 5.3(b), so that the indexing overhead is only necessary for the off-diagonal elements. In addition, sparse matrices present in finite element calculations are symmetric; a property that could be exploited to reduce the storage requirements further. A format benefiting such a structure is the PCGPACK storage scheme[1] described in Numerical Recipes [115]. It involves only two arrays: one array, $sa$, of length $N + M_{\mathrm{off-dia}}$ stores the values of all diagonal elements, even if they are zero, and of all non-zero off-diagonal elements. The first $N$ elements are the diagonal elements followed by the remaining non-zero elements like in the Yale structure. The second array, $ija$, is an indexing array of length $N + M_{\mathrm{off-dia}} + 1$, in which the first $N+1$ elements correspond to the $ja$ array elements of the Yale format, whereas the last $M_{\mathrm{off-dia}}$ indices correspond

[1] It appears from many publications, *e.g.* [115], that the PCGPACK storage scheme was outlined in the PCGPACK user's guide in 1984 for the first time. [118]

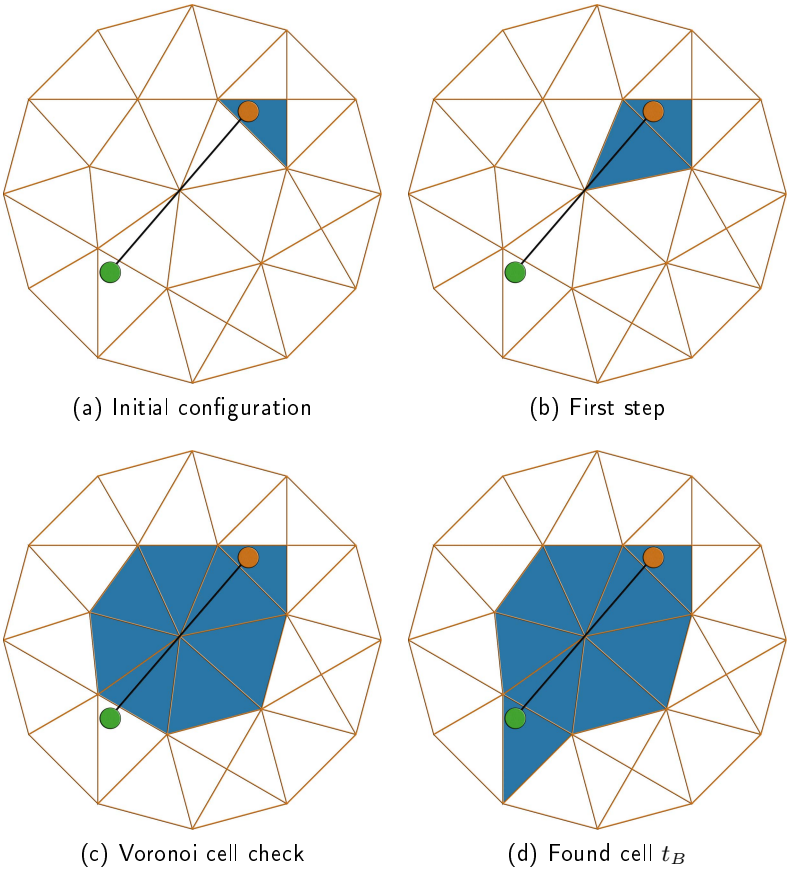

(a) Initial configuration (b) First step

(c) Voronoi cell check (d) Found cell $t_B$

**Figure 5.4** – Sketch of the mapping process from mesh B with initial vertex $v_B$ (orange dot) to vertex $v_A$ (green dot).

to the $ia$ array elements of the Yale format without diagonal element indices. For performance reasons $sa$ can have one dummy element at index $N$ so that $sa$ and $ija$ have the same length.

Within this thesis we have also the special situation that some vertices of one mesh $A$ are spatially located inside a second mesh $B$. In that case we use a format similar to the Yale format, because the diagonal elements are not necessarily non-zero. An additional filtering array $ra$ stores the indices of those vertices of $A$, which are influenced by $B$. Such a matrix pattern is sketch in Fig. 5.3(c).

## 5.2 Mapping between finite element meshes

Two overlapping finite element meshes $A$ and $B$ modeling the same physics need to be synchronized to avoid numerical artifacts or spurious effects resulting from virtual internal boundaries. If both meshes consist of conforming tetrahedral elements, every node of mesh $A$ within the overlapping region $A \cap B$ is inside of exactly one tetrahedron of mesh $B$. Having found the tetrahedron $t_B$ in mesh $B$ surrounding a point $\mathbf{r}_A$ in mesh $A$, shape functions can be used to interpolate from the tetrahedron $t_B$ to the position $\mathbf{r}_A$.

The most obvious but slow search technique to locate the tetrahedron $t_B$ in mesh $B$ for each vertex $v_A$ of mesh $A$ would be to check each tetrahedron of the mesh $B$ and to verify whether $v_A$ is located inside of $t_B$. The drawback of this method is the high numerical price, which scales with the product of the number of nodes in $A$ and the number of cells in $B$. Such a method cannot be afforded for large meshes as they are used in our simulations.

A more sophisticated method uses a ray-tracing approach, which works well in convex structures. The algorithm to find the tetrahedron $t_B$ in mesh $B$ containing the point $\mathbf{r}_A$ in mesh $A$ is sketched in Fig. 5.4. It operates in the following way:

1. Choose a strategically reasonable tetrahedron $t_B^{[0]}$ in mesh $B$. This can be the center of mass of $B$ or, in the case of moving meshes, a cell that surrounded $\mathbf{r}_A$ in an earlier time step.
2. Take one point $\mathbf{r}_B^{[0]}$ that is known to be inside of $t_B^{[0]}$. This could be, *e.g.*, the center of the insphere of $t_B^{[0]}$.
3. Follow the line segment $\overline{\mathbf{r}_B^{[0]}\mathbf{r}_A}$ until a boundary of $t_B^{[0]}$ is reached. The line can only continue on the opposite side of the face of the tetrahedron with index $t_B^{[1]}$. The penetration point with the face is $\mathbf{r}_B^{[1]}$.
4. Perform the third step $R$ times until $\mathbf{r}_A$ is reached before the connection line $\overline{\mathbf{r}_B^{(R-1)}\mathbf{r}_A}$ penetrates one of the faces of $t_B^{[R]}$. In that case $t_B^{[R]}$ is the sought tetrahedron surrounding $\mathbf{r}_A$.

In general, this algorithm is straightforward, but there are some pitfalls that need further treatment. First, if mesh $B$ is non-convex the connection line $\overline{\mathbf{r}_B^{[0]}\mathbf{r}_A}$ can leave the mesh $B$ even though $\mathbf{r}_A$ is located inside of $B$. Since this case is avoided in this thesis due to convex mesh shapes, we mention this problem only for completeness.

Second, the connection line $\mathbf{l}(\mathbf{r}) = \overline{\mathbf{r}_B^{[i]}\mathbf{r}_A}$ can cross exactly through the vertex $v_B^{[i+1]}$, as shown in Fig. 5.4(c). In that case all tetrahedra forming the Voronoi cell of $v_B^{[i+1]}$ besides $t_B^{[i]}$ need to be checked by the ray-tracer in order to locate the next tetrahedron on the pathway of $\mathbf{l}(\mathbf{r})$. An analogous pitfall is the crossing of a tetrahedral edge $e_B^{[i+1]}$ — in that case all tetrahedra except $t_B^{[i]}$ having $e_B^{[i+1]}$ as an edge have to be checked to follow the path of $l(\mathbf{r})$ correctly. Owing to the limited numerical precision those pathological cases are most likely to occur several times during one

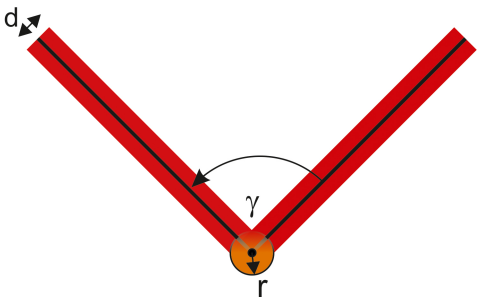


**Figure 5.5** – If we associate to two edges enclosing the angle $\gamma$ a thickness $d$ a region exists around the common vertex inside of which both edges overlap. The circumscribing sphere has a radius $r = d/\sin(\gamma/2) > d$.

simulation. Therefore, it is necessary to implement algorithms, which deal with the possibilities:

- $l(\mathbf{r})$ can penetrate face $f_B^{[i]}$ very close to a second face $f_B^{[k]}$
- $l(\mathbf{r})$ can pass by the edge $e_B^{[i]}$ in a very short distance.
- $l(\mathbf{r})$ can pass by the vertex $v_B^{[i]}$ in a very short distance.

These three problems can cause an endless loop of jumps between adjacent tetrahedra if they are not recognized and handled correctly. In our experience the computationally fastest solution is to ascribe a thickness to all faces, a radius to all edges as well as to the vertices, resulting in cylinders and spheres, respectively. Figure 5.5 provides a schematic representation thereof for the two dimensional case. In a three dimensional mesh, the thicknesses and radii can be preprocessed for each mesh. The thickness of a face is initialized with a value close to the numerical machine precision. In a second step the radii of all edges are determined by calculating the resulting radius for each pair of faces having one edge in common. The maximum radius is then used as the edge radius during the simulations. Analogously, for each vertex of the mesh we choose the sphere radius $r_i^{(v)}$ according to

$$r_i^{(v)} = \left[\max\left(d_\alpha^{(e)}, d_\beta^{(e)}\right)\sin(\gamma_{\alpha\beta}/2)\right] \quad , \tag{5.39}$$

where $d_\alpha^{(e)}$ and $d_\beta^{(e)}$ are the radii of the edges $\alpha$ and $\beta$ of which $r_i^{(v)}$ is a vertex and where $\gamma_{\alpha,\beta}$ is the angle between those two edges.

If during a mapping process $l(\mathbf{r})$ passes through the associated volume of a vertex, edge or face the corresponding entity is considered to be penetrated. We check for those special cases according to the following priority hierarchy: 1. vertices, 2. edges and 3. faces.

## 5.3 Mesh generation

In section 5.1.5 we have presented an example of the importance of high quality finite element meshes in order to reduce numerical errors to a minimum. In contrast to the finite difference method, the mesh generation for a finite element simulation is a remarkably complex task with ongoing research by mathematicians. Therefore, we did not develop and implement a proprietary mesh generator, but use the freely available program GMSH [109], which is licensed under the terms of the GNU General Public License [119] with a modification [120] to generate meshes constructed of tetrahedra as simplex elements.

In GMSH, an ASCII file describes the geometry of the sample by means of 1D, 2D or 3D geometric entities. Points define 1D elements, such as lines or curves. Accordingly, several ($n$-1) dimensional entities define $n$ dimensional elements which eventually provide the shape of a 3D object. The meshing algorithm of GMSH starts with 1D elements and subdivides them into line segments with a user defined characteristic length. The 1D mesh serves as a seed for the subsequent Delaunay triangulation [121] which provides a triangular mesh on the surface of the sample. This surface mesh then represents the starting point for the generation of a 3D mesh which is either assembled by a generalized 3D Delaunay or the 3D Netgen algorithm [122]. The manual of the GMSH project [109, 123] describes the details of the underlying techniques.

GMSH provides three different measures to determine the quality of each created tetrahedron:

1. $\gamma$ represents the ratio of the insphere radius over the circumsphere radius of each finite element.
2. $\eta$ is the ratio of the 2/3 power of the volume divided by the sum of squares of the tetrahedral edge lengths.
3. $\rho$ is the ratio of shortest edge length divided by the longest edge length of each tetrahedron.

A practically perfect mesh consisting of equilateral tetrahedra would have values of $\gamma = 1/3$, $\eta \approx 0.04$, and $\rho = 1$. Nevertheless, GMSH normalizes these values to an ideal value of 1. Very small values of $\gamma$ and $\rho$ have been proven to be reliable indicators for non-ideal,*e.g.*, flat, sliver, or needle-type tetrahedra which can give rise to problems concerning the numerical accuracy. Especially for more complicated mesh structures an examination of the minimum values of $\gamma$ and $\rho$ is necessary in order to prevent wrong simulation results.

# 6
# Implementation

The Landau-Lifshitz-Gilbert equation describes the magnetization dynamics of ferromagnetic mesoscopic samples. While the equation appears, at a first glance, to be an ordinary differential equation, it is in fact an integro-differential equation, since the calculation of the demagnetizing field involves a volume integration. A further complication results from the dependence of the exchange field on the second derivative of the magnetization, which represents a highly non-trivial coupling of the three equations of motion of the individual Cartesian components. Hence, it is difficult to solve the equation of motion analytically, even for simple geometries. The magnetization dynamics of a finite sized cylinder with a domain wall is already too complex to be treated analytically in full extent.

Several simulation algorithms have been developed during the last decades to tackle micromagnetic problems numerically. While several freely available packages, such as OOOMF [15], use a finite difference approach to perform micromagnetic simulations, the group of R. Hertel implemented a hybrid finite element/boundary element method code called TetraMag, which uses the boundary element method to solve the surface integral term of the magnetostatic scalar potential (Eq. 2.34). The use of finite elements allows for an accurate simulation of arbitrarily shaped ferromagnetic samples such as round discs [10, 124, 125], nanotubes [18, 19], or cylindrical nanowires [61].

To develop a hybrid micromagnetic/Heisenberg code it was necessary to integrate regions with a regular atomic lattice structure into the finite element mesh. While the edge lengths of the finite element mesh are in the range of some nanometers, the atomic lattice constant has typical values of some ångström. Therefore, besides a seamless transition between the different models, a multi-model code also needs to bridge the different discretization length scales.

For that purpose we split the numerical problem into three different types of functional units. The first one is the ferromagnetic sample itself discussed in Sec. 6.1, the second type represents the multi-model structures discussed in Sec. 6.2, and

the last type represents auxiliary structures explained in Sec. 6.3, which we call calottes.

For performance reasons matrix vector multiplications are implemented to be carried out on graphical processing units resulting in a dramatic speedup of several 100%.

## 6.1 Sample

The sample structure in the multi-model simulation kit corresponds to the object of interest in classical micromagnetic simulations with TetraMag. For our simulations we use GMSH [109] to generate a finite element mesh from a geometry definition file. The sample mesh represents the backbone of the simulation process by defining the sample geometry. Furthermore, it plays an important role for the calculation of the demagnetizing field. While the exchange interaction or influences of an external field on the magnetic orientation are calculated for all meshes in the multi-model program individually and get synchronized between the meshes afterwards (see Sec. 6.4), the demagnetizing field is calculated only inside of the sample mesh. The physical reason is that in the vicinity of a Bloch point the exchange field is by far the dominant quantity — much more dominant than it is the case for typical domain walls or vortices. In our model we benefit from this physical interpretation, since an inclusion of the other structures into the calculation of the demagnetizing potential $U_{\mathrm{dem}}$ would be numerically expansive.

Analogous to the traditional version of TetraMag the first step of the simulation process is the preprocessing, which carries out all calculations which are only geometry-dependent, *i.e.*, independent of the magnetic system configuration. This allows one to save computational time later during dynamic calculations. The preprocessing includes the calculation of various matrices that do not depend on the magnetic orientation, *e.g.*, those needed for the exchange field calculation or for the demagnetizing field. The most beneficial preprocessing step is the assembly of the hierarchical matrices needed by the HLIB library for the boundary element method that is used to calculate the demagnetizing potential. Contrariwise to the pure micromagnetic version of TetraMag, the multi-model version needs access to the geometry and to the mesh information of the sample during dynamic simulations in order to perform various synchronizations between different entities, *i.e.*, the mesh, the multi-model spheres and the calottes. Hence, an additional preprocessing step is inserted which generates numerical structures to obtain a fast access to the connectivity information of vertices, edges, faces and tetrahedra. As a result, the preprocessing of the sample transforms the shape-dependent micromagnetic field equations into shape-independent matrix vector multiplications or algebraic equations, which need to be evaluated or solved by the main program several times during each step of the time integration.

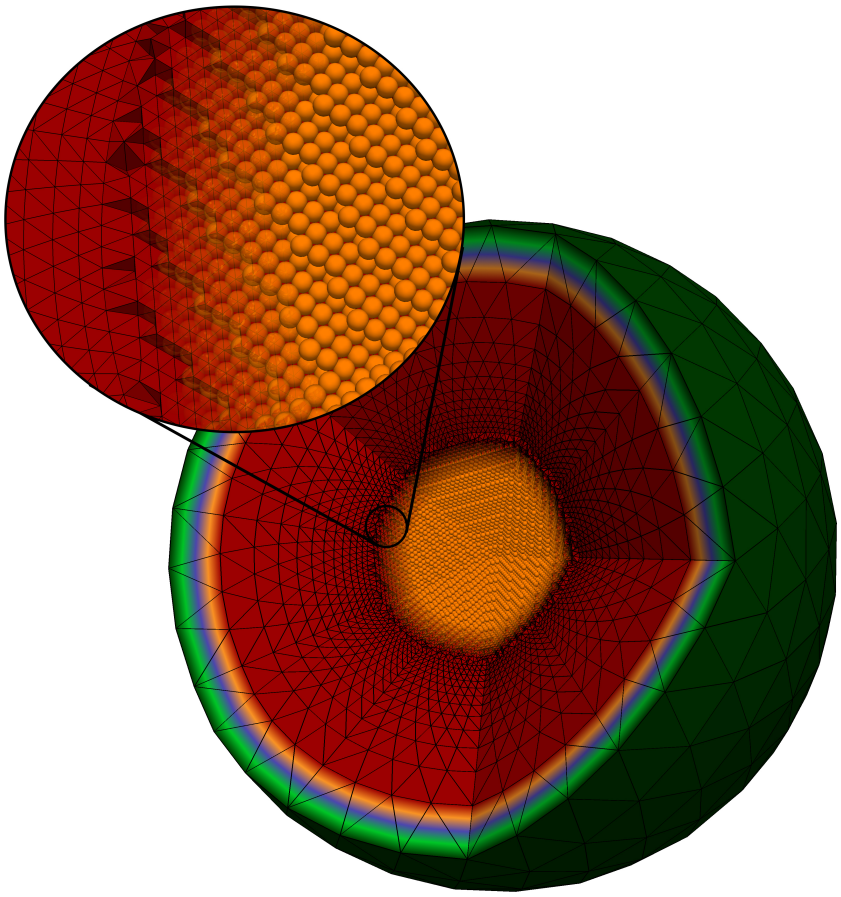

**Figure 6.1** – Inside of the multi-model the exchange field is calculated with the Heisenberg model (orange spheres) in the center with a seamless transition to micromagnetic part (red). The boundary (green) receives all magnetic properties from the surrounding structures

## 6.2 Multi-model sphere

Previous implementations of atomistic/continuum multiscale models [27] typically started from an initial mesh in finite element or finite difference formulation and performed a consecutive reduction of the cell size, so that inside of a large volume it decreases smoothly from the original value down to atomic distances. Into that coarsening region an atomic region can be implanted with the vertices at the position of lattice sites of the simulated material. As long as the region of interest remains at the same position, the remeshing process has to be performed only once and the interaction matrices can be preprocessed making such simulations efficient in terms of computational costs. Jourdan et al. [24, 25, 126], *e.g.*, followed such an approach on the basis of a finite difference micromagnetic algorithm.

In the case of Bloch points propagating through the sample the region that requires an atomistic treatment is not defined *a priori*, so that a dynamic remeshing would be necessary, which would result in very high numerical costs. For that reason we follow a different approach and prepare a template of a spherical structure in a preprocessing step, which incorporates the full multi-model functionality as well as the coarsening. This multi-model sphere can be placed inside or removed from the sample without the need to change its background mesh or geometry. An illustration of such a multi-model sphere is shown in Fig. 6.1, with the atomic region in its center (orange part in Fig. 6.1) and the coarsened finite element mesh as a surrounding shell (green and red regions in Fig. 6.1).

### 6.2.1 Core region

We treat the exchange interaction inside the core region of the multi-model sphere with a classical Heisenberg model, as described in Sec. 2.1. The multi-model preprocessor reads the additional configuration file with suffix .Hpar, in which the user defines all external calculation parameters. Note that this file is not part of the original version of TetraMag.

In a Bravais lattice we can define different spherical shells of nearest neighbors around a lattice site $i$. The lattice sites $j$ belonging to one shell $n$ have the same distance $d_{ij} = d^{(n)}$ and the same exchange constants $J_{ij} = J^{(n)}$ due to the isotropy of the exchange interaction.

In a first step the multi-model preprocessing algorithm generates a Bravais lattice inside a spherical region with diameter $R_c$ and defines for each lattice site $i$ the number of Bohr magnetons $\mu_i$. Using a set of exchange shells it generates the exchange-matrix $\underline{\underline{D_{\mathrm{Hei}}}}$, with which the main program calculates the exchange field by a matrix vector multiplication

$$\mathbf{H}_{\mathrm{xc}} = \underline{\underline{D_{\mathrm{Hei}}}} \cdot \mathbf{m} \tag{6.1}$$

during the time integration.

Close to the boundary of the core region some magnetic moments do not have the full coordination number. We call those lattice sites virtual nodes — in other publications such nodes are labeled ghost nodes [27] — for the Heisenberg model calculation, because their proper treatment needs additional information from the outside of the core region. Analogously, we call lattice sites having a full set of exchange partners real nodes. Hence, we can define an effective maximum radius of the Heisenberg calculation $R_H^{(\max)}$ by finding the smallest radial position of a real node connected to a virtual node.

For a better visualization of the results and to have a possibility of comparing multi-model simulations with pure micromagnetic ones, the space between the lattice sites is meshed with a finite element mesh, using the lattice sites as vertices of the tetrahedra.

### Seamless transition

Inside the multi-model spheres both models, the micromagnetic approximation and the Heisenberg model are applied in different regions with a common interface. As pointed out in Sec. 2.2.1 the Heisenberg and the micromagnetic model are only equivalent for small changes of the homogeneous magnetic state on the atomistic length scale. However, magnetic inhomogeneities corresponding to a spin-spiral with a half wavelength between 9 and 29 lattice constants result in a tolerable systematic error of micromagnetism in comparison to the Heisenberg model.

As will become clearer from the results discussed in chapter 9, the magnetic inhomogeneity in a small distance $r$ from a Bloch point is comparable to the magnetic inhomogeneity of a spin-spiral with half-wavelength $r$. For that reason one can expect that at a distance between 9 and 29 lattice constants from the Bloch point both models are almost equivalent with an error margin below 1 %. Therefore, we chose a radius of approximately 30 lattice sites for the atomistic core region and use micromagnetism for larger distances from the Bloch point or rather from the center of the multi-model sphere.

The immediate application of pure micromagnetism outside of the atomistic core region would result in a collision of the two models and would give raise to numerical errors. We suppress such errors almost completely by means of a seamless transition between the two models. For geometric reasons the natural shape of the transition region is a spherical shell with minimum radius $r_{\min}$ and maximum radius $r_{\max}$. Within that shell we calculate the exchange interaction with both models and perform a position-dependent weighted summation afterwards.

The matrix vector multiplications apply to the same set of nodes which is used for both exchange calculation methods. It is therefore possible to obtain a seamless transitions during a preprocessing step by a weighted summation of the exchange-field matrices:

$$\{\underline{\underline{D}}\}_i = f(r_i)\{\underline{\underline{D_{\mathrm{Hei}}}}\}_i + (1 - f(r_i))\{\underline{\underline{D_{\mathrm{MM}}}}\}_i \tag{6.2}$$

with

$$f(r) = \left\{ \begin{array}{lll} 1 & r & < & r_{\min} \\ \cos(\frac{\pi(r-r_{\min})}{2(r_{\max}-r_{\min})}) & r_{\min} & \leq r \leq & r_{\max} \\ 0 & r & > & r_{\max} \end{array} \right\} \quad . \tag{6.3}$$

The cosine shape of the transition function maintains the differentiability of the interpolated function at the boundaries of the transition region. Even though we did not compare different shapes of transition functions, a linear slope might not lead to additional numerical errors.

Inside the spherical shell both models need to be applicable. The maximum radius is given by $r_{\max} = R_H^{(\max)}$, while the thickness of the shell in the Hpar-file is a parameter provided by the user. Tests have shown that at a thickness of the transition shell of 2 nm numerical errors are not detectable.

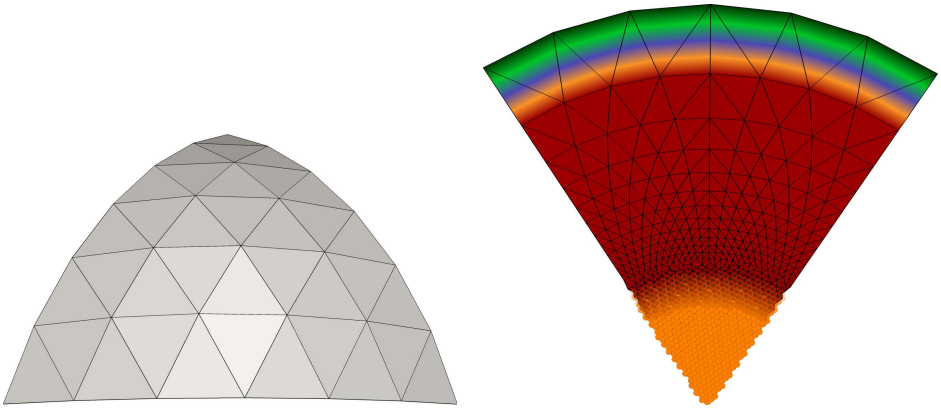

(a) Spherical triangle meshed with $\nu_{\text{geo}} = 7$ (b) Profile of MS pie slice

**Figure 6.2** – Top and slice view on one of the twenty pieces of the multi-model sphere (MS) created from an icosahedron as scaffolding structure. a) View on the outer shell scaffolded by a spherical triangle. (b) The subdivision frequency $\nu_{\text{geo}}$ increases with decreasing radius until the cell size corresponds to distances of nearest neighbors and attaches to the core region.

### 6.2.2 Coarsening

For radii larger than $r_{\max}$ we represent the exchange interaction only with the model of micromagnetism. If we implant the core region directly into the sample mesh, vertices on the surface of the spherical core would need to receive their magnetic orientation from the surrounding sample. In that case the sample mesh with cell sizes of several nanometer would stamp the magnetic orientation on tetrahedra with a cell size of some ångström. Such a collision of disparate length scales would give rise to numerical errors [27]. Instead of remeshing the sample we attach a coarsening region to the mesh of the atomic lattice core. In order to bridge the order of magnitude in cell edge length, which corresponds to three orders of magnitude in cell volume, we construct a coarsening shell of concentric spherical surface layers, whose cell sizes increase from layer to layer, until the average cell size of the last layer corresponds to the average cell size of the sample mesh.

For the finite element approximation of a sphere surface we use a geodesic dome in analogy to Buckminster Fuller's work [127]. The advantage of using geodesic domes is that the edge lengths of the constructing (spherical) triangles are almost equilateral. This results in a high-quality finite element mesh on each shell within the coarsening region. For its construction we start from an icosahedron as scaffolding structure, since it is the Platonic solid which is most similar to a sphere and has the highest number of vertices of all Platonic solids.

There are two typical approaches to construct a geodesic dome over a Platonic solid. In both methods each of its equilateral triangles is processed in the same way. The first one is relatively simple and involves only basic trigonometry: The three edges of the faces with vertices $\mathbf{P}_0$, $\mathbf{P}_1$ and $\mathbf{P}_2$ are subdivided into $\nu_{\text{geo}} > 2$ equidistant lines

resulting in $3\nu_{\text{geo}}$ vertices on the boundary, where the parameter $\nu_{\text{geo}}$ is called the frequency of the dome. A pairwise connection of those vertices, whose connection line is parallel to one of the three original edges, results in a subdivision of each original triangle into $\nu_{\text{geo}}^2$ new triangles. This results in $(\nu_{\text{geo}}^2 + 2)/2$ vertices including those on the boundary. The locations of the new vertices are determined by

$$\begin{aligned} \mathbf{P}_{ij} =& n\left(\mathbf{P}_0 + (\mathbf{P}_1 - \mathbf{P}_0) * \frac{i}{\nu_{\text{geo}}} + (\mathbf{P}_2 - \mathbf{P}_1) * \frac{j}{\nu_{\text{geo}}}\right) \\ n =& \frac{|\mathbf{P}_0|}{\left|\left(\mathbf{P}_0 + (\mathbf{P}_1 - \mathbf{P}_0) * \frac{i}{\nu_{\text{geo}}} + (\mathbf{P}_2 - \mathbf{P}_1) * \frac{j}{\nu_{\text{geo}}}\right)\right|} \end{aligned} \qquad \text{with } j \leq i \quad . \tag{6.4}$$

The drawback of the method is that the areas of the resulting triangles can differ significantly especially for high frequencies $\nu_{\text{geo}}$. The second approach to construct the geodesic dome does not generate boundary vertices by subdividing the edges of the Platonic solid, but by subdividing great circles equiangularly, which contain two vertices of the Platonic solid, and which have the same center as the Platonic solid. The resulting vertices are then connected by circles having the same center as the Platonic solid, similar to the procedure in the first approach. But in contrast to the first approach, three circle segments over the face of the Platonic solid do not intersect in one point. Rather, they enclose a spherical triangle $ST_1$ which is much smaller than the spherical triangle spanned over the scaffolding face. By choosing the center of mass of $ST_1$ projected on the spherical surface one can define uniquely the position for the new vertices. The resulting triangles show less areal variation than in case of the first approach. Although it is more complex to obtain the spherical surfaces that way, we chose the second approach to generate the spherical shells in the coarsening region with best achievable quality of triangles. A review of geodesic math has been presented by H. Kenner [128].

For the construction of the shells we start from an icosahedron as scaffolding structure. The equation

$$r_{\text{geo}}^{(1)} = R_c + b^{(1)} \tag{6.5}$$

defines the radius of the first shell with a desired edge length $b^{(1)} = a$ of the geodesic triangles equal to the atomic lattice constant $a$. Using the angle between two scaffolding vertices of the icosahedron

$$\sin(\vartheta_S/2) = \sqrt{\frac{2}{5+\sqrt{5}}} \quad , \tag{6.6}$$

we find the initial frequency

$$\nu_{geo}^{(1)} = \left\lfloor \frac{\vartheta_S r_{\text{geo}}^{(1)}}{a} \right\rfloor \quad , \tag{6.7}$$

where $\lfloor x \rfloor$ represents the integer part of $x$.

For the case of a core with 7 nm diameter and $a = 0.286\,\mathrm{nm}$ we derive $\nu_{\mathrm{geo}}^{(1)} = 27$. For each additional layer we reduce the frequency by a small integer $\Delta_l$. To achieve a distance between two layers corresponding to the triangle edge length of the spherical surfaces, we calculate the radius of layer $n$ according to

$$r_{\mathrm{geo}}^{(n)} = r_{\mathrm{geo}}^{(n-1)} \frac{\nu_{geo}^{(n)}}{\nu_{geo}^{(n)} - \vartheta_S} \tag{6.8}$$

and add shells as long as

$$lc_S > \frac{\vartheta_S \cdot r_{\mathrm{geo}}^{(n)}}{\nu_{geo}^{(n)}} \tag{6.9}$$

is fulfilled with $lc_S$ the average mesh edge length of the sample mesh. The spherical shells represent the boundary of a three dimensional geometry, for whose 3D meshing we use GMSH [109].

The boundary nodes of the multi-model sphere are virtual nodes, which receive the magnetic orientation from the surrounding sample. A positive side effect of this approach is that the number of boundary nodes of the multi-model sphere is much smaller than the number of virtual nodes of the core region, which results in significantly reduced numerical costs for the synchronization process of multi-model spheres and the sample.

## 6.3 Calottes

The matching of sample cell size and multi-model sphere cell size works well as long as the multi-model sphere remains completely inside the sample. As soon as parts of the sphere leave the sample, nodes of the sphere located outside of the sample have to be deactivated. A simple removal of the nodes outside the sample mesh would result in a new effective boundary of the multi-model sphere located inside of the original one. Hence, cells with significantly different cell sizes would need to get synchronized, and this would give rise to important numerical errors.

One possibility of treating such situations could consist in remeshing the sample and the multi-model sphere, but for simple sample geometries like cylinders a *calotte* approach can be taken. Apart from its two caps, the surface of a cylinder has the same shape everywhere, which is defined by the radius of the cylinder and its orientation in space. Therefore, one can preprocess a set of tube segments having the same outer radius as the sample, a specific opening angle covering only a fraction of the surface of the tube, a length comparable to the diameter of the multi-model sphere and a thickness of twice the average sample cell size effectively act as a patch, in order to match the different cell size distributions of the sample and the multi-model sphere. An example of such a calotte set is shown in Fig. 6.3.

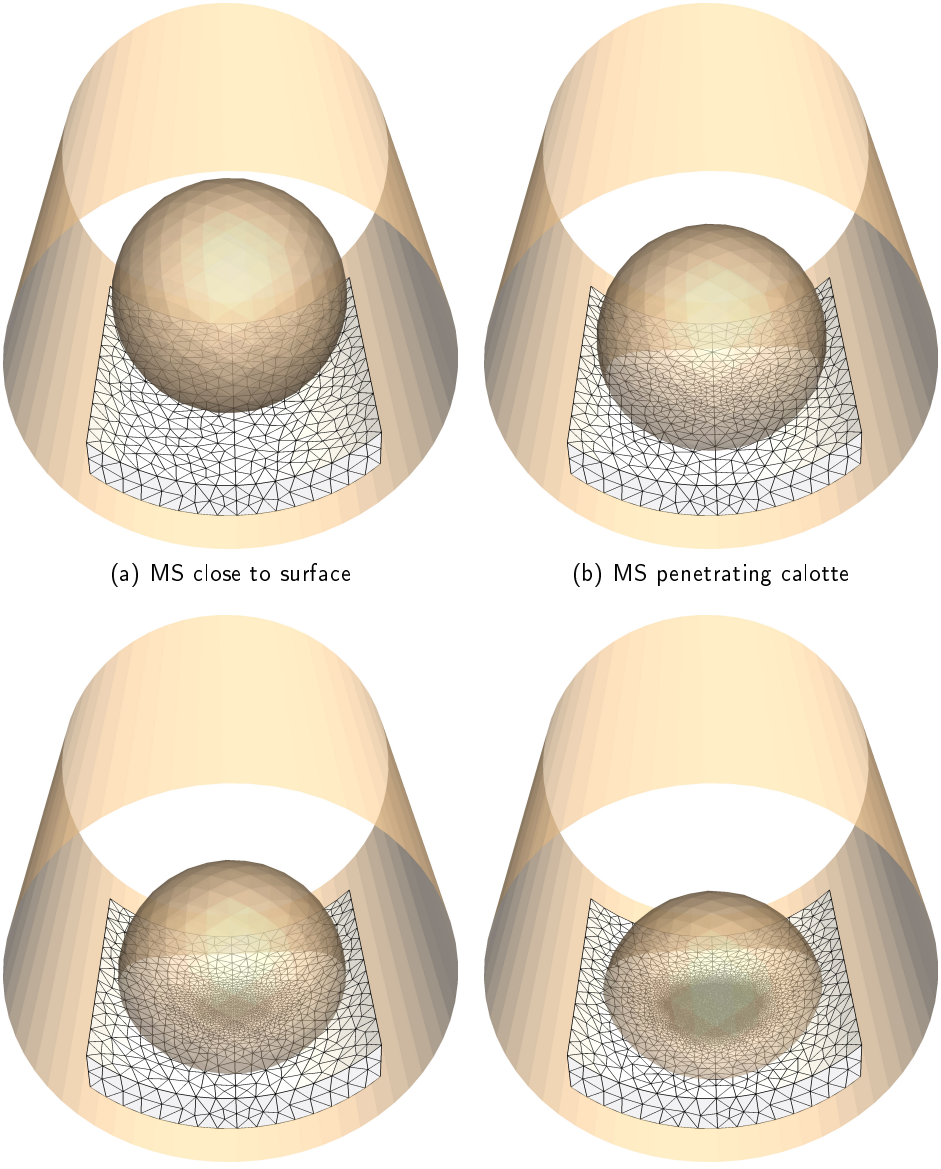

(a) MS close to surface

(b) MS penetrating calotte

(c) MS intersecting the sample surface

(d) MS penetrating the sample surface deeply

**Figure 6.3** – Subset of calotte structures visualizing the "refinement patch" procedure. When a multi-model sphere (MS) approaches the surface of the sample a calotte mesh is inserted by the algorithm. The algorithm chooses from a predefined set of calotte meshes the one for which the local cell sizes match those of the multi-mode sphere best depending on the penetration depth.

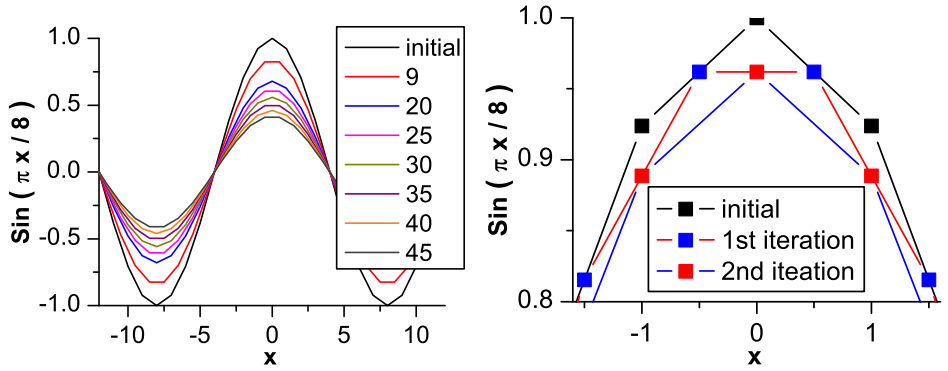


(a) Multiple mapping (b) First two iterations

**Figure 6.4** – A sine function flattens out, when a mapping between two different discretization schemes is applied several times. Panel (a) shows the development after 45 mappings, and (b) visualizes the two discretization schemes.

We design the mesh of each calotte element according to the average cell size distribution of a multi-model sphere located inside of a certain distance interval between sample surface and sphere center. Since all interaction matrices of the set can be preprocessed and stored as a template, the numerical effort to include them into the simulation is much smaller than that to remesh the sample.

During the dynamic simulation the program calculates the distance between the multi-model sphere and the sample boundary after each propagation of the multi-model sphere. If the distance falls inside the distance interval, for which a calotte element is designed, the program nucleates such a calotte element. The algorithm places the new calotte on the boundary of the sample closest to the center of the multi-model sphere.

## 6.4 Synchronization

In addition to the background mesh of the sample, simulations can incorporate several multi-model spheres and calotte elements. All their discretization points interact and need to be synchronized. For the synchronization between two meshes we use the mapping process as described in section 5.2 to find the location of a vertex $V_A$ belonging to mesh $A$ inside mesh $B$. The cell $C_B$ of mesh $B$ enveloping $V_A$ has the vertices $v_B^{(i)}$. Once the position of $V_A$ inside of $C_B$ is known, any functional value, such as the normalized magnetic orientation, can be interpolated from $C_B$ to $V_A$ by using the shape functions of $C_B$. If $B$ maps a quantity to $A$ but not in the opposite direction, as it is the case for the demagnetizing field that is mapped from the sample mesh onto the multi-model spheres and the calottes, we can apply the interpolation directly. In general, however, a synchronization of two structures is bidirectional, like in the case

of the exchange field, so that not only $B$ maps to $A$, but also $A$ to $B$. If the vertices in $A$ as well as $B$, which both provide and receive mapping information, are pairwise disjoint sets, the problem splits into two unidirectional mappings. On the other hand, if the sets of information receiving and providing nodes are overlapping, then the two mapping operations do not permute, and this results in a sequence-dependent result of the synchronization. As a consequence, the mapped function becomes increasingly homogeneous ("flattens out") as visualized in the example shown in Fig. 6.4 for a one dimensional sine function. Hence, the procedure is numerically more stable if only those vertices which do not receive a mapping provide the information for a mapping to another structure.

For the synchronization there are two groups of vertices being subject of receiving a mapping in any case: first, the boundary vertices of multi-model spheres and second, boundary vertices of calottes which are not located at the outer surface of the sample. In addition, properties of some vertices located inside an overlapping region with another mesh are overwritten. In order to perform this mapping procedure consistently, we need to define a hierarchical relationship between the two meshes.

In a multi-mesh environment several cells might represent a possible source of mapping for a given vertex. By distinguishing three principal entities, namely multi-model spheres, calottes, and the background mesh of the sample, we can define a superior inter-group hierarchy and an inferior intra-group hierarchy.

Concerning the inter-group hierarchy, the highest accuracy is obtained in the atomic core region of the multi-model spheres, whereas the local degree of accuracy of the simulation decreases radially in the shell. Furthermore, all cells formed by internal vertices of the multi-model sphere have a higher hierarchy than cells of the other groups. By construction, a calotte has a similar or larger cell size than the multi-model sphere, to which it belongs. Hence, calottes can map only to the boundary nodes of multi-model spheres or to the sample. The cell size of the sample mesh is everywhere larger than that of multi-model spheres as well as that of calottes and therefore forms the end of the mapping source inter-group hierarchy. The nodes of the background mesh can map only to boundary vertices of multi-model spheres or boundaries of calottes, which do not belong to the geometric sample boundary simultaneously.

Concerning the intra-group hierarchy, if several multi-model spheres could serve as a mapping source, the radial position of vertices represents a natural criterion for a hierarchy. Hence, we define that the tetrahedron $t_A$ of multi-model sphere $A$ serves as source for which the receiving node $v_B$ is closest to the center of $A$. In order to prevent the aforementioned cross-mapping between two meshes we apply an additional condition: if the receiving mesh is part of a multi-model sphere, all donating source nodes in $A$ must have a smaller radius in the coordinate system of the source mesh $A$ than the receiving node in the coordinate system of the receiving mesh $B$. This criterion gives rise to a neutral zone inside of which two multi-model spheres coexist without overwriting the values at the vertices of each other. This situation is visualized in Fig. 6.5.

The natural criterion to formulate an intra-group hierarchy between calottes is the local cell size. Following this spirit, if several calottes could provide a mapping to

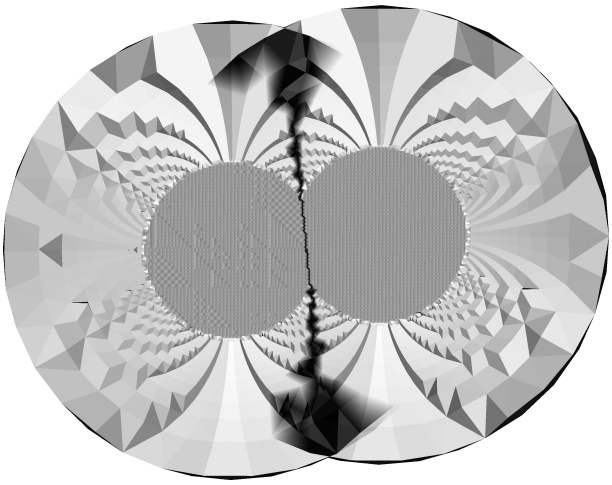

**Figure 6.5** – When two multi-model spheres overlap partially the values at their discretization points need to be synchronized. For the white colored regions in the figure the normal mapping hierarchy for two multi-model spheres is used. The dark colored regions indicate the "neutral" zone between the two multi-model spheres inside of which vertices of the receiving multi-model sphere do not receive magnetic properties from the donating sphere even though those vertices are closer to the center of the donating sphere than to the center of their own sphere.

a vertex, then the calotte is chosen as donating mesh for which the cell size providing the mapping is smallest. Analogous to the case of the multi-model spheres a neutral zone can be introduced to prevent cross-mapping between two calottes. Intra-group mapping is allowed only from one calotte to the other, if the maximum cell size of the vertices [1], which form the source cell, is smaller than the minimum cell size of the receiving node.

The mapping hierarchy is also visualized in Fig. 6.6 for the cases that the receiving vertex belongs to a multi-model sphere (Fig. 6.6(a)) or to a calotte (Fig. 6.6(b)). In order to be able to apply the mapping hierarchy and to ensure that no cross-mappings between two or more structures occur, we calculate first all possible mappings between the different structures and apply then the mapping hierarchy as shown in the flow chart in Fig. 6.7

## 6.5 Time integration of the equation of motion

Simulating the magnetization dynamics of the multi-model system involves the time integration of the Landau-Lifshitz-Gilbert equation for the sample, the calottes, and the multi-model spheres at the same time. During the dynamic process Bloch points

[1] We define the maximum (minimum) cell size of a vertex as the maximum (minimum) cell size inside of its Voronoi cell.

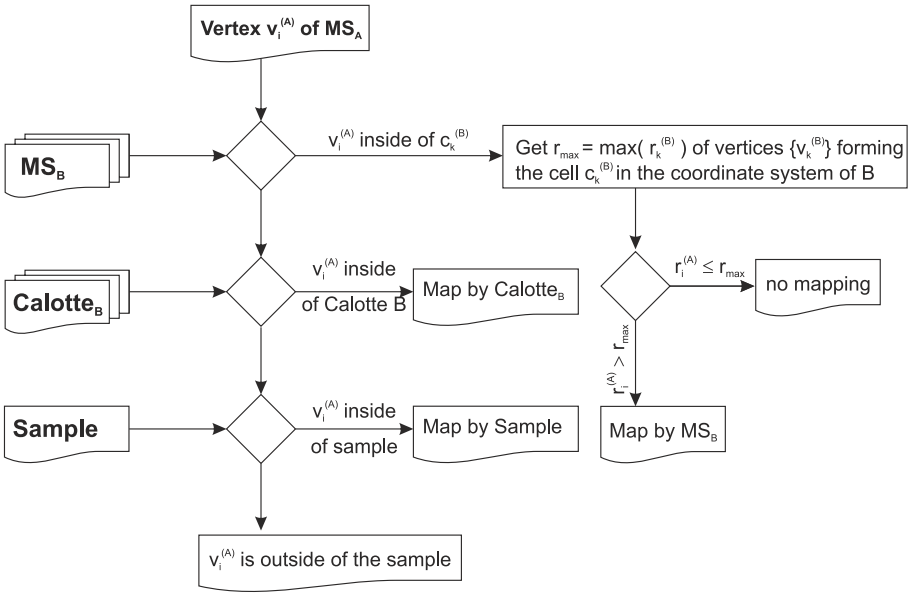


(a) Mapping hierarchy for a receiving vertex inside of multi-model sphere (MS) A

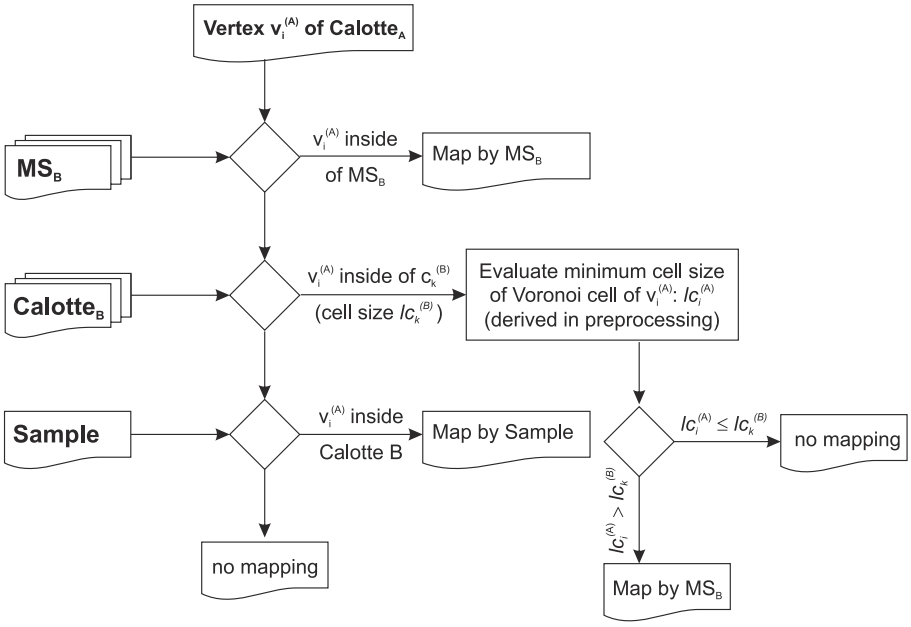


(b) Mapping hierarchy for a receiving vertex inside of calotte A

**Figure 6.6** – Flow chart of the mapping hierarchy for the two cases of a vertex $v_i^{(A)}$ inside of a multi-model sphere and inside of calotte structure $A$, respectively.

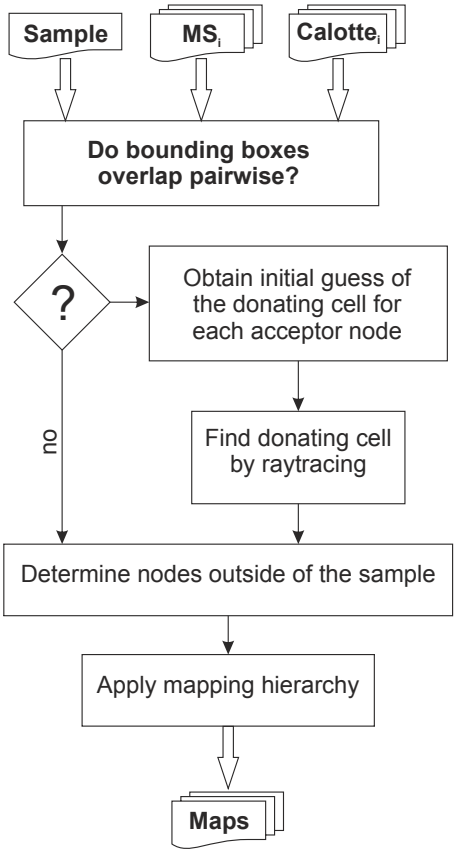


**Figure 6.7** – Flowchart of the map generation process between multi-model spheres (MS), calottes and the sample.

can propagate, nucleate or annihilate and regions of high exchange energy density can form and disappear again. Thus, not only the magnetic orientation may change during the time integration process, but also the number and the position of multi-model spheres. One can estimate that a Bloch point will not propagate much faster a few thousand meters per second, as justified *a posteriori* by our results. Since the multi-model spheres have a core region with a diameter of approximately 10 nm an off-centering of a Bloch point by one nanometer or below inside its multi-model sphere is tolerable. These considerations allow us to use two time-scales in the simulation. First, the time scale of several 10 fs in which the magnetic orientation changes according to the Landau-Lifshitz-Gilbert equation, and second, the time scale on which we perform the propagation and insertion and removal of multi-model spheres and calottes. Note that the 10 fs are merely a user defined quantity which can be reduced as shown, *e.g.*, for the simulations in chapter 14.

### 6.5.1 Time integrator routine

The dynamics of the magnetic system is governed by the Landau-Lifshitz-Gilbert equation which we need to apply to the magnetization configuration of the sample, the multi-model spheres and the calottes at the same time. Since the discretized form of the Landau-Lifshitz-Gilbert equation is an initial value problem, our simulation starts from an externally provided starting configuration. The nature of numerical integration is to discretize the time steps and to extrapolate a function $f(t)$ to the value $f(t+\Delta t)$ after the time step $\Delta t$. The numerical task often uses, if available, the functional form of the time derivative $f'(t)$. A typical example is the explicit Euler method, where the integration takes the form

$$f(t+\Delta t) = f(t) + \frac{\partial f(t)}{\partial t}\Delta t \tag{6.10}$$

Analogous to the generation of finite-element meshes, numerical time integration of ordinary differential equations has a large number of possible pitfalls. Therefore, using powerful and specialized external software libraries can provide a decisive advantage. One of those powerful libraries is the Sundials [129] package CVODE, which implements two different implicit integration schemes using predictor-corrector methods [115] to gain a large degree of numerical stability.

The Adams-Moulton method is recommended [31] for non-stiff problems, while Backward Differentiation Formulas (BDF) are recommended for stiff problems. Assuming a Lipschitz-continuous function $f(t)$ a problem is considered as stiff, if the constant $L$ in the Lipschitz condition is large:

$$\begin{aligned} g(t, f(t)) =& f'(t) = \frac{\partial f(t)}{\partial t} \\ |g(t, f(t_1)) - g(t, f(t_2))| \leq& L\,|f(t_1) - f(t_2)| \end{aligned} \tag{6.11}$$

For a smooth magnetization configuration in a sample without a Bloch point, $L$ can be sufficiently small so that the problem can be categorized as non-stiff. In that case the Adams-Moulton method is preferable. In contrast to this, in the multi-mesh simulations the value of $f'(t)$ is independent of $f(t)$ for vertices, which receive their exchange field from another structure. For that reason we use the BDF method for the time integration. The CVODE library expects as inputs an array representing the spatial distribution of $f(t)$ — in our case the array of the magnetic orientation —, a pointer to a routine calculating $f'(t) = \partial f(t)/\partial t$, which is where the Landau-Lifshitz-Gilbert equation enters the program, and the full step size $\Delta t$.

The value $\Delta t$ represents an initial guess of the step size, which the CVODE solver internally subdivides if necessary to a certain extent. In order to obtain a good initial guess we consider that the internal magnetic fields $H_{\text{int}}$ in a ferromagnetic material have values of up to several tesla. From the Larmor precession with angular frequency

$$\omega_L = \gamma_e H_{\text{int}} \tag{6.12}$$

we estimate that at $H_{\text{int}} = 10\,\text{T}$ a period lasts approximately 3 ps. This value represents an appropriate upper boundary for changes in the magnetic orientation by 360° due to Larmor precession. This estimate justifies an initial step size in the range of 10 fs to 100 fs.

### 6.5.2 Propagation of multi-model spheres and calottes

Between two steps of time integration we implemented the propagation of the multi-model spheres and calottes. It starts with an algorithmic determination of regions of interest, in which multi-model spheres or calottes are needed. In general, any kind of point of interest can be implemented, since the propagation method only calls a subroutine, which generates a list of multi-model sphere positions and assigns each of those positions to one multi-model sphere, while all remaining multi-model spheres are marked for deletion.

After the assignment step we derive for each multi-model sphere which has not been marked for deletion its distance to the sample boundary. If the distance is within the distance interval for which a calotte structure is designed the algorithm continues with the conditioning of the appropriate calotte structure: if the same type of calotte was assigned to that multi-model sphere prior to the propagation routine, the new position and orientation of the calotte is stored in an additional list. Otherwise, we generate a new calotte, which is selected from a set of the calotte templates, and mark any redundant calotte for deletion.

By using all structures that were required in the system before the next propagation step as sources and those which will be present after the propagation step as destinations, the program maps the current magnetic orientation to all multi-model spheres and calottes which have not been marked for deletion. Once the new system configuration is established, we delete any structure marked for deletion from the computation, and generate in a last step the synchronization maps for the remaining structures that are used in the time integration of the Landau-Lifshitz Gilbert equation.

### 6.5.3 Multi-model spheres for (potential) Bloch points

In this thesis we use three different definitions to identify points of interest. First, a single vortex tracked during the gyration process, second, a list of artificially generated points of interest, and third, Bloch points tracked during their field driven propagation in cylindrical nanowires. The first two cases are only for test purposes. The main focus of this section will therefore be on the detection of real and potential Bloch point positions. In order to generate such a list of Bloch points (or candidates thereof), we search in all multi-model spheres as well as in the background mesh of the sample for the existence of Bloch points by examining the finite element meshes. The searching procedure finds in a first step all of those cells, inside which the three perpendicular magnetization components $m_\alpha$ change their sign. This displays a necessary criterion for the existence of a Bloch point and narrows the number of cells which are then scheduled for further examination to about a few ten cells per structure.

For those cells $\{c\}$ found before we solve the set of linear equations

$$\mathbf{0} = \sum_{i}^{4} \mathbf{m}_i^{(c)} \left( a_i^{(c)} + \mathbf{r}_{\mathrm{BP}} \cdot \mathbf{b}_i^{(c)} \right) \quad . \tag{6.13}$$

using the shape functions of each cell $c$ in order to find the Bloch point center $\mathbf{r}_{\mathrm{BP}}$. The center is not necessarily inside the tetrahedron $c$, hence we check in a further step that $\mathbf{r}$ lies inside of the circumsphere of the tetrahedron. By applying that method a multiple occurrence of one Bloch point in adjacent cells of the same mesh is possible. Such cases are detected by requesting that two Bloch points shall have a distance of at least two lattice constants. The opposite problem occurs only in the moment of creation or annihilation of a Bloch point pair, but a single multi-model sphere is sufficient for that situation.

The resulting list of Bloch points may contain further doublets, since the same Bloch point can be detected in several multi-model spheres and the sample. We filter out those doublets by assuming that there is only one Bloch point inside the circumsphere of a finite element cell. In case that circumspheres of cells that contain Bloch points overlap, we extract the Bloch point position only from the atomic core region of the multi-model spheres in which the Bloch point is closest to the center. If none of the cells hosting the Bloch point belongs to the core region of a multi-model sphere, the cell with the smallest cell size determines the Bloch point position.

After the list of all Bloch point locations has been established, we check the sample for additional regions of high exchange energy density, with values above a predefined threshold. These regions, however, do not contain a Bloch point. Those regions are prominent candidates for the nucleation of a Bloch point pair; an event that could occur several time integration steps in the future. From Fig. 2.4 we can estimate the threshold by considering that the maximum local error that is allowed for the finite-element calculation within the sample's background mesh must remain below some percent in comparison to a Heisenberg model. The positions of multi-model spheres that are required to cover the regions of high exchange energy density are then added to the list of real Bloch point positions.

In order to avoid a frequent change of the number of multi-model spheres, the chosen exchange energy density threshold exhibits a hysteresis: in the case that less multi-model spheres are needed than those which are currently present in the system, the algorithm extends the high exchange energy volume using a lower threshold energy density. All multi-model spheres, which are not necessary to fill this increased volume of high exchange energy are marked to be removed from the computation, which is performed at the end of the propagation procedure.

Contrariwise, if the length of the final list of needed multi-model spheres is larger than the number of multi-model spheres that are currently used in the system, the algorithm generates additional multi-model spheres from the template and marks them as not initialized. Afterwards, the algorithm assigns each multi-model sphere, which is not marked for deletion, to a position in the list of required multi-model spheres. Computation time can be saved if a multi-model sphere propagates as little

as possible. Hence, we designed the assignment algorithm so that it minimizes the total propagation distance of those multi-model spheres which were already present in the system prior to the ongoing propagation step.

## 6.6 Execution pipeline

In the previous sections we have described the parts of the simulation kit we have implemented in order to perform multiscale-multi-model simulations. The flowchart in Fig. 6.8 summarizes the execution pipeline of our implementations, which consists of a series of subprograms that need to run in consecutive order. The first step consists in the definition of the sample geometry and the meshing process using GMSH. In a second step we perform the micromagnetic preprocessing covering the geometry-dependent part of the micromagnetic interactions. For historic reasons of the code development the calculation of the supermatrix needed by HLib is outsourced into a second preprocessing program.

We decoupled the additional preprocessing steps needed for the multi-model calculations from the micromagnetic preprocessor of the sample, which allows for a compatible usage of the pure micromagnetic and the multi-model version of TetraMag. The multi-model preprocessor has the purpose to generate the multi-model sphere template and to condition the geometric information of sample and multi-model spheres for the mapping and propagation procedure undertaken during dynamic simulations. A third preprocessor takes care of the calotte structure generation, the geometric as well as the micromagnetic preparation, for which the knowledge of the sample mesh and the multi-model sphere mesh is decisive.

After the preprocessing we define an initial magnetic configuration for the sample, which is then relaxed with the pure micromagnetic version of TetraMag. After the pure micromagnetic relaxation follows the multi-model relaxation step. This splitting of relaxation into two steps serves purely for a reduction of computational processing time. Possessing the relaxed state the actual multi-model studies can be carried out using a variety of external field strengths and shapes.

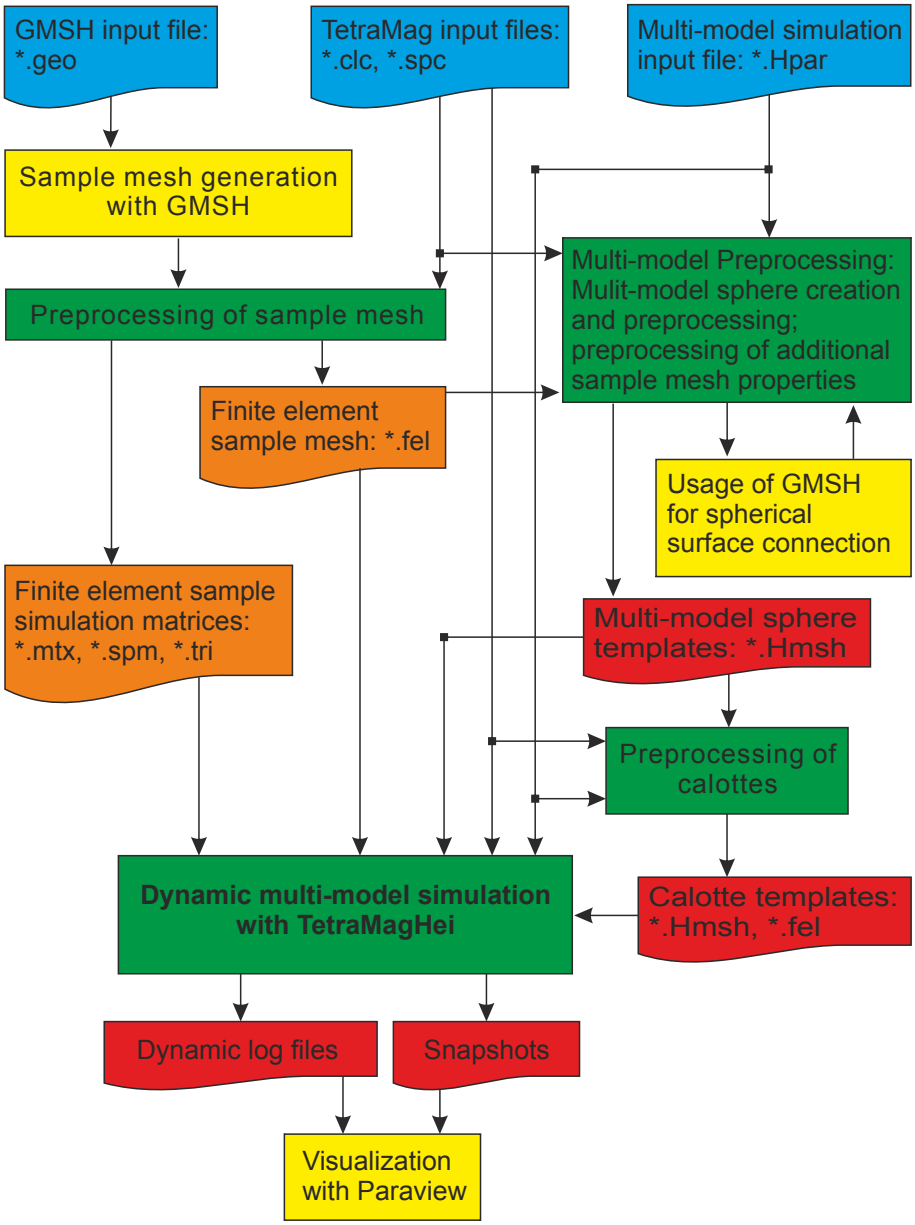


**Figure 6.8** – Flowchart of the execution pipeline employed to run multi-model simulations. We color user-defined input files in blue, external programs in yellow, internally used files in orange, outputs from the multi-model version of TetraMag in red and in-house executables in green.

# 7
# Numerical stability tests

The algorithms described in the previous chapter contain two core elements, whose possible numerical errors cannot be derived analytically by means of simple models. The first possible source of important numerical errors is the abrupt change between two meshes due to the abrupt steps connected with the mapping hierarchy. In Sec. 7.1 we will discuss this issue using the system of a gyrating vortex in a ferromagnetic disc, which is well understood and documented in the framework of classic numerical micromagnetism [32–34]. The second possible problem originates from the perturbation of the system due to the introduction, removal or propagation of multi-model spheres and calottes in the sample. This aspect will be discussed in section 7.2.

## 7.1 Abrupt mesh transitions

The core-shell structure of multi-model spheres allows for seamless transitions between the atomic and the continuum region, resulting in a smooth conversion of the data describing the different models. The coupling between multi-model spheres and the sample is less obvious and more abrupt, because the quality of a mapping from one mesh to another changes depending on the position within the mesh. This effect can be understood in a one-dimensional system. In one dimension a finite element mesh corresponds to a chain of vertices (which are not necessarily equally spaced) that are connected by line segments which represent the cells. If a sine wave with wave length $\lambda$ is represented in a discretized form by vertices of distance $\Delta x \ll \lambda$, then the largest deviation of the approximation from the analytic description can be found in the middle between two vertices. In an analogous way, the error connected with a mapping from mesh $A$ to a vertex $v_B$ of mesh $B$ is most accurate, if the position of $v_B$ coincides with the position of one of the vertices of mesh $A$, and it deteriorates for positions closer to the center of the circumsphere of the cell.

In order to reduce those numerical errors a further transition region could be

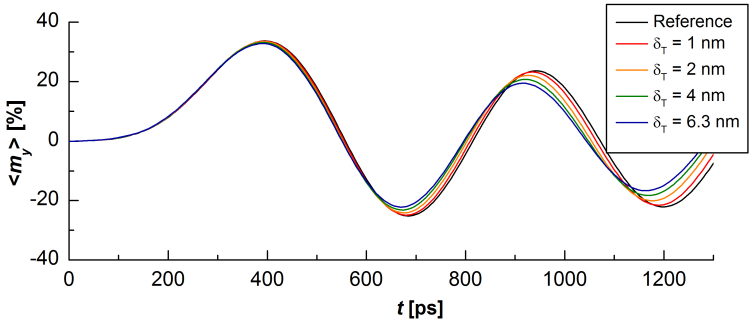


(a) Average $m_y$ component during the vortex gyration inside the disc

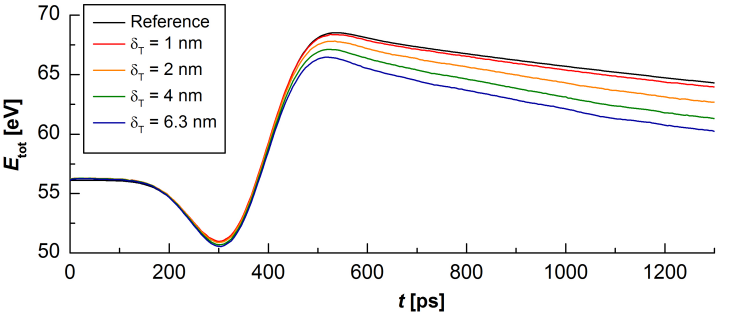


(b) Energy evolution during the vortex gyration

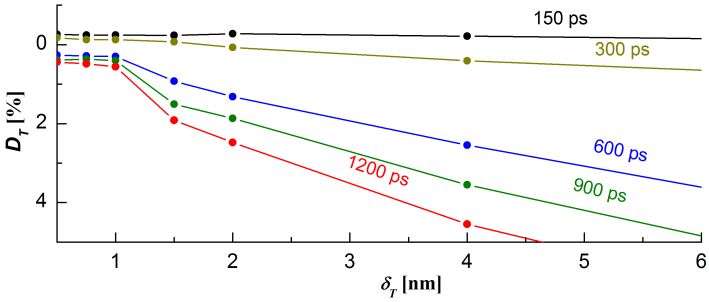


(c) Energy deviation from the micromagnetic reference

**Figure 7.1** – Panel (a) and (b) compare the evolution of the average $m_y$ component and total energy in the system, respectively, for different transition region thicknesses $\delta_T$ as well as for the micromagnetic reference. Panel (c) shows the relative deviation of the multi-model simulations from the micromagnetic reference system at different timesteps versus the transition region thickness, from which it gets clear that the introduction of a transition region increases numerical errors instead of reducing them.

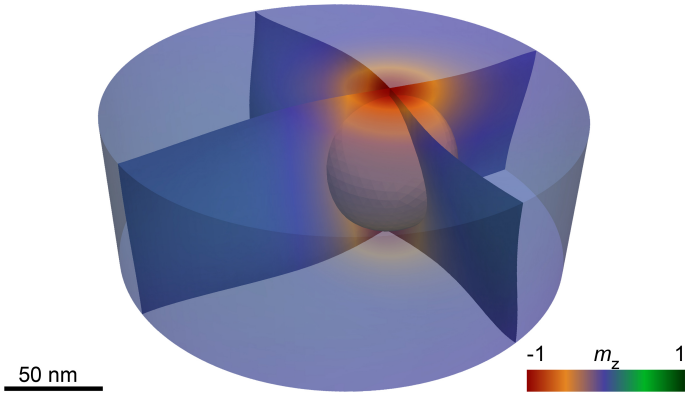


(a) Snapshot of the disc with a vortex state (the position is highlighted by the crossing of the $m_x = 0$ and $m_y = 0$ surfaces) and one multimodel sphere following the position of the vortex core at $t = 750\,\mathrm{ps}$.

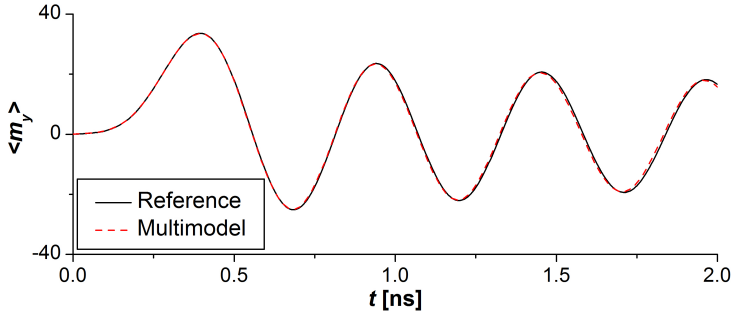


(b) Average $m_y$ component inside the disc

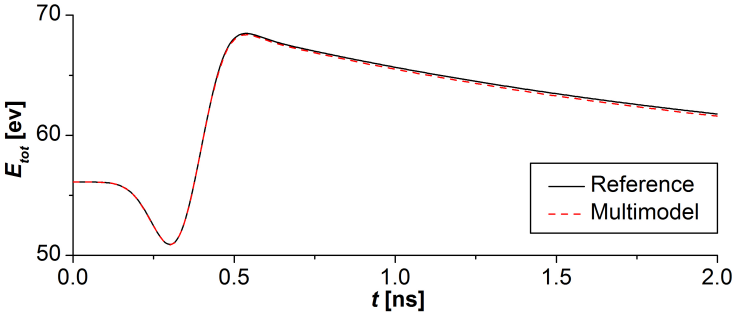


(c) Energy evolution during gyration

**Figure 7.2** – A gyrating vortex in a Permalloy disk serves as testing system to determine qualitatively the change of magnetization dynamics due to the usage of a multimodel sphere. (a) displays a snapshot during the gyration with the multimodel sphere in the center of the vortex, (b) shows the evolution of the average in-plane magnetization component $< m_y >$ over time for the pure micromagnetic reference as well as the multi-model simulation and (c) plots the total energy of the system, respectively.

introduced, inside of which the simulation results of both structures are weighted in analogy to the transition region between the Heisenberg and micromagnetic region in the core of the multi-model sphere (section 6.5.3). Unlike the transition region between the two models in the core of the multi-model spheres, a transition region between different meshes smoothens the interpolated function, which introduces another type of numerical errors. Since those two sources of errors would be minimal for opposite sizes of the transition region, an optimum width should exist displaying a tradeoff that minimizes the total numerical error.

To obtain this optimum width of the transition region between two meshes we use the system of a gyrating vortex inside a ferromagnetic disc. The gyrotropic motion is triggered by an excitation with a short Gaussian in-plane field pulse. It has an amplitude of 50 mT, a width $\sigma = 100\,\mathrm{ps}$, and a peak-delay of $t_{\mathrm{Max}} = 300\,\mathrm{ps}$. The disc has a diameter of 250 nm and a height of 100 nm. We mesh the structure with a cell size of 1.75 nm resulting in 66840 vertices and 370842 cells. The multi-model sphere has a core region with a diameter of 7 nm including a 2 nm broad transition region between the Heisenberg and the micromagnetic model. The atomic region consists of 122157 lattice sites, and a total of 175973 vertices form the complete multi-model sphere including the shell region. For the Heisenberg model we use nearest-neighbor interaction in a bcc lattice with lattice constant $a = 2.866\,\text{Å}$, exchange constant $J = 11.78\,\mathrm{meV}$ and $1\mu_{\mathrm{B}}$ per lattice site, corresponding to a micromagnetic exchange stiffness of $A = 1.3 \times 10^{-11}\,\mathrm{J/m}$ and saturation polarization $\mu_0 M_s = 1\,\mathrm{T}$. The $z$ direction corresponds to the axial direction of the disc, while the $x$ and $y$ axis span the in-plane directions.

Without an applied field the vortex resides in the center of the disc. The field pulse displaces the vortex from the center and, for field pulses below the threshold at which the vortex polarity switches [9, 10, 130], the vortex gyrates around the equilibrium position after the field pulse has faded out. Using the pure micromagnetic simulation by the traditional version of TetraMag as a reference we compare the temporal development of the gyration radius and the rotation frequency to the result obtained with the multi-model version with the center of the vortex core as region of interest for the tracing algorithm. In a systematic study we vary the width of the transition region at the outer shell of the multi-model sphere as displayed in Fig. 7.1. The plots of the average $m_y$ position indicate that the numerical error reaches a minimum for a vanishing width of the transition region. For a finite transition region the oscillations are more strongly damped than in the micromagnetic reference case (black line in Fig. 7.1). The stronger damping decreases the mass of the vortex [64] resulting in a higher gyration frequency [32, 33].

Therefore, we conclude that a transition is neither necessary nor decisive between the different meshes as long as the cell sizes correspond to each other. The results of the vortex gyration test without a transition region are shown in Fig. 7.2, visualizing that a numerical error generated by the presence of the multi-model sphere remains in any case in the sub-percent regime. A part of this error might also be attributed to the propagation of the multi-model sphere, which is the subject of the next section.

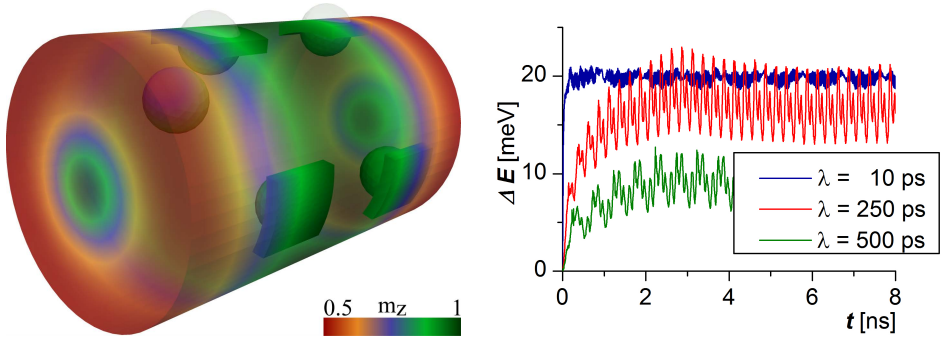


(a) Snapshot (b) Energy increase

**Figure 7.3** – We use an artificial nucleation, propagation and removal procedure involving five multiscale spheres in order to determine whether those actions result in an artifact of increased total energy. Panel (a) shows a snapshot during the simulation with five multimodel spheres and four calotte structure. The deactivated volume of the two spheres at the top of the cylinder is displayed in light gray. The graph in panel (b) shows the evolution of the total energy for three different periodicities of multimodel sphere propagation.

| $\lambda$ [ps] | $\Delta E$ [meV] | $\mu_0 H_{\mathrm{err}}$ [mT] |
|---|---|---|
| 10 | 20 | 0.014 |
| 250 | 17 | 0.012 |
| 500 | 8.7 | 0.006 |

Table 7.1 – Energy offset due to artificial periodic nucleation, propagation and deletion of five multi-model spheres in a test cylinder with 60 nm diameter and 100 nm length for different periods $\lambda$.

## 7.2 Energy artifacts of multiple structures

In the previous section we have discussed the intrinsic error of the multi-model system due to the sharp mapping hierarchy at the mesh boundaries. To test the influence of the propagation, nucleation and deletion of multi-model spheres and calottes on a system we study a relaxed single-domain state in a short nanocylinder with a length of 100 nm and a diameter of 60 nm, in which the magnetization points along the cylinder axis, while at the two cylinder caps vortex-like states form [131]. Note that we define a magnetic system inside of a volume $V$ as relaxed, if it fulfills the condition

$$|\mathbf{H}_{\mathrm{eff}}(\mathbf{r}) \times \mathbf{m}(\mathbf{r})|\ \mu_0 < 1 \times 10^{-10}\,\mathrm{T} \qquad \forall\, \mathbf{r} \in V \quad . \tag{7.1}$$

We mesh the sample with a 3 nm cell size resulting in 12614 vertices. In order to reduce numerical costs we use in that test smaller multi-model spheres with a total diameter of 14 nm, from which 7 nm correspond to the core region, having 16093 vertices in total. The micromagnetic parameters are the same as in Sec. 7.1.

In that test we introduce five multi-model spheres which are inserted, displaced and removed in the cylinder periodically with wave length $\lambda$

$$\begin{aligned} x = &\quad (-1)^i \sin(2\pi t/\lambda) \cdot 30\,\mathrm{nm} \\ \phi = &\quad 8\pi t/3\lambda(1-2i/3) \\ r = &\quad \sin(4\pi t/\lambda) \cdot 30\,\mathrm{nm} \\ n = &\quad \lfloor 5\sin(\pi t/\lambda) + 1 \rfloor \quad , \end{aligned} \tag{7.2}$$

where $n$ is the number of multi-model spheres and $i$ their index. A snapshot of this artificial manipulation is shown in Fig. 7.3(a).

The test branches into three different regimes defined by the velocities of the multi-model spheres. The first branch corresponds to the low propagation velocity regime of the spheres and represents a laminar perturbation scheme, for which we use a periodicity of 500 ps. The second propagation scheme refers to supermagnonic velocities [18], where the velocity is slightly faster than the minimum spin wave phase velocity in such samples. The used frequency is 250 ps, which corresponds to velocities of the spheres between 1100 m/s and 1700 m/s. The last branch deals with ultrafast propagation, for which we use a periodicity of 10 ps corresponding to velocities between 30 000 m/second and 40 000 m/second. In that branch the system would not have enough time to dissipate energy by damping, if numerical errors due to the propagation of the spheres could accumulate. Note that the wave length of spin waves excited by propagating multi-model spheres would be unresolvable for the finite element mesh, but the perturbation would nevertheless be clearly visible in the total energy of the system.

All systems have in common that the spurious energy introduced by the multi-model spheres and calottes should result in a continuous increase of the total energy due to the low damping of $\alpha = 0.01$ if the method resulted in a significant artificial manipulation and destabilization of the magnetic system. As can be determined from Fig. 7.3(b) the total energy exhibits only an initial increase during the first periods. This energy offset can be compared to an external field $H_{\mathrm{err}}$ according to

$$\Delta E = \mu_0 M_s H_{\mathrm{err}} V \quad , \tag{7.3}$$

where $V$ is the volume of the cylinder. Table 7.1 lists the energy offsets and corresponding fields $H_{\mathrm{err}}$ for the three different period lengths. From those results we conclude that the influence due to the multi-model spheres and calottes are negligible, since the maximum error in the field value yields $\mu_0 H_{\mathrm{err}} \approx 0.014\,\mathrm{mT}$. Hence, the multi-model spheres and calottes are suitable to study magnetic systems without risking a sizable manipulation of the magnetic system.

# Part III.
# Numerical results

# 8

# Bloch points in nanowires

The high amount of exchange energy needed to nucleate Bloch points inhibits their existence, hence they appear only in few magnetic structures and processes. So far, in the literature the most often discussed occurrences of Bloch points are within a transient structure [9, 10, 130] that develops during the reversal of vortex cores. Another example are Bloch points located in the center of vortex domain walls in cylindrical nanowires [41, 63, 78]. In the former case a thorough analysis of the Bloch point properties is difficult due to their short life times in the range of some picoseconds [10]. In the latter case they can be studied more easily since vortex domain walls in such wires can be generated and equilibrated numerically as well as measured experimentally – at least in principle.

Cylindrical nanowires provide a suitable system to study a broad range of Bloch point configurations. For anti-Bloch point structures different geometries would be necessary for an efficient stabilization, which will not be subject of this thesis. A vortex domain wall contains a Bloch point in its center, as previously displayed in Fig. 3.5(b) on page 33, in which the cylinder axis corresponds to the polar direction of the Bloch point. During the last years a growing attention regarding vortex domain walls was paid to the geometry of cylindrical nanotubes [18, 132, 133]. Those tubular geometries have the advantage that a Bloch point is not formed in the vortex wall (due to the cavity in the center) and therefore they can be simulated reliably with a single-model approach, namely with pure micromagnetism. In this thesis we benefit from those prior studies of nanotubes. Especially by comparing effects between those two systems we can identify the effects originating from the Bloch point, as opposed to those related to the vortex structure surrounding it.

For the studies in this numerical part of the thesis we use micromagnetic material parameters of Permalloy ($Ni_{80}Fe_{20}$) with a saturation polarization of $\mu_0 M_s = 1\,\mathrm{T}$, exchange stiffness $A = 1.3 \times 10^{-11}\,\mathrm{J/m}$ and zero magneto-crystalline anisotropy. For the Heisenberg model we assume a bcc lattice structure with lattice constant $a = 2.866\,\text{Å}$. The choice of the saturation magnetization in conjunction with the

lattice configuration lead to a magnetic moment of $\mu = 1.01\mu_B$ per lattice site. The Heisenberg exchange interaction in the case of a nearest-neighbor (n.n.) interaction is $J = 1.889 \times 10^{-21}$ J $= 11.79$ meV. We compare the nearest-neighbor configuration with a long-range exchange interaction material which takes into account a total of 144 neighbors. The values of the Heisenberg exchange constants correspond to those of iron calculated by Pajda et al. [79], which have been normalized to be consistent with the above given micromagnetic exchange stiffness by using Eq. 2.23. We label this material as *Fe-like*.

The reason for the choice of this particular material configuration is twofold: first, non-singular magnetic configurations of Permalloy have been studied thoroughly in the past. In particular, the prior studies of vortex-domain wall dynamics in cylindrical nanotubes reported in the last years by our group provided a solid theoretical starting point that helps avoiding to a large extent possible pitfalls from the material point of view. Second, since Permalloy is a polycrystalline material, the explicit use of its fcc lattice structure would not provide any further insight into the real magnetization dynamics than the use of any other monocrystalline structure. Hence, we decided to apply for the atomistic part of the simulations the properties of iron, which resulted in the actual choice of the lattice constant and the lattice type.

The ferromagnetic cylinders used in the simulations have a length of 4 µm with the $z$-direction, which represents the axial direction. The cylinder length of 4 µm has proven to be a reasonable tradeoff between the need to minimize computational costs and a sufficiently long propagation distance of the domain wall. We perform the simulations in wires of two different diameters: 60 nm and 80 nm. The diameter of 60 nm has been chosen because for the given material parameters the transition radius between transverse walls and vortex walls is in the range of 40 nm [134] in the field-free configuration. Therefore, to avoid a transition from the vortex wall to the transverse wall configuration, we considered a safety margin of 50 % and chose the value of 60 nm. Hence, we used this thinner geometry for most of the systematic studies. The geometry with a diameter of 80 nm serves as validation system to prove the generality of the effects observed in the thinner geometry.

We use a cell size of 3 nm to mesh the two cylinder geometries, which results in 494.914 vertices for the 60 nm and in 825.746 vertices for the 80 nm cylinder. In the system with nearest-neighbor exchange interaction as well as in the one with *Fe-like* material the multi-model spheres have a diameter of 36.6 nm resulting in 174.555 vertices. The atomic region inside it has a diameter of 14 nm, including a model-transition shell with 2 nm thickness.

## 8.1 Spin wave dispersion relation

In analogy to the sonic boom generated by objects flying with supersonic velocity in air or the Cherenkov radiation [135] induced by charged particles propagating faster than the phase velocity of light in a dielectric medium, supermagnonically propagating domain walls [18] couple to and resonantly excite spin wave eigenmodes of the system [136]. It has recently been shown [40] that resonant coupling of moving

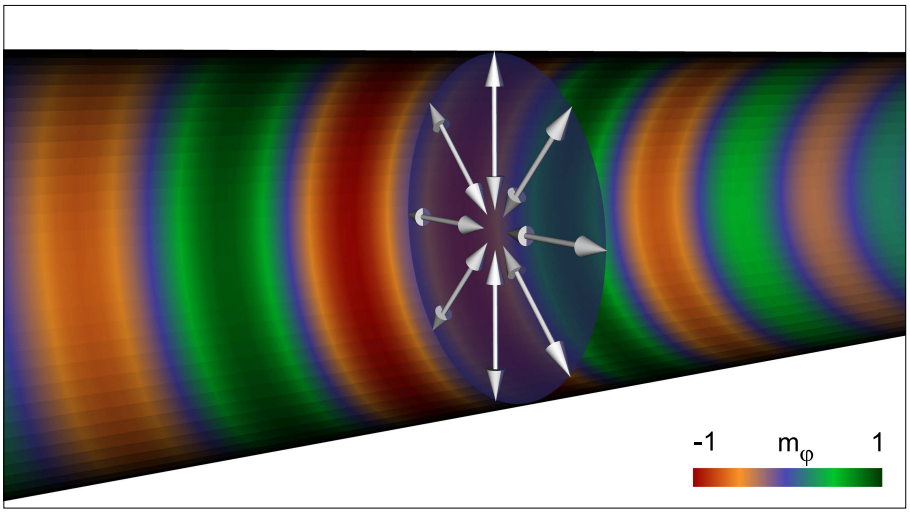


**Figure 8.1** – An oscillating radial magnetic field in a central two-dimensional plane excites spin-waves inside the single-domain state of a nanowire. The spin waves generated by this localized, "breathing"-type of perturbation are propagating in positive and negative axial directions.

magnetic inhomogeneities to spin wave eigenmodes is a general phenomenon that becomes dominant for velocities above those of propagating spin waves.

Because the dispersion relation of phonons in air shows a mostly linear behavior, the resulting phase velocity is to a good extent independent of the phonon frequency. In air the sonic barrier forms for a velocity around 340 m/s. In contrast to this, the typical spin-wave modes in magnetic samples, the Damon-Eshbach mode which is characterized by a $\mathbf{k}$ vector perpendicular to $\mathbf{m}$ [137, 138] and the backward-volume modes with the $\mathbf{k}$ vector parallel to $\mathbf{m}$ [137, 139], have a highly non-linear dispersion relation. Hence, instead of a magnonic barrier, a broad supermagnonic propagation regime can be found for magnetic structures.

In order to calculate the spin wave dispersion relation of a cylindrical nanowire we start from an equilibrated single-domain state. Since the mesh of the wire is generated by linear extrusion of a circular plane in axial direction, a single layer of vertices at the axial center $z_c$ exists and can get excited by a radial oscillating field with frequency $f$, as sketched in Fig. 8.1. Note that in the following $f$ denotes the frequency, while $\omega = 2\pi\ f$ refers to the angular frequency. Using a low damping constant ($\alpha = 0.02$) spin waves with frequency $f$ develop and propagate over a region of several spin wave lengths in axial direction. As the spin waves propagate along a magnetic domain oriented in the axial direction, mainly backward-volume modes are observed. Once a spin wave is developed over a range of several wave length we perform a radial and azimuthal averaging of the magnetization. This procedure removes efficiently any spurious radial and azimuth spin wave modes. Afterwards, the resulting one-dimensional vector function $\mathbf{m} = \mathbf{m}(z)$ is Fourier transformed. For the analysis of a single snapshot, we found that a combination of the $m_z$ component

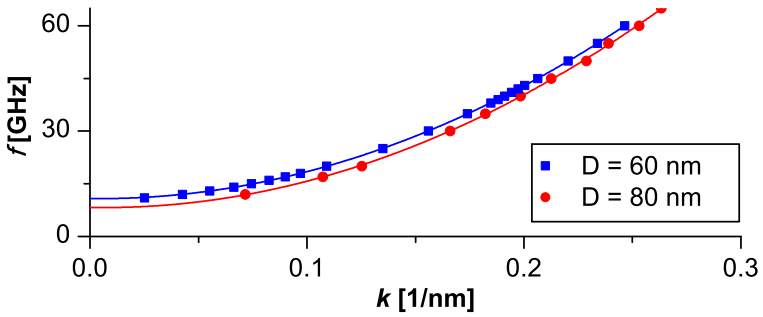


**Figure 8.2** – Spin wave dispersion relation of axial modes in a wire with a diameter of 60 nm and 80 nm, respectively. The solid lines are fits to quadratic functions.

as real part and the $m_r$ component as imaginary part leads to a very good signal-to-noise ratio of single magnetic snapshots in time. An even better signal-to-noise ratio has been obtained by averaging the Fourier components resulting from $m_z + \imath m_\phi$ over several hundred picoseconds.

We determine the wave vector corresponding to the exciting frequency $f$ applying the peak finding algorithm of Origin®[140]. Due to the intrinsic property of both, the Damon-Eshbach and the backward volume mode, only frequencies $f$ higher than a minimum frequency result in the excitation of spin wave eigenmodes. Figure 8.2 shows the spin wave dispersion relations for both wire diameters with a quadratic function fit of the data. In addition to the modes displayed in Fig. 8.2 we find that for the wire with 80 nm diameter a further excitation unfolds, which is independent of the frequency with $k = (4.9 \pm 0.2) \times 10^7\,\mathrm{m}^{-1}$. We also detect higher harmonics of this mode by using single snapshots of the Fourier transformed function of $m_z + \imath m_r$. The origin of these modes is still not understood. One might speculate that it stems from finite-size effects. Whatever the microscopic origins may be, this particular mode tends to overlay the mode that we wish to study. As a consequence, we obtained the low frequency data points of the dispersion relation from the averaged Fourier transformation of $m_z + \imath m_\phi$.

From the dispersion relations the spin wave phase velocity distribution by $v_{ph} = \omega / k_z$ can be derived. This value is plotted as a function of $k_z$ and $f$ in Fig. 8.3 for the two different wire diameters. The graphs show that spin waves in the nanowire with 60 nm diameter have a minimum spin wave phase velocity of $v_{min}^{(ph)} \approx (1150 \pm 10)\,\mathrm{m/s}$, whereas the minimum spin wave phase velocity in the nanowire with 80 nm diameter is lower and has a value of $v_{min}^{(ph)} \approx (989 \pm 9)\,\mathrm{m/s}$.

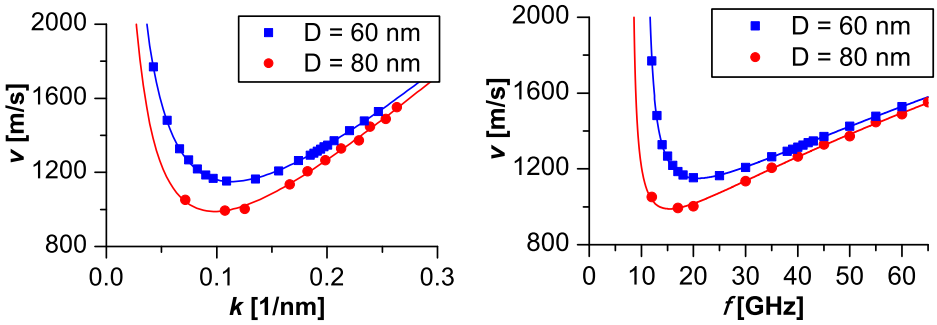


(a) Spin wave phase velocity vs. $k_z$

(b) Spin wave phase velocity vs. $f$

**Figure 8.3** – From the dispersion relation in Fig. 8.2 we calculate the spin wave phase velocity distributions as a function of $k_z$ (a) and of the frequency $f$ (b) by which the spin waves are excited for nanowires with diameter of $60\,\mathrm{nm}$ and of $80\,\mathrm{nm}$.

# 9

# Equilibrium Bloch point configuration

In chapter 4 we discussed possible analytic estimates of the Bloch point properties. Using the multi-model simulation kit we can now compare those estimates with the much more accurate numerically calculated configuration. Two system parameters are of particular interest here. First, the distribution of the inflow-angle $\gamma$ in dependence of the radial distance from the Bloch point position. Second, the domain wall width as an important parameter for the analysis of domain wall propagation in general. The results reported in this chapter were extracted from simulations with nearest neighbor-interaction, yet no difference could be observed for the *Fe-like* material configuration.

First, we determine the Bloch point position with very high accuracy of some picometer which allows us to determine its position within the atomic crystal lattice. This localization is performed using the same method as in Sec. 6.5.3. Afterwards we generate the $m_z = 0$ isosurface inside the multi-model sphere and the sample, based on which we derive the distribution of $\gamma$. After an averaging process, we eventually obtain the functional dependence of $\gamma = \gamma(r)$ on the isosurface with the Bloch point positioned at $r = 0$. Using the $m_z = 0$ isosurface we can also determine the domain wall width according to Lilley's definition (Eq. 3.2). In contrast to domain walls in thin strips, where variations along the film thickness are usually negligible, the domain wall width in the cylinder is strongly radius-dependent, since at the Bloch point position the magnetization orientation in $z$-direction changes by 200 % within one lattice constant $a$, which results in a minimum domain wall width in the range of

$$\Delta_{DW} \approx \frac{\pi}{2} a \quad . \tag{9.1}$$

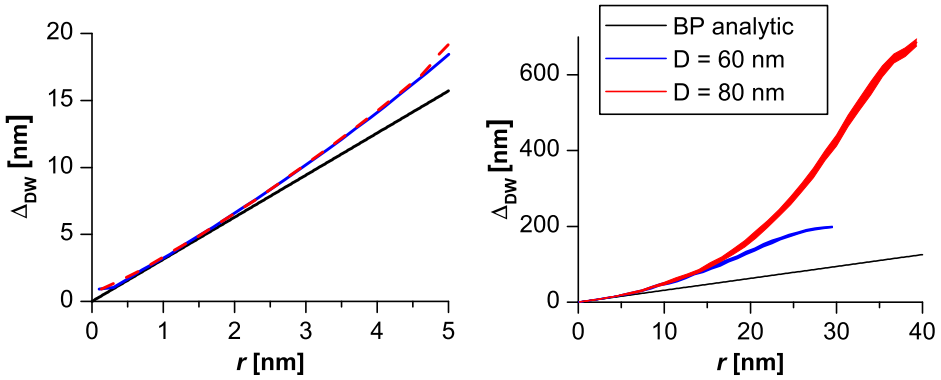


(a) Domain wall width BP vicinity (b) Domain wall width full range

**Figure 9.1** – The domain wall width of vortex domain walls is radius dependent. In the vicinity of the Bloch point the domain wall width corresponds well to the analytic value derived from Döring's description (Eq. 4.1), whereas over the full radius of the wire a strong deviation from the analytic value can be observed. At larger distances from the Bloch point the domain wall width becomes geometry dependent, resulting in broader domain walls in thicker wires than in thinner ones.

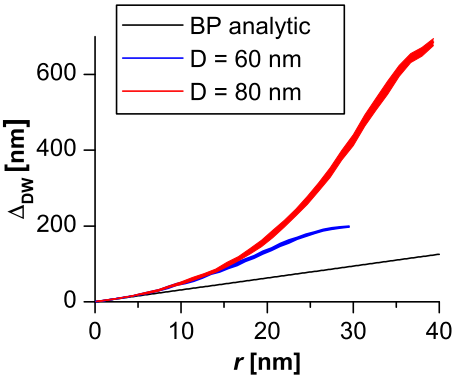


**Figure 9.2** – Azimuthal average of $\gamma$ vs. radial distance to the Bloch point (BP). In the proximity of the Bloch point $\gamma$ is geometry independent and has a value between the estimates for spherical samples by Döring and Pylypovskyi. In the more distant range, a geometry dependence of $\gamma$ can be observed. While we do not obtain any significant difference between the nearest-neighbor and the *Fe-like* approximation, an important a difference is found between the cases of (100) and the (110) orientation of the cylinder axis.

Figure 9.1 shows a comparison between the numerically derived domain wall width in the two wires with different diameter and the result obtained from the analytic Bloch point description in equilibrium (Eq. 4.1). We observe that in the vicinity of the Bloch point the simulated domain wall widths for wires with a diameter of 60 nm and 80 nm are equal and correspond well to the analytically expected result. With increasing distance from the Bloch point position the difference between the analytic and the simulated results becomes more significant. Moreover, we find a strong geometry dependence of the domain wall width, but only in the far range of the Bloch point and, most prominently, close to the wire surface. Note that the domain wall width is independent of the orientation of the cylinder axis with respect to the atomic lattice. Due to this strong dependence of the domain wall width on $r$ , we suggest a modification of its definition for vortex domain walls, namely, to define it by the average value of Eq. 3.2 evaluated on the surface of the sample.

Figure 9.2 displays the equilibrium distribution of $\gamma(r)$ for the two cylinder geometries. It shows that in the case of the wire with 60 nm diameter the angle on the surface is by 1.2° lower than in the close vicinity of the Bloch point, while in the case of the wire with a diameter of 80 nm the angle $\gamma$ is 2.3° higher on the surface than in the vicinity of the Bloch point. The wire diameter influences $\gamma$ mainly in the far range of the Bloch point, while the orientation of the cylinder axis with respect to the atomic lattice influences $\gamma(r)$ in the near range of the Bloch point indicated by the dashed line in Fig. 9.2, even though it should be noted that the deviation between the two orientations (100) and (110) is almost negligible. In general, the numerical results match the analytic value of $\gamma(r = 0) = 76°$ [36] remarkably well considering that the analytic values were derived assuming a spherical shape, whereas the results presented here correspond to cylindrical samples.

# 10
# Depinning of Bloch points

In the early years of Bloch point studies the – from a micromagnetical point of view – vanishing magnetization in the center of a Bloch point gave rise to discussions about its ability to propagate through a sample under the influence of an external magnetic field and, in general, about its mobility. Recent studies, such as those by H.-G. Piao et al [141] and by S. K. Kim and O. Tchernyshyov [142] tried to derive the depinning field of a Bloch point. The former study suffers from the problem that pure micromagnetic simulations were employed with cell sizes in the order of 2 nm, to describe the Bloch point structure, whose core-region, however, has a subnanometer diameter as already derived by Reinhardt in 1973 [37] and discussed in chapter 9. S. K. Kim and O. Tchernyshyov also presented an analytic model treating the lattice potential as a sinusoidal function to emulate an energy barrier, which needs to be overcome to allow for a Bloch point propagation. This appears to be a reasonable approach on the first glance. Nevertheless, in the second part of their article, the authors try to simulate a simple-cubic material with a lattice constant of 1.7 nm with an ordinary micromagnetic code (OOMMFF). This approach appears to be questionable. Note that apart from the limitations of micromagnetic codes and their inaccuracy in treating strongly inhomogeneous structures as discussed in chapter 4, Polonium is the only known element crystallizing in a simple cubic lattice [143].

Realistic simulations need to consider the precise atomic lattice sizes and the crystalline structure. For that purpose we relax a vortex domain wall in the center of the two nanocylinder geometries as introduced in chapter 8 by using a high damping constant of $\alpha = 0.5$. We then apply an external field to the domain wall in axial direction which increases linearly in time. We start at zero field strength and increase the field by 2 mT/ns until a continuous propagation is detected [1]. This field rate

[1] Our simulations have shown that for external fields below 2 mT the size of the domains on either side of the domain wall influence the dynamics, because they generate demagnetizing fields of opposite, but unequal strength. We place the domain wall in the center of the wire for this study in order to avoid such finite size effects.

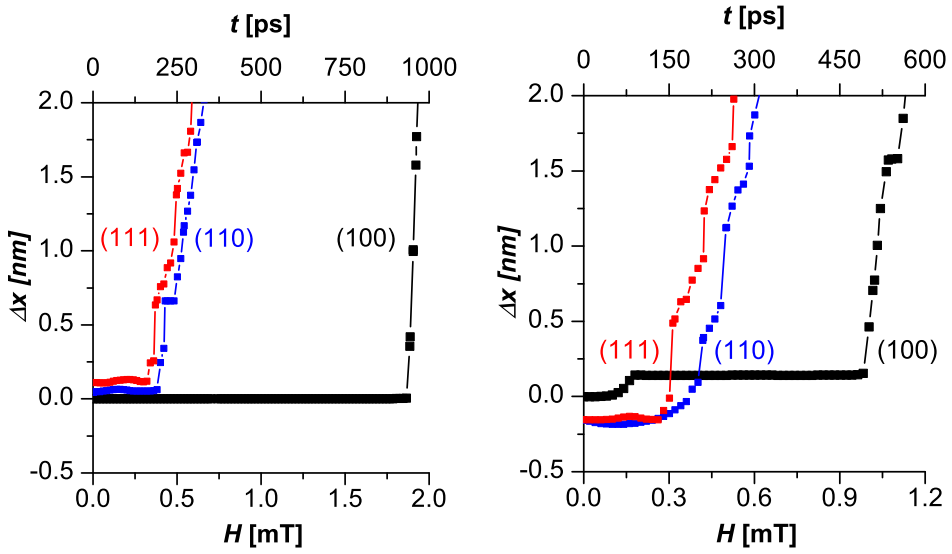


(a) Nearest-neighbor approximation (b) *Fe-like* approximation

**Figure 10.1** – The depinning field of a Bloch point in the middle of the vortex domain wall depends on the approximation of the Heisenberg form of the exchange interaction and on the lattice orientation with respect to the cylinder axis. The labels (100), (110) and (111) represent the lattice direction with respect to the axial direction.

of $2 \times 10^6\,\mathrm{T/s}$ is sufficiently small to ensure an adiabatic change of the magnetic configuration. Figure 10.1 shows the evolution of the axial Bloch point position as a function of the applied magnetic field, correspondingly, as a function of time. We distinguish three different cases, namely those in which the axial direction of the wire corresponds either to the (100), (110) or the (111) lattice direction. Considering the (110) and (111) direction we find depinning fields in the range of 0.3 mT to 0.4 mT for both material configurations. But considering the (100) direction a depinning field of 0.9 mT results in the case of the *Fe-like* material and a significantly larger field of 1.8 mT was found in the case of nearest-neighbor interaction. A systematic study of the depinning field reveals that a strong depinning field occurs mainly along the (100) direction, whereas the depinning field of all other directions is in the range of 0.3 mT to 0.5 mT for both approximations of the exchange interaction.

Besides the depinning field Fig. 10.1(b) shows a second feature of Bloch point pinning: A small field of some 180 µT moves already the Bloch point by half a lattice constant before it is pinned more strongly. This indicates the existence of more than one energy minimum, at which a Bloch point can be located inside of a unit cell of the lattice. Further elaboration of the energy landscape of a Bloch point inside a unit cell might be a fruitful topic of future research.

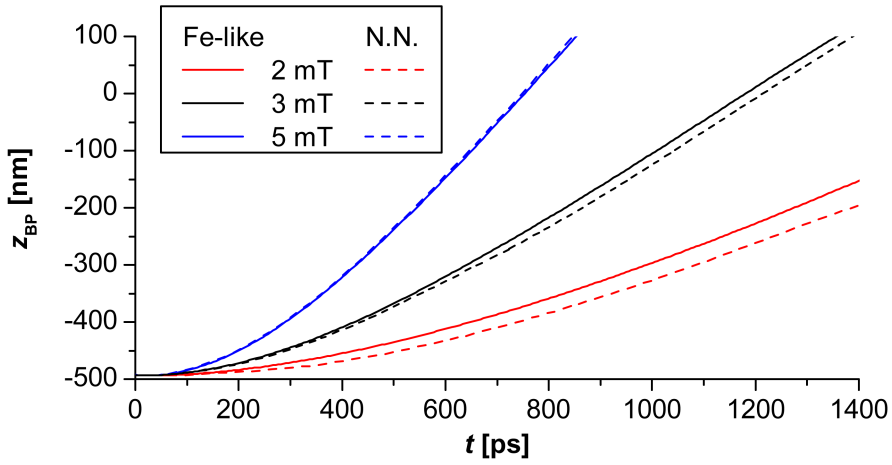


**Figure 10.2** – Axial Bloch point position for three different fields and the two material configurations of nearest-neighbor and *Fe-like* exchange interaction. Only for low external field values the choice of Heisenberg exchange parameters influences the dynamics of the domain wall, whereas for stronger external fields the difference between the sets of exchange parameters becomes negligible.

## 10.1 Differences between nearest-neighbor and *Fe-like* exchange interaction in the dynamic regime

As we found for the depinning fields in the beginning of this chapter, the set of Heisenberg exchange constants influences the depinning field especially for the (100) orientation of the cylinder axis. In order to determine the influence of different choices for the set of Heisenberg exchange constants for the propagation regimes, too, we have performed simulations for selected external field values for the *Fe-like* material parameters as well as for the nearest-neighbor approximation of the Heisenberg exchange constants. Figure 10.2 shows the propagation of the Bloch point along the cylinder axis for three different strengths of the external field. It indicates that with increasing external field the influence of the details of the choice of Heisenberg exchange parameters loses its importance as far as the dynamics is concerned. Only in the low field regime a deviation between the nearest-neighbor model and the *Fe-like* set of Heisenberg exchange parameters can be noticed, which, nevertheless, does not indicate that additional physical effects must be considered. Hence, we conclude that the actual set of the Heisenberg exchange constants influences mainly the depinning behavior of the Bloch point, but not the propagation dynamics in general. Therefore, we restrict our following analysis to the case of nearest-neighbor exchange interaction.

# 11
# Chiralities of vortex domain walls

Chirality dependence is an effect often found in nature. The most obvious difference in chirality (which is also the etymological root of this term) is given by the inequalities of the two human hands, but a more often discussed typical example from biology is the preferred handedness of snails varying from species to species, the majority form of Helix pomatia, better known as Burgundy snail, which is dextral, whereas only a sub-percent ratio of this species has the aberrant sinistral shell shape [144]. Another example is the molecule of glucose, which is found in nature as D-glucose only, whereas the opposite chirality, namely the L-glucose, cannot be absorbed and used by biologic creatures.

In physics, chiralities result from broken rotational symmetry operations, which is also the case for the two above given examples since no rotational operation can

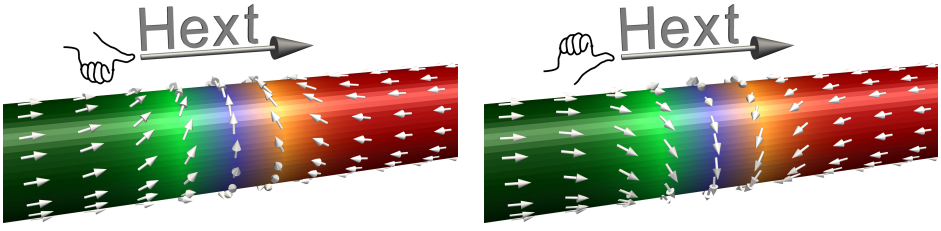


(a) Left handed chirality (b) Right handed chirality

**Figure 11.1** – Sketch of a vortex domain wall with left handed (a) and right handed (b) chirality, respectively. We define the chirality by combining the sign of the in-flow angle $\gamma^{(S)}$ on the surface and the direction of the applied field.

transform the right handed chirality into the left handed one. In the specific case of nanotubes driven by an axial magnetic field we published in earlier works a definition of the vortex domain wall chirality [19] by combining the spiraling direction of the vortex domain wall and the orientation of an applied magnetic field, as sketched in Fig. 11.1. In the field free case a rotation of the system by 180° correspond to a rotation of the coordinate system, which does not influence the system. Yet, with an applied field the symmetry is broken resulting in two different chiralities.

It is known from those vortex domain walls in nanotubes [18, 19] that the dynamics of the right handed chirality in case of head-to-head domain walls and the left-handed chirality in case of tail-to-tail domain walls are more stable under the influence of an external field than the respective opposite ones. Hence, we label the more stable chirality *good chirality* and the less stable one *bad chirality*. The behavior of the different chiralities can be explained by two lines of argumentation, both leading to the same result.

First, in cylindrical structures there exists an intrinsic radial magnetization component in equilibrium [19] caused by the curvature of the sample. For the case of a ferromagnetic nanotube a vortex domain wall can be imagined as a rolled-up transverse domain wall, for which a Walker breakdown is known to occur at elevated domain wall velocities [38][1]. For transverse walls in flat thin strips, a critical angle $\gamma_{crit}^{(W)}$ can be associated with a magnetization component perpendicular to the sample surface and, analogously, a critical angle for cylindrical samples can be represented by a critical radial magnetization component. Due to the intrinsic radial magnetization in the nanotubes, the required change of this component to reach this critical value is smaller for one direction than for the other. Therefore, for head-to-head domain walls a positive radial torque destabilizes the domain wall while a negative one tends to do the opposite. By reducing the inner diameter of a nanotube the geometry of a solid cylinder is obtained, when the inner diameter reaches zero. Also in that case an intrinsic radial magnetization component can be observed in solid cylindrical wires, so that the above argumentation keeps its validity. The intrinsic radial component of the vortex walls in tubes and wires is a magnetostatic effect, which results from the combination of (a) confluent flux lines due to the oppositely oriented adjacent domain walls, (b) the radial symmetry of the structure, and (c) Maxwell's equation $\boldsymbol{\nabla} \cdot \mathbf{B} = 0$.

While the first line of argumentation is more of qualitative nature, the second pathway considers the energy landscape in a more quantitative manner. Calculations of the total energy for nanotubes have been reported by Landeros and Núñez in 2010 [132]. In their article they display in Fig. 4 a slightly higher energy barrier for chirality changes in one direction than in the other. The analytic calculations in chapter 4 point in the same direction for individual Bloch points. Figure 4.2 on page 41 shows the total demagnetizing energy inside of a sphere around a Bloch point in dependence of the in-flow angle $\gamma$. There, the bad chirality corresponds to an equilibrium condition

[1] The Walker breakdown takes place if an external field tilts the magnetization out of plane beyond a critical angle $\gamma_{crit}^{(W)}$. In their original work Schryer and Walkers derived a critical angle of $\gamma_{crit}^{(W)} = 45°$.

starting at a negative angle $\gamma = -75°$. For the increasing direction of $\gamma$ the energy barrier with a maximum at $\gamma = 0°$ is much lower than the one for the decreasing direction of $\gamma$ with a maximum at $\gamma = \pm 180°$.

Focusing now on solid cylindrical wires, the distinction of the type of domain wall as a head-to-head or tail-to-tail wall can be expressed as the polarization $p$ of the Bloch point. The spiraling direction is then described in terms of the in-flow angle $\gamma$. Applying external fields in the axial direction with sign $h$ and strength $H$ and considering the dependence $\gamma = \gamma(t, p, n, H, h)$ with the time $t$, we obtain a total of eight different dynamic pathways. Without the influence of external currents, Maxwell's equations obey space inversion symmetry, so that one can equate

$$\begin{aligned} \gamma(t, p = 1 \quad , n = \pm 1 \quad , H, h = 1 \quad\;\; ) &= \gamma(t, p = \;\; -1, n = \;\; \pm 1, H, h = \;\; -1) \\ \gamma(t, p = 1 \quad , n = \pm 1 \quad , H, h = -1 \quad ) &= \gamma(t, p = \;\; -1, n = \;\; \pm 1, H, h = \;\;\; 1) \end{aligned} \tag{11.1}$$

which reduces the number of dynamic pathways to four. Note that this consideration is only true in the absence of electric currents, since currents break space inversion symmetry.

A cylindrical sample has, in addition to the space-inversion symmetry, a symmetry plane perpendicular to the cylinder axis, due to which the transition $\gamma \to -\gamma$ equals the parity operation $h \to -h$ resulting in

$$\gamma(t, H, p, n, h = -1) = -\gamma(t, H, p, n, h = +1) \quad . \tag{11.2}$$

This consideration further reduces the number of different dynamic pathways to two, which need to be examined individually.

In conclusion, in order to characterize the response of Bloch points and vortex domain walls in nanocylinders on external magnetic fields applied along the cylinder axis only two studies are necessary. One may either vary the two field directions, or the two possible polarities of the domain wall/Bloch point, or change between the two possible spiraling direction of the system. Each of these changes is sufficient to cover all possible pathways of the dynamics.

In the following two chapters dealing individually with the good and bad chirality we will use only head-to-head domain walls corresponding to Bloch point configurations with $p = -1$ and $n = 1$. Therefore, the Pontryagin index of the system is fixed to $Q = -1$. In order to keep the influence of mesh inhomogeneities on the dynamics comparable between the different chiralities, we place the domain wall for all propagation studies at the same initial position, apply the external field in positive axial direction, and distinguish the two chiralities by inverting the rotational sense of the domain wall. This means that the propagation direction is always in the positive axial direction. In equilibrium, the Bloch point has a distance of 500 nm from one end of the wire, which leaves a propagation distance of approximately 3 µm before it has again a distance of 500 nm from the other end of the wire.

# 12
# Bad chirality Bloch points

To investigate and understand the physical properties of Bloch points traveling inside of a vortex domain wall in bad chirality, we performed a systematic study of domain wall/Bloch point propagation and its dependence on the external magnetic field strength. The results presented in this chapter are similar to those obtained for nanotubes [19], which suggests that the effects depend mainly on the cylinder geometry and to a lesser extent on the lattice structure or on the Bloch point. Hence, we restrict our analysis only to one case in which the cylinder axis is oriented in the (100) direction of the lattice, and we moreover only consider nearest-neighbor interaction for the reasons discussed in Sec. 10.1.

Besides the pinning regime (chapter 10), both wire geometries with a diameter of 60 nm and 80 nm, respectively, display three different dynamic regimes. The first regime, in which the domain wall propagation is laminar, can be observed for external field values between the depinning field $H_{\mathrm{dep}}$ and a breakdown field $H_{\mathrm{BD}}$. In the second regime the Bloch point is expelled from the system, which results in a dramatic change of the dynamic behavior. In the third regime a change from the bad to the good chirality takes place. These three regimes will be discussed in detail in the three following sections.

## 12.1 Low field regime

External fields higher than the depinning field $H_{\mathrm{dep}}$ drive the domain wall and the Bloch point with velocities up to approximately 530 m/s and 680 m/s in the 60 nm diameter and 80 nm diameter wire, respectively. Since no qualitative differences have been detected between the two geometries, we focus on the 60 nm diameter wire. Figure 12.1(a) indicates that with increasing external field also the velocity of the Bloch point and domain wall increases. Under the influence of low field strength, such as 2 mT and 3 mT, the Bloch point propagates smoothly after an initial acceleration

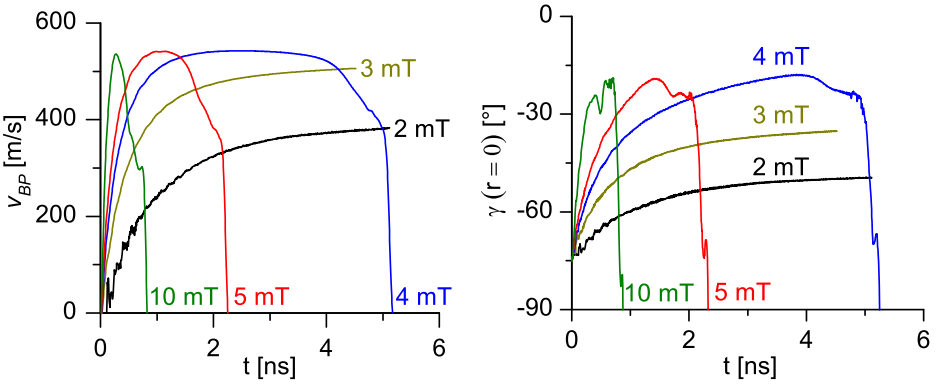


(a) BP velocity evolution for different external fields

(b) $\gamma$ evolution at the BP core for different external fields

**Figure 12.1** – The Bloch point (BP) velocity (a) and in-flow angle $\gamma$ at the vortex core (b) evolution for different external field strengths for the wire diameter of 60 nm. Both quantities show a critical value, at which the domain wall breaks down. This behavior is characteristic for the bad chirality and can be found also for wires with higher diameters, such as 80 nm.

phase in the center of the domain wall. The velocity of the Bloch point and the domain wall is determined at the center of the wire, yielding propagation velocities of 380 m/s and 500 m/s for the 2 mT and the 3 mT simulation, respectively. In both cases a minor acceleration is visible in Fig. 12.1(a) even after 3 ns of propagation time. This can be attributed to finite size effects emerging from the different domain length on both sides of the domain wall, which results in a net demagnetizing field pointing in the same direction as the external field. As shown by Fig. 12.1(b) the in-flow angle $\gamma$ in the vicinity of the Bloch point evolves in a way analogous to the domain wall velocity, indicating a strong correlation between $\gamma$ and the propagation velocity of the domain wall and the Bloch point.

"Heat maps", *i.e.*, continuous color-code representations displaying the contour plot of the inflow-angle $\gamma$ vs. time and distance $r$ to the Bloch point provide a more detailed view on the dynamics of the Bloch point and the surrounding domain wall. For each time step taken during the simulation we calculate the in-flow angle $\gamma$ on the $m_z = 0$ isosurface of the domain wall and perform an averaging process over spherical shells with radius $r$ using the Bloch point position as the center of the sphere. Such a radial and temporal distribution of $\gamma$ is plotted in Fig. 12.2. Those heat maps indicate that $\gamma$ undergoes only a small and very smooth transition during the propagation for the two low-field cases displayed in that figure.

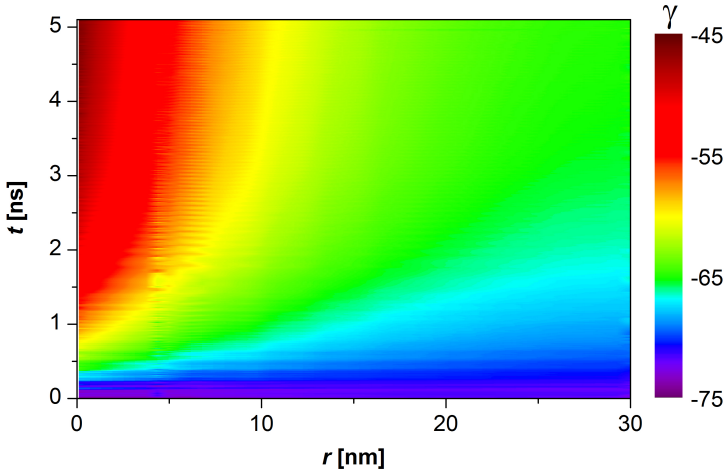


(a) $H = 2\,\mathrm{mT}$

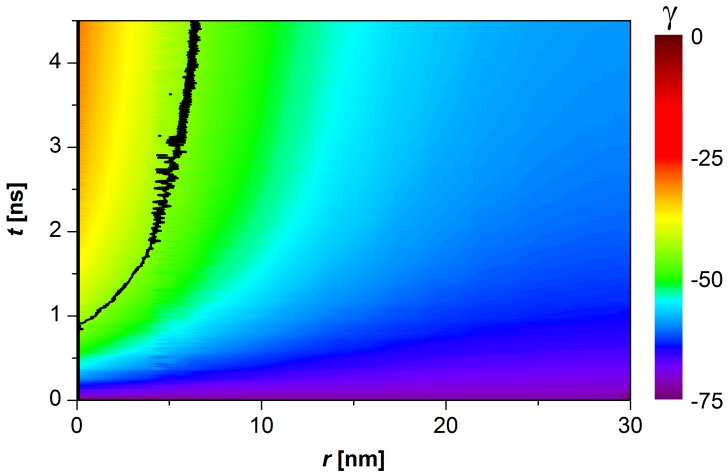


(b) $H = 3\,\mathrm{mT}$

**Figure 12.2** – By calculating the in-flow angle $\gamma$ on the $m_z = 0$ isosurface we determine for each propagation snapshot its radial distribution. The value is obtained by averaging over spheres of constant distance $r$ from the Bloch point. The resulting heat maps show the evolution of the in-flow angle $\gamma$ as a function of time for the two low-field cases of $H = 2\,\mathrm{mT}$ (a) and $H = 3\,\mathrm{mT}$ (b) for the wire diameter of $60\,\mathrm{nm}$. The black line in (b) marks an angle of $\gamma = 45°$. The magnetization configuration remains smooth and stable during the entire propagation process.

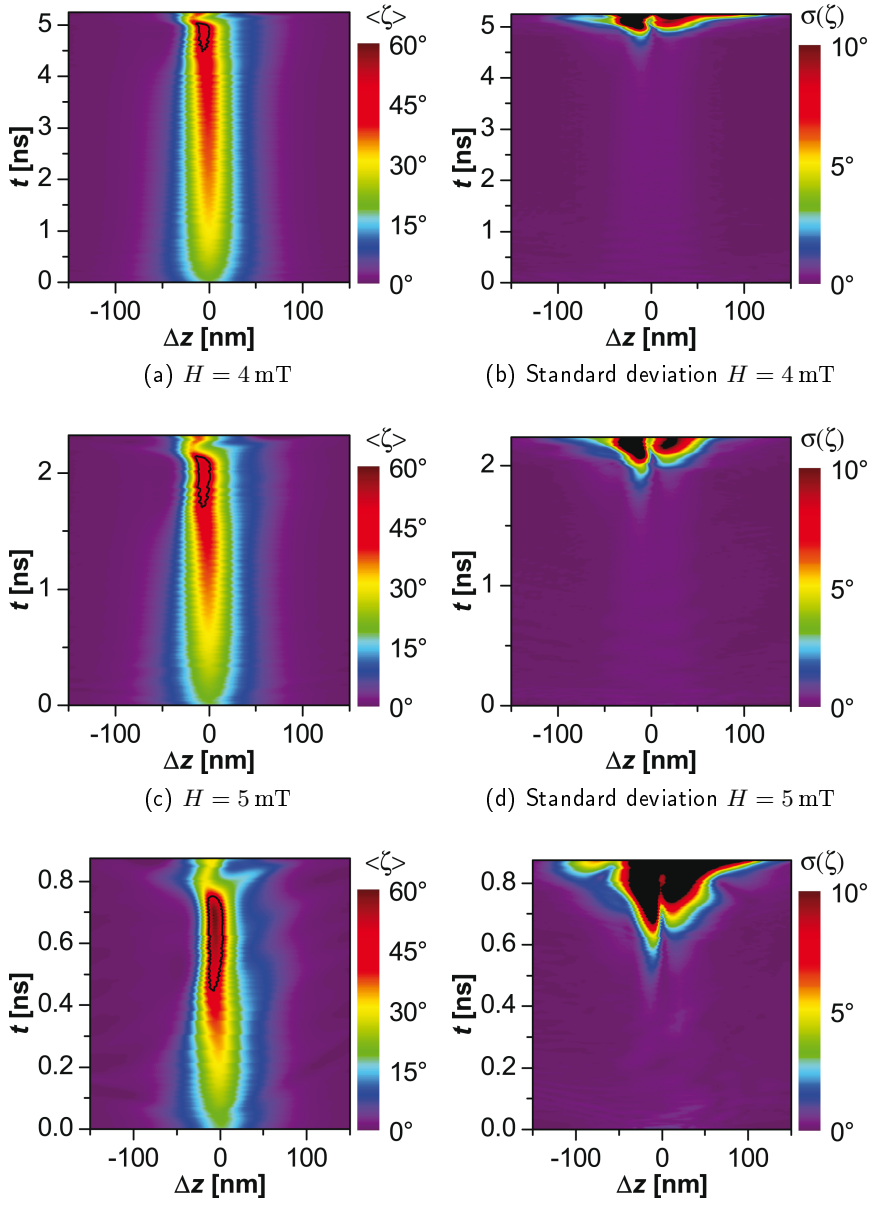


(a) $H = 4\,\mathrm{mT}$ (b) Standard deviation $H = 4\,\mathrm{mT}$

(c) $H = 5\,\mathrm{mT}$ (d) Standard deviation $H = 5\,\mathrm{mT}$

(e) $H = 10\,\mathrm{mT}$ (f) Standard deviation $H = 10\,\mathrm{mT}$

**Figure 12.3** – The azimuthal average of $<\zeta>=\left\langle \arcsin\left(m_r^{(S)}\right)\right\rangle$ on the surface of the sample as a function of the axial distance $\Delta z$ from the Bloch point is shown in (a), (c) and (e) for an applied magnetic field of $4\,\mathrm{mT}$, $5\,\mathrm{mT}$ and $10\,\mathrm{mT}$, respectively, in a wire with $60\,\mathrm{nm}$ diameter. The increase of the standard deviations shown in (b), (d), and (f) indicates the point in time at which the domain wall destabilizes, and the process of Bloch point ejection begins. The solid lines in (a), (c) and (e) indicate the contour line of the critical angle $\zeta_{\mathrm{crit}} = 45°$ in Walker's model [38].

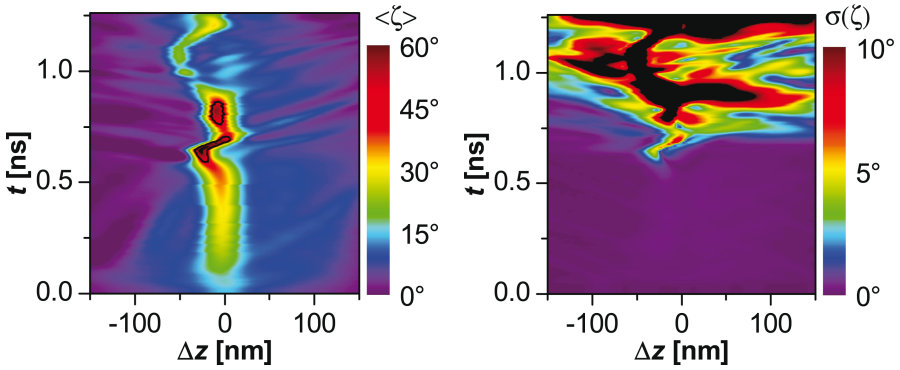


(a) $H = 10\,\mathrm{mT}$ (b) Standard deviation $\sigma(\zeta)$

**Figure 12.4** – Heat maps in analogy to Fig. 12.3 visualize the temporal evolution of the axial dependence of the tilting angle $< \zeta >$ on the surface of the sample and its standard deviation. The heat maps show the case of a wire with $80\,\mathrm{nm}$ diameter for an applied field of $10\,\mathrm{mT}$. The solid lines in (a) indicate the critical angle of $\zeta_{\mathrm{crit}} = 45°$ in Walker's model [38].

## 12.2 Walker breakdown of vortex domain walls

The second propagation regime is characterized by a destabilization of the domain wall as shown in Fig. 12.1(a) for fields of $4\,\mathrm{mT}$, $5\,\mathrm{mT}$ and $10\,\mathrm{mT}$ in the wire geometry with a diameter of $60\,\mathrm{nm}$. From Fig. 12.1 two possible critical quantities of domain wall propagation can be identified. First, the propagation of the domain wall and Bloch point becomes unstable as soon as the velocity reaches a value of $v = 530\,\mathrm{m/s}$. With increasing field the destabilization occurs sooner, but at the same critical velocity. Second, Fig. 12.1(b) indicates that not only the velocity displays a critical value but also suggests the existence of a critical angle $\gamma$, since in the three cases of $4\,\mathrm{mT}$, $5\,\mathrm{mT}$ and $10\,\mathrm{mT}$ the breakdown is triggered when $|\gamma|$ reaches a value of $19°$.

These criteria for the onset of an instability appear to be size-dependent, since we find other critical values in the thicker wire geometry. There, a higher critical velocity and a different critical angle $\gamma$ in the vicinity of the Bloch point was found. In view of these differences, we examined a third possibility to establish universal criteria related to the Walker breakdown [38]. In the one-dimensional case it is known that a purely translational domain wall propagation becomes impossible as soon as the tilting angle $\zeta$ reaches a critical value of $\zeta_{\mathrm{crit}} = 45°$. In order to compare the vortex wall propagation in bad chirality with this Walker breakdown criterion, we consider the magnetization on the surface of the wire in the moving frame centered on the axial position of the Bloch point. Analogous to $\gamma(r = 0)$, the magnetization on the surface of the wire tilts out-of-plane with increasing field and develops a radial magnetization component $m_r^{(S)}$. In the translational propagation of the domain wall the azimuthal symmetry of the system is preserved in good approximation enabling us to average $m_r^{(S)}$ in azimuthal direction, which results in the quantities $< m_r^{(S)} >$

and its standard deviation $\sigma(m_r^{(S)})$. Note that this averaging process involves only vertices located at the same $z$ coordinate, whereas the averaging process for Fig. 12.2 involves an averaging on the $m_z = 0$ isosurface.

The radial magnetization in the cylinder can be related to the tilting angle in a flat strip by $\zeta = \arcsin\left(m_r^{(S)}\right)$. This analogy allows for a good comparability with Walker's model by using the azimuthal averaged quantity $< \zeta >$ combined with the standard deviation $\sigma(\zeta)$. We plot in Fig. 12.3 $< \zeta >$ and $\sigma(\zeta)$ as a function of time $t$ and of the axial distance from the Bloch point $\Delta z$ for applied fields of 4 mT, 5 mT and 10 mT in the 60 nm wire. Fig. 12.4 shows these quantities for the case of an applied field of 10 mT in the 80 nm wire. We mark the contour line $< \zeta >= 45°$ matching the critical angle in Walker's model with a solid black line. From the consideration that in all simulations the standard deviation $\sigma(\zeta)$ increases strongly shortly after $< \zeta >$ has overcome the angle of 45° we conclude that, indeed, the angle $\zeta = 45°$ represents a critical angle, above which a breakdown of the domain wall is triggered.

### 12.2.1 Details of the Walker breakdown process

Figure 12.5 shows characteristic snapshots of the destabilization process for the case of an applied field of 4 mT in the 60 nm diameter geometry on which we will focus in the following. After the field is applied, a short period of acceleration of the domain wall with the Bloch point in its center unfolds, until a velocity of approximately 530 m/s is reached. At that critical velocity the magnetization tilts out of plane at the surface of the sample, as shown in Fig. 12.3(a) and Fig. 12.5(b). Once the critical angle $\zeta_{\text{crit}}$ is reached the azimuthal symmetry of the system is broken and between the Bloch point and the surface a region forms, in which the radial magnetization reaches a maximum, as indicated by the blue $m_z = 0.95$ isosurfaces in Fig. 12.5(c). The amount of surface charges increases locally in the area with maximal radial magnetization, whereas the average value of $\zeta$ decays, resulting in a global reduction of surface charges. This is displayed in Fig. 12.3(e) and can also be recognized in the transition between Fig. 12.5(b) and Fig. 12.5(c). This region is the nucleation point of a vortex anti-vortex pair with equal polarity, whose elements propagate in opposite directions, as shown by the change between Fig. 12.5(c) to Fig. 12.5(e).

A concentration of surface charges accompanied by the formation of a vortex and/or anti-vortex structure is a well-known step of the Walker breakdown in thin strips [39] and in nanotubes [19]. In the case of thin strips a vortex *or* an anti-vortex nucleates on the lateral boundary, whereas a pair creation of one vortex *and* one anti-vortex is necessary in a cylindrical structures due to the absence of a lateral boundary and the need to conserve the winding number as a topological constant. For the case of the Walker breakdown in nanotubes it was observed before that the elements of the vortex anti-vortex pair propagate in opposite directions.

For all external fields we observed in the simulations that the vortex anti-vortex pair stops propagating around the perimeter of the wire when the elements of the vortex anti-vortex pair have reached diagonally opposite positions. Afterwards, the Bloch point starts to approach the anti-vortex until it reaches the sample surface near

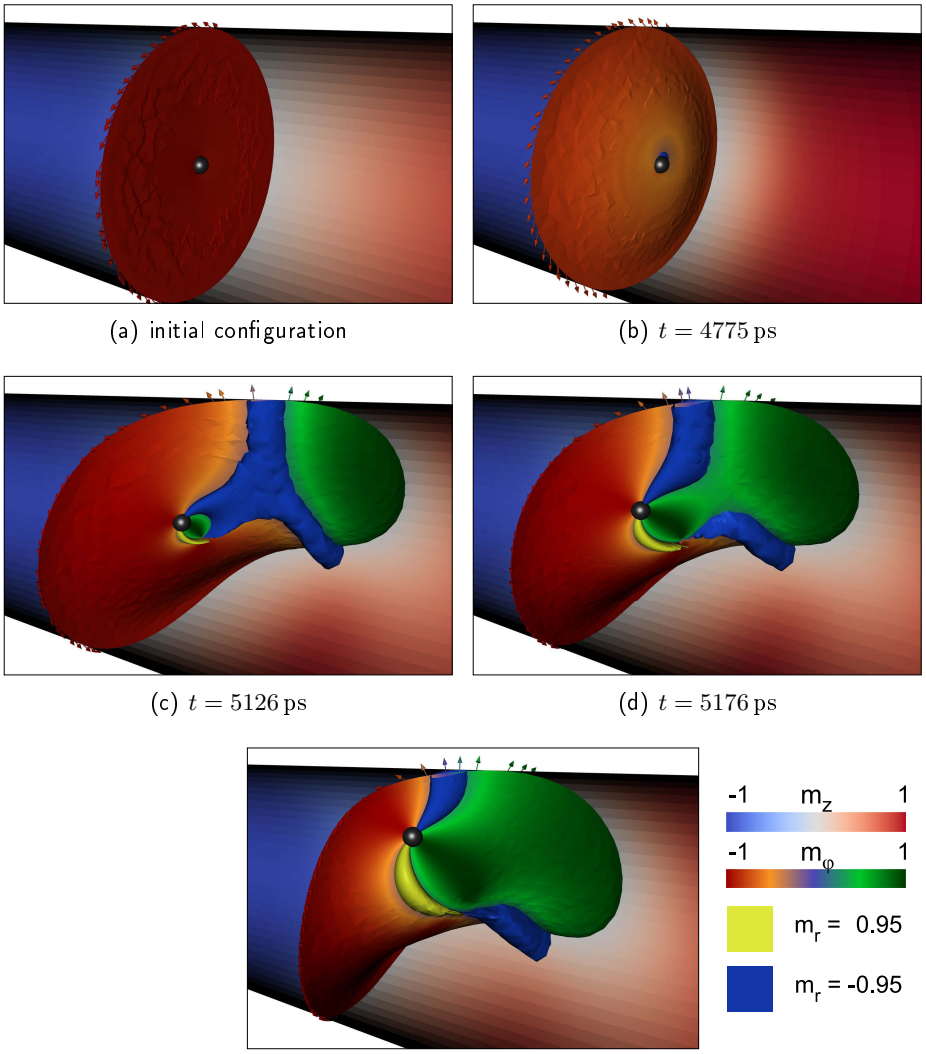


(a) initial configuration (b) $t = 4775\,\mathrm{ps}$

(c) $t = 5126\,\mathrm{ps}$ (d) $t = 5176\,\mathrm{ps}$

(e) $t = 5227\,\mathrm{ps}$

**Figure 12.5** – Steps of domain wall propagation in a moving frame showing a process that is analogous to the Walker breakdown in cylindrical nanowires. The applied magnetic field has a strength of $4\,\mathrm{mT}$ and results first in a metastable propagation of the domain wall with a Bloch point (marked as black sphere) lagging behind by a few nanometers (b). The breakdown starts with the formation of a vortex anti-vortex pair on the surface of the wire. A region with maximal radial magnetization includes also the Bloch point so that a flux channel from one vortex through the Bloch point to the anti-vortex develops (d). After the formation of this channel the Bloch point propagates to the anti-vortex structure and is expelled from the sample.

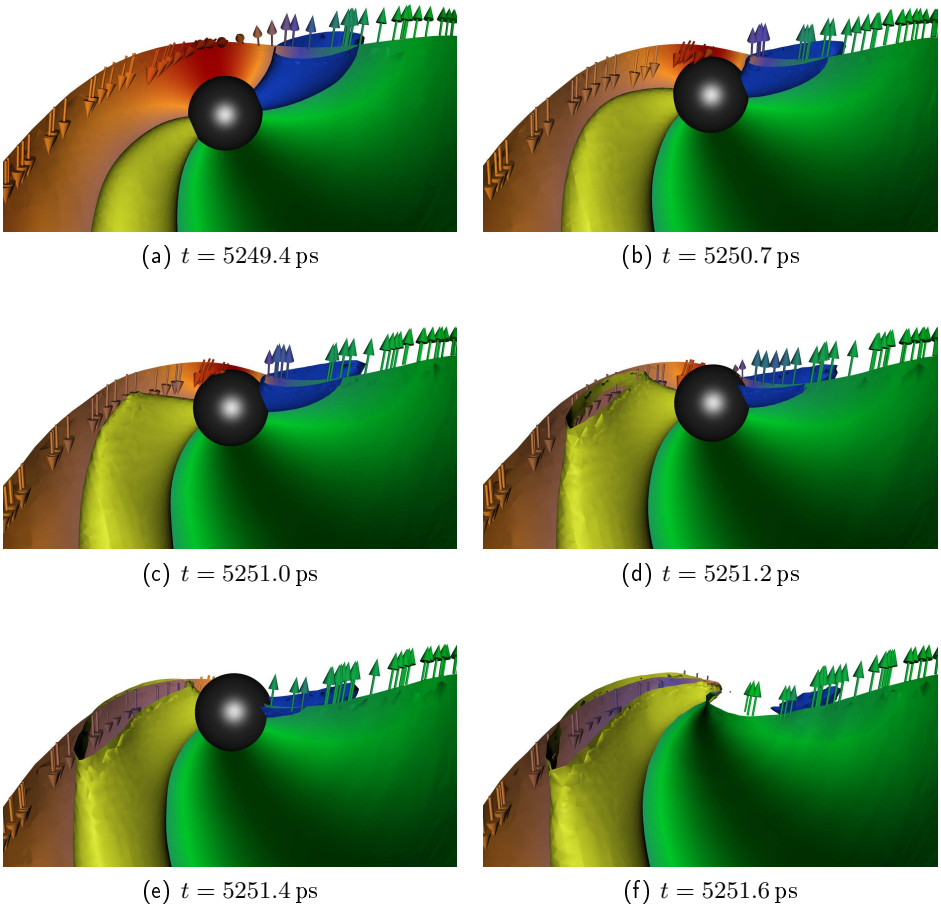

(a) $t = 5249.4\,\mathrm{ps}$ (b) $t = 5250.7\,\mathrm{ps}$

(c) $t = 5251.0\,\mathrm{ps}$ (d) $t = 5251.2\,\mathrm{ps}$

(e) $t = 5251.4\,\mathrm{ps}$ (f) $t = 5251.6\,\mathrm{ps}$

**Figure 12.6** – Process of Bloch point ejection for the case of an applied field of $4\,\mathrm{mT}$. The images show the details of the magnetic structure during the expulsion of the Bloch point. In particular, the process is displayed on the part of the $m_z = 0$ isosurface, where the Bloch point exits the sample. The color codes are the same as in Fig. 12.5. The Bloch point, marked as a black sphere approaches the surface of the wire (a) and thereby generates a strong negative radial magnetization component, as can be seen from the yellow $m_r = -0.95$ isosurfaces (b). The negative radial magnetization results in the formation of an anti-vortex with opposite polarity in comparison to the original anti-vortex, which is visualized by the blue $m_r = 0.95$ isosurface. When the Bloch point leaves the sample the core of the original anti-vortex shrinks ((d) and (e)). Eventually the Bloch point exits the sample, leaving the new anti-vortex structure with inwards pointing polarity behind (f).

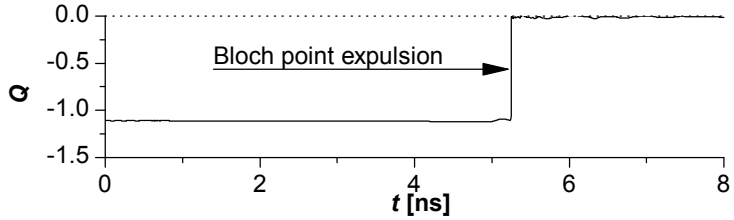


**Figure 12.7** – Temporal evolution of the Skyrmion number Q integrated over the wire surface, but excluding the two ends of the wire. During the last picoseconds in which the Bloch point can be located inside of the domain wall the total Skyrmion number reduces to zero.

the anti-vortex. The snapshots displayed in Fig. 12.6 show the magnetic configuration within the last 2 ps of the Bloch point ejection process. They visualize that the Bloch point causes the nucleation of a new anti-vortex with inwards pointing polarity (yellow isosurfaces in Fig. 12.6) accompanied by a dissolution of the original anti-vortex with outwards pointing polarity (blue isosurfaces in Fig. 12.6).

After the expulsion of the Bloch point the vortex and the anti-vortex approach each other to a certain extent, thereby forming a bent transverse wall. In that configuration the domain wall is stable with an ultra-low propagation velocity in the range of only a few meters per second. This corresponds to a drop by two orders of magnitude compared to the velocity prior to the breakdown. The new domain wall structure circulates around the wire axis with the Larmor frequency. Our simulations indicate that, as long as the external field acts on the domain wall, a nucleation of a new Bloch point and thereby a back transformation of the domain wall to a vortex wall is efficiently suppressed.

### 12.2.2 Walker breakdown from a topological point of view

For an examination of the topological domain wall configuration we calculate numerically the Skyrmion number density

$$q = \left( \frac{\partial \mathbf{m}}{\partial \mathbf{e}_1} \times \frac{\partial \mathbf{m}}{\partial \mathbf{e}_2} \right) \cdot \mathbf{m} \quad , \tag{12.1}$$

where $\mathbf{e}_1$ and $\mathbf{e}_2$ are the two orthonormal unit vectors spanning the local surface element of the wire. By integrating $q$ over the surface of the wire we obtain an estimate of the total Skyrmion number of the magnetic structure according to

$$Q = \frac{1}{2\pi} \int_S q \, \mathrm{d}S \quad , \tag{12.2}$$

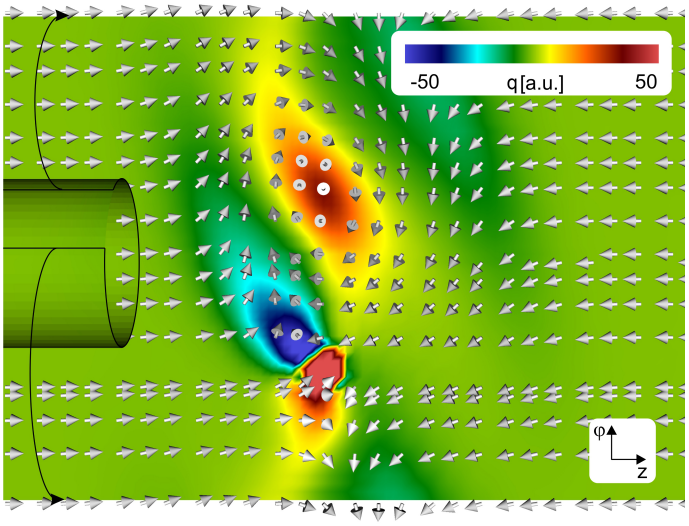


(a) $t = 5.25\,\mathrm{ns}$ at the moment of Bloch point expulsion

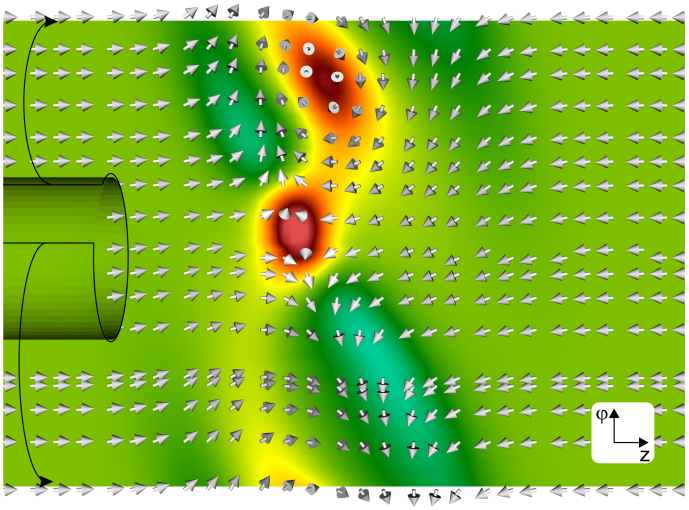


(b) $t = 8\,\mathrm{ns}$, which is $2.75\,\mathrm{ns}$ after the Bloch point expulsion

**Figure 12.8** – Skyrmion number densities on the surface of the domain wall driven by a $4\,\mathrm{mT}$ field in the $60\,\mathrm{nm}$ diameter wire. The snapshots represent the system right at the moment of the Bloch point expulsion (a) and after $t = 8\,\mathrm{ns}$ of simulation time (b). We represent the Skyrmion number densities in a $z, \phi$ coordinate system corresponding to an *unrolling* of the wire surface, which allows for an overview of the complete surface at the domain wall position.

where $S$ is the surface of the cylinder[1]. Near the two caps of the wire vortex-like magnetic patterns are present owing to the reduction of surface charges. Those vortex-like states would have a non-zero contribution to the Skyrmion number $Q$ of the system, which would represent a physically non-important offset. We remove those contributions from the calculation by excluding the area of the first 200 nm near to the wire caps from the integration. For an applied field of 4 mT in the case of the 60 nm wire the evolution of the total Skyrmion number in time is shown in Fig. 12.7. Within the last picoseconds in which the Bloch point resides inside of the wire $Q$ drops from a constant negative value to zero.

We also analyzed the Skyrmion number density distribution for different snapshots during the propagation of the domain wall driven by a 4 mT field. In the equilibrium configuration the negative Skyrmion number density concentrates in an azimuthally symmetric fashion in the axial center of the domain wall. With the nucleation of the vortex anti-vortex pair a region of positive Skyrmion number density develops around the vortex structure. This is in agreement with the well-known topological charge of $Q = 1/2$ of a vortex with positive polarity. Since the simultaneously nucleated anti-vortex also has a positive polarity, yet negative vorticity, its Skyrmion number of $Q = -1/2$ compensates that of the vortex.

As the anti-vortex is approached by the Bloch point (Fig. 12.5(e)) a region with positive Skyrmion number density develops in the close vicinity of the position of the anti-vortex, which is compensated by a decrease of the Skyrmion number density on the remaining surface of the domain wall. Figure 12.8(a) shows the Skyrmion number density distribution on the domain wall surface at the moment of the breakdown, where the vortex with a positive Skyrmion number, the original anti-vortex with negative Skyrmion number next to the new anti-vortex with positive Skyrmion number are visible.

In general, a Bloch point with $Q = \pm 1$ entering a sample nucleates a vortex anti-vortex pair, with each of the created structures carrying half of the Skyrmion number of the Bloch point. Analogously, in our specific configuration, the Bloch point with $Q = -1$ leaving the sample must annihilate or generate two vortex or anti-vortex structures in order to change the total Skyrmion number to $Q = 0$. The first structure is the original anti-vortex carrying $Q = -1/2$ that dissolves, as soon as the Bloch point leaves the sample. Since the system does not contain a vortex with negative polarity that could be dissolved by the Bloch point, it nucleates an anti-vortex with negative polarity carrying $Q = 1/2p \cdot n = 1/2 \cdot (-1) \cdot (-1) = 1/2$. Thereby the system maintains also the topological constant of the winding number, since the winding number of an anti-vortex is independent of its polarity.

As a result, the domain wall has a total Skyrmion number of zero, although it contains a vortex and an anti-vortex each carrying $Q = 1/2$ as well as two regions carrying $Q = -1$ distributed over the domain wall. Figure 12.8(b) shows the Skyrmion number density distribution 2.75 ns after the breakdown, where not only the vortex and anti-vortex structure, but also the delocalized regions of negative Skyrmion number density are visible. Hence, the final configuration of the bent transverse wall

[1] In case of an integration over the surface of a sphere the prefactor would be $1/4\pi$

with a global Skyrmion number of $Q = 0$ is formed by a quadrupole configuration of regions with different non-zero Skyrmion numbers.

## 12.3 Chirality change

The third propagation scheme of the bad chirality is reached for external field values higher than $(25 \pm 5)$ mT in the case of a wire with a diameter of 60 nm. The processes occurring in this high-field regime are discussed in this section. Since a low field strength would lead to an expulsion of the Bloch point, we apply the external field with a steep slope, so that it reaches its maximum value within 20 ps. This non-adiabatic field application with a high final field strength triggers a switching of the domain wall chirality from the bad to the good one. As a typical example of the chirality switching process we discuss the case of an applied field of 30 mT.

We examine the process from two different perspectives: first, we consider snapshots of the magnetization configuration especially on the $m_z = 0$ isosurfaces as shown in Fig. 12.9, which are color-coded according to the $m_\phi$ component. The increase of radial magnetization is faster in the vicinity of the Bloch point than on the surface of the wire. Figure 12.9(d) and 12.9(e) indicate that the vortex anti-vortex channel develops only in the final stages of the process, when the chirality switching process is mostly finished. After less than 800 ps the switching process is completed and the Bloch point propagates in the center of the vortex wall in good chirality, as shown in Fig. 12.9(f).

The second viewing angle is based on the axial and temporal evolution of the average tilting angle $< \zeta >$ on the surface of the wire relative to the axial Bloch point position. Figure 12.10 indicates that even though $< \zeta >$ reaches the critical angle of 45°, the chirality changes before the Bloch point is expelled. As soon as the good chirality is reached the system stabilizes again and spin wave tails develop in front of and behind the propagating unit of Bloch point and domain wall, as can be seen from Fig. 12.10(a).

From these observations we draw the conclusion that the process of Bloch point ejection is subject to inertia, and that due to this inertia a sufficiently rapidly applied field can switch the bad chirality to the good chirality. It might be possible to connect the inertia of the system with the mass [64] of the Bloch point, which could be a subject of future studies.

## 12.4 Summary

In this chapter we discussed the vortex domain wall and the Bloch point dynamics in ferromagnetic cylindrical wires of different diameters driven by an external magnetic field in bad chirality. We showed that in addition to a pinning regime, where the Bloch point remains pinned at a lattice site prohibiting a propagation of the domain wall, there exist three different propagation modes in bad chirality. The first one

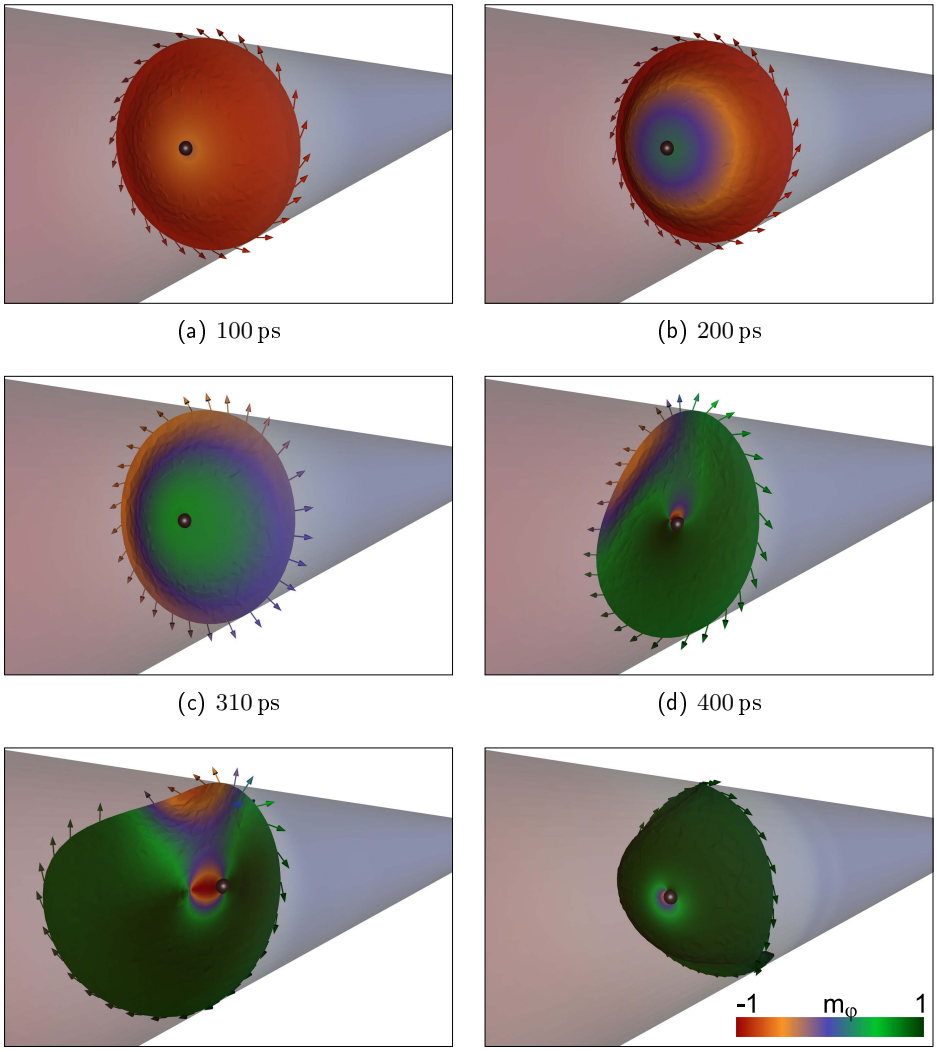


(a) 100 ps (b) 200 ps

(c) 310 ps (d) 400 ps

(e) 500 ps (f) 800 ps

**Figure 12.9** – The application of an external field larger than $20\,\mathrm{mT}$ results in a chirality switch. The Bloch point lags behind the domain wall center as can be seen by the deformation of the $m_z = 0$ isosurface (a), a homogeneous rotation (b) and (c) results in a sizable radial component of the magnetization at the boundary of the sample so that only a small channel with maximum radial magnetization develops (d), which closes (e) very quickly when the chirality switching process (f) is accomplished.

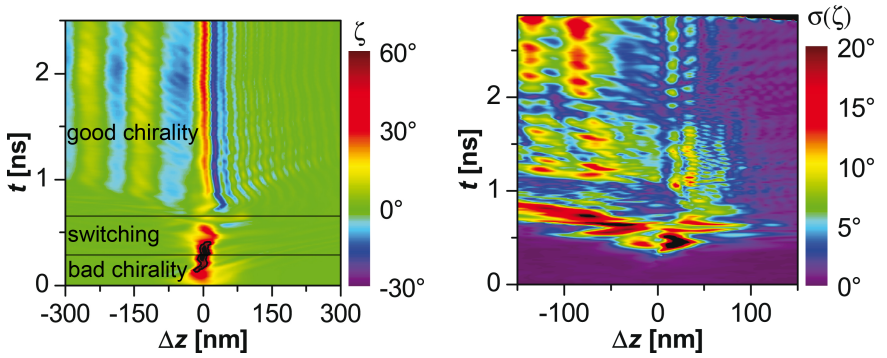


(a) $H = 4\,\mathrm{mT}$ (b) Standard deviation $H = 30\,\mathrm{mT}$

**Figure 12.10** – "Heat map" of the temporal evolution of the $z$-dependent tilting angle $< \zeta >$ in the case of an applied field of $30\,\mathrm{mT}$ in the $60\,\mathrm{nm}$ diameter wire. The solid line indicates the contour line corresponding to the critical angle $\zeta_{\mathrm{crit}} = 45°$ in Walker's model. The chirality changing process terminates after $0.8\,\mathrm{ns}$, after which spin wave tails develop in front of and behind the Bloch point as it is characteristic for the supermagnonic propagation regime in good chirality.

is a low field regime characterized by a steady state propagation with a maximum out-of-plane tilting angle $< \zeta >$ on the surface of the wire below $45°$.

In the second regime $< \zeta >$ reaches and overcomes $45°$, thereby triggering an expulsion of the Bloch point. The resulting domain wall is of transverse type carrying an effective Skyrmion number of zero, although it contains a vortex and an anti-vortex structure each carrying $Q = 1/2$ as well as a broad region of negative Skyrmion number density that compensates the topological charge of the vortex and the anti-vortex. The propagation velocity of the transverse domain wall spiraling with Larmor frequency is two orders of magnitude lower than the original vortex wall velocity.

We also demonstrated that a switch from the bad to the good chirality can be triggered if a sufficiently high field is applied with a steep slope. In this third regime the inertia of the Bloch point prevents its ejection and enables the system to change the chirality.

# 13
# Good chirality Bloch points

In the second chirality, the good chirality, the compound of domain wall and Bloch point shows a high stability without experiencing an instability such as the Walker breakdown. Hence, velocities in the range of the magnonic limit can be reached in this chirality, a phenomenon which was reported before only for vortex domain walls in nanotubes [18].

Figure 13.1 visualizes the dependence of the velocity versus the external field for both wire diameters (60 nm and 80 nm). In addition to the pinning regime, we find for this chirality four different propagation regimes: one for submagnonic and three for supermagnonic velocities. The three supermagnonic velocity regimes consist of, first, a laminar propagation (green part in Fig. 13.1), in which the Bloch point propagates only in axial direction and remains in the center of the nanowire, second, an oscillatory propagation (yellow area in Fig. 13.1), in which the Bloch point starts to oscillate around the cylinder axis, but remains attached to the domain wall, and third, a turbulent regime (red part in Fig. 13.1), in which a detachment of the initial Bloch point from the domain wall is accompanied by a Bloch point pair creation.

The plots in Fig. 13.1 for the two wire diameters differ strongly concerning the value of the field ranges which correspond to different propagation regimes. The values of total energy stored in the magnetic systems in equilibrium can provide an explanation for this observation: in the thin wire the total magnetic energy, which is the sum of demagnetizing and exchange energy, yields approximately 392 eV, whereas in the thicker wire the total energy has a value of 775 eV, *i.e.*, about a factor of two higher than in the thin wire. Since the main energy contribution of a Bloch point stems from a geometry independent volume around its core yielding an essentially constant term, the effect of the Bloch point on the domain wall propagation can be expected to be at least a factor of two lower in the thicker wire than in the thinner one, which coincides at least qualitatively well with Fig. 13.1. The further factor of different transition fields that were obtained from the simulations for the two wire diameters might be attributed to the different domain wall width during the propagation.

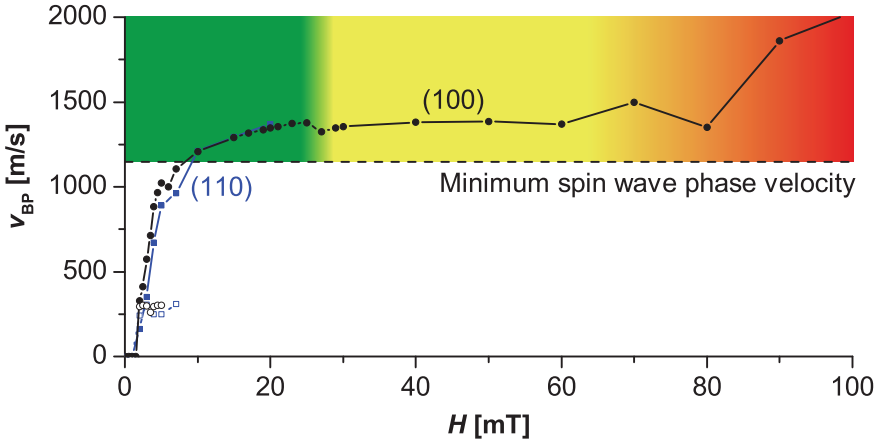


(a) Bloch point velocity vs. field in a $60\,\mathrm{nm}$ diameter wire

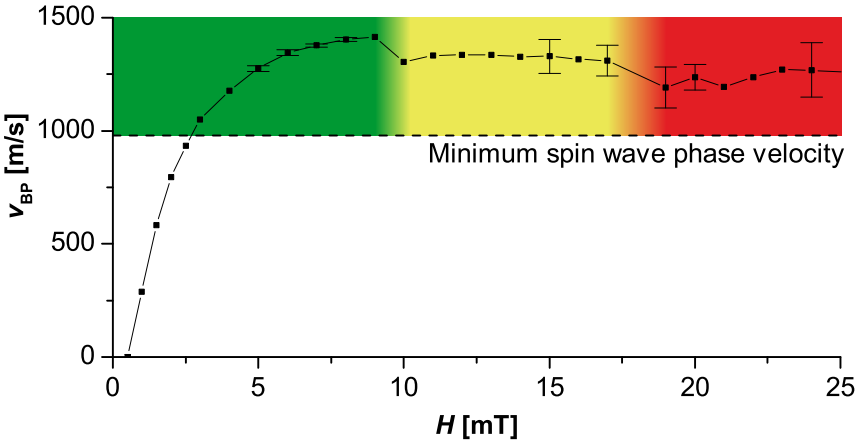


(b) Bloch point velocity vs. field in a $80\,\mathrm{nm}$ diameter wire

**Figure 13.1** – Bloch point velocity vs. externally applied field in wires with diameters of $60\,\mathrm{nm}$ (a) and $80\,\mathrm{nm}$ (b) diameter, respectively. We distinguish the different supermagnonic regimes of laminar, oscillatory and chaotic Bloch point propagation by different colors from green over yellow to red.

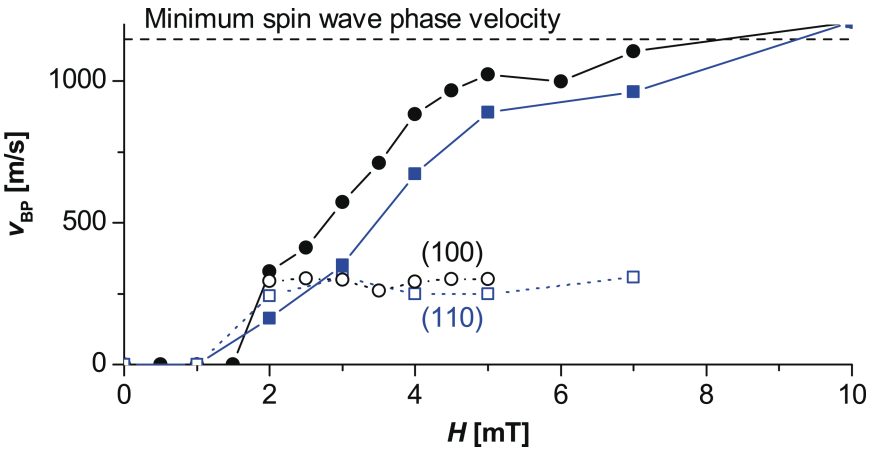


**Figure 13.2** – The Bloch point velocity as a function of the external field in a wire with a diameter of 60 nm shows different propagation behaviors depending on the orientation of the cylinder axis with respect to the atomic lattice. In both orientations shown above two metastable configurations can be distinguished. First, an almost field-independent velocity indicated by empty symbols, and second, a configuration for which the velocity increases monotonously with the external field.

As we have shown in chapter 10 the pinning of a vortex domain wall in a nanowire is dominated by the Bloch point in its center. To initiate the motion an energy barrier must be surmounted that depends on the orientation of the cylinder axis with respect to the lattice. Analogously, the cylinder axis orientation with respect to the lattice plays a role for the submagnonic propagation regime, as can be seen from Fig. 13.1(a). In Sec. 13.1 we describe in detail the effects that distinguish between the orientation of the cylinder axis in (100) and in (110) direction. In contrast to this, in the supermagnonic propagation regimes, the axis orientations seems to be irrelevant, as can be seen in Fig. 13.1(a). For this reason we only focus on the (100) orientation of the cylinder axis in the parts where these propagation regimes are discussed (Sec. 13.2 to Sec. 13.4).

Note that all results discussed in this chapter were obtained by using nearest-neighbor exchange interaction for the reasons explained in Sec. 10.1.

## 13.1 Submagnonic propagation

External fields higher than the depinning field result in an acceleration of the joint system of Bloch point and vortex wall. In the low field regime the lattice structure influences the propagation process shown in Fig. 13.2, which displays the same data as Fig. 13.1, but focuses on the submagnonic velocities, which are velocities below the minimum spin wave phase velocity. As can be seen in Fig. 13.2 for both orientations and for basically each field value two different metastable modes of steady-state prop-

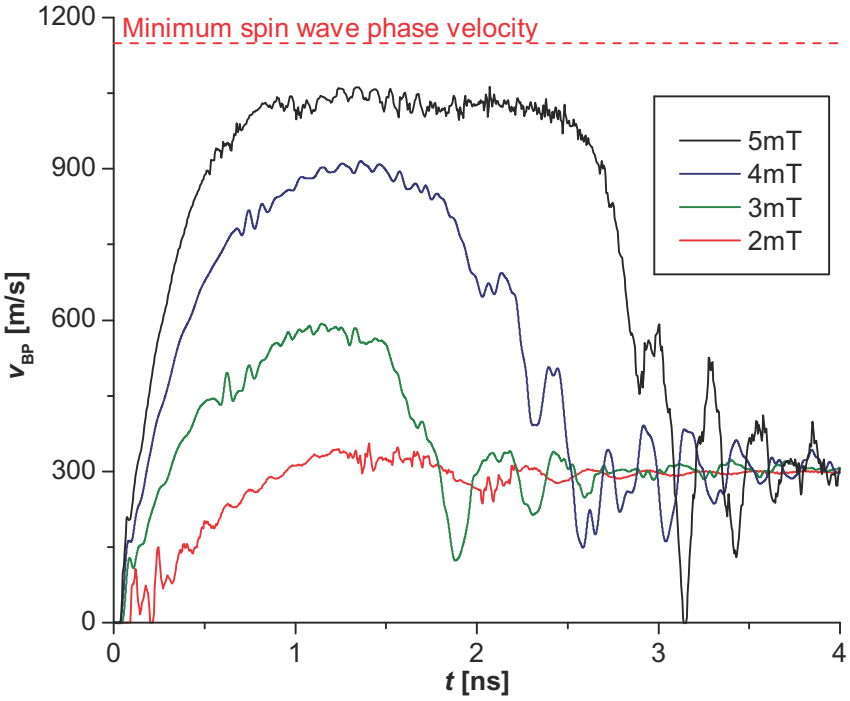


**Figure 13.3** – Evolution of the Bloch point velocity with time in the low field regime (below the magnonic limit) for a wire with a diameter of $60\,\mathrm{nm}$ and with the cylinder axis oriented in (100) direction.

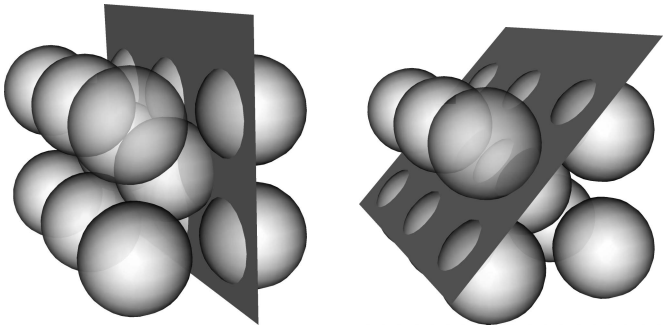

(a) $m_z = 0$ isosurface perpendicular to (100) direction

(b) $m_z = 0$ isosurface perpendicular to (110) direction

**Figure 13.4** – Sketches of the two orientations of the $m_z = 0$ isosurface which are most favorable in view of the exchange energy in the case of a bcc lattice. In average the largest distance from the magnetic moments can be achieved with the alignment shown in (b).

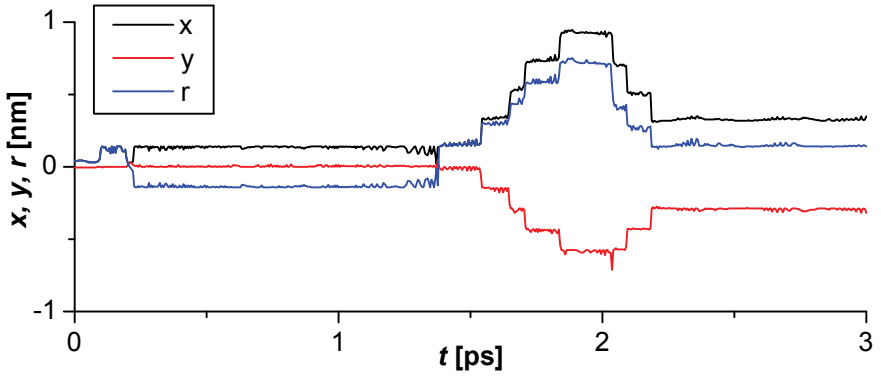


**Figure 13.5** – Deflection of the Bloch point in the case of a good chirality domain wall driven by a 2 mT external field. The excitation is step-like and it adopts the high probability density planes of the Wigner-Seitz cell (see Chap. 14).

agation can develop. The velocities of the first mode indicated by filled symbols in Fig. 13.2 increase monotonously with the external magnetic field. These stationary velocities develop after an initial acceleration period, as shown for different fields in Fig. 13.3 for the (100) axis orientation. For low fields the high velocities only result in a weakly pronounced peak, but for increasing external fields the high velocities stabilize in a plateau that becomes longer with increasing field strength. For fields higher than 6 mT we are not able to determine whether the plateau ends, because the domain wall reaches the end of the wire before a transition of the propagation mode sets in.

Below the minimum spin wave phase velocity we observe repeatedly in the simulations a transformation of the Bloch point and domain wall resulting in a change of velocity. In this second mode of propagation the velocity is constant with values between 250 m/s and 300 m/s for a range of several milli tesla. Without an applied field, during the acceleration period and in the high velocity propagation phase the $m_z = 0$ isosurface orientation is perpendicular to the axis direction, whereas in the second mode of propagation the isosurface tilts to a different orientation. Figure 13.4 sketches the preferred isosurface orientations inside the bcc lattice. Considering that the strongest change in magnetic orientation is present in the vicinity of the $m_z = 0$ isosurface, we attribute the tilting to a tendency to maximize the distance between the isosurface and the location of the magnetic moments at atomic lattice sites in order to minimize the exchange energy. The tilting process breaks the azimuthal symmetry, which results in an energy increase as the domain wall area effectively becomes larger. In the thicker wire the tilting has not been observed, from which we draw the conclusion that either the energy barrier between the two propagation phases is significantly higher, or the break of symmetry would require more energy than the system can gain by the tilting of the $m_z = 0$ isosurface in the vicinity of the Bloch point.

All simulations addressing the submagnonic propagation regime show a radial

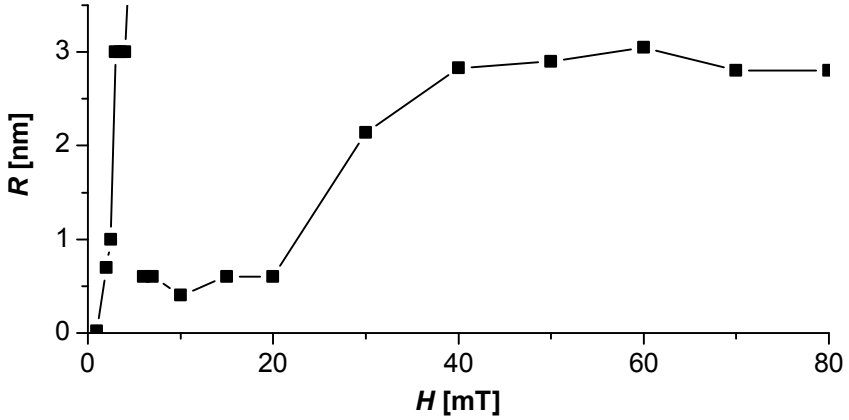


**Figure 13.6** – Maximum Bloch point deflection from the center of the wire with 60 nm diameter. The low-field region corresponds to submagnonic propagation. The strong drop of the radial deflection at $H = 6\,\mathrm{mT}$ marks the transition from the submagnonic to the supermagnonic propagation regime. The change from low deflections to those in the range of 3 nm for external fields between 20 mT and 30 mT corresponds to the transition from the laminar to the oscillatory propagation regime.

deflection of the Bloch point, which starts after 1 ns and reaches its maximum within another nanosecond. Nevertheless, the Bloch point neither lags behind nor propagates in front of the domain wall significantly. A field of 2 mT, *e.g.*, results in a deflection of 0.9 nm, which drops to 0.3 nm within 250 ps as shown by Fig. 13.5.

The figure indicates that the Bloch point deflection is governed by jumps inside the atomic lattice, which will be elaborated more precisely in chapter 14. The maximum deflection of a Bloch point reaches 5 nm for an applied field of 4 mT, but also for fields of 5 mT deflections up to 3 nm can be observed.

Figure 13.6 shows a diagram summarizing the observed deflection radii during the propagation versus the applied field. It indicates that the deflection radius increases as the field increases in the low field regime, but drops below one nanometer for external fields higher than 6 mT. Therefore, we conclude that at a field of 6 mT a qualitative change, a transition of the propagation regime occurs.

## 13.2 Laminar supermagnonic propagation

In the case of the 60 nm wire fields larger than 6 mT drive the Bloch point together with the domain wall at a speed $v > 1150\,\mathrm{m/s}$, which matches the minimum spin wave phase velocity. As the external field increases, the maximum velocity of Bloch point and domain wall increases further, too, until it reaches a maximum at approximately $v \approx 1300\,\mathrm{m/s}$. Once the domain wall velocities are above the minimum spin wave phase velocity, different orientations of the cylinder axis with respect to the atomic

lattice have no detectable influence on the result. We find the same behavior also for 80 nm diameter wires, for which a field of 3 mT is sufficient to drive the Bloch point and the domain wall with supermagnonic velocities. It is noteworthy that the maximum velocity of 1400 m/s is very similar to that one in 60 nm diameter wires. Furthermore, the factor of two between the minimum field strength necessary to drive the domain walls with supermagnonic velocities in the two wires of different diameters matches well with the considerations described previously in this chapter on the energetic impact of the Bloch point on the total domain wall.

Since the propagation is of supermagnonic type, spin wave tails develop in front of and behind the domain wall. Such spin wave tails correspond to those modes of the dispersion relation whose phase velocity equals the domain wall velocity [40]. During the propagation the Bloch point remains axially centered inside the domain wall and is radially deflected by a few lattice constants without a tilting of the $m_z = 0$ isosurface. In analogy to hydrodynamics this propagation regime can be labeled as laminar, due to the steady state and the non-turbulent propagation of the Bloch point.

## 13.3 Oscillatory supermagnonic propagation

At external fields higher than 21 mT in wires of 60 nm diameter and 10 mT in the case of wires with 80 nm diameter the Bloch point deflects during the propagation much stronger than in the laminar propagation regime. The transition region is displayed in Fig. 13.6 between 21 mT and 25 mT in terms of the deflection radius. As a characteristic example of this propagation regime, Fig. 13.7 shows the time evolution of the deflection, namely the $r$, $x$, and $y$ component of the Bloch point position for an applied field of 30 mT. For better visibility we show a magnified view on the time interval between 600 ps and 800 ps in Fig. 13.7(b), which indicates an oscillation of the Bloch point along a spiral trajectory. The most dominant frequency is $f = 38.4 \pm 0.8$ GHz, but a careful analysis with a Fourier transform of $m_x + \imath m_y$ reveals also a frequency of $f = -14.5 \pm 1.5$ GHz. Those frequencies match perfectly the frequency of the two spin wave tails, where the lower frequency can be attributed to a spiraling opposite to the direction of the 38.4 GHz mode.

Unlike the propagation regimes found for lower external fields, the Bloch point now lags behind the domain wall. With increasing external field the distance between the Bloch point and the domain wall increases, too, as shown in Fig. 13.8. As the center of the domain wall in axial direction we use the average $m_z = 0$ isosurface position on the surface of the sample, in analogy to our modified definition of domain wall width (chapter 9).

The transition from the laminar to the oscillatory supermagnonic propagation

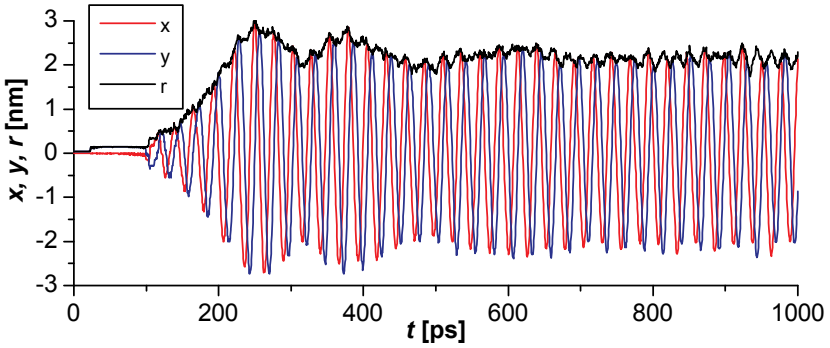


(a) Evolution of the spontaneous Bloch point oscillation

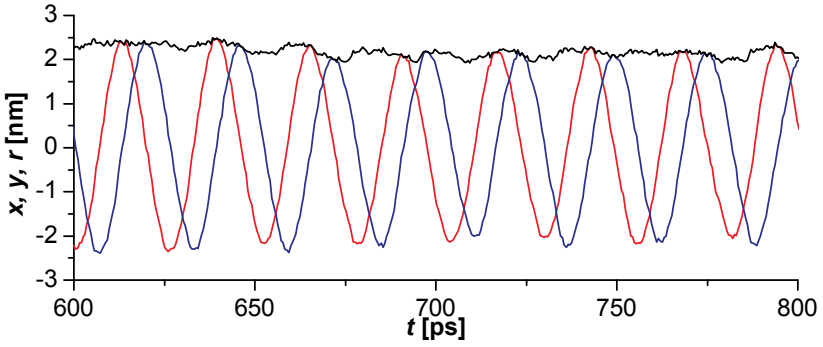


(b) Magnified view on a $200\,\mathrm{ps}$ time interval

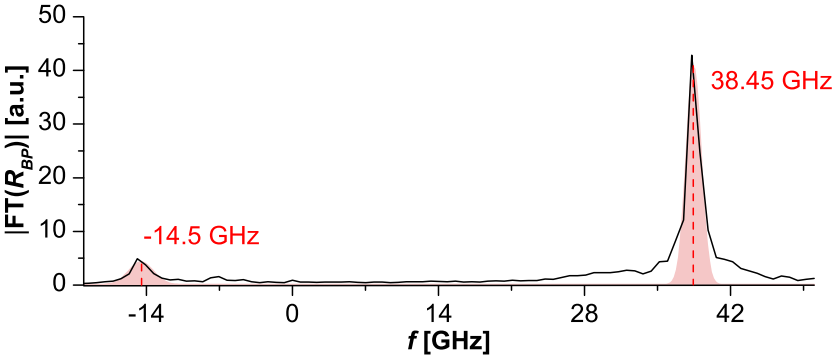


(c) Fourier transform of the Bloch point position

**Figure 13.7** – Diagram displaying the two Bloch point position components perpendicular to the axial directions, namely the $x$ and $y$ component, for the case of the $60\,\mathrm{nm}$ wire with an applied field of $30\,\mathrm{mT}$. A circular oscillation around the cylinder axis is immediately recognized. A Fourier transform of those polar positions reveals two peaks at $14.5\,\mathrm{GHz}$ and $38.45\,\mathrm{GHz}$ in opposite directions. The two frequencies correspond to those of the spin wave tails excited by the propagating domain wall.

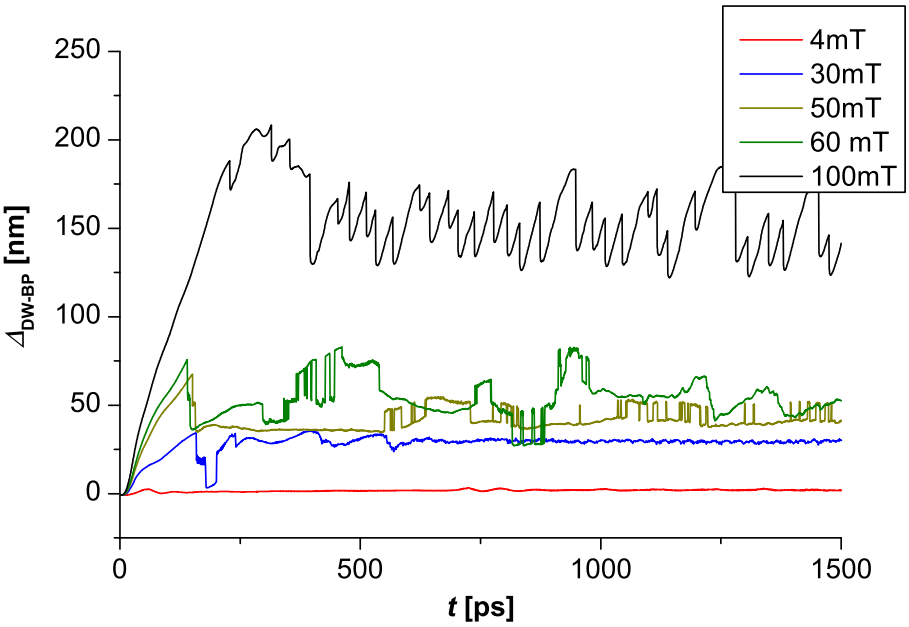


**Figure 13.8** – Time evolution of the distance between the Bloch point and the domain wall center on the surface of the sample. In the submagnonic regime, *e.g.*, at an external field of 4 mT, the Bloch point does not lag behind the domain wall. In the supermagnonic regime the distance between Bloch point and domain wall increases with time resulting in the pair creation and annihilation regime depicted by the case of a 100 mT field.

regime can be understood in terms of Eq. 4.34, which we recall here

$$\begin{aligned} v_z &= v_{\max}\frac{\sin(\gamma)+4p\sin(\gamma)\cos(\gamma)}{\Gamma}+\frac{9}{24}\alpha\pi v_\phi \\ v_{\max} &= \frac{2}{15}\Gamma M_s R\mu_0\gamma_0 \\ \Gamma &= \max\left(\sin(\gamma)+4p\sin(\gamma)\cos(\gamma)\right)\approx 2.736 \quad . \end{aligned} \tag{13.1}$$

Equation 13.1 incorporates the maximum velocity $v_{\max}$ representing the limiting velocity, with which a Bloch point can propagate in $z$ direction without additional oscillations. From the simulations we draw the conclusion that this critical velocity is $v_{\max} = 1300\,\mathrm{m/s}$. Higher fields result in a change of the inflow-angle $\gamma^{(S)}$ on the surface, due to which the inflow-angle at the Bloch point center adjusts, too. The modified $\gamma(r=0)$ can get compensated according to Eq. 13.1 by an angular velocity of the Bloch point, which opens a channel for a coupling to the spin wave tails: the strong magnetic inhomogeneity of a Bloch point is an important source of spin wave excitation [40] and therefore of the spin wave tails. However, in analogy to Newton's third law, the excitation of spin waves results also in an excitation of the Bloch point

itself. The domain wall structure is slightly destabilized, which results in a spatial elongation of the domain wall with the Bloch point lagging behind and the domain wall at the surface of the wire propagating beforehand. In terms of Döring's definition of domain wall mass [64], the deformation of the domain wall increases the mass, which prohibits any further acceleration and the propagation regime stabilizes over a broad range of external fields.

It is evident from Fig. 13.1 that the oscillatory regime extends over a broader range of external fields in the case of 60 nm diameter wires than in 80 nm diameter case. To understand this strong difference the energy consideration about the influence of the Bloch point on the total domain wall mentioned in the beginning of the chapter for the equilibrium configurations are not sufficient. In the thicker wire the domain wall stretches over a much longer distance than in the thinner wire, which diminishes the overall influence of the Bloch point on the remaining domain wall. Hence, the energy argumentation remains qualitatively valid.

The resulting buffering of the velocity over a broad range of external fields makes the domain wall propagation insusceptible to perturbations of the external field. Due to this property of constant domain wall velocity the oscillatory Bloch point propagation might represent an advantageous feature for domain-wall based magnetic storage [17] or logic devices [145].

## 13.4 Turbulent Bloch point propagation

In 2004, R. Hertel and J. Kirschner approached the dynamics of vortex domain walls micromagnetically [41, 63]. They found that the propagation of vortex walls lead to a strong elongation of the domain wall, which can result in the nucleation of Bloch point pairs causing the generation of a "drop" behind the domain wall. Inside of such a drop one Bloch point of the newly nucleated Bloch point pair and the original Bloch point can be found. Similar results were recently reproduced by Piao et al. [141]. Even though the application of pure micromagnetic theory for Bloch point simulations can lead to inaccurate results, the drop-formation regime could be reproduced also by our multi-model simulations for the geometry with a diameter of 60 nm. In the 80 nm diameter we would expect also such a drop formation, but due to the limited amount of memory of the GPUs it was not possible to introduce a sufficient amount of multimodel spheres in order to simulate the drop formation properly.

At a specific critical field the distance between the Bloch point and the domain wall reaches some hundreds of nanometer as shown in Fig. 13.8. Between the Bloch point and the domain wall position a superposition of those spin wave tails which propagate ahead of the Bloch point, and those which travel behind the domain wall center are present. Our simulations reveal that micromagnetic inhomogeneities arising from the spin waves serve as nucleation sites, at which exchange energy accumulates. Figure 13.10 shows a series of snapshots during the propagation with an applied field of 100 mT, which serves as a typical example for the mode of propagation in this regime. For the same field strength the time evolution of the Bloch point position along the $z$-axis is displayed in Fig. 13.9. We observe in Fig. 13.10(b) that the generation of

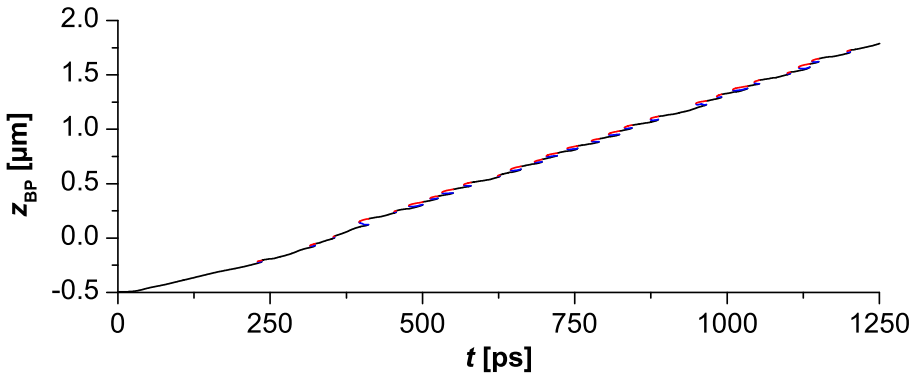


(a) Evolution of the Bloch point position in time

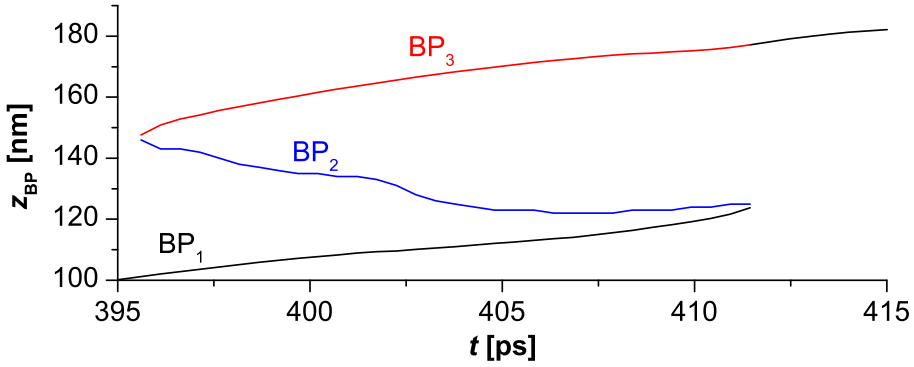


(b) Bloch point pair creation

**Figure 13.9** – Bloch point propagation along the axial direction ($z$) driven by a 100 mT field. During the propagation several Bloch point pairs nucleate and annihilate. Panel (b) shows the Bloch point pair creation and annihilation process between 396 ps and 412 ps.

Bloch point pairs with opposite polarity begins at the nucleation sites formed by the superposition of spin waves. Since both Bloch points have the same vorticity, but opposite polarity, the topological rule of Skyrmion number conservation is obeyed. For geometric reasons the new Bloch point $BP^n_{-1}$, which is closer to the domain wall center, has the same polarity as the original Bloch point $BP^o_{-1}$.

The nucleation of the Bloch point pair decouples the old Bloch point $BP^o_{-1}$ from the domain wall, whereas $BP^n_{-1}$ propagates together with the domain wall. The second new Bloch point $BP^n_{+1}$ is located on the same $m_z = 0$ isosurface as $BP^o_{-1}$ forming a drop that encloses a volume with antiparallel magnetization compared to the direction of the external field, as shown in Fig. 13.10(c) and Fig. 13.10(d). When the two Bloch points approach each other the volume enclosed between them reduces as well as the exchange energy stored inside the drop. Since the two Bloch points

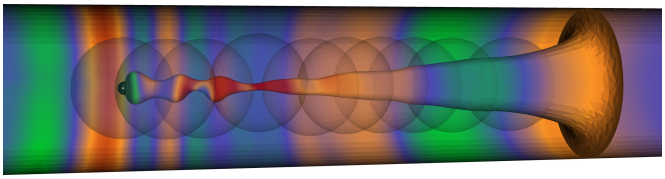

(a) $t = 390\,\mathrm{ps}$

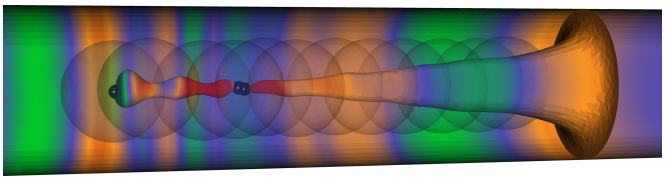

(b) $t = 396\,\mathrm{ps}$

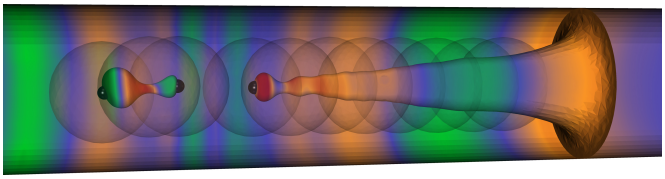

(c) $t = 401\,\mathrm{ps}$

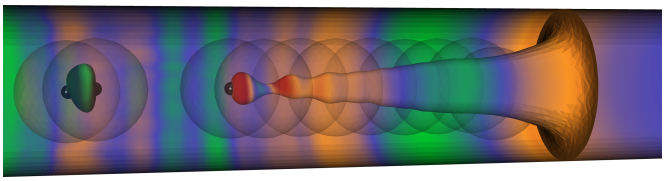

(d) $t = 406\,\mathrm{ps}$

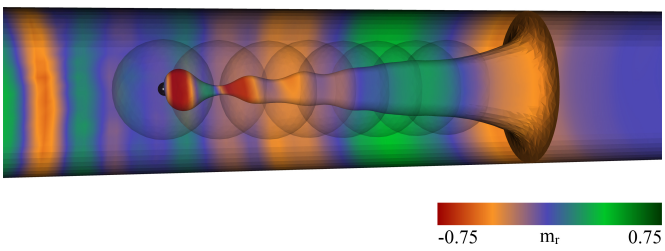


(e) $t = 413\,\mathrm{ps}$

**Figure 13.10** – Snapshots of the Bloch point pair creation and annihilation process, taken while the domain wall is driven by an external field of $100\,\mathrm{mT}$. Panel (a) shows the extended $m_z = 0$ isosurface, (b) the nucleation of the Bloch point pair, (c) the separation of the new Bloch point pair and the formation of a drop containing the old Bloch point and one element of the newly nucleated pair. The Bloch point annihilation process is shown in (d), and finally the single Bloch point configuration is restored, before the process repeats (e).

have the same vorticity, yet different polarity, they can annihilate without a change of the Skyrmion number, as shown in Fig. 13.10(e).

Therefore, the higher velocity of this regime as shown in Fig. 13.1 can be explained by the periodic reduction of the domain wall length accompanied by recurrent Bloch point pair creations and annihilations.

## 13.5 Summary

In this chapter we discussed four propagation regimes of a vortex domain wall under the influence of an external field for the case of good chirality. We have shown that for fields driving the domain wall with submagnonic velocities two different propagation phases can be found, one with positive and one with zero mobility, with the latter resulting in a constant velocity of the compound of Bloch point and domain wall. We have explained the differences in the magnetic configuration of both propagation phases and we have pointed out that the constant velocity phase is accompanied by a tilting of the domain wall and a deflection of the Bloch point by several nanometers.

We have discussed three distinct supermagnonic propagation regimes, which are equal for different orientations of the cylinder axis with respect to the atomic lattice. The first supermagnonic regime can be characterized by a laminar propagation of the Bloch point in the center of the domain wall without a tilting of the $m_z = 0$ isosurface or the occurrence of a second velocity phase. We demonstrated that the defining attribute of the second supermagnonic propagation regime, namely the oscillatory regime, is a deflection of the Bloch point by a few nanometers accompanied by spiraling motion of the Bloch point with frequencies corresponding to those of the spin wave tails attached to the domain wall. In addition, we pointed out that those first supermagnonic propagation regimes show a constant propagation velocity of Bloch point and domain wall, which has a very similar value even in the case of different diameters.

In the last section of this chapter we described the third supermagnonic propagation regime, where the unit of Bloch point and domain wall ceases to be stable. We explained the mechanism of Bloch point pair creation and annihilation resulting in a higher domain wall velocity than the one resulting for the two first supermagnonic regimes.

# 14

# Bloch point positions inside of the lattice

The method used in chapter 9 to calculate the inflow-angle $\gamma$ includes an exact determination of the Bloch point position with sub-lattice constant precision and with errors in the range of less than one percent of the lattice constant. Due to its propagation the Bloch point resides only for a short time inside one atomic unit cell. Hence, a picture of typical Bloch point positions cannot be assembled directly from snapshots taken every 5 ps. Nevertheless, from simulations with some 1000 snapshots a statistical distribution of the shortest distance of a Bloch point to a lattice site can be deduced, which reveals that, for the material parameters that we have used, a Bloch point never approaches a lattice site closer than 0.41 lattice constants in the case of the bcc lattice. Note that the minimum distance between two lattice sites in the bcc lattice is 0.866 lattice constants. This gives a first indication that a Bloch point avoids positions close to lattice sites. In order to confirm this hypothesis, we calculated for an applied field of 4 mT in good chirality inside of the 60 nm diameter wire the Bloch point positions for all 2605 snapshots and projected the locations into the atomic primitive unit cell of the bcc lattice. Figure 14.1 shows the resulting distribution during the propagation process, which is qualitatively the same as the distribution found for an applied field of 30 mT. We find the highest probability on the quadratic surfaces of the Wigner-Seitz cell of the bcc lattice, whereas the probability distribution inside the hexagonal surfaces is negligible. From this, it follows immediately that the Bloch point prefer positions on the square surfaces of the Wigner-Seitz cell and its edges, which is also indicated by Figure 14.1(c), where we combine the Wigner-Seitz-cells around three adjacent lattice sites.

The projection into the unit cell can be associated with the probability distribution of the Bloch point position, but it does not provide the information about the pathway that a Bloch point takes during its propagation. To investigate this question,

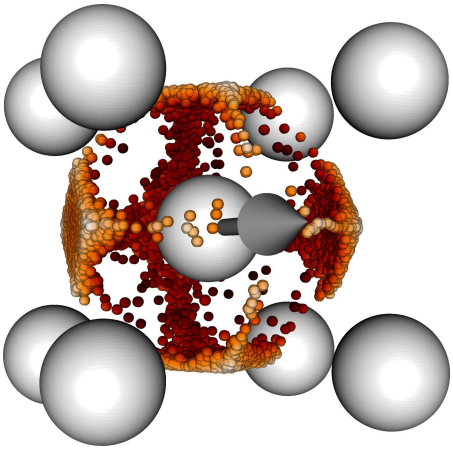

(a) View perpendicular to the propagation direction

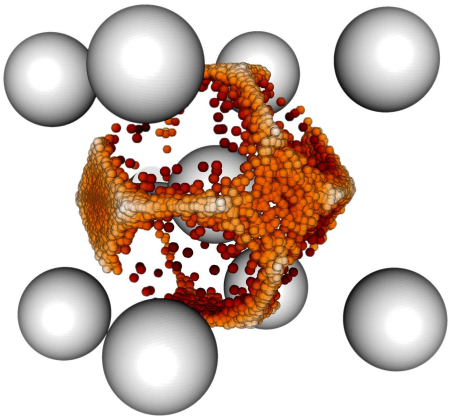

(b) View along the propagation direction

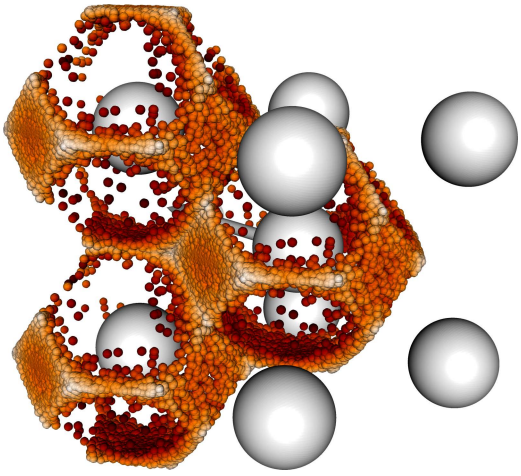

(c) Reproduction on three adjacent lattice sites

**Figure 14.1** – Projections of Bloch point positions – visualized as small colored spheres – into the unit cell of the bcc lattice during a dynamic propagation. The lattice sites are shown as big grey spheres and the propagation direction is indicated by an arrow. All Bloch point positions are found to be located on the surface of the Wigner-Seitz-cell [146] with highest probability distribution on the quadratic surface elements. The strong difference of the probability distribution between the two squares with a surface normal parallel to the propagation direction indicate that the Wigner-Seitz-cell is shifted by some picometer along the propagation direction of the Bloch point. Panel (c) reproduces the unit cell on three adjacent lattice sites, thereby indicating possible tracks that a Bloch point can take during the propagation. We detect this kind of distribution for all simulations with a bcc lattice structure. The data originates from simulations of the vortex domain wall in good chirality (chapter 13) with a driving field of $4\,\mathrm{mT}$.

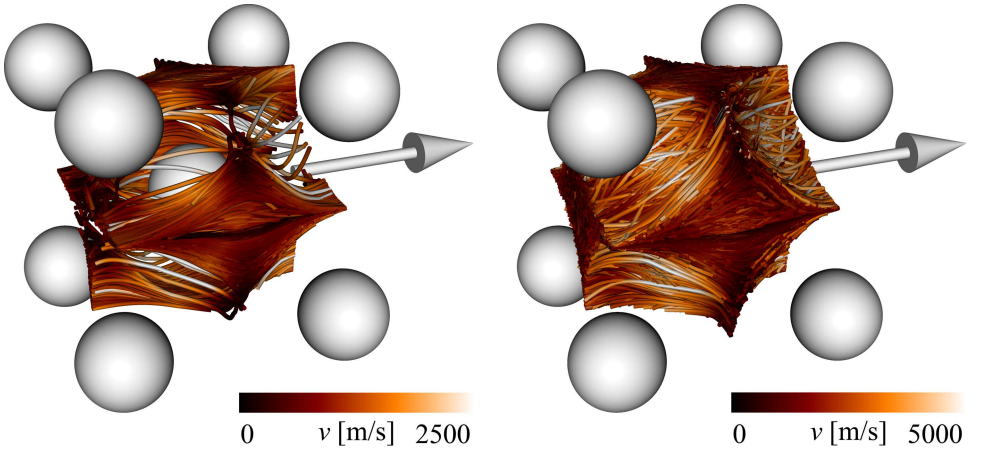


(a) $H = 4\,\mathrm{mT}$ (b) $H = 30\,\mathrm{mT}$

**Figure 14.2** – The pathways of a propagating Bloch point in a 60 nm wire projected into one atomic cubic cell in the bcc lattice for applied fields of 4 mT (a) and 30 mT (b) in good chirality confirm the tendency of the Bloch point to avoid the vicinity of atomic lattice sites. The arrow shows the direction of the field pointing in (100) direction. In the low field regime the Bloch point also avoids a change of the trail, as can be seen by the low amount of paths crossing from a surface perpendicular to the (010) to those perpendicular to the (001) direction and vice versa. In the oscillatory regime the Bloch point propagates also along the hexagonal surfaces of the Wigner Seitz cell, but it significantly accelerates in these regions, as the color coding shows.

we performed the simulations for 4 mT as well as for 30 mT in good chirality in the 60 nm wire again, but now the Bloch point position was tracked more precisely; every 3 fs. Due to the extremely high temporal and spatial resolution we obtained approximately 70 points in space per atomic cubic cell. As the results show *a-posteriori* it is justified and helpful to project the motion of the Bloch point into the atomic cubic cell of the lattice. This representation reveals more information than a projection into the primitive unit cell. Figure 14.2 visualizes the pathway of the Bloch point for the two applied magnetic fields by tubes (the colored lines depicting the motion) which are cut as soon as the Bloch point leaves the actual cubic cell. The figures show the characteristic pathways for the low field regime and for the oscillatory regime. In the low field regime the Bloch point propagates continuously along the (100) direction and avoids jumps from surfaces of the Wigner Seitz cell perpendicular to the (010) to those perpendicular to the (001) direction. The propagation along those tracks explains the jumps in the deflection radii, *e.g.*, which can be seen in Fig. 13.5.

In the oscillatory regime, on the other hand, the propagation is sufficiently irregular and turbulent so that the Bloch point can leave the favored tracks along the surfaces perpendicular to the (010) or (001) direction and can enter (at least for a short time) also the hexagonal surfaces of the Wigner Seitz cell. The higher energy on

those surfaces results in a repulsion of the Bloch point onto the lower-energy facets. In the low field regime this causes a strong acceleration of the Bloch point above the average 1300 m/s. Nevertheless the shape of the Wigner Seitz cell is still well reproduced visible in that regime, so that it is still largely constraining the possible propagation pathways.

Obviously, when the Bloch point propagates in good chirality in the super-magnonic regime, it performs an oscillation while changing from one cubic cell to the next one. Those oscillations have a wave length corresponding to the lattice constant resulting in a k-vector of $k_z = 2\pi/a \approx 2.19 \times 10^{10}\,\mathrm{m}^{-1}$ and a frequency of $f \approx 4.5\,\mathrm{THz}$. Future experiments might reveal whether those frequencies are of measurable amplitude in a realistic sample.

# 15
# Conclusion

The goal of this thesis was to determine and to describe the dynamics of the micromagnetic structure of a Bloch point and to understand thereby the dynamics of vortex domain walls in solid cylindrical wires. In order to achieve these objectives we started from an analytic description of a Bloch point in the theory of micromagnetism and found in a first-order approximation that a maximum propagation velocity of a Bloch point can be expected. As a cautious reminder, we pointed out that the micromagnetic description of the highly inhomogeneous Bloch point structure is beyond the validity range of the theory.

Hence, for a detailed description of the Bloch point dynamics, we demonstrated within this thesis the development of a multiscale multimodel simulation code combining a Heisenberg model applied in the vicinity of the inhomogeneity and with a micromagnetic description in the remaining part of a ferromagnetic, mesoscopic sample. The key features of the code are its ability to trace a structure of interest with a Heisenberg model region taking into account a user-defined number of interacting neighbors, introduce Heisenberg model regions and remove them from the sample automatically depending on their necessity, as well as to perform fast simulations on the basis of GPU accelerated calculations.

We described in the thesis that the transition from a pure micromagnetic method to the multimodel code causes only negligible numerical artifacts if it is applied to a magnetic problem that is perfectly treatable in the framework of micromagnetism. From this agreement we concluded that the multimodel method can be applied to Bloch point dynamics.

On the basis of the combined micromagnetic/Heisenberg code we were able to achieve the main objective of the thesis, *i.e.*, to analyze the Bloch point dynamics in vortex domain walls in the geometric structure of soft-magnetic cylinders. We demonstrated in chapter 9 that the Bloch point structure in the vicinity of the Bloch point in the center of a vortex domain wall is independent of the geometry of the

hosting nanocylinder, yet a deviation of the structure depending on the different lattice orientation with respect to the wire axis was obtained.

We demonstrated that the combined Bloch point/domain wall dynamics splits up into three groups of regimes, which we treated individually:

1. Pinning/depinning of Bloch point and domain wall
2. Propagation in bad chirality
3. Propagation in good chirality

Using the results of those simulations we were able to determine the Bloch point position probability density inside the primitive unit cell as well as inside the cubic unit cell of the underlying lattice.

**The pinning and depinning of Bloch points** from the equilibrium position under the influence of an external field were analyzed in chapter 10. We demonstrated in that chapter that a field in the range of 1 mT is sufficient to depin a Bloch point and to start a propagation along the cylinder axis. Moreover, we showed in the chapter that only if the cylinder axis is oriented along the cubic axis of the lattice, *i.e.*, the (100) direction, a higher depinning field is obtained, whereas all other axis orientation configurations result in a constant and much lower depinning field. We demonstrated further that a similar behavior can be found for different material configurations, such as nearest-neighbor interaction in comparison to a *Fe-like* interaction.

**The Bloch point propagation in bad chirality** was discussed in chapter 12. In the case of that propagation chirality we demonstrated that only for low external fields a steady state propagation of the domain wall and Bloch point is obtained, whereas for sufficiently high fields an expulsion of the Bloch point occurs. In the corresponding chapter we analyzed and discussed the detailed process from a graphical as well as from a topological point of view. Using the radial magnetization component on the surface of the wire we were able to describe the necessary conditions, namely an out-of-plane (radial) angle of magnetization of at least 45°, and the mechanism of the breakdown process. Furthermore, we demonstrated that the theoretically expected change of the Skyrmion number by $\Delta Q = \pm 1$ during the expulsion of the Bloch point from the wire takes place within some 5 ps making it one of the fastest field-induced processes in magnetism. Despite the dynamics of a breakdown we described also the possibility of a chirality change that can occur in the case of sufficiently high magnetic fields. We explained that the condition for the chirality switch is that the magnetic helicity on the surface of the wire changes sufficiently fast, so that the inertia of the Bloch point prevents its expulsion.

**The Bloch point propagation in good chirality** was the topic of chapter 13, labeled after the higher stability known from vortex domain wall dynamics in nanotubes as well as from analytic considerations of the Bloch point itself. We described in that chapter that only for low driving fields the relative orientation of the lattice and the cylinder axis affects the Bloch point propagation. This occurs only at velocities below

the magnonic limit. We showed that the influence of the lattice can distort the domain wall around the Bloch point resulting in different quasi-static propagation velocities, depending on the lattice orientation with respect to the cylinder axis. Furthermore, we demonstrated that for supermagnonic velocities three lattice orientation independent regimes can be distinguished. We showed that low fields drive the unit of Bloch point and the domain wall in a quasi-static manner along the wire. We revealed that the Bloch point starts an oscillatory motion as soon as a critical velocity is reached, which is accompanied by a limit of the domain wall velocity. Further, we demonstrated in that chapter that the oscillating Bloch point stabilizes the domain wall/Bloch point velocity over a broad range of external fields and wire diameters. This unexpected feature makes the system a promising candidate for future applications. In addition, we discussed that the oscillatory regime is followed by a turbulent propagation one, in which a series of nucleation and annihilation of Bloch point pairs unfolds, which allows for a further acceleration of the domain wall, however at the cost of a strongly excited magnetic system.

**A determination of Bloch point position on a picometer/femtosecond scale** was discussed in chapter 14. In that chapter we explored the pathway and the local velocity of the Bloch point inside the lattice. First, we determined the Bloch point position probability distribution projected into the primitive unit cell of the lattice. These results demonstrate that Bloch points tend to avoid the vicinity of lattice sites and that they can be found almost exclusively on the surface of the Wigner-Seitz cell. By determining the position of the Bloch point with very high temporal accuracy, every 3fs, we discussed the possible Bloch point propagation pathways under the influence of different external fields using the example of a bcc lattice. This analysis demonstrated that, for a short time, a strong acceleration of the Bloch point occurs if it enters a hexagonal facet of the Wigner-Seitz cell. Such an energetically unfavorable location of the Bloch point is however only possible for sufficiently high fields.

**In conclusion,** we provided with this thesis a first dynamic multimodel study of the fundamental micromagnetic structure of Bloch points. Even though some results might be beyond the actual experimental resolution, several effects, like the propagation velocities in the different propagation regimes could be experimentally accessible. Especially the very stable supermagnonic velocity regime of the good chirality might be interesting not only from a fundamental perspective, but also from an application point of view. The multimodel methods developed for this thesis should also be applicable for other simulation fields where an interaction between atomistic effects and large-scale domain structures are important, such as future multiferroic simulators.

# Appendix

# List of abbreviations

**Abbreviations**

| | |
|---|---|
| bcc | Body centered cubic |
| BP | Bloch point |
| fcc | Face centered cubic |
| Hei | Indicates a Heisenberg model quantity |
| LLB | Landau-Lifshitz-Bloch equation |
| LLG | Landau-Lifshitz-Gilbert equation |
| MM | Indicates a micromagnetic quantity |
| RKKY | Ruderman-Kittel-Kasuya-Yoshida interaction [147–149] |
| sc | Simple cubic |

**Constants**

| | |
|---|---|
| $e$ | Electron charge |
| $\gamma_0$ | Gyromagnetic ratio |
| $g$ | Landé factor |
| $\imath$ | Imaginary unit $\imath = \sqrt{-1}$ |
| $\mu_0$ | Vacuum permeability |
| $m_e$ | Electron mass |

**External parameters of the system**

| | |
|---|---|
| $\alpha$ | Damping constant |
| $A$ | Exchange stiffness in J/m |
| $a$ | Lattice constant |
| $J^{(s)}$ | Heisenberg exchange constant of the magnetic moment on the $s^{\text{th}}$ sphere shell around the magnetic moment of interest. |
| $K_c^{(1)}$ | Cubic anisotropy constant for mixed terms |
| $K_c^{(2)}$ | Cubic anisotropy constant for quadratic terms |
| $K_s$ | Surface anisotropy constant |
| $K_u^{(n)}$ | Uniaxial anisotropy constant of order $n$ |
| $M_s$ | Saturation magnetization given in A/m |

| | |
|---|---|
| $R_c$ | Radius of the core region of the multi-model spheres |
| $\mathbf{k}_\mathrm{U}$ | Uniaxial anisotropy axis. |
| **Geometry** | |
| $D$ | Diameter |
| $d$ | Dimensionality in finite element calculations |
| $\eta_i^{(n)}$ | Shape functions of finite element $n$ associated to vertex $i$ |
| $h$ | Denotes a thickness or height |
| $R$ | Radius of a sphere |
| $R_H^{(\max)}$ | The maximum radius in the core region up to which a correct Heisenberg exchange calculation would be possible |
| $U$ | Circumference |
| $V$ | Volume |
| $\mathbf{n}$ | Normal of a surface |
| **Coordinates** | |
| $\Theta$ | Azimuthal angle in a second coordinate system |
| $\vartheta$ | Azimuthal angle. |
| $r$ | Radial coordinate |
| $t$ | Time |
| $\Phi$ | Polar angle in a second coordinate system |
| $\phi$ | Polar angle. |
| $\mathbf{r}$ | Coordinate vector |
| $x, y, z$ | Cartesian coordinates |
| **Operators, matrices and functions** | |
| $P_l(\cos\vartheta)$ | Legendre polynomials |
| $Y_{l,m}(\vartheta, \phi)$ | Spherical harmonics |
| $\{f_a\}$ | Vector with elements $f_a$ |
| $\lfloor x \rfloor$ | Mathematical symbol to rounding $x$ down |
| $\Delta$ | Laplace operator in continuum descriptions. In combination with an indexed quantity, *e.g.* $x_{i,j}$, it denotes the difference, *e.g.* $x_i - x_j$. |
| $\delta_{i,j}$ | Kronecker delta: $\delta_{i,j} = 1 \forall i = j, \delta_{i,j} = 0 \forall i \neq j$ |
| $\nabla$ | The nabla operator $\left(\frac{\partial}{\partial x}\mathbf{e}_x + \frac{\partial}{\partial y}\mathbf{e}_y + \frac{\partial}{\partial z}\mathbf{e}_z\right)^T$ |
| $\mathfrak{V}_\mathfrak{a}$ | Set of finite elements forming the Voronoi cell of vertex $\mathfrak{a}$. |

| | |
|---|---|
| $\underline{\underline{D}}$ | Matrix to derive the exchange field by a matrix vector multiplication with the orientation of magnetic moments/magnetization. A subscript Hei or MM indicate that it is only the matrix for Heisenberg regions or micromagnetic regions, respectively. |
| $J_{ij}$ | Heisenberg exchange constant between magnetic moment $i$ and $j$ - derived from $J^{(s)}$ |

**Mathematical/physical symbols**

| | |
|---|---|
| $\Delta_{\mathrm{DW}}$ | Domain wall width |
| $E_0$ | Energy offset |
| $E_{\mathrm{Dem}}$ | Total demagnetization energy calculated in a continuum model |
| $E_{\mathrm{Dip}}$ | Total dipolar energy |
| $e_{\mathrm{xc}}$ | Exchange energy density |
| $E_{\mathrm{Xc}}$ | Total exchange energy |
| $\mathrm{err}_{MM}$ | Systematic error of micromagnetic exchange energy density in comparison to the Heisenberg exchange energy density. |
| $E_{\mathrm{tot}}$ | Total energy |
| $e_{\mathrm{tot}}$ | Total energy density |
| $E_{\mathrm{Zee}}$ | Total Zeeman energy |
| $e_{\mathrm{zee}}$ | Zeeman energy density |
| $\zeta$ | Tilting angle of magnetization out of the surface plane |
| $\gamma$ | Inflow angle of the Bloch point structure |
| $\vartheta_{i,j}$ | Angle between elements with index $i$ and $j$ |
| $\lambda$ | Wave length |
| $l_K, \quad l_s, \quad l_{xc}$ | Exchange length formulations $l_{xc} = \max(l_K, l_s)$ |
| $\mathfrak{R}^3$ | Three dimensional space |
| $\rho$ | Magnetic volume charge |
| $\sigma$ | Magnetic surface charge |
| $U_{\mathrm{dem}}$ | Magnetostatic scalar potential |
| $v$ | Velocity |
| $\mathbf{A}$ | Magnetic vector potential |
| $v_{\mathrm{max}}$ | Maximum velocity |
| $\mathbf{B}$ | Magnetic induction |
| $\mathbf{E}$ | Electric field |
| $\mathbf{H}$ | Magnetic field |
| $\mathbf{H}_{\mathrm{eff}}$ | Effective magnetic field |

| | |
|---|---|
| $\mathbf{H}_{\text{ext}}$ | External fields, which include all solenoidal contributions to the magnetostatic field, such as the Zeeman field, Oersted field, etc. |
| $\mathbf{H}_{\text{xc}}$ | Exchange field |
| $\mathbf{H}_{\text{dem}}$ | Magnetic stray field, inside of a ferromagnetic material also called demagnetizing field |
| $\mathbf{H}_{\text{zee}}$ | Zeeman field: Externally applied magnetic field |
| $\mathbf{j}$ | Electric current |
| $\mathbf{k}$ | Wave vector |
| $\mathbf{L}$ | Angular momentum associated with a magnetic moment |
| $\mathbf{M}$ | Oriented magnetization $\mathbf{M} = M_s\mathbf{m}$ |
| $\mathbf{m}$ | Normalized orientation of magnetization |
| $\boldsymbol{\mu}$ | Oriented magnetic moment |
| $\boldsymbol{\tau}$ | Torque acting on a magnetic moment |
| $\Omega$ | Region in the $\Re^3$, *e.g.* the volume of a ferromagnetic sample. |
| $\omega$ | Solid angle spanned by the surface vectors of a region $\Omega$ |
| **Topology** | |
| $n$ | Vorticity of a Bloch point ($n = 1$) or an anti-Bloch point ($n = -1$). Corresponds to the winding number of vortices. |
| $p$ | Polarization of a Bloch point. |
| $Q$ | Skyrmion number of a magnetic structure - also called Pontryagin index |
| $q$ | Skyrmion number density of a magnetic structure |

# List of Figures

# English résumé

The understanding of micro- and nanoscopic magnetic structures has made significant developments in the last century, during which the techniques to gather knowledge as well as the motivation for research increased with enormous speed. While research on magnetic patterns was mainly of fundamental scientific interest in the beginning of the 20th century, it became more technology oriented during the last decades. With the establishment of the micromagnetic theory in the 1960s [1–5] a mathematical frame became available to study magnetic structures theoretically. The results of this continuum theory are in perfect agreement with experiments for the typical structures observable in ferromagnetic materials such as domain walls [6–8],vortices [9, 10] or spin waves. Usually, the atomistic structure can be neglected since the length scales (domain wall width, vortex size etc.) of these magnetic configurations with typical values around 10 to 100nm are far beyond the atomistic lattice size. The only exceptions of reliable simulations in the framework of micromagnetism are micromagnetic singularities, Bloch points [11, 12], because in their center the magnetization changes by 180° within one lattice constant. As micromagnetism neglects the atomistic structure of matter, the exchange energy density shows a singular behavior if calculated within the micromagnetic framework. Hence, in micromagnetism Bloch points are topological defects and cannot be studied reliably within this theory. Bloch points occur, *e.g.*, as transient structures during the switching of vortex cores [9], when bubble domains are nucleated [13], or in the archetypal example of the magnetic switching of a soft-magnetic cylinder [14].

While the fundamental equations of micromagnetism are well known, it is very difficult to derive solutions on the magnetic structure from them, at least analytically. Already the magnetization dynamics involving a single domain wall in a thin ferromagnetic strip is analytically treatable only by using strong approximations and, therefore, requires numerical approaches for more reliable predictions. The most widespread numerical methods differ by their discretization methods, which are known as *finite differences* and *finite elements*. The finite difference approach typically assumes a grid of equidistant cube- or prism-shaped discretization cells, which makes it rather easy to approximate spatial differentiation operations and integration methods by means of difference quotients. Difficulties arise at the boundaries of samples if the geometry contains boundaries that do not follow exactly the edges of the discretization cells. In these cases, a "staircase" approximation is used, which may introduce more or less pronounced spurious numerical effects. Unlike the finite-difference method, the discretization scheme of the finite element method (FEM) uses discretization points at freely adjustable positions, which allows for a far more accurate approximation of the sample shape by placing a subset of nodes, *i.e.*, of discretization points, exactly on

the boundary of the sample. The nodes are usually connected by lines or flat surface elements. Micromagnetic simulations codes based on both, the finite difference [15] and the finite element method [16], have been developed during the last decades and have reliably proven their accuracy and predictive power for various magnetic patterns.

In the first half of the last century nano- to micrometer dimensioned magnetic patterns were of fundamental research interest only; yet the demands for the advancing storage technology became a driving force of research during the last two decades. In addition to the interest due to the storage of data on magnetic films, *e.g.*, magnetic tapes or discs, an early approach to use complex magnetic structures for storage devices tried to exploit magnetic domain walls in bubble materials [13] as units of information. But, the technological obstacles of bubble material devices were higher than those that had to be overcome to achieve the high density of data storage that is nowadays used conveniently in hard drive technology. A transition from a two-dimensional magnetic storage solution on rotating discs to a novel type of storage systems might be necessary, if the demand for higher data storage densities increases further. Retrieving and storing large amounts of data also requires high operating speeds of the devices. This represents an exciting topic for both, fundamental and industrial research.

A candidate for future storage devices is the racetrack memory proposed by S. Parkin in 2008 [17]. There, a chain of magnetic domain walls, which serve as units of information, is driven by a spin polarized electric current along a magnetic nanowire. Owing to the spin-transfer torque effect, the domains or domain walls can be relocated to the reading and writing devices without any mechanical movement. This approach could have the potential of replacing rotating magnetic disks as they are used in modern hard-disk drives. A two-dimensional racetrack memory can be represented by a shift register formed, *e.g.*, by arrays of thin ferromagnetic strips that are placed on a substrate, usually prepared by means of electron lithography techniques. Cylindrical nanowires might be a promising candidate for a three dimensional version of the racetrack memory, in which the properties of vortex domain walls could be exploited. Such a vertical arrangement of nanowires could significantly increase the storage density. For the case of nanotubes it has recently been shown [18, 19], by using computer simulations based on the framework of micromagnetism, that this type of domain wall is extremely stable and that it can reach velocities beyond 1000 m/s without experiencing structural instabilities or turbulences. In a gedanken experiment, reducing the inner diameter of a nanotube hosting a vortex domain wall to zero results in the geometric transition to a solid wire. It also necessitates a point in the center of the domain wall, inside of which not only a head-to-head or tail-to-tail pattern, but also the vortex-like structure needs to be maintained at the same time. Hence, every possible direction of magnetization is present in the vicinity of that point, which corresponds directly to the definition of a Bloch point given by A. Hubert [20] and is the above mentioned archetypal example of a Bloch point in a ferromagnetic cylindrical nanowire [21, 22].

The description of *strongly inhomogeneous structures*, *e.g.*, like Bloch points, lies outside the limits of a continuum theory. Such structures must be treated with

atomistic models [23], especially when the magnetic inhomogeneity occurs on length scales comparable to the atomistic lattice constant. Within this thesis, we derived in a first step the necessary analytic expressions to obtain a link between a given set of Heisenberg model exchange parameters, lattice structure, lattice constant as well as the number of Bohr magnetons per lattice site and the micromagnetic properties of saturation magnetization and the exchange stiffness. In order to find a criterion for such strongly inhomogeneous structures we used the analytically treatable system of a uniform spin spiral. To study this spin-spiral system we used a material with micromagnetic properties of Permalloy (saturation polarization of 1 T and exchange stiffness of $1.3 \times 10^{-11}$ J/m ) and a bcc lattice structure adapted from $\alpha$-iron. With this system we analyzed the systematic error of micromagnetism in comparison with a classical Heisenberg model. From the results we obtained that as the spin-spiral half wavelength increases to 9 and 29 lattice constants, the systematic micromagnetic error drops to 1 % and 0.1 %, respectively. Systematic errors of such order of magnitude can be tolerated and we use this criterion to estimate the required size of a region that needs to be simulated with a Heisenberg model if a strongly inhomogeneous structure is present. One of the most important earlier multiscale studies simulating Bloch points was reported by Jourdan et al. [24, 25]. The authors presented a combination of a Heisenberg with a micromagnetic model. They used a finite difference method as background mesh with local refinement to atomistic cell sizes in the vicinity around the structure of interest, *i.e.*, a Bloch point, to study the equilibrium configuration of the Bloch point. In spite of In spite of this important first step, until the beginning of this PhD no multimodel simulation had been reported that was capable of studying the dynamics of propagating Bloch points.

We developed a multiscale multimodel simulation package running on graphical processing units utilizing the CUDA framework. The simulation package treats the exchange interaction in the vicinity of the Bloch point with an atomistic Heisenberg model, while the surrounding background sample is simulated by means of the existing CUDA enhanced micromagnetic program TetraMag [26] developed in our group. Since Bloch points and other strongly inhomogeneous structures develop and propagate dynamically, we encapsulated the regions calculated within the Heisenberg model into the connection of the Heisenberg model to the framework of micromagnetism by using well-defined spherical volumes. Those multimodel spheres can be added to, removed from or displaced within inside the micromagnetic sample. Those processes of insertion, removal, and displacement are performed automatically by the simulation kit. This allows for a dynamic tracing of propagating Bloch points. In a synchronization process the finite–element sample mesh stamps the magnetic orientation on the boundary of the multimodel sphere, whereas the multimodel sphere imprints the magnetic orientation onto vertices of the sample mesh inside the volume of the multimodel sphere. This bidirectional synchronization process is described in detail in section 6.4.

Structurally, a multimodel sphere consists of three functional entities:

1. a core with a radius of about 30 lattice constants where the orientation of the magnetic moments is simulated with a Heisenberg model.

2. a transition region shaped like a spherical shell with a width of some ten lattice constants. Inside of this shell, both models are applied to calculate the exchange interaction. Owing to a carefully calibrated interpolation and position-dependent weighting procedure we achieve a seamless transition between the models.

3. a purely micromagnetically modeled spherical shell region of about 10 nm width, inside of which the cell size increases radially from the atomistic length to the average finite element cell size in the sample region.

This structure ensures that, first, calculations in a sufficiently large volume containing the Bloch point use the accurate Heisenberg model, second, that the two models are compatible, thereby preventing possibly important numerical errors, and third, that only donating finite element cells of a mesh B stamp their properties on accepting vertices in a mesh A, if the donating cell size is comparable to or smaller than the cell sizes of the Voronoi cell surrounding the receiving vertex. The last point is only ensured as long as the multimodel-sphere remains inside the sample structure, but as soon as a Bloch point approaches the sample surface, the situation can occur where a part of the multimodel sphere can leave the sample volume. In this situation the outside part of the multimodel sphere needs to be deactivated to maintain the shape of the sample. In that case the surface of a multimodel sphere is formed by vertices, whose Voronoi cell elements might have a much smaller cell size than the mesh of the donating background sample [27]. To take care of this situation we implemented refinement patches, which we call *calottes*. These structures act like a patch on the surface of the sample, effectively bridging the different cell sizes between the background mesh of the sample an the mesh of the multimodel sphere that has left the sample partially. In the case of cylindrical wires one calotte geometry is sufficient for symmetry reasons. To discretize the calotte geometry we use different meshes, whose structure is chosen such that the position-dependent mesh size corresponds to the case of a multimodel sphere located within a predefined distance interval from the surface of the sample. Several such meshes are prepared, and they are chosen depending on the distance between the center of the multiscale sphere and the surface. Hence, these patches bridge the gap that develops in terms of cell sizes between multimodel sphere and sample when a part of the multimodel sphere is located outside of the sample.

The Landau Lifshitz-Gilbert equation [28–30] governs the temporal evolution of the local magnetic orientation, *i.e.*, the magnetization direction in the continuum regions. But with minor modifications it can be applied as well to calculate the orientation of magnetic moments in the Heisenberg model. We use the CVODE solver of the sundials library [31] for the numerical time integration of the Landau-Lifshitz-Gilbert equation in either model.

The multimodel simulation kit has been thoroughly tested for a couple of cases. The first test addresses possible differences between the multimodel implementation and a pure micromagnetic calculation for the case of a vortex gyrating in a ferromagnetic disc. This system is well understood and documented in the framework of classic numerical micromagnetism [32–34]. With that test we demonstrate that the difference between the two programs, the pure micromagnetic and the multimodel

one, is negligible. A second test is used to investigate possible changes in the energy due to the generation, the deletion and the motion of several multimodel spheres. For this test we used a short cylindrical sample in a single domain state. The test shows that the numerical error introduced by the method corresponds to a random field fluctuation below 0.1 mT, which is tolerable since the typical externally applied fields studied within this thesis are between 1 mT and 100 mT.

To study Bloch point dynamics we chose the two systems of a vortex-domain wall in a softmagnetic cylindrical nanowires with the above mentioned micromagnetic parameters of Permalloy, a length of 4 µm and a diameter of 60 nm and 80 nm, respectively. The two different diameters were used in order to compare effects in two different systems and to ensure that the obtained effects are not restricted to a particular set of system parameters. The geometry enables us to study both, the statically equilibrated magnetic pattern with one domain wall and a Bloch point inside the sample as well as the dynamic properties of that system. For that purpose we simulated the dynamics as it unfolds with an applied magnetic field in axial direction.

The first study focusses on the structure of the Bloch point in the static equilibrium, *i.e.*, without an external magnetic field. For that purpose we analyzed the domain wall structure with respect to the distance from the Bloch point, where two quantities are of particular interest. First, the in-flow angle $\gamma$ and second the domain wall width. The absolute value of the former corresponds to the radial magnetization component on the $m_z = 0$ isosurface of the domain wall with the $z$-axis corresponding to the cylinder axis. The sign of $\gamma$ represents a measure of the helicity of the Bloch point. Most studies on the structure of Bloch points reported in literature [11, 12, 35, 36] treat $\gamma$ as the only free parameter with which the Bloch point is modeled, and it is generally assumed that this value is isotropic.

Our results show that its equilibrium value, which we calculated in the multimodel framework, depends on the distance to the Bloch point. Furthermore, our results demonstrate that only in the close vicinity of the Bloch point (in the range of some nanometers) the value of $\gamma$ can be considered as isotropic and is comparable to earlier estimates of $\gamma$, which used a continuum model for the calculation. While for a small cylinder radius the in-flow angle $\gamma$ varies only in the range of a few degrees, the spatial variation increases strongly for cylinders with a larger radius.

The second important quantity is the local domain wall width, which is proportional to the derivative of $\partial m_z/\partial z$ on the $m_z = 0$ isosurface. Owing to the change of the magnetic orientation by 180° within one lattice constant at the position of the Bloch point, the domain wall width has intrinsically a strong radial dependence. Analytic models assuming an isotropic value of $\gamma$ correspondingly result in a linear increase of the domain wall width with $r$. With our multimodel approach we showed that the domain wall width increases in strongly non-linear fashion and much faster than predicted by previous analytic models (see also chapter 9)

From an atomistic point of view, an exchange energy landscape can be defined within one atomic unit cell. Such a spatial profile of the energy results in preferential and unfavorable Bloch point positions [37]. In order to drive a Bloch point along the axial direction – the easy axis of ferromagnetic nanocylinders – it is straightforward to predict the existence of a minimum external field, required to initiate the propagation

of a Bloch point. By performing simulations in which an external axial field is assumed with a slow and continuous increase in time, we determined the depinning field for different orientations of the lattice with respect to the cylinder axis and for different interaction configurations of neighboring magnetic moments. If only nearest-neighbor interaction is taken into account a comparatively large depinning field in the range of 1.8 mT was found for the case of the cylinder axis oriented in the (100) lattice direction, whereas we detected much lower depinning fields, of approximately 0.4 mT, in the case of a (110) and (111) oriented cylinder axis. Using not only nearest-neighbor interaction but taking into account ten shells of nearest neighbors, which corresponds to 144 neighbors in a bcc lattice, we found an important reduction of the depinning field for the (100) axis direction, whereas for the (110) and (111) direction the depinning field remained constant. From these results we conclude that the atomistic structure plays an important role, especially for low external field values.

Possessing the information about the depinning field we studied the Bloch point dynamics under the influence of higher fields which allow for a propagation of the ensemble of domain wall and Bloch point. For vortex domain walls in cylindrical nanowires driven by an axial magnetic field two distinct dynamic pathways exists for symmetry reasons (see also Chap. 11), which can be distinguished as a *good* and *bad* chirality in analogy to previous studies on the dynamics of vortex domain walls in nanotubes [18, 19]. Domain walls in good chirality are more stable than those in bad chirality, which is the origin of the labeling.

The dynamics of bad chirality domain walls is qualitatively similar for different wire diameters. We therefore restrict the study of these domain wall mostly to the 60 nm diameter wire. In this case the dynamics splits into three different regimes: First, a stable low-field regime, second, an unstable regime characterized by a breakdown of the domain wall structure and a change of the domain wall geometry, third, a regime showing a chirality inversion. The low field regime is stable for external fields up to 4 mT. With increasing field the maximum velocity increases, too, from about 380 m/s for an applied field of 2 mT up to 500 m/s for a field of 4 mT. Our simulations show that the inflow-angle $\gamma$ as well as the angle $\zeta$ , which represents an analogue angle to $\gamma$ on the surface of the wire, increase with increasing external field. Above 4 mT $\zeta$ reaches a critical angle of 45°. This results in a destabilization of the domain wall. This critical angle of $\zeta$ is found for the 60 nm as well as the 80 nm diameter wire and matches perfectly the critical angle in Walker's model [38], above which a change of the mode of domain wall propagation was predicted: the *Walker breakdown*.

According to our simulations, external fields tilting the magnetization on the wire surface to larger angles $\zeta > 45°$ drive the domain wall to the second regime. As soon as the critical angle of $\zeta$ is reached, a pair of a vortex and an anti-vortex forms on the surface of the wire, which propagate in opposite directions along the perimeter of the wire. As soon as the vortex and the anti-vortex have reached diagonally opposing positions on the surface of the wire the Bloch point is expelled in close vicinity to the anti-vortex. This process inverts the Skyrmion number of the anti-vortex by changing its polarity. In result, the global Skyrmion number of the wire reduces to zero. Locally, two regions with positive Skyrmion number density remain around the vortex and the anti-vortex as well as two regions with negative Skyrmion number. Those two pairs of

regions compensate exactly each others Skyrmion number contribution. The resulting domain wall configuration is similar to a C-state, which is a known configuration in soft-magnetic discs. The C-state domain wall configuration propagates with a very low velocity in the range of a few meters per second, which is by two orders of magnitude slower than the original propagation velocity.

In the third mode of the bad chirality, the external field triggers an inversion of $\zeta$ before the Bloch point can be expelled. Thereby the chirality changes from the bad to the good one, after which the domain wall propagates like in the case of the good chirality.

Good chirality domain walls are much more stable and suppress a breakdown or chirality inversion efficiently. They have a different set of propagation patterns. The first one is a submagnonic regime, in which the domain wall and the Bloch point reach velocities below the minimum spin wave phase velocity of the nanowire. Domain walls and Bloch points propagating with supermagnonic velocities, on the other side, display either a laminar, an oscillatory, or a turbulent mode of propagation. The submagnonic propagation occurs for fields that are sufficiently large to overcome the pinning barrier of Bloch points, but low enough to drive the unit of Bloch point and domain wall with velocities below the minimum spin wave phase velocity, which has a value of $v_{min}^{ph} = 1150\,\mathrm{m/s}$ for the cylinder with 60 nm diameter and $v_{min}^{ph} = 980\,\mathrm{m/s}$ for the cylinder with 80 nm diameter. These values were derived numerically from the simulated spin wave dispersion relations. In this *submagnonic* regime we find a dependence of the Bloch point/domain wall mobility on the orientation of the cylinder axis with respect to the lattice orientation. In equilibrium, the domain wall and the Bloch point exhibit a cylindrical symmetry, which reflects the symmetry of the sample. If a low field is applied, with a value just above the depinning field, the Bloch point and the domain wall begin to propagate along the cylinder axis and thereby preserve the cylindrical symmetry. An increase of the external field strength results in a higher velocity of the domain wall, in close analogy to the well-known case of domain wall propagation in flat nanowires [39] or in nanotubes [18]. Similar to the observations that we made concerning in case of the depinning field, different cylinder axis orientations with respect to the lattice result in different maximum velocities for a given field value. For those submagnonically propagating domain walls we observe a second mode of propagation, at least for the thinner wire diameter geometry. After a certain period of time, which increases with the field strength, the domain wall center exhibits a tilting, which results in the loss of cylindrical symmetry. This is accompanied by a change of velocity to a value of approximately 300 m/s, which (within the corresponding range) neither depends on the value of the applied field nor on the relative orientation of the field and the crystal lattice. From this result we conclude that in the submagnonic regime two system states exist, which allow for steady-state propagation.

As soon as the external field is strong enough to drive the domain wall and the Bloch point with supermagnonic velocity, the 300 m/s propagation state becomes unstable and a new propagation mode emerges, which does not depend on the lattice orientation. In a first interval of external fields, the Bloch point propagates smoothly without oscillations. It also does not lag behind the center of the

cylindrically-symmetric vortex domain wall. It was recently reported by our group [40] that supermagnonic propagation results in a spontaneous and strong excitation of spin-wave tails in front of and behind the domain wall. We observe the same phenomenon also for vortex walls with a Bloch point, where the phase velocity of the spontaneously formed spin-wave tails is equal to the propagation velocity of the domain wall and the Bloch point. Once the domain wall and the Bloch point velocity reach a critical velocity in the range of 1300 m/s, an additional increase of the external field does not increase the propagation velocity further, which corresponds to a drop of the domain wall mobility to 0 m/sT. This result is obtained for both wire diameters.

We derive a simplified one-dimensional model in the framework of pure micromagnetism, which allows only for a spatial invariant in-flow angle $\gamma$. Like in our simulation results the model yields a maximum Bloch point velocity as well as a possible channel which allows the moving Bloch point to couple to the spontaneously generated spin-waves. We found such a coupling for both studied wire diameters. This coupling of the Bloch point motion in the wake of the spin waves excited by the Spin-Cherenkov Effect [40] is characteristic for a second supermagnonic propagation range. There, the Bloch point couples to the spin-wave tails attached to the domain wall and performs a spiraling motion around the cylinder axis with the same frequency as the attached spin wave tails. Thereby, the Bloch point lags behind the domain wall, and we find that the distance between the Bloch point and the domain wall increases with increasing external field. In spite of this non-linear coupling, the simulations show that the spiraling motion effectively stabilizes the propagation of both, the domain wall and the Bloch point velocity. As a result the velocity is buffered over a broad interval of external fields, meaning that the velocity of the domain wall remains constant even if the external field increases. This occurs within the interval between 25 mT and 70 mT in case of the 60 nm diameter wire and between 10 mT and 17 mT in the case of the 80 nm diameter wire.

Obviously, the buffering of the domain wall velocity by the spiraling Bloch point lagging behind the domain wall cannot be sustained for arbitrary high fields. In a last propagation regime the distance between the Bloch point and domain wall reaches several hundred nanometers, resulting in a strong accumulation of exchange energy. This local accumulation of exchange energy continues until it reaches a certain threshold value, which is high enough to permit the nucleation of Bloch points with opposite polarity. If such a pair of Bloch points is nucleated within the wire, there are temporarily three Bloch points in the system. Such a behavior was predicted previously by pure micromagnetic simulations [41] and could now be confirmed with our multiscale-approach. After the nucleation of the pair, one of the new Bloch points remains connected to the domain wall at the $m_z = 0$ isosurface, whereas the previously existing Bloch point and the other new Bloch point form a "drop". Afterwards, within a few picoseconds, the two Bloch points in the "drop" approach each other and annihilate eventually. Owing to their configurations with opposite polarities, their annihilation does not influence the total Skyrmion number of the system. The nucleation and annihilation process allows for a faster domain wall

motion, since the velocity is no longer limited by the maximum Bloch point velocity, owing to the additional hopping-like propagation channel.

The depinning field and the submagnonic propagation regime in good chirality indicate that Bloch point propagation can be strongly influenced by the underlying atomic lattice. As the code enables us to determine precisely the position of the Bloch point during the motion, and since this can be achieved with a spatial resolution of a few picometers, we analyzed the Bloch point position and its motion inside a primitive cell of the lattice, as well as in a cubic unit cell, thereby further focusing on the bcc lattice structure. By projecting the position of the Bloch point at different time steps into the primitive unit cell of the lattice, we obtained a map of the probability density of the Bloch point during the propagation. This probability density is almost perfectly localized on certain surfaces of the Wigner-Seitz cell. In the submagnonic propagation regime we found that the Bloch point prefers to propagate along the center of the quadratic facets and tends to avoid the hexagonal ones. In the case of supermagnonic propagation, the distribution of the probability density changes only slightly. But the higher amount of energy introduced to the system by the external field allows the Bloch point to enter the hexagonal facets in addition to the quadratic ones. Nevertheless, the probability density to find a Bloch point on the hexagonal facets remains strongly reduced, by several orders of magnitude, in comparison to the quadratic ones.

In order to analyze the propagation dynamics in more detail we repeat the simulations on the field-driven Bloch point propagation under the influence of a 4 mT as well as 30 mT, but now we calculated the Bloch point position every 3 fs. This high temporal resolution gives access to some 20 to 100 data points of the Bloch point position inside of each cubic unit cell during the propagation. It thereby allows for a calculation of the Bloch point velocity with high temporal and spatial accuracy. Those studies demonstrate that a Bloch point entering a hexagonal surface accelerates up to 5000 m/s, whereas the global average is much lower in the range of 1300 m/s. This behavior provides an indication for the strong repulsive forces which restrict the Bloch point to the square surfaces of the Wigner Seitz cell in the case of a bcc lattice.

In conclusion, we demonstrated in this thesis a first dynamic multimodel study of the fundamental micromagnetic structure of Bloch points. After a detailed description of the algorithms, that have been developed and used, we gave a description of the Bloch point properties using the system of a soft-magnetic nanocylinder. For vortex domain walls in such cylinders we derived the depinning field for different diameters of the nanocylinder and demonstrated that the depinning field depends on the lattice orientation. We analyzed in detail the different propagation patterns and regimes of Bloch points and domain walls that develop in the two chiralities. Depending on the strength of the applied field, we found three characteristic propagation modes for the case of good chirality, namely a slow laminar motion, a breakdown regime and a regime in which the chirality is inverted. For the good chirality we demonstrated a strong difference between submagnonic and supermagnonic propagation, particularly in terms of the influence of the lattice orientation with respect to the propagation direction. For supermagnonically propagating Bloch points/domain walls we identified three typical propagation modes, namely a laminar, an oscillatory and a turbulent

one. By means of analytical calculations we concluded that the maximum velocity found in the first two supermagnonic propagation modes can be attributed to an intrinsic property of the Bloch point structure. In addition, we analyzed the Bloch point propagation with particular focus on the probability density inside of its position within the unit cell of the atomic lattice and showed that Bloch points can be found almost exclusively on specific surfaces and edges of the Wigner-Seitz cell.

Even though some results might be beyond the currently available experimental resolution, several effects, like the qualitative field dependence of the propagation velocities in the different propagation regimes might be experimentally accessible. Especially the very stable supermagnonic velocity regime of the good chirality could be interesting – not only from a fundamental perspective, but also from an application point of view. A field-independent constant domain wall motion could be a very advantageous feature for future storage devices and shift registers exploiting domain walls as units of information. The multimodel methods developed for this thesis should also be applicable for other simulation fields, such as future multiferroic simulators, where the interaction of domain patterns and domain walls with the atomic structure can be expected to be more important than in classical ferromagnetic materials.

# References


[1] W. Brown. *Micromagnetics*. Interscience tracts on physics and astronomy, no. 18. Interscience Publishers, 1963.

[2] W. F. Brown. *Magnetostatic Principles in Ferromagnetism*. en. North-Holland Pub. Co., 1962.

[3] H. Kronmüller and S. S. P. Parkin. *Handbook of magnetism and advanced magnetic materials*. Hoboken, NJ: John Wiley & Sons, 2007. ISBN: 978-0-470-02217-7.

[4] A. Aharoni. *Introduction to the theory of ferromagnetism*. Oxford; New York: Oxford University Press, 2000. ISBN: 978-0-19-850809-0.

[5] A. Hubert and R. Schäfer. *Magnetic Domains: The Analysis of Magnetic Microstructures*. en. Springer, 1998. ISBN: 978-3-540-64108-7.

[6] S. Middelhoek. *Domain Walls in Thin Ni -Fe Films*. In: *Journal of Applied Physics* **34** (4) (1963), p. 1054. DOI:10.1063/1.1729367.

[7] F. Bloch. *Zur Theorie des Austauschproblems und der Remanenzerscheinung der Ferromagnetika*. de. In: *Zeitschrift für Physik* **74** (5-6) (1932), p. 295. DOI:10.1007/BF01337791.

[8] L. Néel. *Energie des parois de Bloch dans les couches minces*. In: *CR Acad. Sci. Paris* **241** (1955), p. 533.

[9] B. Van Waeyenberge, A. Puzic, H. Stoll, K. W. Chou, T. Tyliszczak, R. Hertel, M. Fahnle, H. Bruckl, K. Rott, G. Reiss, I. Neudecker, D. Weiss, C. H. Back, and G. Schutz. *Magnetic vortex core reversal by excitation with short bursts of an alternating field*. In: *Nature* **444** (7118) (2006), p. 461. DOI:10.1038/nature05240.

[10] R. Hertel, S. Gliga, M. Fähnle, and C. M. Schneider. *Ultrafast Nanomagnetic Toggle Switching of Vortex Cores*. In: *Physical Review Letters* **98** (11) (2007), p. 117201. DOI:10.1103/PhysRevLett.98.117201.

[11] E. Feldtkeller. *Mikromagnetisch stetige und unstetige Magnetisierungskonfigurationen*. In: *Zeitschrift für angewandte Physik* **19** (1965), p. 530.

[12] W. Döring. *Point Singularities in Micromagnetism*. In: *Journal of Applied Physics* **39** (2) (1968), p. 1006. DOI:10.1063/1.1656144.

[13] A. P. Malozemoff and J. C. Slonczewski. *Magnetic domain walls in bubble materials*. Academic Press, 1979. ISBN: 978-0-12-002951-8.

[14] A. S. Arrott, B. Heinrich, and A. Aharoni. *Point Singularities And Magnetization Reversal In Ideally Soft Ferromagnetic Cylinders.* In: *IEEE Transactions on Magnetics* **MAG-15** (5) (1979), p. 1228. DOI:10.1109/TMAG.1979.1060342.

[15] M. J. Donahue and D. G. Porter. *OOMMF User's Guide, Version 1.0.* (Gaithersburg, MD: National Institute of Standards and Technology). 1999. URL: http://math.nist.gov/oommf/.

[16] R. Hertel. *Statische und dynamische Magnetisierungen in Nanostrukturen.* Habilitationsschrift Martin-Luther-Universität Halle-Wittemberg. 2005.

[17] S. S. P. Parkin, M. Hayashi, and L. Thomas. *Magnetic Domain-Wall Racetrack Memory.* In: *Science* **320** (5873 2008), p. 190. DOI:10.1126/science.1145799.

[18] M. Yan, C. Andreas, A. Kákay, F. García-Sánchez, and R. Hertel. *Fast domain wall dynamics in magnetic nanotubes: Suppression of Walker breakdown and Cherenkov-like spin wave emission.* In: *Applied Physics Letters* **99** (2011), p. 122505. DOI:10.1063/1.3643037.

[19] M. Yan, C. Andreas, A. Kákay, F. García-Sánchez, and R. Hertel. *Chiral symmetry breaking and pair-creation mediated Walker breakdown in magnetic nanotubes.* In: *Applied Physics Letters* **100** (25) (2012), p. 252401. DOI:10.1063/1.4727909.

[20] A. Hubert. *Mikromagnetisch singuläre punkte in bubbles.* In: *Journal of Magnetism and Magnetic Materials* **2** (1-3) (1975), p. 25. DOI:10.1016/0304-8853(75)90100-6.

[21] A. S. Arrott, B. Heinrich, T. L. Templeton, and A. Aharoni. *Micromagnetics of curling configurations in magnetically soft cylinders.* In: *Journal of Applied Physics* **50** (B3 1979), p. 2387. DOI:10.1063/1.326961.

[22] A. Hubert and W. Rave. *Arrott's ideal soft magnetic cylinder, revisited.* In: *Journal of magnetism and magnetic materials* **184** (1) (1998), p. 67. DOI:10.1016/S0304-8853(97)01125-6.

[23] C. Andreas, S. Gliga, and R. Hertel. *Numerical micromagnetism of strong inhomogeneities.* In: *Journal of Magnetism and Magnetic Materials* **362** (2014), p. 7. DOI:10.1016/j.jmmm.2014.02.097.

[24] T. Jourdan, A. Marty, and F. Lançon. *Multiscale method for Heisenberg spin simulations.* In: *Physical Review B* **77** (22) (2008), p. 224428. DOI:10.1103/PhysRevB.77.224428.

[25] T. Jourdan, A. Masseboeuf, F. Lançon, P. Bayle-Guillemaud, and A. Marty. *Magnetic bubbles in FePd thin films near saturation.* In: *Journal of Applied Physics* **106** (2009), p. 073913. DOI:10.1063/1.3243318.

[26] A. Kákay, E. Westphal, and R. Hertel. *Speedup of FEM Micromagnetic Simulations With Graphical Processing Units.* In: *IEEE Transactions on Magnetics* **46** (6) (2010), p. 2303. DOI:10.1109/TMAG.2010.2048016.

[27] R. E. Miller and E. B. Tadmor. *A unified framework and performance benchmark of fourteen multiscale atomistic/continuum coupling methods*. In: *Modelling and Simulation in Materials Science and Engineering* **17** (5) (2009), p. 053001. DOI:10.1088/0965-0393/17/5/053001.

[28] L. Landau and E. Lifshitz. *On the theory of magnetic permeability in ferromagnetic bodies*. In: *Phys. Z. Sowjetunion* **8** (1935), p. 153.

[29] T. Gilbert. *A Lagrangian formulation of the gyromagnetic equation of the magnetic field*. In: *Phys. Z. Sowjetunion* **100** (1955), p. 1243.

[30] T. Gilbert. *A phenomenological theory of damping in ferromagnetic materials*. In: *IEEE Transactions on Magnetics* **40** (6) (2004), p. 3443. DOI:10.1109/TMAG.2004.836740.

[31] A. C. Hindmarsh and R. Serban. *User Documentation for cvode v2.7.0*. Center for Applied Scientific Computing, Lawrence Livermore National Laboratory, 2012. URL: http://computation.llnl.gov/casc/sundials/documentation/documentation.html.

[32] D. L. Huber. *Dynamics of spin vortices in two-dimensional planar magnets*. In: *Physical Review B* **26** (7) (1982), p. 3758. DOI:10.1103/PhysRevB.26.3758.

[33] B. E. Argyle, E. Terrenzio, and J. C. Slonczewski. *Magnetic Vortex Dynamics Using the Optical Cotton-Mouton Effect*. In: *Physical Review Letters* **53** (2) (1984), p. 190. DOI:10.1103/PhysRevLett.53.190.

[34] J. P. Park, P. Eames, D. M. Engebretson, J. Berezovsky, and P. A. Crowell. *Imaging of spin dynamics in closure domain and vortex structures*. In: *Physical Review B* **67** (2) (2003), p. 020403. DOI:10.1103/PhysRevB.67.020403.

[35] R. G. Elías and A. Verga. *Magnetization structure of a Bloch point singularity*. In: *The European Physical Journal B* **82** (2011), p. 159. DOI:10.1140/epjb/e2011-20146-6.

[36] O. V. Pylypovskyi, D. D. Sheka, and Y. Gaididei. *Bloch point structure in a magnetic nanosphere*. In: *Physical Review B* **85** (22) (2012), p. 224401. DOI:10.1103/PhysRevB.85.224401.

[37] J. Reinhardt. *Gittertheoretische Behandlung von mikromagnetischen Singularitäten*. In: *Int. J. Magn* **5** (1973), p. 263.

[38] N. L. Schryer and L. R. Walker. *The motion of* 180° *domain walls in uniform dc magnetic fields*. In: *Journal of Applied Physics* **45** (12) (1974), p. 5406. DOI:10.1063/1.1663252.

[39] A. Thiaville and Y. Nakatani. *Domain-Wall Dynamics in Nanowires and Nanostrips*. In: *Spin Dynamics in Confined Magnetic Structures III*. Ed. by B. Hillebrands and A. Thiaville. Topics in Applied Physics 101. Springer Berlin Heidelberg, 2006, p. 161. ISBN: 978-3-540-20108-3.

[40] M. Yan, A. Kákay, C. Andreas, and R. Hertel. *Spin-Cherenkov effect and magnonic Mach cones*. In: *Physical Review B* **88** (22) (2013), p. 220412. DOI:10.1103/PhysRevB.88.220412.

[41] R. Hertel and J. Kirschner. *Magnetization reversal dynamics in nickel nanowires.* In: *Physica B: Condensed Matter* **343** (1-4) (2004), p. 206. DOI:10.1016/j.physb.2003.08.095.

[42] G. Binasch, P. Grünberg, F. Saurenbach, and W. Zinn. *Enhanced magnetoresistance in layered magnetic structures with antiferromagnetic interlayer exchange.* In: *Physical Review B* **39** (7) (1989), p. 4828. DOI:10.1103/PhysRevB.39.4828.

[43] *Magnetic field sensor with a thin ferromagnetic layer.* DE3820475 (C1) (Kernforschungsanlage Jülich GmbH). P. Grünberg. 1989.

[44] M. N. Baibich, J. M. Broto, A. Fert, F. N. Van Dau, F. Petroff, P. Etienne, G. Creuzet, A. Friederich, and J. Chazelas. *Giant Magnetoresistance of (001)Fe/(001)Cr Magnetic Superlattices.* In: *Physical Review Letters* **61** (21) (1988), p. 2472. DOI:10.1103/PhysRevLett.61.2472.

[45] T. Miyazaki and N. Tezuka. *Giant magnetic tunneling effect in Fe/Al2O3/Fe junction.* In: *Journal of Magnetism and Magnetic Materials* **139** (3) (1995), p. L231. DOI:10.1016/0304-8853(95)90001-2.

[46] Y. Martin and H. K. Wickramasinghe. *Magnetic imaging by "force microscopy" with* 1000 Å *resolution.* In: *Applied Physics Letters* **50** (20) (1987), p. 1455. DOI:10.1063/1.97800.

[47] P. Grütter, H. J. Mamin, and D. Rugar. *Magnetic Force Microscopy (MFM).* In: *Scanning Tunneling Microscopy II.* Ed. by R. Wiesendanger and H.-J. Güntherodt. Springer Series in Surface Sciences 28. Springer Berlin Heidelberg, 1992, p. 151. ISBN: 978-3-642-97365-9.

[48] M. Bode. *Spin-polarized scanning tunnelling microscopy.* In: *Reports on Progress in Physics* **66** (4) (2003), p. 523. DOI:10.1088/0034-4885/66/4/203.

[49] K. Koike and K. Hayakawa. *Scanning Electron Microscope Observation of Magnetic Domains Using Spin-Polarized Secondary Electrons.* In: *Japanese Journal of Applied Physics* **23** (Part 2, No. 3 1984), p. L187. DOI:10.7567/JJAP.23.L187.

[50] J. Unguris, G. G. Hembree, R. J. Celotta, and D. T. Pierce. *High Resolution Magnetic Microstructure Imaging Using Secondary Electron Spin Polarization Analysis in a Scanning Electron Microscope.* In: *Journal of Microscopy* **139** (2) (1985), RP1. DOI:10.1111/j.1365-2818.1985.tb02628.x.

[51] J. Kerr. *XLIII. On rotation of the plane of polarization by reflection from the pole of a magnet.* In: *Philosophical Magazine Series 5* **3** (19) (1877), p. 321. DOI:10.1080/14786447708639245.

[52] G. van der Laan, B. T. Thole, G. A. Sawatzky, J. B. Goedkoop, J. C. Fuggle, J.-M. Esteva, R. Karnatak, J. P. Remeika, and H. A. Dabkowska. *Experimental proof of magnetic x-ray dichroism.* In: *Physical Review B* **34** (9) (1986), p. 6529. DOI:10.1103/PhysRevB.34.6529.

[53] G. Schütz, W. Wagner, W. Wilhelm, P. Kienle, R. Zeller, R. Frahm, and G. Materlik. *Absorption of circularly polarized x rays in iron.* In: *Physical Review Letters* **58** (7) (1987), p. 737. DOI:10.1103/PhysRevLett.58.737.

[54] J. Stöhr, Y. Wu, B. Hermsmeier, M. Samant, G. Harp, S. Koranda, D. Dunham, and B. Tonner. *Element-specific magnetic microscopy with circularly polarized X-rays.* In: *Science* **259** (1993), p. 658.

[55] P. Fischer, G. Schütz, G. Schmahl, P. Guttmann, and D. Raasch. *Imaging of magnetic domains with the X-ray microscope at BESSY using X-ray magnetic circular dichroism.* In: *Zeitschrift für Physik B Condensed Matter* **101** (3) (1997), p. 313. DOI:10.1007/s002570050214.

[56] D. Weller and A. Moser. *Thermal effect limits in ultrahigh-density magnetic recording.* In: *IEEE Transactions on Magnetics* **35** (6) (1999), p. 4423. DOI:10.1109/20.809134.

[57] D. Thompson and J. Best. *The future of magnetic data storage techology.* In: *IBM Journal of Research and Development* **44** (3) (2000), p. 311. DOI:10.1147/rd.443.0311.

[58] J. C. Slonczewski. *Current-driven excitation of magnetic multilayers.* In: *Journal of Magnetism and Magnetic Materials* **159** (1) (1996), p. L1. DOI:10.1016/0304-8853(96)00062-5.

[59] A. P. Li, F. Müller, A. Birner, K. Nielsch, and U. Gösele. *Hexagonal pore arrays with a 50–420 nm interpore distance formed by self-organization in anodic alumina.* In: *Journal of Applied Physics* **84** (11) (1998), p. 6023. DOI:10.1063/1.368911.

[60] K. Nielsch, J. Choi, K. Schwirn, R. B. Wehrspohn, and U. Gösele. *Self-ordering Regimes of Porous Alumina: The 10 Porosity Rule.* In: *Nano Letters* **2** (7) (2002), p. 677. DOI:10.1021/nl025537k.

[61] M. Yan, A. Kákay, S. Gliga, and R. Hertel. *Beating the Walker Limit with Massless Domain Walls in Cylindrical Nanowires.* In: *Physical Review Letters* **104** (5) (2010), p. 057201. DOI:10.1103/PhysRevLett.104.057201.

[62] B. Heinrich and A. S. Arrott. *Critical slowing down of magnetic fluctuations.* In: *Physica B+C* **86–88, Part 3** (1977), p. 1293. DOI:10.1016/0378-4363(77)90887-7.

[63] R. Hertel and J. Kirschner. *Magnetic drops in a soft-magnetic cylinder.* In: *Journal of Magnetism and Magnetic Materials* **278** (3) (2004), p. L291. DOI:10.1016/j.jmmm.2004.02.032.

[64] W. Döring. *Über die Trägheit der Wände zwischen Weißschen Bezirken.* In: *Zeitschrift Naturforschung Teil A* **3** (1948), p. 373.

[65] W. Heisenberg. *Über quantentheoretische Umdeutung kinematischer und mechani scher Beziehungen.* In: *Zeitschrift für Physik* **33** (1) (1925), p. 879. DOI:10.1007/BF01328377.

[66] E. Feldtkeller and H. Thomas. *Struktur und Energie von Blochlinien in dünnen ferromagnetischen Schichten.* de. In: *Physik der kondensierten Materie* **4** (1) (1965), p. 8. DOI:10.1007/BF02423256.

[67] R. M. White. *Quantum theory of magnetism.* Berlin: Springer, 2007. ISBN: 978-3-540-69025-2.

[68] W. Nolting and A. Ramakanth. *Quantum theory of magnetism.* Heidelberg; New York: Springer, 2009. ISBN: 978-3-540-85415-9.

[69] N. W. Ashcroft and N. D. Mermin. *Solid state physics.* New York; London: Harcourt College Publishers, 1976. ISBN: 978-0-03-083993-1.

[70] J. D. Jackson. *Classical electrodynamics.* New York: Wiley, 1999. ISBN: 978-0-471-30932-1.

[71] W. Nolting. *Grundkurs Theoretische Physik 3.* Berlin [u.a.]: Springer, 2004. ISBN: 978-3-540-20509-8.

[72] H. Kronmüller. *Magnetische Eigenschaften fester Körper Teil I.* Vorlesungsskript. Institut für Theoretische und Angewandte Physik der Universität Stuttgart und Institut für Physik am Max-Planck-Institut für Metallforschung, 1988.

[73] M. Fähnle, A. Slavin, and R. Hertel. *Role of the sample boundaries in the problem of dissipative magnetization dynamics.* In: *Journal of Magnetism and Magnetic Materials* **360** (2014), p. 126. DOI:10.1016/j.jmmm.2014.02.031.

[74] D. A. Garanin. *Fokker-Planck and Landau-Lifshitz-Bloch equations for classical ferromagnets.* In: *Physical Review B* **55** (5) (1997), p. 3050. DOI:10.1103/PhysRevB.55.3050.

[75] N. Kazantseva, D. Hinzke, U. Nowak, R. W. Chantrell, U. Atxitia, and O. Chubykalo-Fesenko. *Towards multiscale modeling of magnetic materials: Simulations of FePt.* In: *Physical Review B* **77** (18) (2008), p. 184428. DOI:10.1103/PhysRevB.77.184428.

[76] C. Kittel. *Physical Theory of Ferromagnetic Domains.* In: *Reviews of Modern Physics* **21** (4) (1949), p. 541. DOI:10.1103/RevModPhys.21.541.

[77] A. Aharoni. *Exchange energy near singular points or lines.* In: *Journal of Applied Physics* **51** (1980), p. 3330. DOI:10.1063/1.328042.

[78] C. Andreas, A. Kákay, and R. Hertel. *Multiscale and multimodel simulation of Bloch-point dynamics.* In: *Physical Review B* **89** (13) (2014), p. 134403. DOI:10.1103/PhysRevB.89.134403.

[79] M. Pajda, J. Kudrnovský, I. Turek, V. Drchal, and P. Bruno. *Ab initio calculations of exchange interactions, spin-wave stiffness constants, and Curie temperatures of Fe, Co, and Ni.* In: *Physical Review B* **64** (17) (2001), p. 174402. DOI:10.1103/PhysRevB.64.174402.

[80] L. D. Landau, E. M. Lifshits, and L. P. Pitaevskii. *Electrodynamics of continuous media.* 2nd ed. Vol. 8. Oxford [England]: Butterworth-Heinemann, 1995. ISBN: 978-0-7506-2634-7.

[81] A. Aharoni. *Useful upper and lower bounds to the magnetostatic self-energy.* In: *IEEE Transactions on Magnetics* **27** (6) (1991), p. 4793. DOI:10.1109/20.278949.

[82] R. Skomski and J. M. D. Coey. *Permanent Magnetism.* Institute of Physics Publishing, 1999. 404 pp. ISBN: 978-0-7503-0478-8.

[83] L. Néel. *L'anisotropie superficielle des substances ferromagnétiques.* In: *CR Acad. Sci. Paris* **237** (1953), p. 1468.

[84] A. Landé. *Über den anomalen Zeemaneffekt (Teil I).* de. In: *Zeitschrift für Physik* **5** (4) (1921), p. 231. DOI:10.1007/BF01335014.

[85] A. Landé. *Über den anomalen Zeemaneflekt (II. Teil).* In: *Zeitschrift für Physik* **7** (1) (1921), p. 398. DOI:10.1007/BF01332807.

[86] P. Indelicato and A.-M. MÅrtensson-Pendrill. *Correlation and Relativistic Effects on Landé g J Factors of Atomic Ions.* In: *Hyperfine Interactions* (1) (2003), p. 127. DOI:10.1023/B:HYPE.0000004215.20631.17.

[87] J. G. Wright. *Ferromagnetism in epitaxial F.C.C. iron films.* In: *Philosophical Magazine* **24** (188) (1971), p. 217. DOI:10.1080/14786437108227381.

[88] N. Usov and S. Peschany. *Magnetization curling in a fine cylindrical particle.* In: *Journal of Magnetism and Magnetic Materials* **118** (3) (1993), p. L290. DOI:10.1016/0304-8853(93)90428-5.

[89] H. A. M. v. d. Berg. *Self-consistent domain theory in soft ferromagnetic media. I. Solenoidal distributions in elliptical thin-film elements.* In: *Journal of Applied Physics* **57** (6) (1985), p. 2168. DOI:10.1063/1.334357.

[90] H. A. M. v. d. Berg. *Self-consistent domain theory in soft-ferromagnetic media. II. Basic domain structures in thin-film objects.* In: *Journal of Applied Physics* **60** (3) (1986), p. 1104. DOI:10.1063/1.337352.

[91] H. A. M. v. d. Berg and A. H. J. v. d. Brandt. *Self-consistent domain theory in soft-ferromagnetic media. III. Composite domain structures in thin-film objects.* In: *Journal of Applied Physics* **62** (5) (1987), p. 1952. DOI:10.1063/1.339533.

[92] P. Weiss. *La variation du ferromagnetisme du temperature.* In: *Comptes Rendus* **143** (1906), p. 1136.

[93] B. Lilley. *Energies and widths of domain boundaries in ferromagnetics.* In: *Philosophical Magazine Series 7* **41** (319) (1950), p. 792. DOI:10.1080/14786445008561011.

[94] R. Hertel and A. Kakay. *Analytic form of head-to-head domain walls in thin ferromagnetic cylinders.* In: *arXiv:1401.0909 [cond-mat]* (2014).

[95] T. Senthil, A. Vishwanath, L. Balents, S. Sachdev, and M. P. A. Fisher. *Deconfined Quantum Critical Points.* In: *Science* **303** (5663) (2004), p. 1490. DOI:10.1126/science.1091806. (Visited on 08/05/2014).

[96] S. Gliga. *Ultrafast Vortex Core Dynamics Investigated by Finite-element Micromagnetic Simulations*. Forschungszentrum Jülich, 2010. ISBN: 978-3-89336-660-6.

[97] K. M. Lebecki, D. Hinzke, U. Nowak, and O. Chubykalo-Fesenko. *Key role of temperature in ferromagnetic Bloch point simulations*. In: *Physical Review B* **86** (9) (2012), p. 094409. DOI:10.1103/PhysRevB.86.094409.

[98] E. Schlömann. *Twisted domain wall structure in bubble films*. In: *Applied Physics Letters* **21** (5) (1972), p. 227. DOI:10.1063/1.1654355.

[99] A. Thiaville, J. M. García, R. Dittrich, J. Miltat, and T. Schrefl. *Micromagnetic study of Bloch-point-mediated vortex core reversal*. In: *Physical Review B* **67** (9) (2003), p. 094410. DOI:10.1103/PhysRevB.67.094410.

[100] M. Kammerer, M. Weigand, M. Curcic, M. Noske, M. Sproll, A. Vansteenkiste, B. V. Waeyenberge, H. Stoll, G. Woltersdorf, C. H. Back, and G. Schuetz. *Magnetic vortex core reversal by excitation of spin waves*. en. In: *Nature Communications* **2** (2011), p. 279. DOI:10.1038/ncomms1277.

[101] W. F. Brown. *Criterion for Uniform Micromagnetization*. In: *Physical Review* **105** (5) (1957), p. 1479. DOI:10.1103/PhysRev.105.1479.

[102] E. H. Frei, S. Shtrikman, and D. Treves. *Critical Size and Nucleation Field of Ideal Ferromagnetic Particles*. In: *Physical Review* **106** (3) (1957), p. 446. DOI:10.1103/PhysRev.106.446.

[103] A. Aharoni and S. Shtrikman. *Magnetization Curve of the Infinite Cylinder*. In: *Physical Review* **109** (5) (1958), p. 1522. DOI:10.1103/PhysRev.109.1522.

[104] R. Hertel. *Computational micromagnetism of magnetization processes in nickel nanowires*. In: *Journal of Magnetism and Magnetic Materials* **249** (1-2) (2002), p. 251. DOI:10.1016/S0304-8853(02)00539-5.

[105] H. Forster, T. Schrefl, W. Scholz, D. Suess, V. Tsiantos, and J. Fidler. *Micromagnetic simulation of domain wall motion in magnetic nano-wires*. In: *Journal of Magnetism and Magnetic Materials* **249** (1–2) (2002), p. 181. DOI:10.1016/S0304-8853(02)00528-0.

[106] E. Galkina, B. Ivanov, and V. Stephanovich. *Phenomenological theory of Bloch point relaxation*. In: *Journal of Magnetism and Magnetic Materials* **118** (3) (1993), p. 373. DOI:10.1016/0304-8853(93)90441-4.

[107] O. C. Zienkiewicz, R. L. Taylor, and J. Z. Zhu. *The finite element method: its basis & fundamentals*. Amsterdam [etc.]: Elsevier Butterworth-Heinemann, 2005. ISBN: 978-0-7506-6320-5.

[108] C. J. García-Cervera, Z. Gimbutas, and W. E. *Accurate numerical methods for micromagnetics simulations with general geometries*. In: *Journal of Computational Physics* **184** (1) (2003), p. 37. DOI:10.1016/S0021-9991(02)00014-1.

[109] C. Geuzaine and J.-F. Remacle. *Gmsh: A 3-D finite element mesh generator with built-in pre- and post-processing facilities*. In: *International Journal for Numerical Methods in Engineering* **79** (11) (2009), p. 1309. DOI:10.1002/nme.2579.

[110] G. Voronoi. *New applications of continuous parameters in the theory of quadratic forms.* In: *Journal für die Reine und Angewandte Mathematik* **133** (1907), p. 97.

[111] H. Kardestuncer, D. H. Norrie, and F. Brezzi. *Finite element handbook.* New York: McGraw-Hill, 1987. ISBN: 978-0-07-033305-5.

[112] D. Fredkin and T. R. Koehler. *Hybrid method for computing demagnetizing fields.* In: *IEEE Transactions on Magnetics* **26** (2) (1990), p. 415. DOI:10.1109/20.106342.

[113] T. R. Koehler and D. Fredkin. *Finite element methods for micromagnetics.* In: *IEEE Transactions on Magnetics* **28** (2) (1992), p. 1239. DOI:10.1109/20.123912.

[114] S. Salon and J. DAngelo. *Applications of the hybrid finite element-boundary element method in electromagnetics.* In: *IEEE Transactions on Magnetics* **24** (1) (1988), p. 80. DOI:10.1109/20.43861.

[115] W. H. Press. *Numerical recipes: the art of scientific computing.* Cambridge [u.a.: Cambridge Univ. Press, 2007. ISBN: 978-0-521-70685-8.

[116] S. Börm. *Construction of Data-Sparse $H^2$-Matrices by Hierarchical Compression.* In: *SIAM Journal on Scientific Computing* **31** (3) (2009), p. 1820. DOI:10.1137/080720693.

[117] S. Börm. *Approximation of solution operators of elliptic partial differential equations by H and $H^2$-matrices.* en. In: *Numerische Mathematik* **115** (2) (2010), p. 165. DOI:10.1007/s00211-009-0278-7.

[118] PCGPAK User's Guide (New Haven: Scientific Computing Associates, Inc.) 1984.

[119] *GNU General Public License, version 3.* http://www.gnu.org/licenses/gpl.html. Last retrieved 2012-05-10. 2007.

[120] *GNU General Public License, version 2 with modification.* http://geuz.org/gmsh/doc/LICENSE.txt. 1991.

[121] B. Delaunay. *Sur la sphere vide.* In: *Izv. Akad. Nauk SSSR, Otdelenie Matematicheskii i Estestvennyka Nauk* **7** (793-800) (1934), p. 1.

[122] J. Schöberl, J. Gerstmayr, and R. Gaisbauer. *NETGEN - automatic 3d tetrahedral mesh generator.* http://www.hpfem.jku.at/netgen/. Austrian Science Fund FWF (Special Research Project "Numerical and Symbolic Scientific Computing", Start Project "hp-FEM"), 2003.

[123] *GMSH online manual.* url=http://geuz.org/gmsh/doc/texinfo/gmsh.html.

[124] R. Hertel and C. M. Schneider. *Exchange Explosions: Magnetization Dynamics during Vortex-Antivortex Annihilation.* In: *Physical Review Letters* **97** (17) (2006), p. 177202. DOI:10.1103/PhysRevLett.97.177202.

[125] Y. Liu, S. Gliga, R. Hertel, and C. M. Schneider. *Current-induced magnetic vortex core switching in a Permalloy nanodisk.* In: *Applied Physics Letters* **91** (11) (2007), p. 112501. DOI:10.1063/1.2780107.

[126] T. Jourdan. *Approche multiéchelle pour le magnétisme. Application aux hétérogénéités structurales et aux singularités magnétiques.* PhD thesis. Université Joseph-Fourier-Grenoble I, 2008. URL: http://hal.archives-ouvertes.fr/docs/00/34/56/21/PDF/These_Jourdan.pdf.

[127] R. B. Fuller. *Building Consteuction.* 2682235. U.S. Classification: 52/81.3. 1954.

[128] H. Kenner. *Geodesic math and how to use it.* Berkeley: University of California Press, 2003. ISBN: 978-0-520-23931-9.

[129] A. C. Hindmarsh, P. N. Brown, K. E. Grant, S. L. Lee, R. Serban, D. E. Shumaker, and C. S. Woodward. *SUNDIALS: Suite of nonlinear and differential/algebraic equation solvers.* In: *ACM Trans. Math. Softw.* **31** (3) (2005), p. 363. DOI:10.1145/1089014.1089020.

[130] M. Weigand, B. Van Waeyenberge, A. Vansteenkiste, M. Curcic, V. Sackmann, H. Stoll, T. Tyliszczak, K. Kaznatcheev, D. Bertwistle, G. Woltersdorf, C. H. Back, and G. Schütz. *Vortex Core Switching by Coherent Excitation with Single In-Plane Magnetic Field Pulses.* In: *Physical Review Letters* **102** (7) (2009), p. 077201. DOI:10.1103/PhysRevLett.102.077201.

[131] C. A. Ross, M. Hwang, M. Shima, J. Y. Cheng, M. Farhoud, T. A. Savas, H. I. Smith, W. Schwarzacher, F. M. Ross, M. Redjdal, and F. B. Humphrey. *Micromagnetic behavior of electrodeposited cylinder arrays.* In: *Physical Review B* **65** (14) (2002), p. 144417. DOI:10.1103/PhysRevB.65.144417.

[132] P. Landeros and Á. S. Núñez. *Domain wall motion on magnetic nanotubes.* In: *Journal of Applied Physics* **108** (3) (2010), p. 033917. DOI:10.1063/1.3466747.

[133] J. A. Otálora, J. A. López-López, P. Vargas, and P. Landeros. *Chirality switching and propagation control of a vortex domain wall in ferromagnetic nanotubes.* In: *Applied Physics Letters* **100** (7) (2012), p. 072407. DOI:10.1063/1.3687154.

[134] C. Andreas. *Field driven dynamics of vortex domain walls in cylindrical nanotubes.* Humboldt-Universität zu Berlin, 2010.

[135] P. A. Cherenkov. *Visible emission of clean liquids by action of $\gamma$ radiation.* In: *Doklady Akademii Nauk SSSR* **2** (1934), p. 451.

[136] D. Bouzidi and H. Suhl. *Motion of a Bloch domain wall.* In: *Physical Review Letters* **65** (20) (1990), p. 2587. DOI:10.1103/PhysRevLett.65.2587.

[137] B. Hillebrands and K. Ounadjela. *Spin Dynamics in Confined Magnetic Structures I.* Springer, 2002. ISBN: 978-3-540-41191-8.

[138] R. Damon and J. Eshbach. *Magnetostatic modes of a ferromagnet slab.* In: *Journal of Physics and Chemistry of Solids* **19** (3–4) (1961), p. 308. DOI:10.1016/0022-3697(61)90041-5.

[139] B. A. Kalinikos and A. N. Slavin. *Theory of dipole-exchange spin wave spectrum for ferromagnetic films with mixed exchange boundary conditions.* en. In: *Journal of Physics C: Solid State Physics* **19** (35) (1986), p. 7013. DOI:10.1088/0022-3719/19/35/014.

[140] Origin (OriginLab, Northampton, MA).

[141] H.-G. Piao, J.-H. Shim, D. Djuhana, and D.-H. Kim. *Intrinsic pinning behavior and propagation onset of three-dimensional Bloch-point domain wall in a cylindrical ferromagnetic nanowire*. In: *Applied Physics Letters* **102** (11) (2013), p. 112405. DOI:10.1063/1.4794823.

[142] S. K. Kim and O. Tchernyshyov. *Pinning of a Bloch point by an atomic lattice*. In: *Physical Review B* **88** (17) (2013), p. 174402. DOI:10.1103/PhysRevB.88.174402.

[143] D. Roundy, R. E. Kraig, and M. L. Cohen. "Why is Polonium simple cubic?" In: *APS Meeting Abstracts*. Vol. -1. 2002, p. 28011.

[144] F. H. D. v. Batenburg and E. Gittenberger. *Ease of fixation of a change in coiling: computer experiments on chirality in snails*. In: *Heredity* **76** (3 1996), p. 278. DOI:10.1038/hdy.1996.41.

[145] D. A. Allwood, G. Xiong, M. D. Cooke, C. C. Faulkner, D. Atkinson, N. Vernier, and R. P. Cowburn. *Submicrometer Ferromagnetic NOT Gate and Shift Register*. en. In: *Science* **296** (5575 2002), p. 2003. DOI:10.1126/science.1070595.

[146] C. Kittel. *Introduction to solid state physics*. Hoboken, NJ: Wiley, 2005. ISBN: 978-0-471-68057-4.

[147] M. A. Ruderman and C. Kittel. *Indirect Exchange Coupling of Nuclear Magnetic Moments by Conduction Electrons*. In: *Physical Review* **96** (1) (1954), p. 99. DOI:10.1103/PhysRev.96.99.

[148] T. Kasuya. *A Theory of Metallic Ferro- and Antiferromagnetism on Zener's Model*. In: *Progress of Theoretical Physics* **16** (1) (1956), p. 45. DOI:10.1143/PTP.16.45.

[149] K. Yosida. *Magnetic Properties of Cu-Mn Alloys*. In: *Physical Review* **106** (5) (1957), p. 893. DOI:10.1103/PhysRev.106.893.

# Publications

## Papers

1. **Christian Andreas**, Attila Kákay, Riccardo Hertel *Multiscale and multimodel simulation of Bloch-point dynamics* Phys. Rev. B **89**, 134403 (2014)
   - Selected as an editors' suggestion in Phys. Rev. B
2. Petru Lunca Popa, Neil T. Kemp, Hicham Majjad, Guillaume Dalmas, Vina Faramarzi, **Christian Andreas**, Riccardo Hertel, Bernard Doudin *The magnetoelectrochemical switch* PNAS **111**, 10433 (2014)
3. **Christian Andreas**, Sebastian Gliga, Riccardo Hertel *Numerical micromagnetism of strong inhomogeneities* JMMM **362**, 7 (2014)
4. Ming Yan, Attila Kákay, **Christian Andreas**, Riccardo Hertel *Spin-Cherenkov effect and magnetic Mach cones* Phys. Rev. B **88**, 220412(R) (2013)
5. Bernard Doudin, Silvia Zanettini, Vina Faramarzi, Riccardo Hertel, **Christian Andreas**, Petru Lunca Popa *A device for controlling a chemical reaction by a magnetic field and different uses of said device* (filed 05. November 2013) European Patent Application 133065169 - 1361
6. Ming Yan, **Christian Andreas**, Attila Kákay, Felipe García Sanchez, Riccardo Hertel *Chiral symmetry breaking and pair-creation mediated Walker breakdown in magnetic nanotubes* Appl. Phys. Lett. **100**, 252401 (2012)
   - Featured on the Applied Physics Letters cover, 18 June 2012 issue 25
   - Selected for the July 2012 issue of Virtual Journal of Nanoscale Science & Technology
7. Ming Yan, **Christian Andreas**, Attila Kákay, Felipe García Sanchez, Riccardo Hertel *Fast domain wall dynamics in magnetic nanotubes* Appl. Phys. Lett. **99**, 122505 (2011)
   - Selected for the October 2011 issue of Virtual Journal of Nanoscale Science & Technology

## Conference/seminar contributions

- *Dynamic multimodel simulations of Bloch points with femtosecond/picometer resolution* (talk)
  IEEE Intermag, Dresden (Germany)(04 – 08 May 2014)
- *Multiscale study of Bloch points and their dynamics* (talk)
  78th Annual Meeting of the DPG, Dresden (Germany) (30 March – 04 April 2014)
- *Multiscale-multimodel simulation of Bloch point dynamics* (poster)
  CNRS-EWHA Winter School 2014, Strasbourg (France) (27 – 31 January 2014)

- *Multiscale - multimodel study of Bloch points in cylindrical nanowires* (talk)
  International Workshop on Magnetic Nanowires and Nanotubes, Kaub am Rhein (Germany) (12 – 15 May 2013)
- *Multiscale study of Bloch points and their dynamics* (talk)
  77th Annual Meeting of the DPG, Regensburg (Germany) (10 – 15 March 2013)
- *Hybrid FEM / atomistic simulation package for ferromagnetic nanostructures* (talk)
  6th International Conference on Multiscale Materials Modeling, Singapore (15 – 19 October 2012)
- *Micromagnetic study of field-driven vortex domain wall dynamics in Permalloy nanotubes* (invited seminar talk) University of Hamburg (24 May 2012)
- *Multiscale simulation of micromagnetic singularities* (talk)
  76th Annual Meeting of the DPG, Berlin (Germany) (25 – 30 March 2012)
- *Cherenkov-like spin wave emission by fast domain walls in Permalloy nanotubes* (talk)
  M-SNOWS Les Houches, France (5 – 10 February 2012
- *Cherenkov-like spin wave emisson by fast domain walls in Permalloy nanotubes* (poster)
  IEEE Intermag Taipei (Taiwan) (25 – 29 April 2011)
- *Cherenkov-like spin wave emission by supermagnonic domain walls in ferromagnetic nanotubes* (talk)
  75th Annual Meeting of the DPG, Dresden (Germany) (13 – 18 March 2011) )

# Acknowledgment

Performing my PhD study was most likely the biggest challenge of my live – at least to date. A successful end of this project would not have been possible without the help from a lot of people and several institutions, from a professional and a personal point of view; two things that seem to mix during such a project. The thesis was performed as a bilateral project between the Peter Grünberg Institut 6 at Forschungszentrum Jülich and the Institut de Physique et Chimie de Matérieux de Strasbourg (CNRS).

First, and for most I want to thank my supervisor Dr. habil. Riccardo Hertel. Riccardo, with your wide experience and deep knowledge of physics, mathematics and numerics you guided me though the challenges of the thesis. You always took the time for discussions, even for long ones, about algorithms, the Bloch point dynamics and many other interesting topics. You inspired and motivated me to find the best possible solutions. I am extremely thankful for your continuous help and your faith in my work. It was a honor to perform my PhD under your supervision.

I want to express my gratitude to my supervisor on the German side of this project, Prof. Claus M. Schneider. Thanks to his confidence in my work, support and kindness I was able to work at the most convenient places during the different periods of the PhD project.

I wish to thank Prof. P. Kratzer, Prof. H. P. Oepen, Prof. S. Haacke, Prof. A. Verga and Dr. A. Thiaville for refereeing this thesis. It is an honor for me to have such high-ranking group of reviewers. To Prof. S. Haacke I want to express my gratitude also for his support in the IPCMS.

I heartily thank Dr. Salia Cherifi who guided me not only through the small and big labyrinths of French conventions and administration but also helped me with many other topics.

My deep gratitude goes to Dr. Attila Kákay. I am extremely glad to have found in you such an outstanding physicists and invaluable friend. You took the time to explain to me the concepts of micromagnetism and their implementation in our code. Your personal and professional guidance meant a lot for me.

I sincerely thank Dr. Felipe Garcia-Sanchez for his friendship and insight in the different models of micromagnetism. You provided me the starting point of the multimodel implementation.

I am thankful to Dr. Ming Yan for many interesting discussions about different topics of micromagnetism. Thank you for the great collaboration concerning the studies of ferromagnetic nanotubes and the Spin-Cherenkov effect.

I also want to thank Dr. Sebastian Gliga for his support in the beginning of my stay in Jülich and especially the good collaboration.

I greatly appreciate the extraordinary support by the administrations of the

University Duisburg-Essen, of the FZ-Jülich, and of the CNRS IPCMS in Strasbourg to establish the cotutelle contract and to match misfitting procedures of the two universities.

To all the colleagues and friends I met in Jülich and in Strasbourg I want to thank you for the great time; in particular Manuel Gruber, Silvia Zanettini, Vina Faramarzi, Gaël Reecht, Céline Etrillard, Ondřej Vlasin and all the other people form Place du Café.

I am indebted to all my friends and family in Berlin who always backed me up and provided a great and warmth welcome whenever I visited them. You encouraged me not to lose faith in the project and helped me to relax.

*Finally I want to thank the most important people for me, my father Wilfried and my mother Regine. No words exists to express my gratitude for your unconditional love, support and unshaken faith in me. To you I dedicate this thesis.*

Band / Volume 76
**Temperature-Induced Metamagnetic Transition and Domain Structures of Single-Crystalline FeRh Thin Films on MgO(100)**
X. Zhou (2013), xi, 104 pp
ISBN: 978-3-89336-919-5

Band / Volume 77
**Interplay between Magnetism and Superconductivity in Iron Based High Temperature Superconductors**
S. Price (2013), 196 pp
ISBN: 978-3-89336-921-8

Band / Volume 78
**Magnetoresistance and transport in carbon nanotube-based devices**
C. Morgan (2013), viii, 131 pp
ISBN: 978-3-89336-926-3

Band / Volume 79
**Development of a relativistic full-potential first-principles multiple scattering Green function method applied to complex magnetic textures of nano structures at surfaces**
D. Bauer (2014), 193 pp
ISBN: 978-3-89336-934-8

Band / Volume 80
**Identifizierung von artifiziellen Liganden eines in Nanodiscs inkorporierten integralen Membranproteins**
M. Pavlidou (2014), 106 pp
ISBN: 978-3-89336-942-3

Band / Volume 81
**Interdomain Functional Dynamics of Phosphoglycerate Kinase Studied by Single-Molecule FRET**
M. Gabba (2014), v, 179 pp
ISBN: 978-3-89336-943-0

Band / Volume 82
**Silizium Nanoribbon Feld-Effekt Transistoren zur Kopplung an elektroaktive Zellen**
M. Jansen (2014), xvi, 181 pp
ISBN: 978-3-89336-944-7

Band / Volume 83
**Microscopic description of the inverse Faraday effect at subpicosecond time scales**
D. Popova (2014), 183 pp
ISBN: 978-3-89336-962-1

Schriften des Forschungszentrums Jülich
Reihe Schlüsseltechnologien / Key Technologies

Band / Volume 84
**Neutron Scattering**
Lectures of the JCNS Laboratory Course held at Forschungszentrum Jülich and at the Heinz Maier-Leibnitz Zentrum Garching
edited by Th. Brückel, G. Heger, D. Richter, G. Roth and R. Zorn (2014), ca. 360 pp
ISBN: 978-3-89336-965-2

Band / Volume 85
**Neutron Scattering**
Experiment Manuals of the JCNS Laboratory Course held at Forschungszentrum Jülich and at the Heinz Maier-Leibnitz Zentrum Garching
edited by Th. Brückel, G. Heger, D. Richter, G. Roth and R. Zorn (2014), ca. 195 pp
ISBN: 978-3-89336-966-9

Band / Volume 86
**Development and Characterization of a Microfluidic Magnetic Oscillation Reactor for Enzymes**
D. Jussen (2014), xxi, 131 pp
ISBN: 978-3-89336-974-4

Band / Volume 87
**Submolecular imaging with atomic force sensor from single molecule or atom**
G. Kichin (2014), 140 pp
ISBN: 978-3-89336-976-8

Band / Volume 88
**Multiscale Multimodel Simulation of Micromagnetic Singularities**
C. Andreas (2014), xix, 188 pp
ISBN: 978-3-89336-983-6

Weitere ***Schriften des Verlags im Forschungszentrum Jülich*** unter
http://wwwzb1.fz-juelich.de/verlagextern1/index.asp

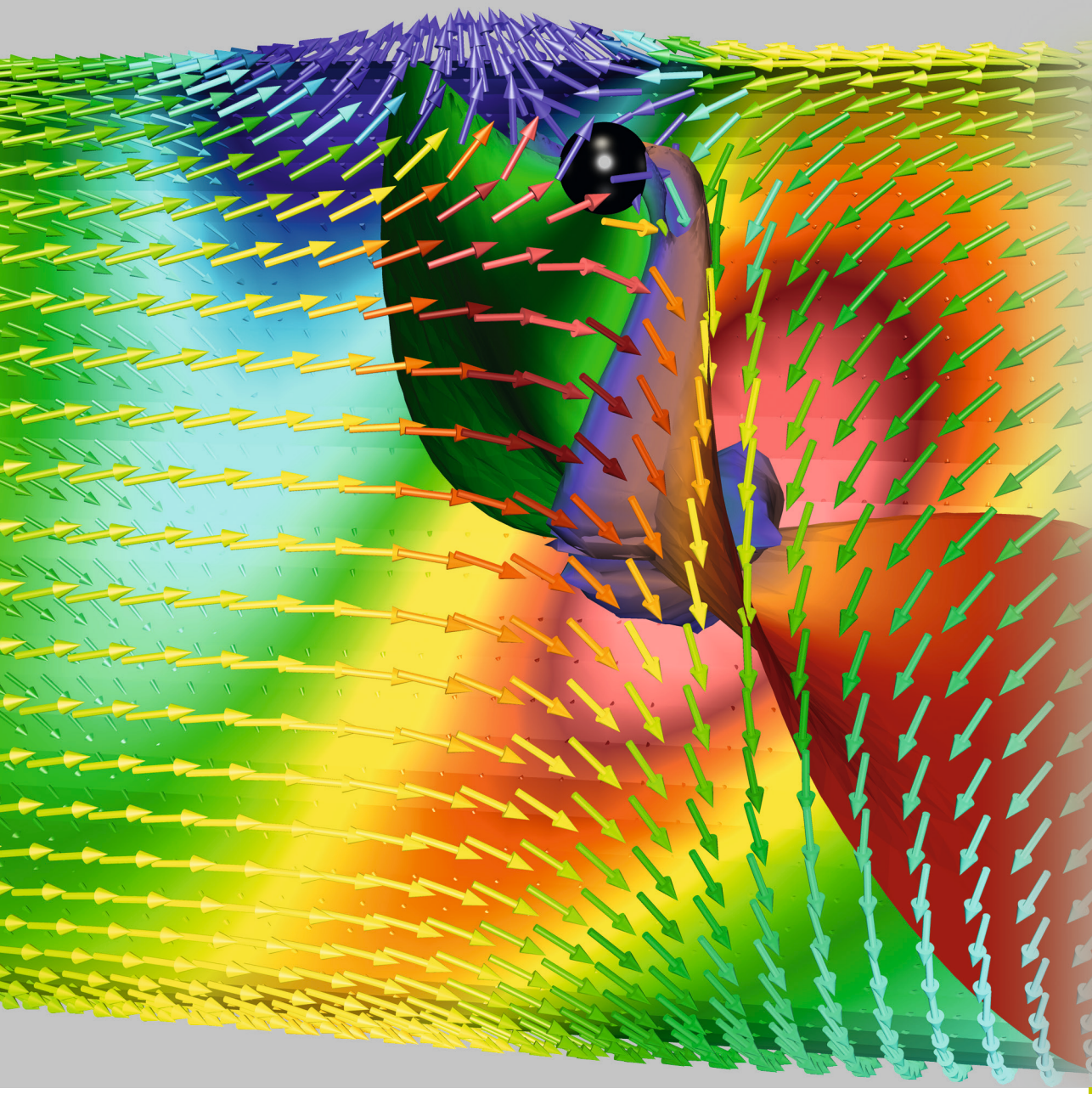

Schlüsseltechnologien / Key Technologies
Band / Volume 88
ISBN 978-3-89336-983-6

JÜLICH
FORSCHUNGSZENTRUM